Wideband Bi-static and Monostatic STAR Antenna Systems

by

Prathap Valale Prasannakumar

B.E., Visvesvaraya Technological University, Belgaum, India, 2011

M.S., University of Colorado, Boulder, USA, 2017

A thesis submitted to the

Faculty of the Graduate School of the

University of Colorado in partial fulfillment

of the requirements for the degree of

Doctor of Philosophy

Department of Electrical, Computer, and Energy Engineering

May 2019

This thesis entitled:

Wideband Bi-static and Monostatic STAR Antenna Systems

written by Prathap Valale Prasannakumar

has been approved for the Department of Electrical, Computer, and Energy Engineering

Dejan S. Filipović

Mohamed A. Elmansouri

Date

The final copy of this thesis has been examined by the signatories, and we

find that both the content and the form meet acceptable presentation standards

of scholarly work in the above mentioned discipline.

Valale Prasannakumar, Prathap (Ph.D., Electrical Engineering)

Wideband Bi-static and Monostatic STAR Antenna Systems

Thesis directed by Professor Dejan S. Filipović

The thesis presents the design, and development of novel wideband Simultaneous Transmit And Receive (STAR) antenna systems. A STAR or in-band full-duplex system has the potential to double the throughput of a communication channel, which is highly important for the next-generation wireless networks. Similarly, these systems could increase the effectiveness of Electronic Warfare (EW) and Support (S) operation, by facilitating spectrum/channel sensing while jamming. A self-interference (SI) phenomenon, where the transmitter disrupts its own receiver is a major challenge in the practical realization of any radio frequency (RF) system. High isolation (>130 dB) is often needed to overcome this SI. A common approach to achieve this high isolation is some combination of cancellation levels such as antenna, analog, digital and signal processing layers. The thesis focuses on maximizing the isolation at the antenna layer, which is crucial for the system implementation. This is attained by researching bi-static, monostatic, and quasi-monostatic architectures that do not rely on polarization multiplexing.

Bi-static configurations use separate TX and RX antennas. Hence, the SI can be minimized by increasing the separation between apertures, embedding high impedance surfaces (HISs), or by recessing the RX antenna inside the absorber, as demonstrated in this thesis. The advantages and limitations of each of these techniques are analyzed through full-wave simulations and measurements. High power capable, wideband, metallic quad ridge horn (QRH) antennas are first developed and bi-static, dual polarized STAR system is realized with them. Measured isolation >60 dB is demonstrated between the TX and RX apertures operating over 6-19 GHz and separated by 4λ at the turn on frequency. Isolation >70 dB is obtained in the 18-45 GHz bi-static dual polarized in-band duplex antenna system. Further, the influence of scatterers on system isolation is discussed.

Bi-static configurations are robust, and system isolation is less sensitive to the asymmetries in the

geometry. However, they require significant area particularly when highly directive apertures are needed. When a bi-static approach is applied to reflector-based systems, the overall size of the system is often prohibitively large. Hence, a monostatic configuration is highly desired for a high gain system. In this thesis, a monostatic STAR configuration, operating from 4-8 GHz, is developed by feeding the designed circularly polarized (CP) reflector antenna with all-analog beamforming network (BFN) consisting of two 90° and 180° hybrids and two circulators. The BFN is arranged to cancel the coupled/leaked signal from the antenna and circulators, by creating 180° phase difference between the TX and RX reflected signals. Theoretically, with ideal devices this approach can provide infinite isolation. In practice, the isolation is limited by the electrical and geometrical imbalances. Nonetheless, using COTS components with noticeable imbalances, average isolation >30 dB is achieved with the fabricated system, which is on average 15 dB higher than the isolation obtained with a conventional circulator approach.

Finally, a quasi-monostatic STAR approach is proposed to address the limitations of bi-static and monostatic configurations. The demonstrated configuration can achieve 30 dB (on average) higher isolation than the monostatic reflector architecture with the same BFN components. The quasi-monostatic STAR antenna system consists of a parabolic reflector antenna for transmission, and a receiving antenna mounted back-to-back with the reflector feed. To increase the system isolation both the TX feed and the RX antenna are CP. Further, to achieve the same TX and RX polarization the TX feed is LHCP, and the RX antenna is RHCP. The LHCP fields from the TX feed undergo polarization reversal after bouncing back from the reflector, thereby, the TX and RX operate in the same polarization. The approach is less sensitive to the BFN imbalances and geometrical asymmetries. An average measured isolation of 61 dB is obtained using COTS components with relatively-high amplitude and phase imbalances. Further, the same concept is extended to mm-waves (18-45 GHz), where a dual reflector antenna with the RX mounted behind the unused area of secondary-reflector is employed to achieve STAR operations.

Dedication

To my parents, sister, and all my teachers.

Acknowledgments

First, I would like to thank my advisor, Prof. Dejan Filipović, for his enduring guidance throughout my Ph.D. The lessons I learned from him in innovative thinking, problem-solving, and teaching methodology have helped me to become a better researcher. I thank my thesis committee: Prof. Zoya Popović, Prof. Taylor Barton, Dr. Mohamed Elmansouri, and Dr. W. Neill. Kefauver for taking the time to be part of the committee and in helping to shape my research.

I extend my warm regards to all the alumni and visiting members of the Antenna Research Group (ARG). My antennas, papers, and presentations wouldn't have been better without the inspiration, supervision, and valuable inputs from Dr. Mohamed Elmansouri. I thank Dr. Ehab Etellisi, Dr. Elie Tianang, Dr. Prathamesh Pednekar, Mauricio Pinto, and John Marino for sharing my joy and pain during this journey. Prof. Gregor Lasser's words have always been motivating and refreshing both academically, and in social life; I thank him for remaining a good mentor and friend. I am grateful to Dr. Maxim Ignatenko and Dr. Jaegeun Ha for sharing their profound knowledge, and Mr. Ljubodrag Boskovic for his precious time in fabricating the antennas. Thank you to the current members of ARG: Liliana Rodriguez, Carlos Mulero Hernandez, Aman Samaiyar, Jake Cazden, Conrad Andrews, Selena Leitner, and Merarys Caquias. I would also like to thank students of Prof. Popović's, Prof. Kuester's, Prof. Barton's, Prof. Psychogiou's, and Prof. Lasser's research groups.

I couldn't have sailed this far without the constant support of my family and friends. Words are inadequate to express gratitude to my mother, father, and sister for putting my wellbeing before their own. I am also thankful to my best friends who patiently read and edited the thesis.

Finally, I thank the funding agencies, Office of Naval Research (ONR), Naval Research Laboratories (NRL), and Army Research Office (ARO) for supporting me and my research.

Contents

List of Tables

List of Figures

Chapter 1

Introduction

Communication is an integral part of our everyday life. It has undergone cycles of evolution alongside human civilization; from wired telephones and telegrams (Fig. 1.1) [1, 2] to modern day mobile networks. On the 17th of December 1902, Guglielmo Marconi demonstrated the first successful radio link across the transatlantic, and since then wireless communication has advanced from 1G to current 4G or long-term evolution (LTE). Resource sharing techniques such as simplex, half-duplex, and full duplex have been extensively explored to accommodate the increase in the number of subscribers and their growing need for higher data rate [3]. Nonetheless, the frequency spectrum is more congested than ever before, and thirst for speed has only multiplied. Additionally, the available radio channels have turned into an expensive commodity, which worsens the situation [4]. Hence, there is a need for new communication systems and

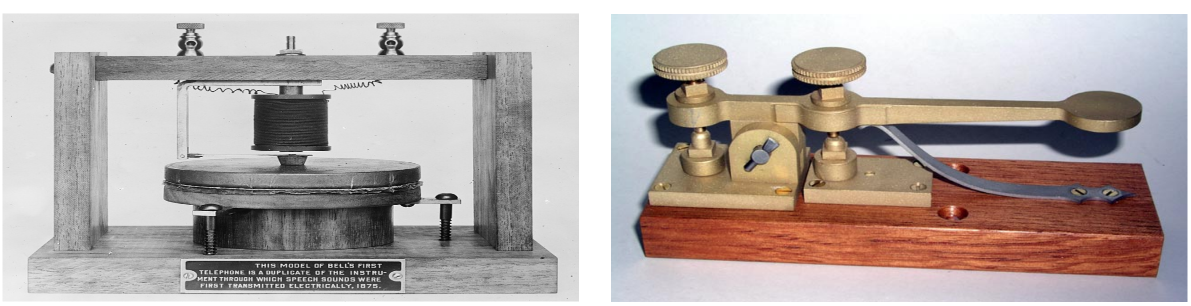

(a) (b)

Figure 1.1: Pictures of (a) Graham Bell phone, and (b) telegraph key.

architectures that can enhance the efficiency of legacy and current radio networks.

In parallel to the commercial needs, the importance of state-of-the-art electronic countermeasure (ECM) methods has increased exponentially since the dawn of Radars in WWII [5]. Recent research and development in high-performance wideband antennas combined with advancement in signal processing units have made the countermeasure a daunting task for the forces [5]. Therefore, to be potent, jammers should be wideband and have the capability to sense the spectrum while transmitting, to be potent.

Simultaneous transmit and receive systems that can send and receive at the same time, frequency, and polarization have the potential to increase the throughput of a communication channel, as well as enhance the effectiveness of electronic warfare (EW) systems. This thesis deals with the passive front ends of these systems.

1.1 Simultaneous Transmit and Receive System Overview

1.1.1 Conventional Full Duplex System

Existing communication systems rely on either time division duplexing (TDD) or frequency division duplexing (FDD) to achieve instantaneous communication. In TDD, each subscriber uses different intervals for transmission (TX) and reception (RX) over the same frequency channel. The proximity of these time slots makes TX and RX to appear simultaneous. Therefore, less than 50% of the available frame period is effectively consumed, for TX or RX as shown in Fig. 1.2 (a). Contrarily, FDD users send and receive at

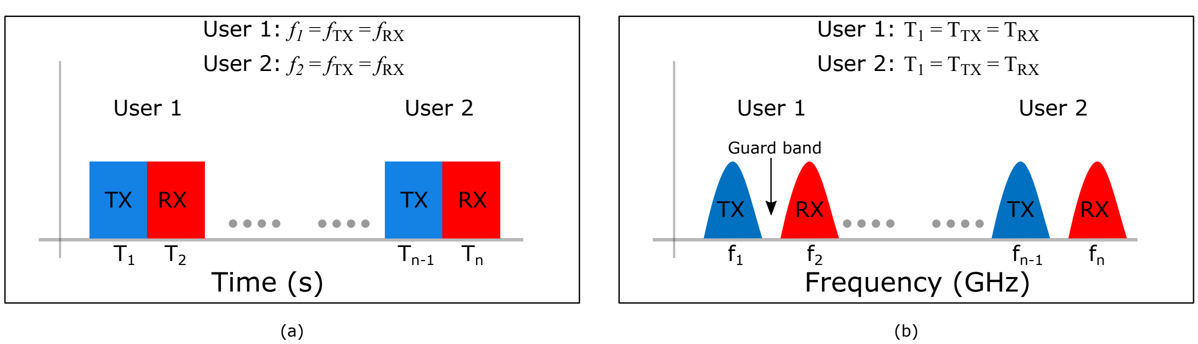

Figure 1.2: (a) TDD time frame, and (b) FDD frequency spectrum.

the same time, however, over different uplink and downlink frequencies (Fig. 1.2 (b)). Therefore, reducing the maximum number of subscribers or channel capacity to less than half. These comparisons signify that neither of the schemes is true full duplex.

Radars, and EW jammers and sensors are few analogous systems that use time multiplexing for transmission and reception. Transmit and Receive switches consisting of pin diodes, tubes and or solid-state devices perform the required transitions [6], as illustrated in Fig. 1.3 (a). This inherent latency could become detrimental in countermeasures, specifically in attempting to jam wideband systems. Devices like diplexers can overcome the limitation of switching time, however, TX and RX will occur at different frequencies. Alternatively, circulator, a non-reciprocal 3-port device, mitigates both the switching and frequency separation problems. The functional schematic shown in Fig. 1.3 (b), indicates that high power from the transmitting amplifier could potentially saturate the receiver LNA if the isolation between the circulator ports is low. Circulators having isolation in the order of 20-30 dB are available as COTS components [7, 8]. However, it is difficult to find wideband circulators that provide high isolation and can handle high power. In the conventional architecture (see Fig. 1.3 (b)), the power coupled to the RX is finally determined by the input impedance match of the antenna, irrespective of the circulator's isolation. This phenomenon is due to the signal leakage between the ports, and the reflected signals from the antenna mismatch, which will eventually end up in the RX. Therefore, there is a need for a system architecture that can mitigate or minimize some of the problems of duplexing and single circulator approaches.

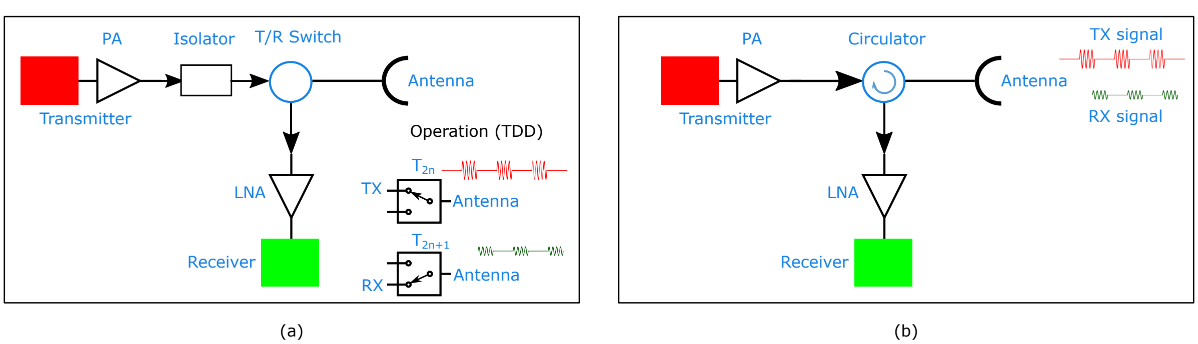

Figure 1.3: Schematic of conventional radar system using (a) time switching, and (b) circulator.

1.1.2 STAR System

A STAR or in-band full duplex system can transmit and receive at the same and in the same frequency channel, as demonstrated in Fig. 1.4. This feature can theoretically double the throughput of a communication system [9–12]. Additionally, a STAR capable EW system can monitor the spectrum while jamming, which increases the effectiveness of the electronic attack [5, 13]. Specifically:

- Demo Wi-Fi networks, and in legacy systems. Specifically, AWS-3 tactical links used by the US Army, which covers NATO band III (1.35-2.7 GHz) [14]. In-band full duplex topology when implemented in these legacy systems aids in overcoming the bandwidth shortage caused due to spectrum reallocation.

- To enhance the effectiveness of EW operations such as in Navy's In-Top [15] and signal processing electronic attack RFIC (SPEAR) programs [13].

- For data links between unmanned aerial vehicle (UAV), and drones to commanding base, as well as among them. The absence of duplexing in time can significantly reduce the latency in control links. Similarly, using the full frequency spectrum will increase the data rates, thus, reducing operational downtime.

- Early adoption of STAR in wireless technologies, such as 5G, will only benefit the improved data speeds. It will also, help in establishing dominance over mm-Wave EW and S operations.

The in-band full duplex system in [9], and [10] uses existing Wi-Fi antennas and systems to achieve

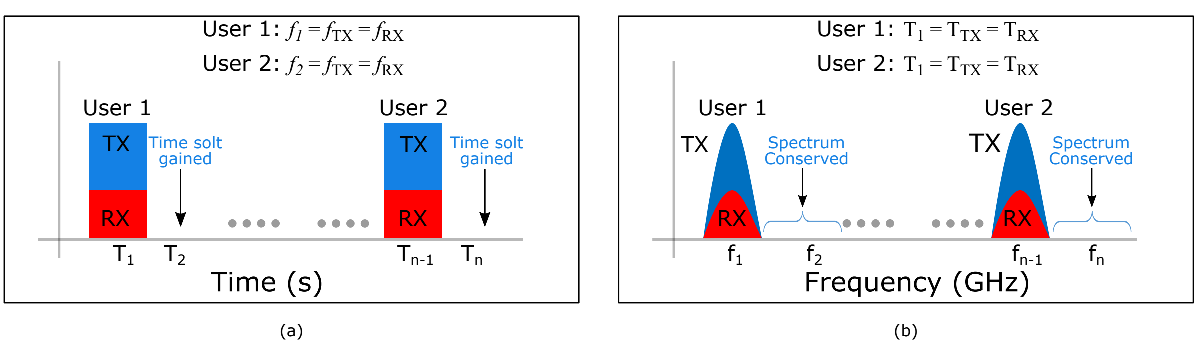

Figure 1.4: (a) Time frame, and (b) frequency spectrum of a conceptual STAR system.

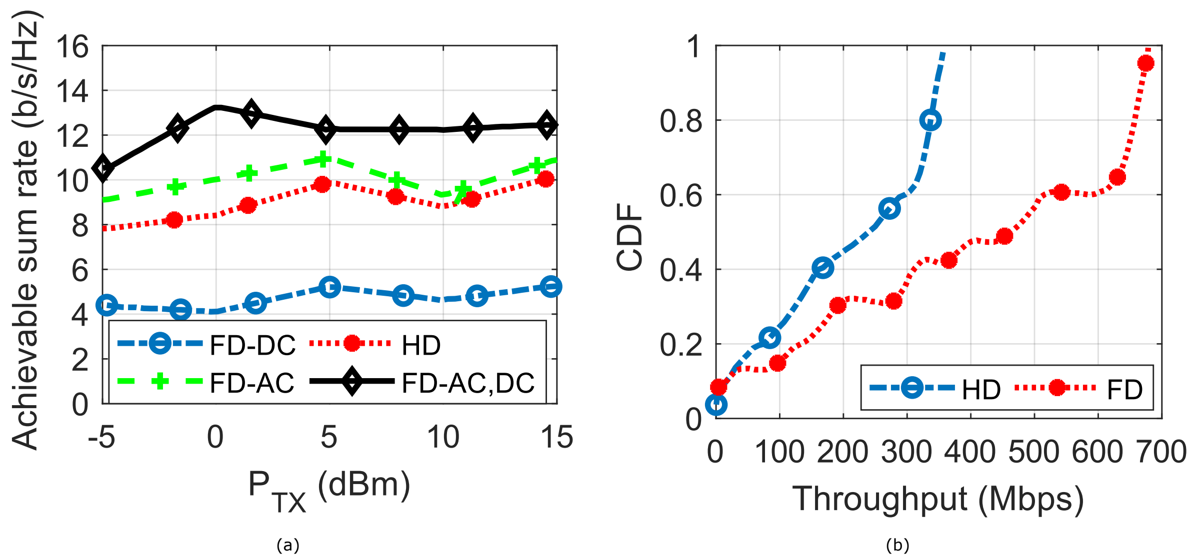

Figure 1.5: (a) Total data rate comparison of half duplex, full-duplex with and without analog and digital cancellation [9], and (b) Cummulative data function (CDF) of half-duplex and in-band full-duplex with cancellation [10].

1.62x and 1.87x (maximum), respectively, improvement in the system throughput (see Fig. 1.5). Importantly, the gain in data rate is influenced by self-interference (SI) between the co-located TX and RX, as computed and practically demonstrated in [9]. Therefore, minimizing the power coupled from the TX to RX is the primary design constraint of any STAR system. The interference can be reduced at various domains and stages to obtain the desired isolation 100 - 150 dB, depends on the output power; channel bandwidth and noise figure of the receiver.

1.1.3 Design Challenges

Generally, it is difficult for radios to transmit and receive on the same frequency band and time slot because of the interference that results, as quoted in [16]. The statement is valid since the power from TX could saturate its own collocated RX.

High power radiated from the TX deteriorates the SNR by injecting additional interference, specifically, increases the signal-to-interference-plus-noise ratio (SINR). In-band harmonics and non-linear components generated by the PA and transmitter chain components further raise the noise floor. Hence, the desired

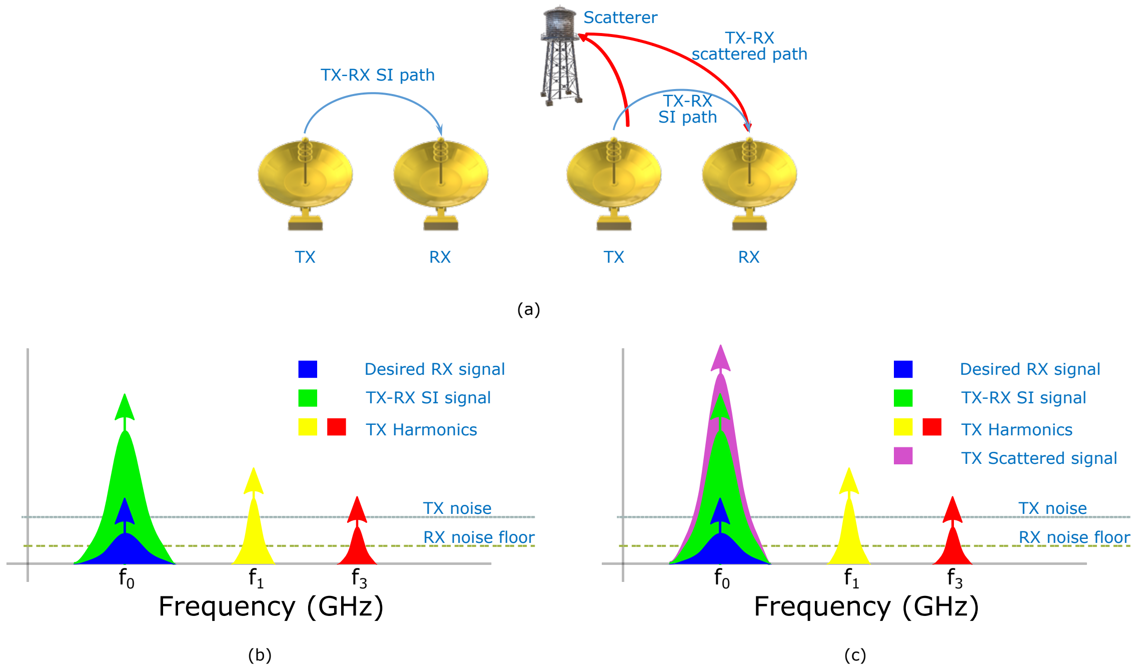

Figure 1.6: (a) Interfering signal paths in bi-static STAR, (b) and (c) signal levels without and with scattering, respectively.

RX signal's power falls below the interference level, as demonstrated in Fig. 1.6 [9, 12]. Also, this leads to quantization errors from the analog-to-digital converters (ADC), despite maintaining the LNA above saturation. Thus, the resulting performance of the in-band full duplex system could be lower than that of the conventional duplexing methods [9]. The scenario worsens in the presence of scattered and multipath signals, which are reflected from the nearby objects, as illustrated in Fig. 1.6. Therefore, minimizing the SI or the coupling between antennas is the primary challenge of the system design. Tolerances in the fabrication, asymmetries in the antenna geometries, and the amplitude and phase imbalances in the feeding and beam forming components intensify the design and implementation challenges of a STAR system. This thesis proposes techniques to increase the isolation from the antenna layer, which alleviates the design problem.

1.1.4 System Architecture

The functional block diagram of a typical in-band full duplex system includes PAs, isolators, antennas (monostatic / bi-static / quasi-monostatic), LNAs, and SI cancelation circuits, as illustrated in Fig. 1.7. The

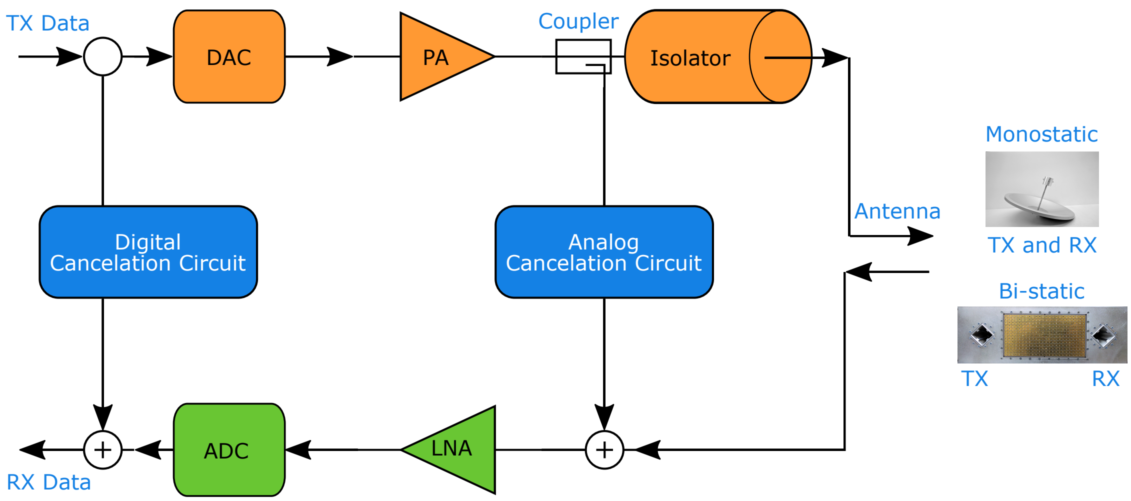

Figure 1.7: Functional block diagram of a STAR system.

antenna sub-system provides the first level of isolation, which is in the order of 15 - 70 dB and it is critical for the following layers to perform effectively. Analog cancelation circuits are second in the hierarchy. These consists of N-segment delay lines and attenuators [10]. A sample of the transmitted signal is tapped from the output of the PA, which is then attenuated and delayed in time before mixing with the received signal. This process will reduce both the linear and non-linear components of TX interference at the RX [10]. Cancellation up to 30 dB is achieved in [9, 10], which is important to prevent LNA from saturating and in reducing quantization errors from ADC. However, the unpredictability of non-linear components generated from the TX chain hampers the efficacy of analog cancelation layer. Digital processing sub-system further minimizes the interference level, typically by 30 dB [10]. Additionally, the availability of the transmitted data, beforehand, aids in recovering intended RX information out of the unwanted interference. Despite these, lowering the non-linear signal's magnitude is a daunting task, due to the non-availability of the accurate models [10].

Therefore, maximizing the isolation from the antenna layer is crucial and beneficial for the following reasons:

- Cancellation applies to both linear and non-linear components.

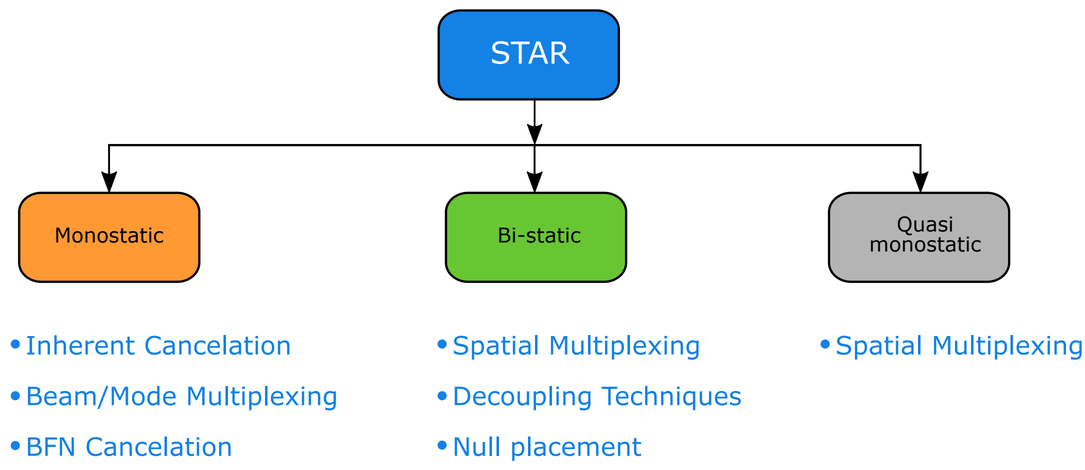

Figure 1.8: Flow chart indicating existing STAR topologies.

- System complexity is reduced; system can be more compact.
- The responsivity of STAR functionality is increased due to the elimination of additional processes and stages, which is desired for EW and S operations.

Hence, the thesis focus is on methods to achieve isolation ranging from 30 dB - 70 dB from the antenna layer itself. Additionally, combing the signal cancellation from digital and analog layers can potentially add 30 dB - 40 dB, which leads to isolation >130 dB (i.e., 40 dB below the noise floor [10]).

1.1.5 STAR Antenna Systems

Monostatic, bi-static, and quasi-monostatic are the typically used approaches to realize STAR antenna systems as illustrated in Fig. 1.8. Monostatic configuration uses single aperture or array of antennas for TX and RX operations. There are three known ways to design a monostatic configuration that does not utilize polarization or beam duplexing. The first approach depends on the geometrical symmetry of the antenna to cancel the coupled signals at the RX port [17] (Fig. 1.9 (a)). Similarly, STAR operation is achieved from a sequentially rotated array (SRA) of dual polarized apertures (patch antennas) by feeding it through the modified Butler matrices [18–21] (Fig. 1.9 (c), (d), and (f)). In the second technique, the transmitted and

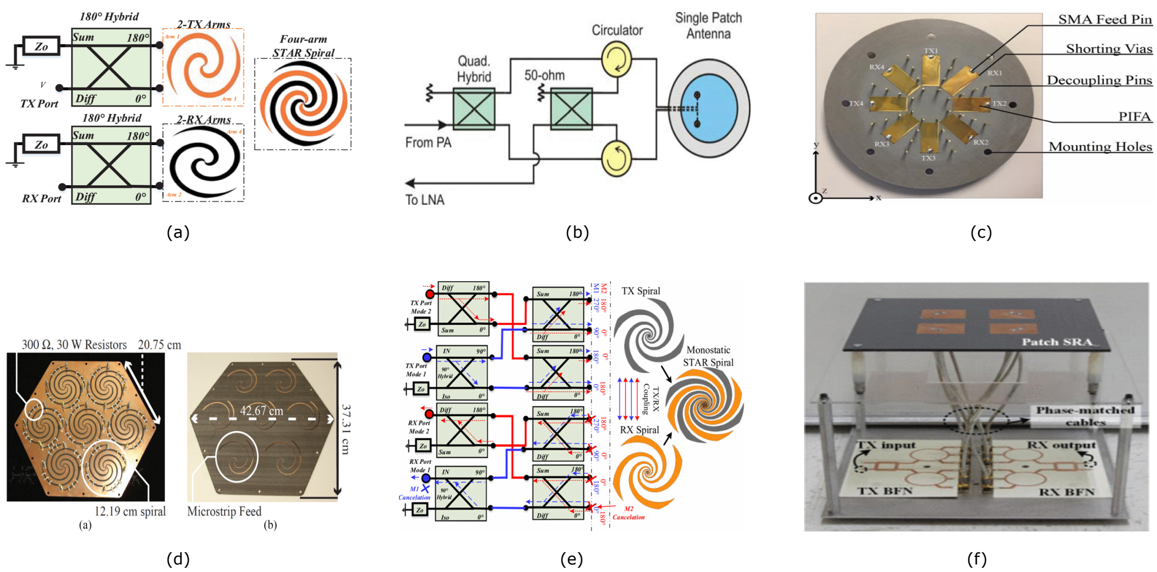

Figure 1.9: Examples of monostatic STAR systems: (a) planar spiral [17], (b) balanced circulator approach [22], (c) circular PIFA array [20], (d) hexagonal spiral array [21], (e) 8-arm mode multiplexed spiral, and (f) SRA STAR [18].

coupled signals are nullified at the receiver terminal by rerouting them through the beam forming network (BFN) components consisting of 90° and 180° hybrids, and circulators [22–25] (Fig. 1.9 (b)). The third approach uses orthogonality between the modes and far field patterns to achieve high system isolation [26]. Monostatic techniques discussed thus far use the same radiating elements as TX and RX antenna, which reduces the overall system size. Hence, it is suitable for space and size constrained platforms. However, the system isolation is sensitive to the asymmetries and imbalances in the BFN and antenna geometry, which limits the maximum level of SI cancellation [22, 27]. Fig. 1.9 shows the pictures of selected monostatic configurations.

On the other hand, in a bi-static STAR, separate antennas function as a TX and RX and typically, they are placed close to each other or share platform. Hence, the system isolation is a function of TX/RX antennas radiation patterns, and the surface currents/waves on the shared ground plane, and near-field multi path. Therefore, desired SI cancellation is achieved by increasing the separation between the antennas (Fig. 1.10 (f)) [28], recessing the RX inside the absorbers [15] (Fig. 1.10 (a)), embedding high impedance surfaces or current absorbers between the flush mounted radiating elements (Fig. 1.10 (c) and (e)) [29], and/or through

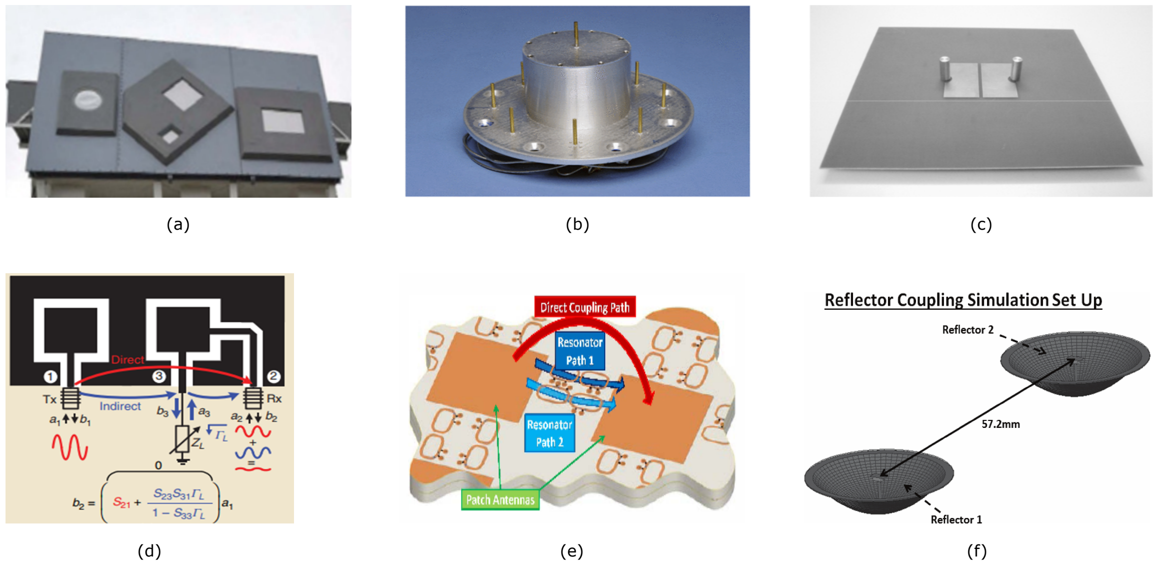

Figure 1.10: Examples of bi-static systems: (a) ONR's In-Top array [15], (b) monopole ring array [30], (c) monopole with decoupling structure, (d) polarization diversity STAR, (e) baffle filter, and (f) parabolic reflector STAR [28].

techniques such as null placement [30] (Fig. 1.10 (b)). The nature of these decoupling techniques provides robustness to system isolation against imbalances and asymmetries. However, the bi-static configuration requires two individual antennas, which increases the overall size especially at low frequencies with high gain antennas. A selected few bi-static antenna systems from the literature are illustrated in Fig. 1.10.

Quasi-monostatic is the middle ground between monostatic and bi-static approaches [31, 32]. The technique relies on spatial separation as well as on additional signal cancellation from BFN to provide high isolation. This phenomenon makes the system isolation more robust to asymmetries and leads to low SI between co-located TX and RX. In its current form [31,32] the overall area occupied by the antenna system is decided by the size of the TX. Thus, the architecture has a smaller footprint analogous to monostatic STAR, however, the system gain for TX and RX is dissimilar due to the difference in their aperture size.

1.2 Thesis Motivation

Wideband antennas are employed in all aspects of EW ranging from spectrum sensing, access denial to jamming. Hence, broadband, dual polarized STAR system is preferred for effective operation. High power capable antennas such as planar spirals, log periodic, and aperture antennas are extensively studied in literature [33–35]. However, high frequency operation imposes constraints on the selection of antennas and feed mechanisms. For example, continuous wave (CW) power handling capacity of N series connectors drops from ~2000 W to 600 W when operating frequency increases from 1 GHz to 9 GHz. Thus, type and class of transmission lines are critical. Waveguides are known to handle power in the order of KW [36]. However, the single mode bandwidth of hollow waveguides is $\leq$ an octave. Double and quad ridged waveguides mitigate this issue and can achieve $\geq$3:1 single mode bandwidth [37]. Hence, quad ridge horn (QRH) may provide desired dual polarization and wideband operation. These antennas require Ortho-mode transducers (OMTs) to achieve dual linear polarization. Despite the extensive works, the bandwidth of existing OMTs in literature is less than 3:1. Therefore, one of the goals of this research is to design a wideband, dual polarized, high power capable antenna and feeding network.

Isolating co-located RX from the TX is crucial for STAR functionality as explained in previous sections. Techniques such as bandgap structures [38], baffle filters [39], defective ground plane [40], metallic quarter-wave chokes or corrugations [41], artificial soft and hard surfaces [42], and bed-of-nails (BON) [43] have been used in the past to minimize coupling between the antennas. Despite the effectiveness of these structures in reducing surface wave/currents, the operation bandwidth is limited to an octave or less. Cascading band gap structures [44] mitigates this restriction to a certain extent. However, the number of cascaded elements determines the bandwidth and hence, the structure needs to be larger to provide the same level of cancellation over the wide range of frequencies. Therefore, in this thesis a printed reactive surface (capacitive) (PRS) is designed and demonstrated to work over 3:1 bandwidth. Additionally, the design trade-offs of three main types of high impedance surfaces (HIS) are discussed. Further, the thesis analyzes the impact of neighboring scatterers and antennas on system isolation, which is demonstrated by designing two shared aperture platforms covering 0.5 - 45 GHz (dual polarized) and 0.5 - 110 GHz (single polarized).

Bi-static STAR systems consume a relatively larger area, which increases with a decrease in frequency. Alternatively, a monostatic approach uses half the physical size, while providing high isolation [17, 22]. However, there has not been any high gain antenna based monostatic configuration. Hence, this thesis describes the design of an axis-symmetric parabolic reflector STAR and analyzes the influence of reflector on system performance. The achievable isolation is sensitive to the imbalances and asymmetries in the BFN and antenna geometry. Therefore, a new configuration called quasi-monostatic STAR is designed and developed in this research. The configuration is more resilient to the imbalances and achieves higher isolation than the monostatic reflector in-band full duplex system.

Recently, various government organizations and companies have been showing interest in mm-Wave frequencies because of its unexplored potential for EW and 5G communications. The higher path loss is one of the parameters that systems must overcome to establish links and to be effective at these frequencies. Therefore, high gain antennas are strongly desired. Prime feed or axis symmetric reflectors could provide the required gain [45]. However, the long feeding lines increase the loss in the TX and RX chain. This signal attenuation is typically overcome by using Cassegrain reflectors where the feed is closer to the transmitter [45, 46]. Additionally, minute anomalies, imperfections, and imbalances will have higher impact on system isolation because of the smaller wavelength. Therefore, the quasi-monostatic configuration is adopted to minimize the influence. Further, this approach uses the unutilized area behind the sub-reflector to house the RX antenna, which has not been discussed in open literature. Finally, STAR functionality is achieved by operating both TX and RX antennas in same polarization, and frequency.

1.3 Thesis Organization

- Chapter 2 focuses on the design of a quad ridge horn (QRH) and ortho-mode transducer (OMT) functioning from 6 GHz to 19 GHz (i.e., 3.1:1 impedance bandwidth). Modeling and performance of E-plane bend, Y-junction or E-plane bifurcation, and the turnstile junction are described. Methods such as split block-CNC machining and wire EDM are employed to fabricate the designed antennas and auxiliary components. The concept is further extended to design a dual polarized QRH operating from 18 - 45 GHz.

- Chapter 3 outlines the theory of operation of high impedance surfaces (HIS), specifically, metallic corrugations, bed-of-nails, and printed reactive surface. The chapter also investigates the design parameters, the bandwidth of operation, and the tradeoffs between these three surfaces. It further discusses the isolation between two flush mounted QRHs configured in bi-static STAR antenna systems. Importantly, the influence of embedding decoupling structures such as corrugations, bed of nails (BON), PRS (or metasurface), and recessing RX in an absorber cavity, on the system isolation are investigated. The impact of these approaches on the impedance match and far field performance of the antennas are described.

- Chapter 4 discusses design of high gain monostatic STAR antenna system. The focus is on the design of broadband CP reflector antenna with STAR functionality and high system isolation. Further, the chapter introduces a balanced circulator BFN, which can provide theoretically infinite isolation due to signal cancellation at the RX port. Impact of imbalances, asymmetries, and the roughness of the reflector surface on achievable isolation are discussed.

- Chapter 5 proposes a new configuration termed quasi-monostatic STAR. The operational principle, the design of feed and the RX antenna are discussed. An in-depth explanation of the coupling mechanism in a quasi-monostatic configuration is given. Further, the advantage and robustness of this architecture over the monostatic approach are illustrated.

- Chapter 6 expands the aforementioned concepts to the design of a Cassegrain reflector antenna with high gain and in-band full duplex capability, operating over mm-Wave frequencies from 18 - 45 GHz. The configuration includes the conventional dual reflector antenna, and an RX antenna mounted behind the sub-reflector. The design of reflector's feed (QRH), the RX antenna, and the working mechanism are explained. This chapter also discusses the trade-offs between the reflector size and its influence on crucial parameters such as gain, isolation, and impedance match of the system. The feasibility and benefits of employing a tightly coupled array as the RX antenna are also outlined.

- Chapter 7 presents the thesis conclusions, contributions, and suggestions for future work.

Chapter 2

Wideband Dual Polarized Quad Ridge Horn Antenna

2.1 Introduction

Long haul communication and EW operations require high power or equivalent isotropically radiated power (EIRP) to be effective. These impose constraints on the antenna design and its performance. Specifically, for application such as SPEAR, the feed should be dual polarized and support 1.5 KW power [13] over minimum of 3:1 (impedance) bandwidth. Hence, the antenna needs to be lossless. Aperture antennas such as pyramidal, conical and ridge horns can meet these requirements [36, 46–48]. Therefore, a dual polarized QRH operating over 6-19 GHz will meet the specification, which also aligns with the requirements of band-III of the SPEAR program [13]. There has been extensive research on design of QRH [48–53]. However, minimizing the antenna profile is still challenging, especially, when the antenna should have an aperture $\leq 0.66\,\lambda^2$ and length as small as possible. These physical restrictions affect the impedance match of the antenna and achieving VSWR ≤ 2 becomes tedious. This low VWSR is preferred to facilitate high input power since high reflections due to mismatch can harm the transmitter and can increase the system loss. Further, the power handling also influences the feeding mechanism. For example, a compact method of feeding QRH by using two orthogonal coaxial probes connecting opposite ridges as described in [49, 52] is not desired, though it provides the required bandwidth. The proximity of the probes could potentially lead to arching and hinder the input power handling capacity. Additionally, the intricacy of fabrication and sensitivity of the antenna performance to manufacturing tolerance is significant, especially at high frequencies. Contrarily, the feeding technique in [50] overcomes the problem of the proximity of the exciting probes. However, the 180° hybrids are required to implement the approach, which could become the bottleneck for input power. Furthermore, recent advancement in non-metal based additive manufacturing can help to fabricate lightweight and low-cost prototypes with shorter turnaround time. However, experimental demonstrations indicate that typical, plastic 3D printed, and copper plated horns will have lower power handling [54]. Therefore, antennas fabricated in metal are preferred. Hence, this research is focused on design of an all metallic, double ridge waveguide based ortho-mode transducer (OMT). The designed OMT has wider operational bandwidth in comparison to the OMTs in [36], and [48]. Also, the antenna has aperture of size $3.3 \times 3.3\,\mathrm{cm}^2$ ($0.66\lambda \times 0.66\lambda$) and length of 19 cm including OMT (10 cm aperture + 9 cm OMT).

Recently, there has been an increased interest in using mm-Wave frequencies for EW applications. A dual polarized, high power capable QRH is even more suitable at these high frequencies. The antenna is designed using a similar approach as that of the 6-19 GHz QRH. However, the performance is more sensitive to the machining tolerances. Hence, suitable measures are taken during the design and fabrication, which is explained in this chapter.

This chapter is organized into five sub-sections:

- Section 2.2 explains the design of a QRH with focus on the importance of the profile of the ridges and the aperture matching. Standard and modified cross-sections of double ridge waveguide along with their cut-off frequencies are also discussed.

- Section 2.3 presents a brief review of QRH feeding techniques and their trade-offs.

- Section 2.4 describes the design of an OMT with great emphasis on designing bends, bifurcations or power dividers, and turnstile junctions. Further, the performance of the OMT with the horn is evaluated.

- Section 2.5 outlines the design, fabrication, and performance of the mm-Wave QRH.

2.2 Antenna Design

The dual-polarized QRH operating from 6-19 GHz is designed in two steps. First, the quad ridge aperture is engineered to have a minimum reflection. Second, a turnstile junction based OMT is designed for a reflection coefficient less than -10 dB. The cross-section of the standard double ridge waveguide (WRD650) is modified to achieve good impedance match with square quad ridge (SQR) waveguide and single mode operation from 6 to 18.6 GHz as illustrated in Fig. 2.1. The dimensions of the modified and standard WRD650 cross sections are shown in Fig. 2.2 (a) and (b), respectively. The increase in a_{dr} lowers the cut-off frequency of the TE_{10} mode. Similarly, reducing the edr and increasing the hdr of the waveguide will increase the turn on frequency of TE_{20} mode by capacitively loading the waveguide [37], [55]. The resulting cross section of the SQR waveguide, which has fundamental mode cut-off frequency below 6 GHz is shown in Fig. 2.2 (c).

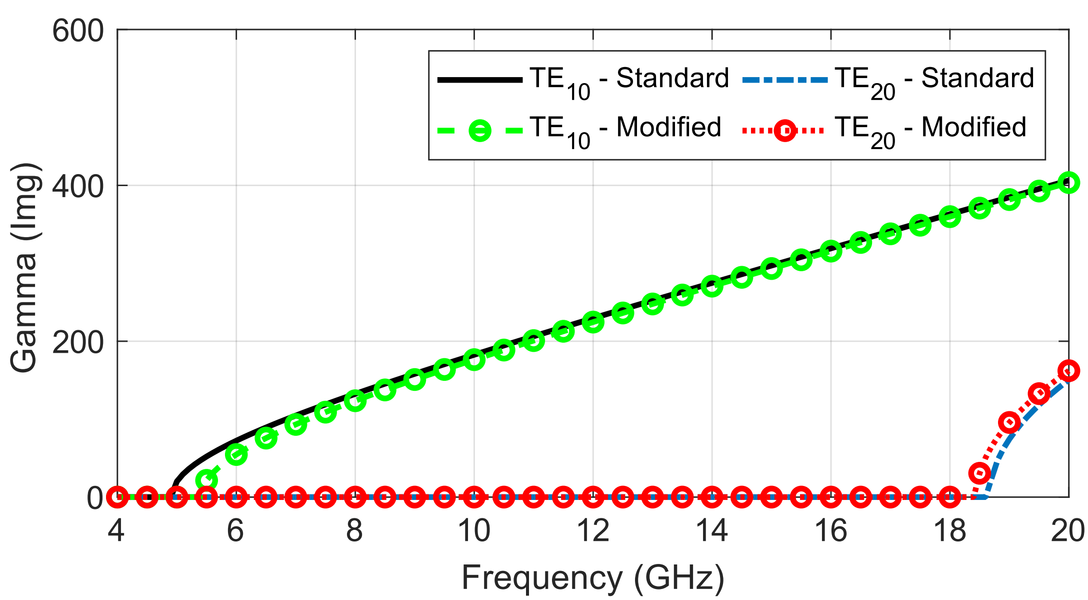

Figure 2.1: Propagation constant of TE_{10} and TE_{20} modes of standard and modified WRD650 waveguides.

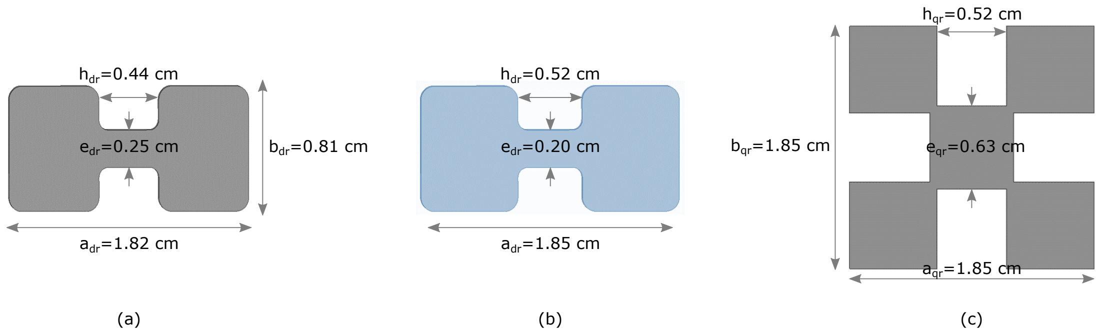

Figure 2.2: Cross section of (a) standard, (b) modified WRD650 double ridge waveguides, and (c) square quad ridge waveguide.

2.2.1 QRH Aperture

The impedance match between the feed waveguide (at the throat of the horn) and the free space is critical for achieving low overall reflection coefficient. The length, width, and the profile of the flare play a significant role in minimizing reflections from the horn aperture [56]. Loading the waveguide with ridges reduces the cut-off frequency of the fundamental mode along with its impedance. Specifically, the Z_0 of the designed SQR waveguide is approximately equal to $50\,\Omega$, which is lower than that of both, a double ridge waveguide, and free space, as illustrated in Fig. 2.3. These impedances are calculated using Z_{pi} (impedance calculated from power (P) and current (I)) definition in HFSS – FEM [57]. The disparity between free space and the SQR cross-section will result in a poor match. Additionally, the ridges confine the electric fields near them (see Fig. 2.4). Hence, the ridge profile and length are essential for the impedance match, along with the horn's flare.

Ridge tapers such as linear, exponential, and $\sin^2$ have been explored in literature [49]. In this work, a Klopfenstein taper is adopted for the horn of length 8 cm and the aperture size of $3\,\text{cm} \times 3$ cm, as depicted in Fig. 2.5. The dimensions of the antenna are chosen based on the strong desire to maintain low profile. The Klopfenstein tapered ridge results in a lower reflection coefficient than the linear taper, for the considered length and aperture size as shown in Fig. 2.6. The diffraction of fields from the aperture edges is another source of deterioration in the impedance match of horn antennas. Typically, these fields are minimized by rolling the edges of the aperture as demonstrated in Fig. 2.5 (c), which is also known as

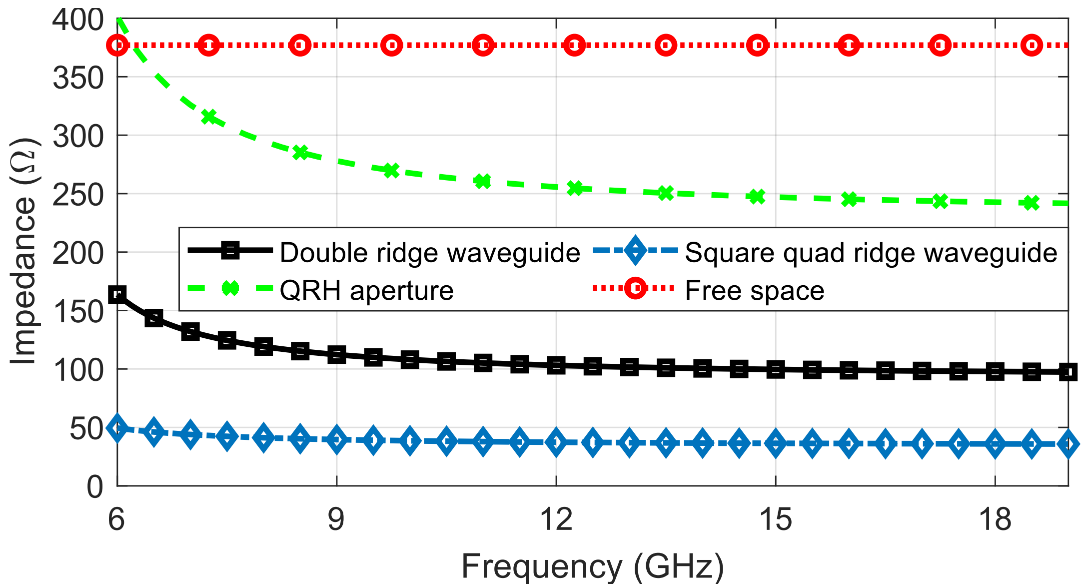

Figure 2.3: Impedance of modified WRD650, SQR waveguides, QRH at the aperture, and free space.

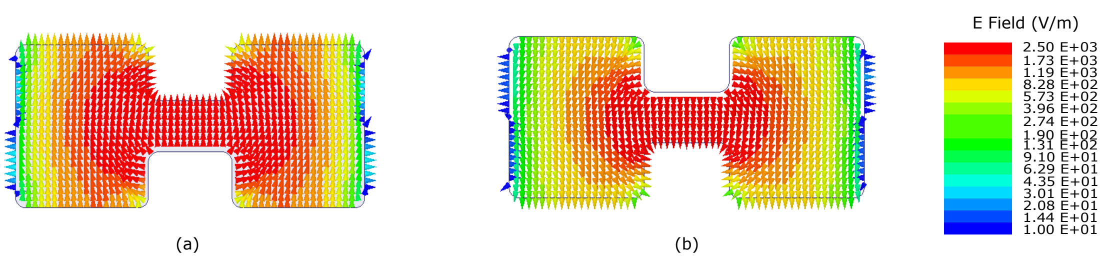

Figure 2.4: Electric field distribution of TE_{10} inside modified WRD650 at frequencies 6 and 19 GHz, computed using FEM in HFSS.

aperture matching [58]; generally, elliptic or convex curved surfaces as employed. A semi-elliptic curve is used in this design to preserve the QRH's flush mountable capability. It is noticed that curving the ridges is also essential to reduce the mismatch due to diffraction at higher frequencies. The improvement in $|S_{11}|$ with aperture matching is clear from Fig. 2.6.

2.3 QRH Feeding Techniques

The feed of the QRH should support the full operation bandwidth of the antenna with VSWR <2 and high input power. Further, the QRH can be excited in various ways. One approach employs two orthogonal coaxial cables to launch the respective TE_{10} modes, as shown in Fig. 2.7 (a). This approach can support

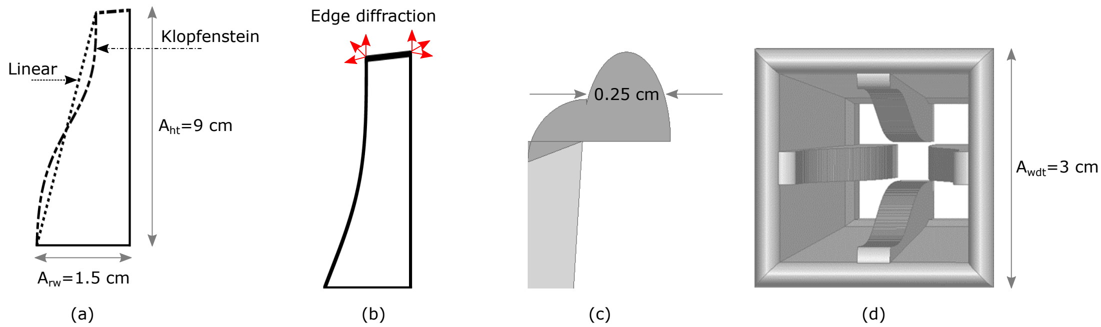

Figure 2.5: (a) Profile of linear and Klopfenstein tapers, (b) illustration of edge diffraction, (c) aperture matching with dimensions, and (d) QRH aperture.

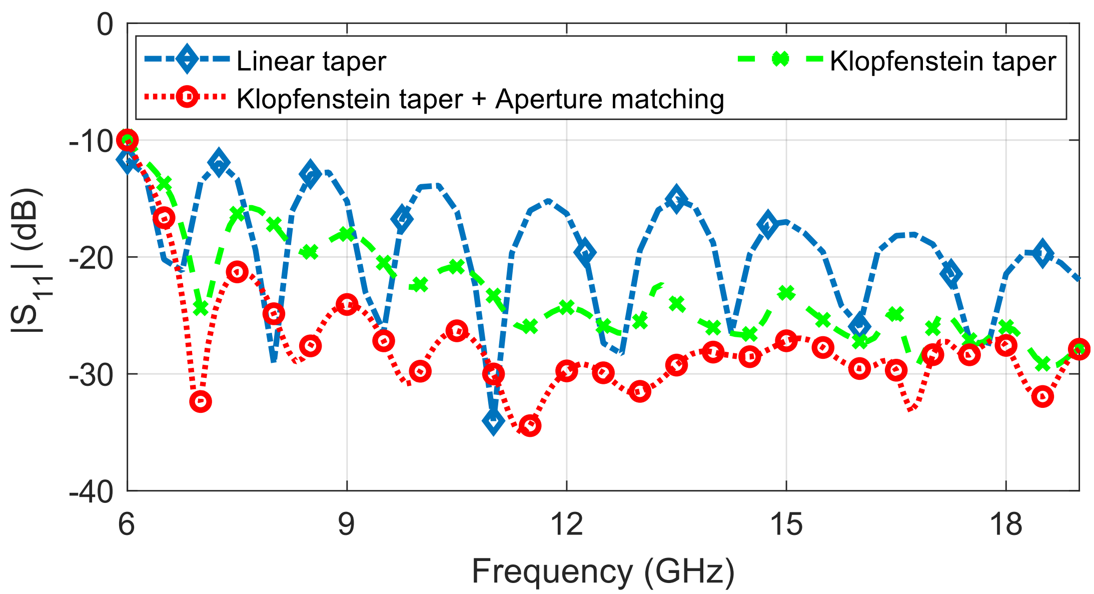

Figure 2.6: |S11| in dB of the QRH with linear and Klopfenstein tapers, and aperture matching.

wideband operation. However, the reflection coefficient of the second polarization (for the probe away from the cavity bottom) has spikes which deteriorate the antenna's performance. Moreover, the proximity between the probes can significantly hinder the high power operation. This limitation can be overcome by using the four ports approach described in [50] Fig. 2.7 (b). The technique in [50] requires two additional 180° hybrids, which now limit the power handling and increase the system complexity. Hence, there is the need for a feeding method which operates over 3.1:1 bandwidth and supports high power operation.

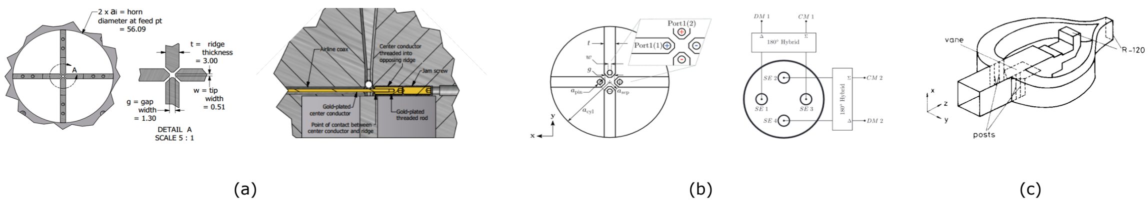

Figure 2.7: QRH fed by (a) two coaxial probes [49], (b) four probes and 180° hybrids [50], and (c) BΦifot junction [59].

2.4 Ortho-Mode Transducer Design

Ortho-mode transducers (OMTs) are typically designed with either a BΦifot [59] Fig. 2.7 (c) or a turnstile junction [60–64]. BΦifot junction based OMTs employ septum and posts, which limit their bandwidth and increase the performance sensitivity to their position and thickness. The presence of ridges in the waveguide further increases the design complexity of the junction. Contrarily, a turnstile junction based OMT can be designed with greater flexibility to operate over wide bandwidth, as explained in the following sections. Importantly, the designed OMT is made of all metallic ridge waveguides and hence can handle the high input power. An OMT is a 4 port device, which combines the two orthogonal polarizations fed at the separate input ports into a common output aperture, as shown in Fig. 2.8. It is composed of turnstile junction, E- or H-plane bends, and Y-junctions or bifurcations, depending on the physical size and shape, and the routing.

2.4.1 Bends and Bifurcations

The E or H-plane bends, and the bifurcation or power dividers, along with the turnstile junction are critical components of an OMT. The bends and Y-junctions aid in routing the waveguide components. An OMT can be designed using only E-plane or H-plane bends or a combination of both, based on the available size (height and width). In this design, only the E-plane bends are employed. The bends are realized using single and double ridge waveguides, as demonstrated in Fig. 2.8. Single ridge bends are used after the bifurcation to connect to the turnstile junction, whereas, the double ridge bends are used to accommodate for

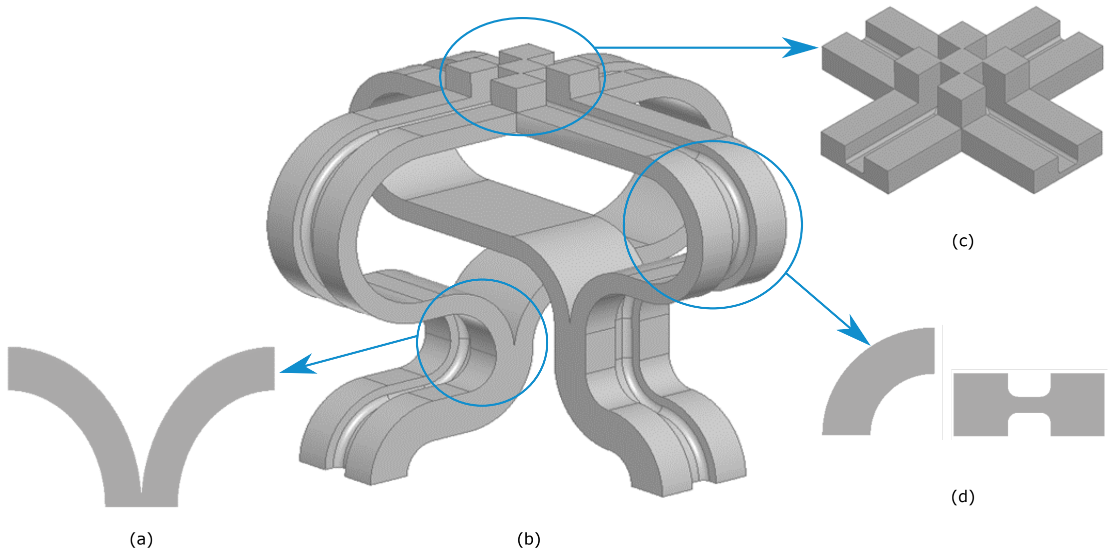

Figure 2.8: CAD model of the OMT with E-plane bends, Y-junction, and turnstile junctions.

the feeding waveguides and the standard WRD650 flanges. COTS WRD650 to N-type adaptors from ATM Microwave are used to feed the OMT for testing purpose. These adaptors can work up to 19 GHz and can handle the rated power of 150 W continuous power, and 3 KW peak power [65].

The design of the E-plane bends is relatively simple, and primarily depends on the radius of the bends. Specifically, the longer the radius, the better will be the impedance match of the component, which is in accordance with the theory in [66]. However, it is important to ensure that the cross-section of the waveguide is maintained throughout the bend and the structure is symmetric. Maintaining the symmetry and the cross-section is important to avoid the excitation of higher order modes. The CAD model of the designed single and double ridge bends along with the $|S_{11}|$ in dB is shown in Fig. 2.9. The bends of radius 1.5 cm, 1.1 cm, and 0.6 cm are designed using extensive parametric study in the full-wave solver, Ansys HFSS [57].

The Y-junction is a 3-port power divider designed by splitting the double ridge waveguide into two single ridge waveguides with equal cross sections [48]. This approach results in bifurcation with shorter overall length compared to that obtained using conventional approaches [60] and, [66]. The study of the Y-junction found that the impedance match of the common port (Port 3 in Fig. 2.9) is a function of the inner radius of the bends (r_{yj}, in Fig. 2.9 (c)), hence r = 1.5 cm is selected, which results in $|S_{11}|$ <-25 dB over the

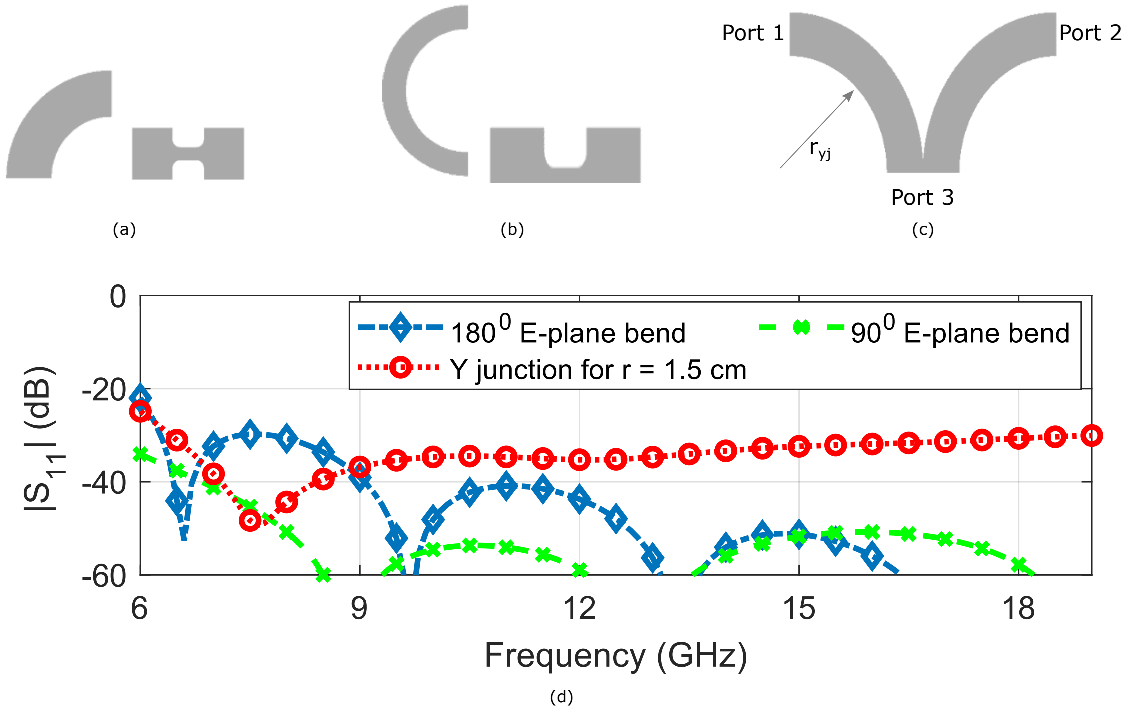

Figure 2.9: (a) CAD model, and (b) impedance match of the designed components.

operation band, see Fig. 2.9 (d). Additionally, the sharpness of the intersection of the waveguides is critical for good impedance match. However, the achievable sharpness is limited by the fabrication process and tolerances. In the designed junction the intersection is 6 mils wide. Furthermore, the Y-junction provides the required 180° phase difference between the arms of the turnstile junction with the equal magnitude as shown in Fig. 2.10.

2.4.2 Turnstile Junction

The turnstile junction is a six port device, where four ports are for the inputs and the remaining two ports represent two output polarizations from a common aperture, or vice-versa. The principle of operation of a turnstile junction is simple and straightforward. Specifically, two signals of one polarization with a 180° phase difference from each other are fed at Arm 1 and Arm 2, illustrated in Fig. 2.11. Similarly, the signals of the second orthogonal polarization are connected at Arm 3 and Arm 4. Therefore, the signals from arms 1 and 2 add in phase at Arm 6, and cancel out with each other at the remaining arms. Conversely, the signal

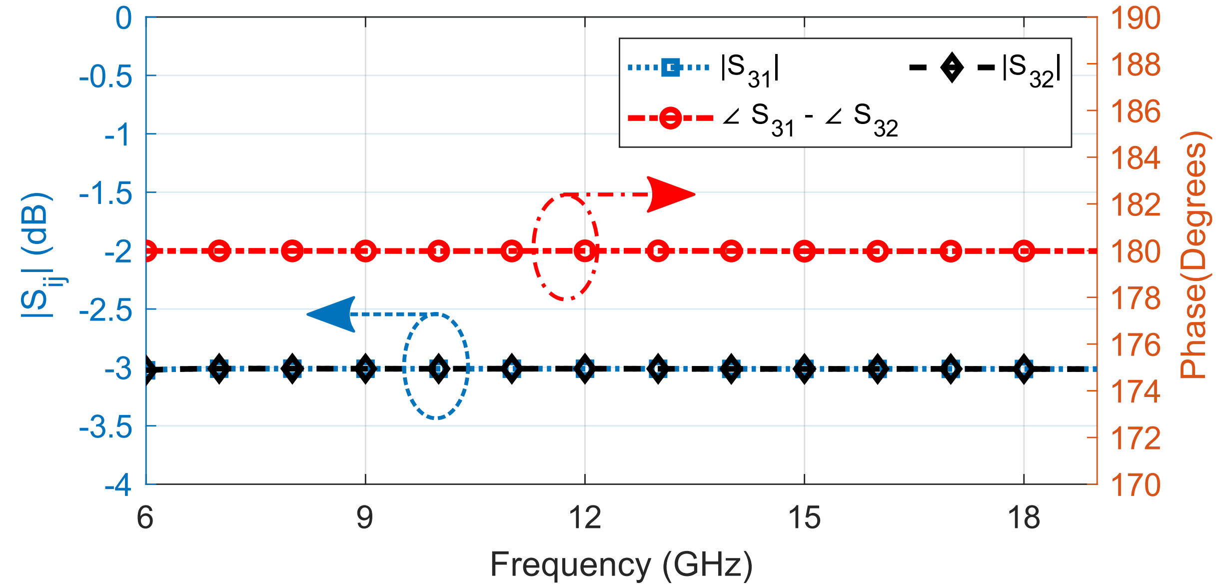

Figure 2.10: Magnitude and phase of Y-junction or bifurcation.

coming from Arm 5 will split into two out of phase signals at arms 3 and 4. Symmetry in the structure and the phases of input signals ensure high isolation between the two polarizations. However, achieving the $|S_{11}|$ below -10 dB over 6 to 19 GHz is the main challenge of the design. Hence, the turnstile junction is the bottle-neck of an OMT design. Furthermore, the shape and size of the matching stub (see Fig. 2.11) is critical to attain good impedance match of junction, as described in [48]. In this design a swept pyramid shaped matching stub is employed, and the dimensions of the stub are obtained by performing a parametric study in a full-wave solver. Additionally, the single ridge waveguides at the input of the turnstile junction are capacitively loaded (as shown in Fig. 2.11) to compensate for the reactance [37]and the resulting $|S_{11}|$ in dB of the junction is shown in Fig. 2.12.

2.4.3 OMT with QRH

The designed turnstile junction, Y-junctions, and bends are combined to form the OMT. For measurement purposes, additional impedance tapers are used to convert the modified double ridge cross-section to the standard WRD650 cross section at the input ports of the OMT. The transition from modified to standard WRD650 is essential to maintain good impedance match of the OMT, when the OMT is fed by commercially

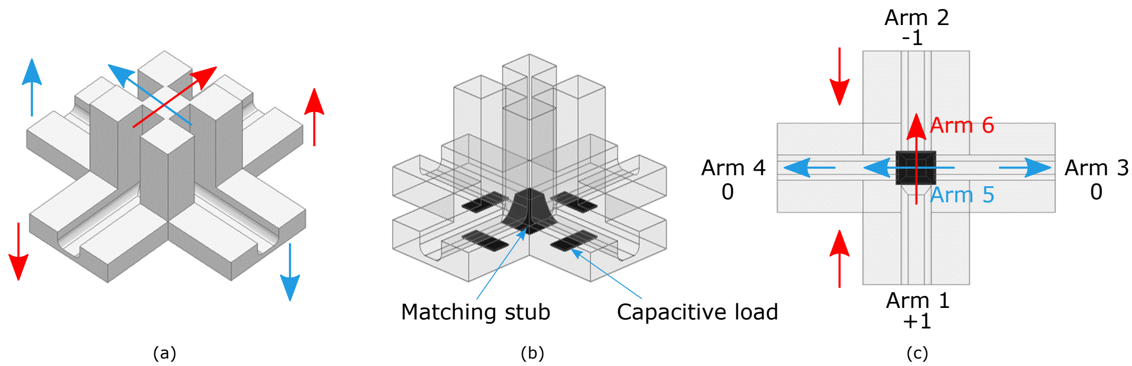

Figure 2.11: CAD model of turnstile junction showing matching stub and working principle.

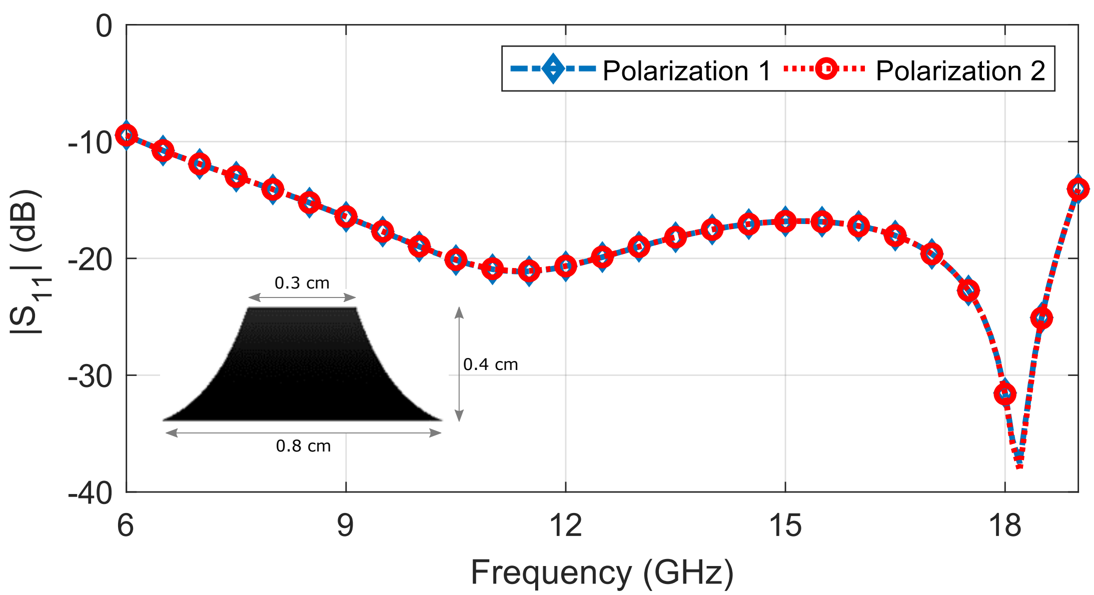

Figure 2.12: Simulated reflection coefficient of designed turnstile junction along with matching stub.

available N-type to WRD650 adapters [65]. The designed OMT has impedance match with $|S_{11}|$ <-10 dB for most of the band as clearly shown in the simulated reflection coefficient in Fig. 2.13. The spikes in reflection coefficient (at 18.7 GHz) are due to the turn-on of TE_{20} mode in the OMT when the bends and junctions are connected with the turnstile junction, as illustrated in Fig. 2.14. The fabricated QRH and OMT are shown in Fig. 2.15. The QRH is built from a single Al block using electrical discharge machining (EDM) and computer numerical control (CNC) machining, whereas the OMT is fabricated using conventional split block and CNC machining. The antenna with OMT has VSWR <2, for 97% of the operational band, as shown in

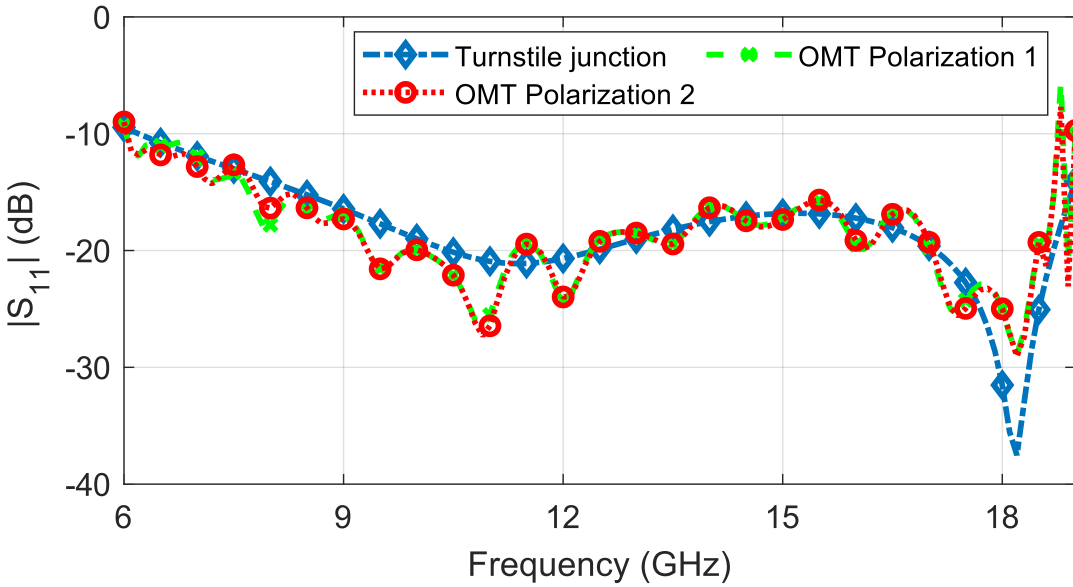

Figure 2.13: Simulated $|S_{11}|$ of the turnstile junction and OMT.

Fig. 2.16, and isolation between the ports >30 dB. Smaller spikes in VSWR at 6.4 and 7.3 GHz are due to imperfections in the fabrication and assembly of the OMT, and the spike at 18.7 GHz is due to the turn on of the TE_{20} mode. Nonetheless, it is observed that the excitation of the TE_{20} mode has an insignificant effect on the far-field performance of the antenna. The antenna has good far-field performance with symmetric and consistent radiation patterns, achieving gain >7 dBi, side lobe <15 dB and low cross-polarization, as shown in Fig. 2.17, and Fig. 2.18 respectively.

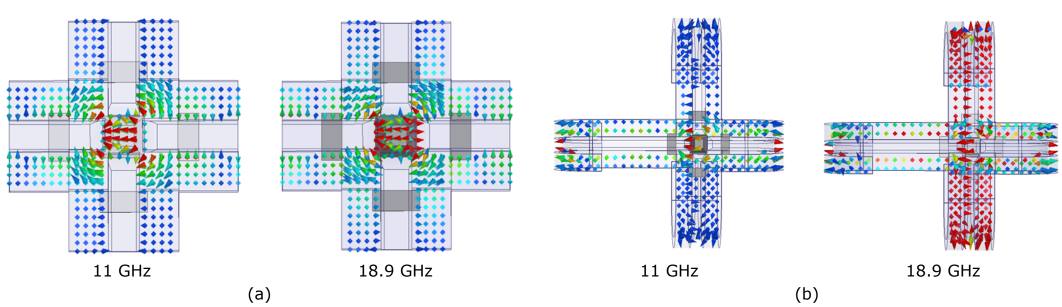

Figure 2.14: E-field inside turnstile junction and OMT at 11 and 18.9 GHz.

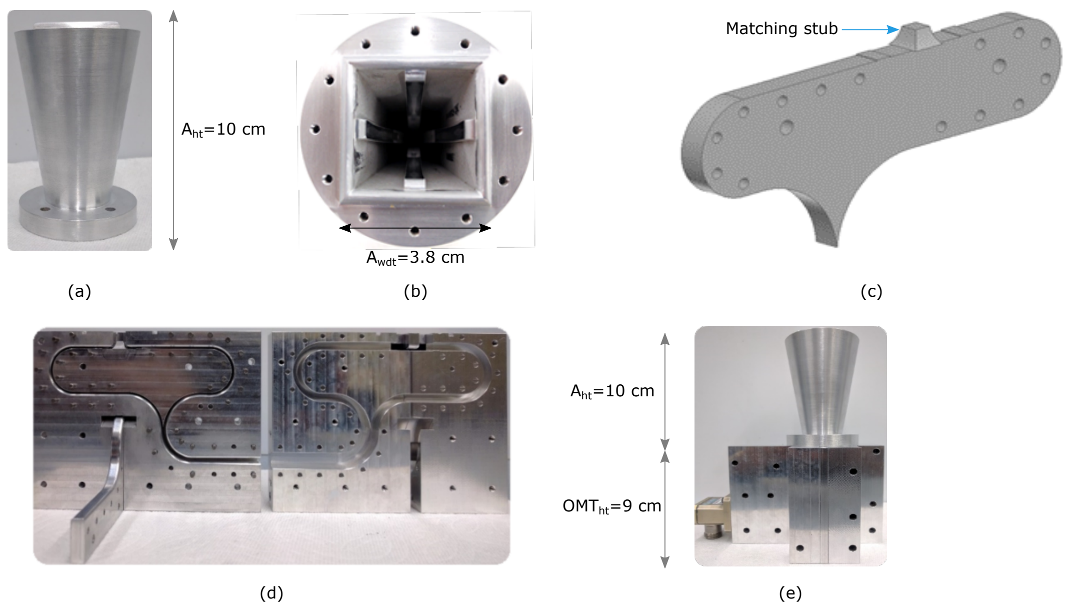

Figure 2.15: Pictures of fabricated quad ridge horn antenna and OMT along with matching stub.

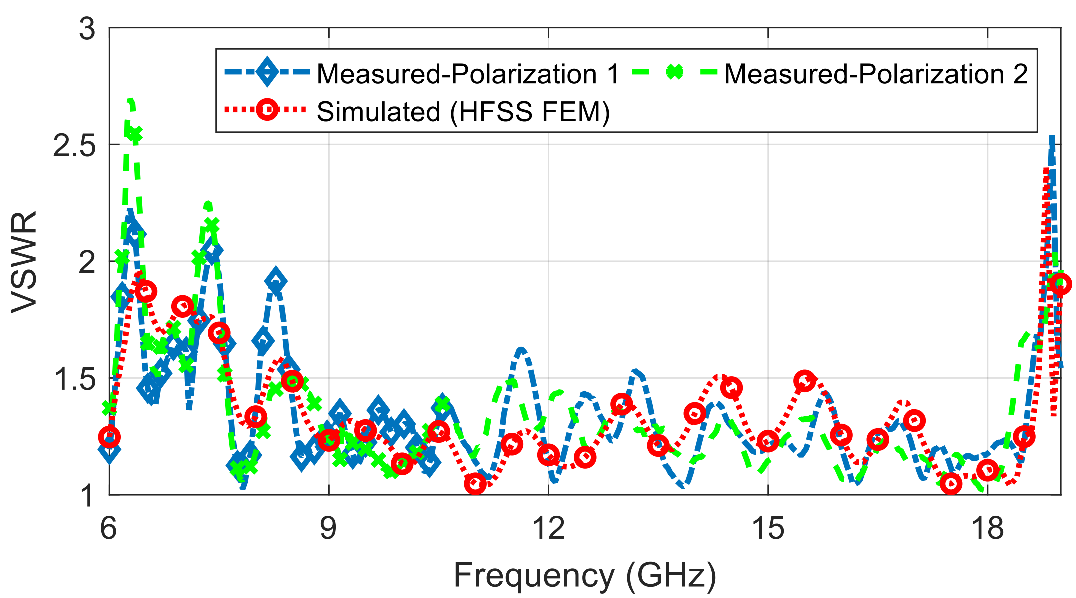

Figure 2.16: Simulated and measured VSWR of QRH fed by the OMT (for both polarization). WRD650 to coaxial adaptor is used to feed the OMT.

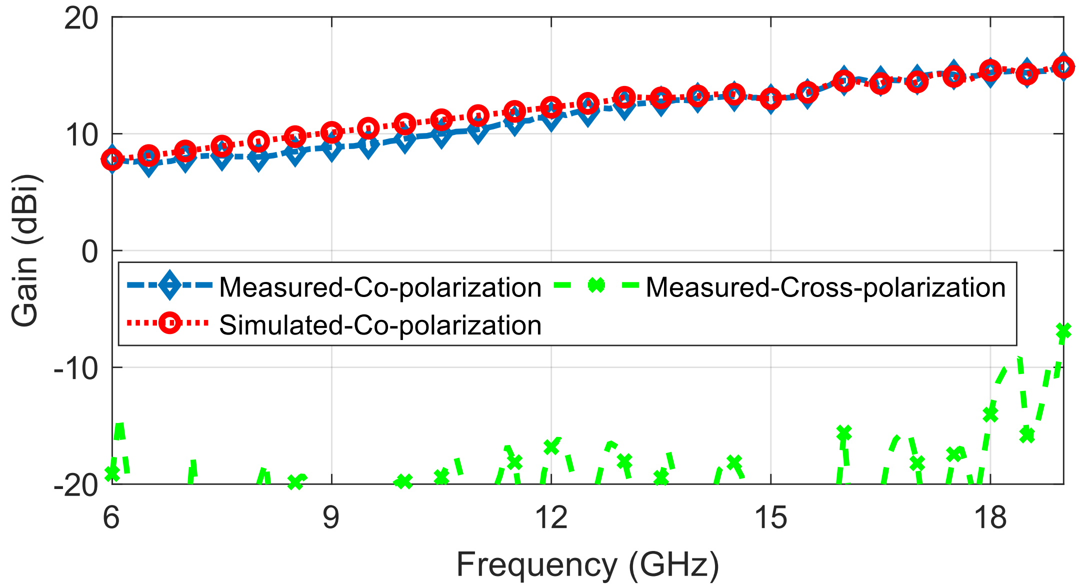

Figure 2.17: Simulated and measured co- and cross-polarized broadside gains of the QRH.

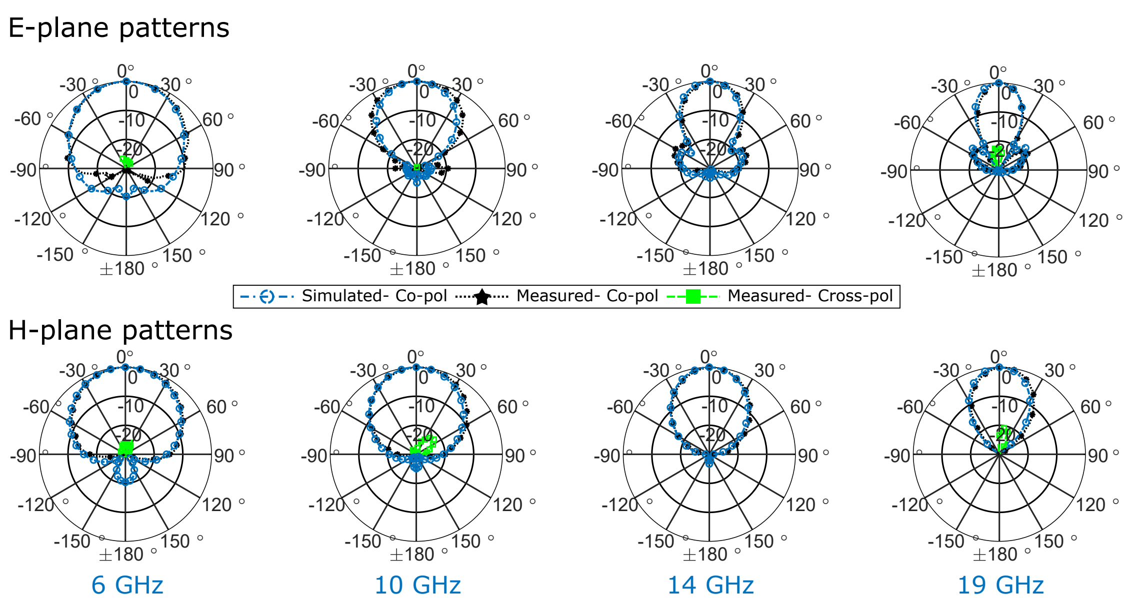

Figure 2.18: Simulated and measured co- and cross-polarized (a) E- and (b) H-plane patterns of the QRH at different frequencies.

2.5 mm-Wave QRH

The horn antenna and OMT are designed using a similar approach of the 6-19 GHz QRH. First, the standard cross-section of the double ridge waveguide is modified to support single mode operation up to 50 GHz and handle 2 kW CW power [36, 48]. The resulting waveguide with its dimensions is depicted in Fig. 2.19. The aperture of the antenna maintains the desired small profile with width and breadth, $1.27 \times 1.27\,\text{cm}^2$, which is $<(0.66\lambda \times 0.66\lambda)$. Furthermore, the asymmetric sine profile [49] is employed instead of Klopfenstein taper for the ridges. Thus, the final horn with aperture matching has |S11| < -15 dB for 99% of the operational bandwidth.

Also, the OMT is redesigned to accommodate the minute details in bends and bifurcations in accordance with the fabrication tolerances. The routing of the waveguide sections is modified to provide ample space for the flange of the feeding waveguide or ridge waveguide to 2.4 mm coaxial launcher. A cone-shaped matching stub is used instead of the swept pyramid in the turnstile junction, for easy fabrication. The CAD model of the aperture and the matching stub with dimensions are illustrated in Fig. 2.20 (a) and (b), respectively. The pictures of the CNC machined antenna are shown in Fig. 2.21, where the aperture and the OMT are combined to avoid the leakage at the junction.

The simulated antenna fed by OMT has VSWR <2 over the operating band. However, the VSWR of the fabricated QRH has spikes at 18.7 and 20 GHz (see Fig. 2.22). These anomalies are mainly due to the imperfections in the fabrication. Therefore, it can be corrected with a better process and tighter tolerances. Nonetheless, the antenna has VSWR <2 for 92% of the operational bandwidth. Also, the fabricated antenna has symmetric radiation patterns with low side lobes, and gain >7 dBi, as shown in Fig. 2.23 and FFig. 2.24, respectively.

2.6 Summary

The design and fabrication of a wideband, dual-polarized, QRH and OMT operating over 3:1 BW is presented. The 6-19 GHz antenna has aperture size 3.3 x 3.3 cm^2 which leads to gain >7 dBi, and side

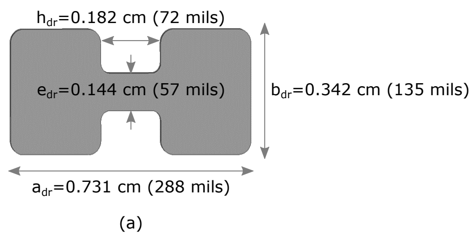

Figure 2.19: Cross section of double ridge waveguides, (a) standard WRD180, and (b) modified WRD1845.

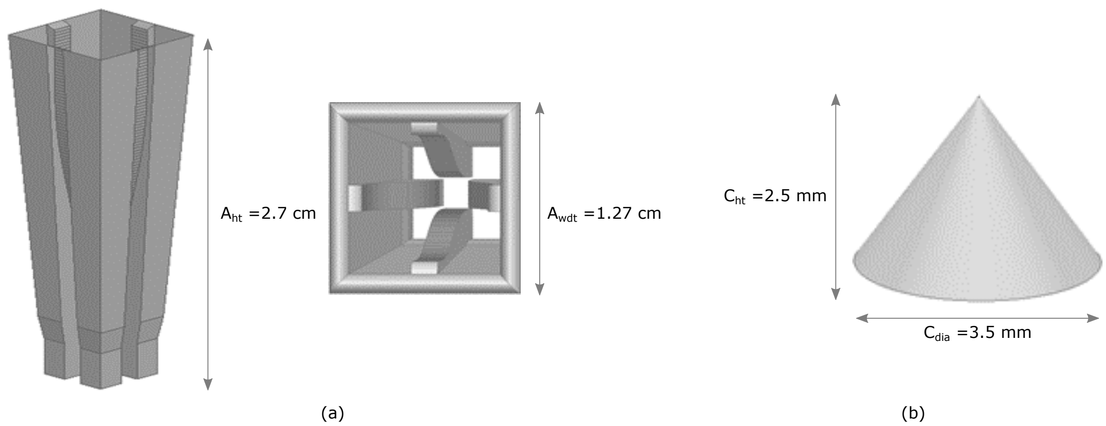

Figure 2.20: CAD model of (a) QRH, and (b) matching stub of the turnstile junction.

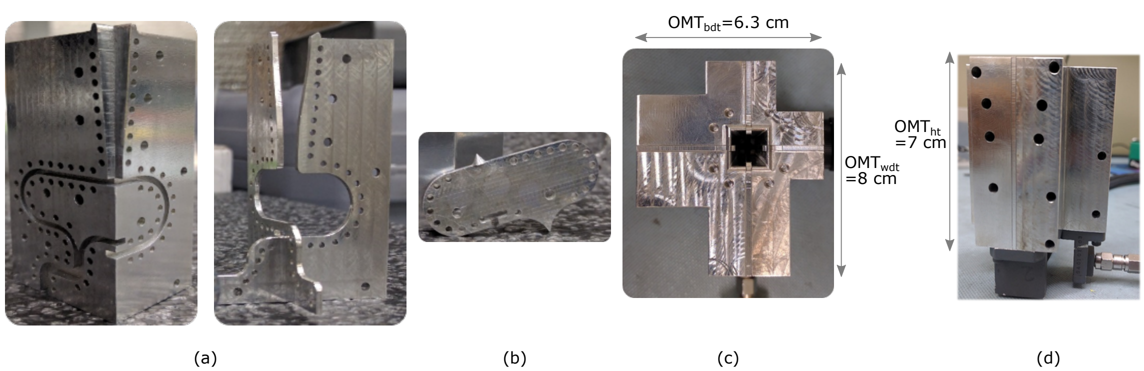

Figure 2.21: Pictures of fabricated OMT and antenna, matching stub, and assembled antenna with measurement setup. The antenna is fabricated using CNC machining.

lobes more than 15 dB below the beam peak. The horn is machined in aluminum, and the dimensions of ridges are selected to facilitate high power, bi-static STAR applications. Further, various dual polarized antenna feeding techniques are briefly compared with the turnstile junction-based approach. The QRH fed

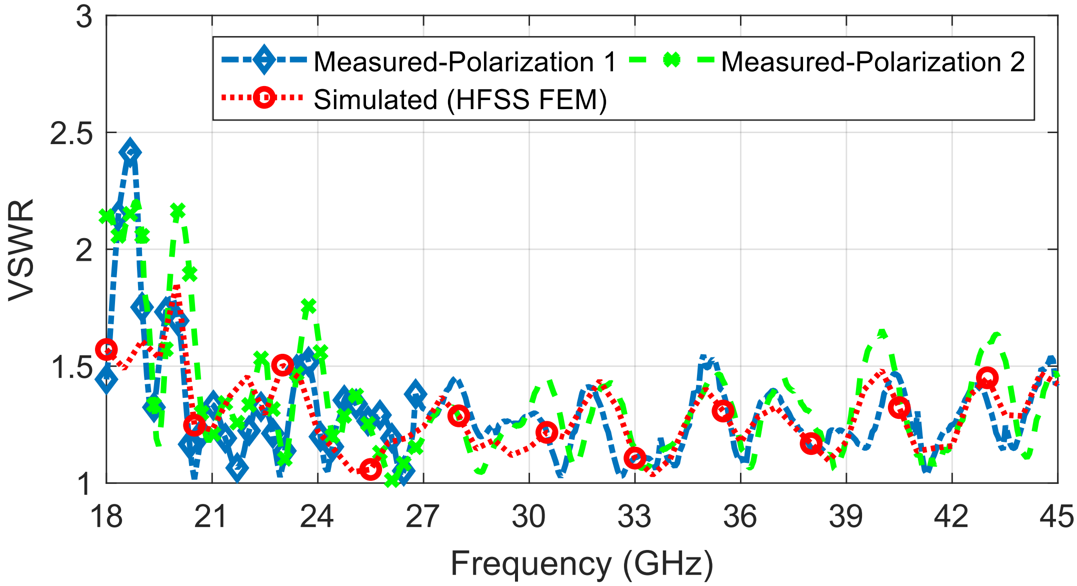

Figure 2.22: Simulated and measured VSWR of QRH fed by the OMT (for both polarization). WRD180 to 2.4 mm adapter is used to feed the OMT.

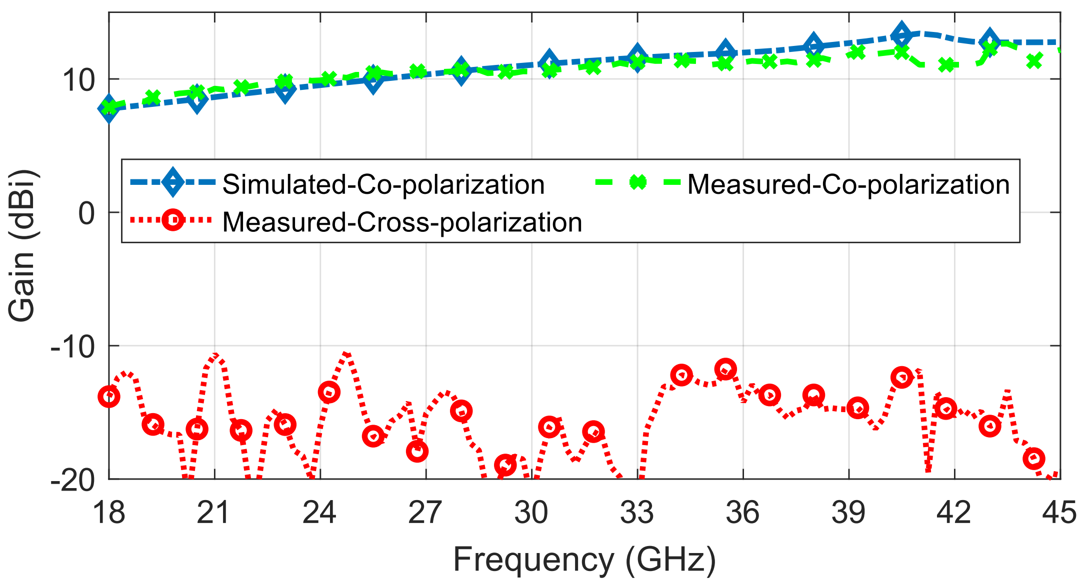

Figure 2.23: Simulated and measured co- and cross-polarized broadside gains of the QRH.

by OMT has VSWR <2 and <2.1 in simulation and measurement, respectively. Additionally, an 18-45 GHz dual polarized antenna is designed using a similar approach, while accounting for the small dimensions and fabrication tolerances. The QRH has gain >7 dBi, VSWR <2.1 for 92% and symmetric radiation patterns.

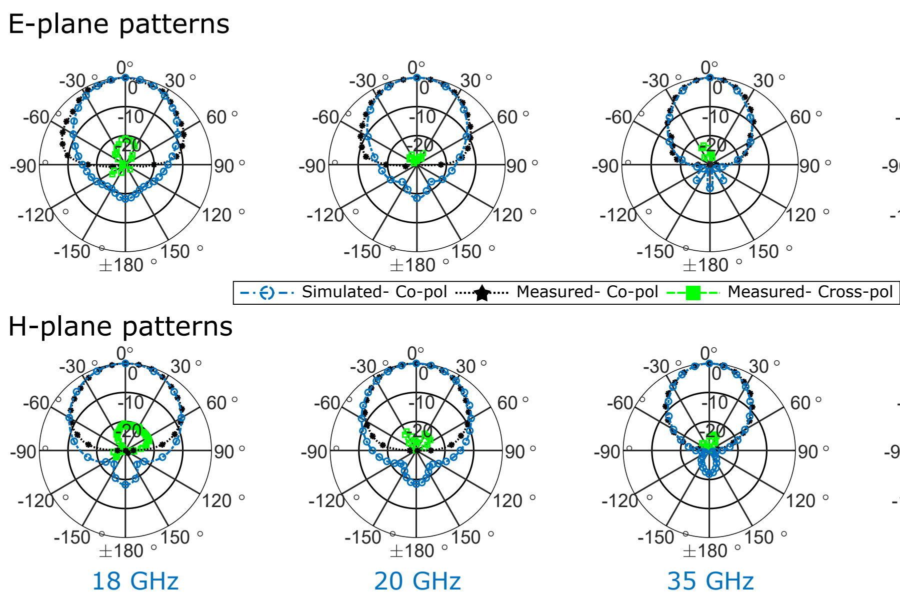

Figure 2.24: Simulated and measured co- and cross-polarized (a) E- and (b) H-plane patterns of the QRH at different frequencies.

Chapter 3

Decoupling Techniques

3.1 Introduction

In STAR systems power is coupled between TX and RX predominantly through two means, radiation through free space and because of surface currents when the apertures are mounted on the ground plane. Antennas sharing a feeding network will have an additional coupling path due to the leakage in the components. Further, scattering and diffractions from the edges of a finite size ground plane will provide an auxiliary route. The coupling is less concerning in a multi-antenna system where each element operates at a different frequency. However, in a STAR system minimizing the SI from each path is critical. Hence it is of primary importance to develop techniques to reduce the power coupled.

Increasing the separation between antennas is a simple approach to maximize the isolation between the TX and RX. However, that multiplies the size of the host platform, hence, it is not preferred in area constrained applications. The coupling between the antennas on a ground plane can be approximated using the Friis equation (3.1) [67], where $G(\phi_{1,2})$ is the gain along the horizon, and C_{12} is the power coupled. Therefore, minimizing $G(\phi_{1,2})$ is another approach to reduce C_{12}. Furthermore, an aperture antenna will have lower gain at $\theta = 90°$ (-∞ dB over an infinite ground plane) in the H-plane than in the E-plane. Hence the TX and RX oriented in their H-plane will have lesser coupling, therefore, this applies only to single polarized systems.

$$C_{12} = \frac{G(\phi_1)G(\phi_2)\lambda^2}{4\pi R^2} \tag{3.1}$$

In the literature, techniques such as polarization diversity [68], null placement, and near field cancellation [30, 39, 69] are proposed to improve the isolation of a bi-static STAR antenna systems. Each of these techniques has drawbacks: the use of polarization diversity is limited to singly polarized systems, null placement technique is narrowband, and near-field cancellation approach requires a complex beamforming network and is sensitive to the electrical and geometrical symmetries.

The suppression of surface currents/waves between the TX and RX antennas on a shared ground plane of finite conductivity is an alternative approach to effectively reduce the coupling. The surface waves excited in the E- and D-plane are mainly TM waves [70]. The extensive studies in [38, 71–73] indicate that the propagation of these waves is a function of the surface impedance. When the impedance satisfies the transverse resonance condition, the wave propagates along the surface [72]. TM_0 waves have capacitive impedance, therefore an inductive structure will support its propagation. Whereas a surface with capacitive impedance forces these waves to radiate [41,73]. For metals with finite conductivity at microwave frequencies, the surface impedance is given by (3.2) [38] (see Fig. 3.1), where δ is the skin depth, and σ is the conductivity. Hence the impedance has small resistive and inductive components [38, 71], which supports the propagation of TM surface waves. High impedance surfaces (HIS) can be realized using metallic corrugations [41, 74], bed of nails [43], or printed reactive surface PRS [75, 76].

$$Z_s = \frac{E_z}{H_y} = \frac{1 + j}{\delta\sigma} \tag{3.2}$$

This chapter is organized into six sub-sections:

- Section 3.2 discusses a single polarized, bi-static STAR system. This section highlights the importance of the orientation of antennas and the aperture dimensions to maximize the system isolation.

- Section 3.3 presents the challenges associated with achieving high isolation in a dual polarized bi-static

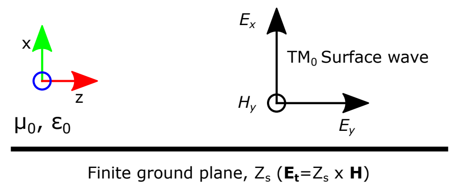

Figure 3.1: Propagation of TM_0 surface wave on finite conductivity ground plane.

system, and techniques to equalize SI for both the polarization.

- Section 3.4 describes the theory and implementation of HIS in depth. Also, this section brings out the trade-offs and bandwidth constraints of these surfaces. Further, its effectiveness in reducing the coupling in a dual-polarized bi-static system is discussed.
- Section 3.5 outlines the benefits and drawbacks of using absorbers to suppress the currents and the gain along the horizon, and its impact on system isolation.
- Section 3.6 briefly delves into the influence of nearby scatterers on the coupling between two apertures mounted on a common ground plane.

3.2 Single Polarized Systems

3.2.1 6-19 GHz Bi-static

A STAR antenna system is designed using double ridge horns to achieve > 3:1 bandwidth. High isolation is obtained by modifying the orientation and the physical parameters of the antenna. The gain along the horizon is a function of the aperture size, that is, the larger the aperture, the lower $G(\theta = 90°)$ will be, as illustrated. Moreover, the coupled power decays as -6 dB/octave and -12 dB/octave in the E- and H-plane, respectively. Hence, horns oriented in their H-plane will have higher isolation for a given distance, which can be further improved by widening the aperture (Fig. 3.2). Contrarily, increasing in size will also raise the side lobe level (SLL) that could deteriorate the STAR performance at higher frequencies, as inferred

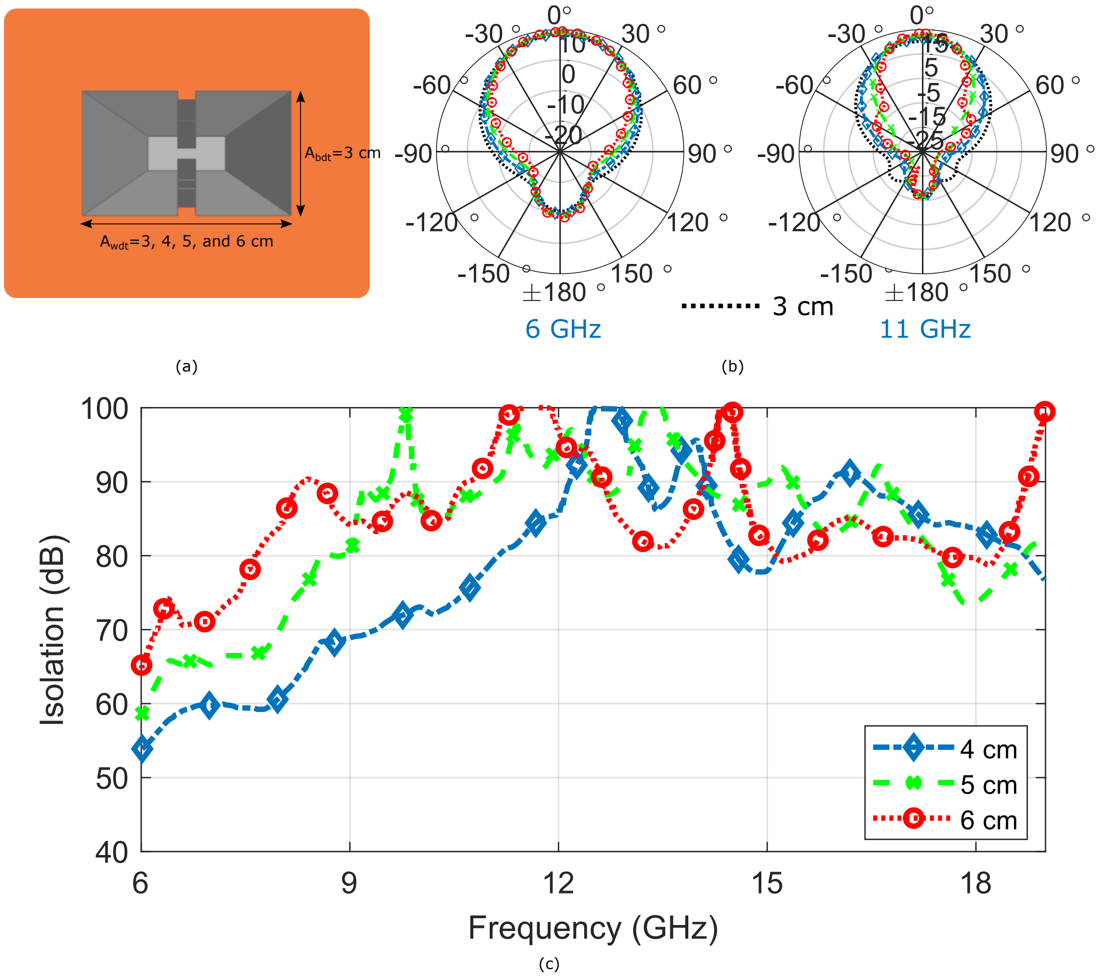

Figure 3.2: (a) Double ridge horn CAD image, (b) simulated H-plane patterns of the double ridge horn at 6 GHz and 11 GHz, and (c) isolation between TX and RX for aperture size: 3×3, 3×4, 3×5, and $3\times6\,\mathrm{cm}^2$.

by comparing the isolation from 13-14 GHz for $A_{wdt}=4$ and 6 cm. Nonetheless, the system has isolation >60 dB over the operating band and >80 dB over 84% of the bandwidth as demonstrated in Fig. 3.3. The isolation between the antennas is simulated using MoM in FEKO, and FE-BI in Ansys HFSS. Also, the size of the aperture and the rate of exponential taper is designed to maintain SLL <15 dB. The complete performance of the horn is presented in Appendix A.

These studies indicate that high isolation, >60 dB, can be achieved easily by varying the antenna dimensions and placement when the separation between the TX and RX is in the order of 4λ. However, this applies only to a single polarized system.

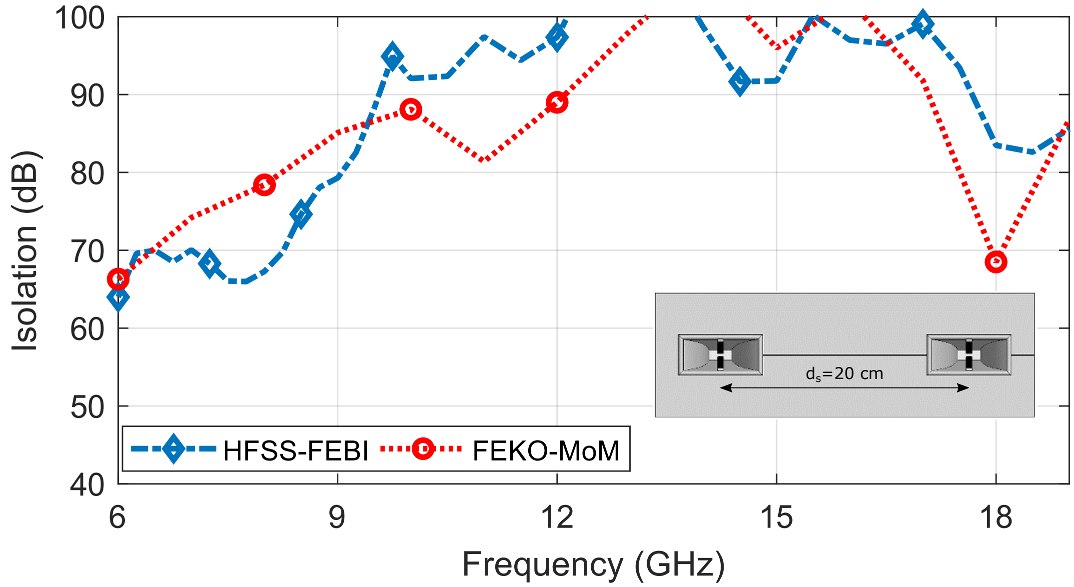

Figure 3.3: Simulated isolation between single polarized TX and RX separated by 20 cm, center-to-center.

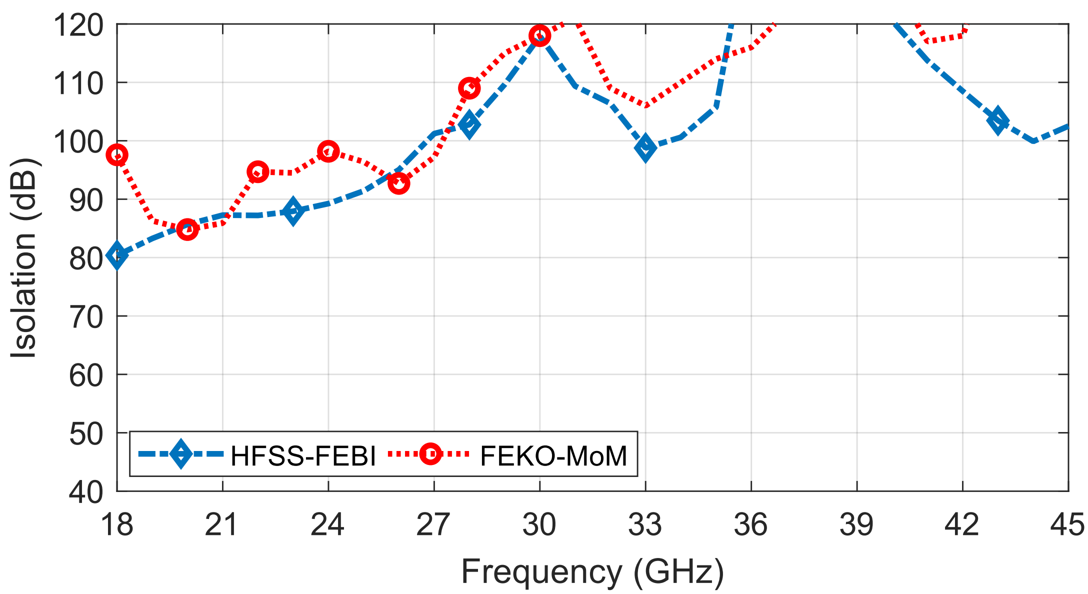

Figure 3.4: Simulated isolation between single polarized TX and RX separated by 20 cm, center-to-center.

3.2.2 18-45 GHz Bi-static

Electrical distance between the antennas is another factor which controls the amount of SI. Specifically, the power coupled is inversely proportional to the square of separation. Hence, a single polarized, double ridged horn operating in 18-45 GHz and oriented in the H-plane has isolation >80 dB when placed 12λ

(20 cm) apart on a finite ground plane. The simulated isolation with the CAD model of the antennas is shown in Fig. 3.4. The detailed characterization of the QRH is outlined in Appendix A.

3.3 Dual Polarized Systems

Orienting the TX and RX antennas in their H-plane is not a preferred solution to achieve isolation >60 dB in a dual-pol system, because the H-plane of one polarization is the E-plane for the other, as shown in Fig. 3.5. Therefore, to improve the isolation for both polarizations, the TX and RX antennas are oriented in their D-plane. In this study the antennas are separated edge-to-edge by 20 cm, which is both practical as well as the maximum distance permitted by the designated platform of the SPEAR program [13]. The antennas are modeled and measured on a ground plane of size 13 cm × 38 cm. Note that the size of the ground plane

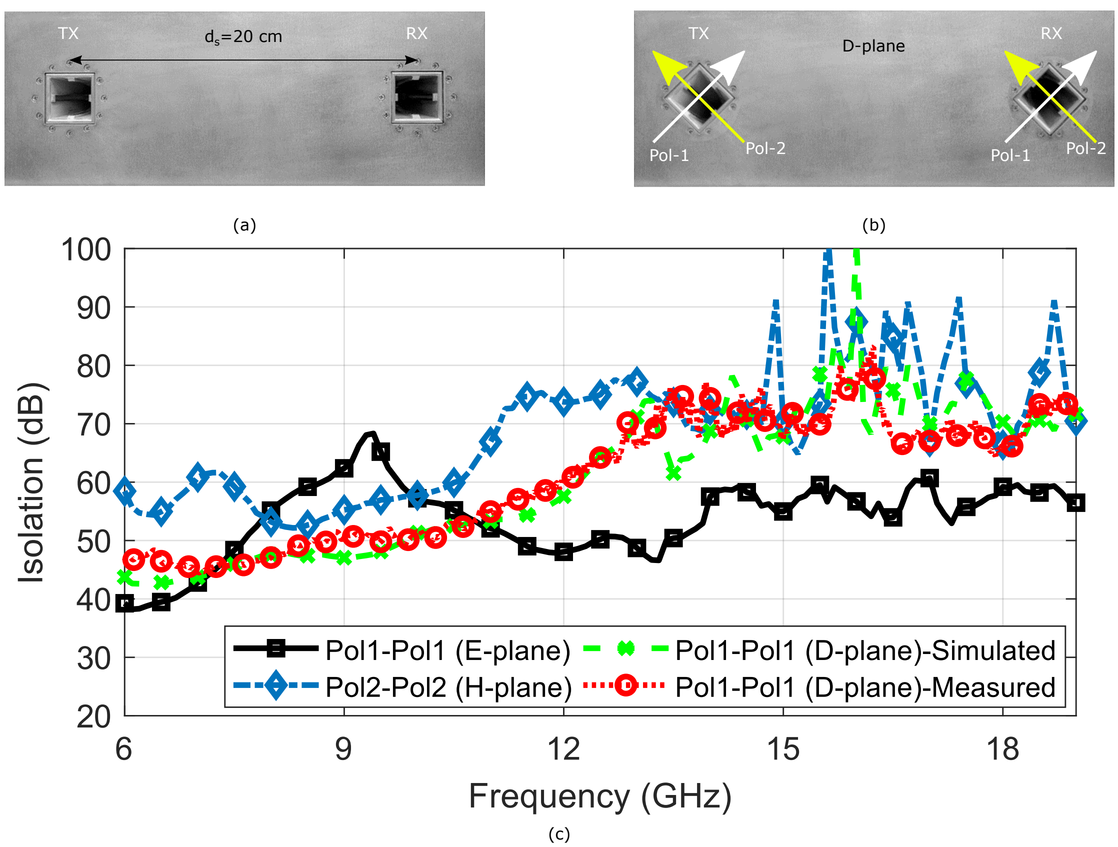

Figure 3.5: Pictures of fabricated antennas on ground plane in (a) E-H-plane and (b) D-plane, (c) simulated isolation in E-, H-, and D-plane.

has limited impact on the coupled power level. However, the dimensions influence the frequency of ripples or peaks and troughs in the coupled power, which can be attributed to scattered signals from the ground plane edges. The measured coupling level is around -40 dB and remains higher than -60 dB up to 12 GHz (see Fig. 3.5). A similar coupling level is measured for the other polarization. Excellent agreement with simulation verifies robustness of both theory and experiment.

3.4 High Impedance Surfaces

3.4.1 Metallic corrugations

Metallic corrugations are single periodic metallic slots of depth $\lambda/4$ (at the anti-resonance frequency) and with the periodicity (or spacing between consecutive slots) much less than the wavelength [41,46,74,77]. These surfaces are also known as hard and soft surfaces, based on the orientation of the slots to the E-field vector and the direction of propagation [78]. The surface can be analyzed using an equivalent surface impedance, Z_s, when the periodicity of the slots is much less than the wavelength. The surface impedance or reactance can be calculated using (3.3) [47,79], where, w_{MC} is the corrugation width, s_{MC} is the periodicity of the slots/corrugations (i.e. corrugation slot width + w_{MC}), k_0 is the free space wavenumber, and h_{MC} is the depth of corrugations. The surface impedance is capacitive when the corrugation depth is between 0.25λ to 0.5λ, and thus the surface prevents the propagation of TM waves in this range. The decay of currents along this surface can be approximated as in [80].

$$X_{MC} = \frac{s_{MC} - w_{MC}}{s_{MC}} \eta_0 tan(k_0 h_{MC}) \tag{3.3}$$

The surface impedance can also be computed using the full wave solvers, where the infinite periodic approximation is used to calculate the reflection coefficient of the surface for a plane wave (TM polarized) incident at a grazing angle. Further, the reflection coefficient is used to compute the surface reactance using the relation in [75]. For a given slot width and the periodicity, the anti-resonance frequency is mainly determined by the depth of corrugations. Specifically, when the depth is $\lambda/4$, $\tan(k_0 h_{MC})$ in (3.3) approaches

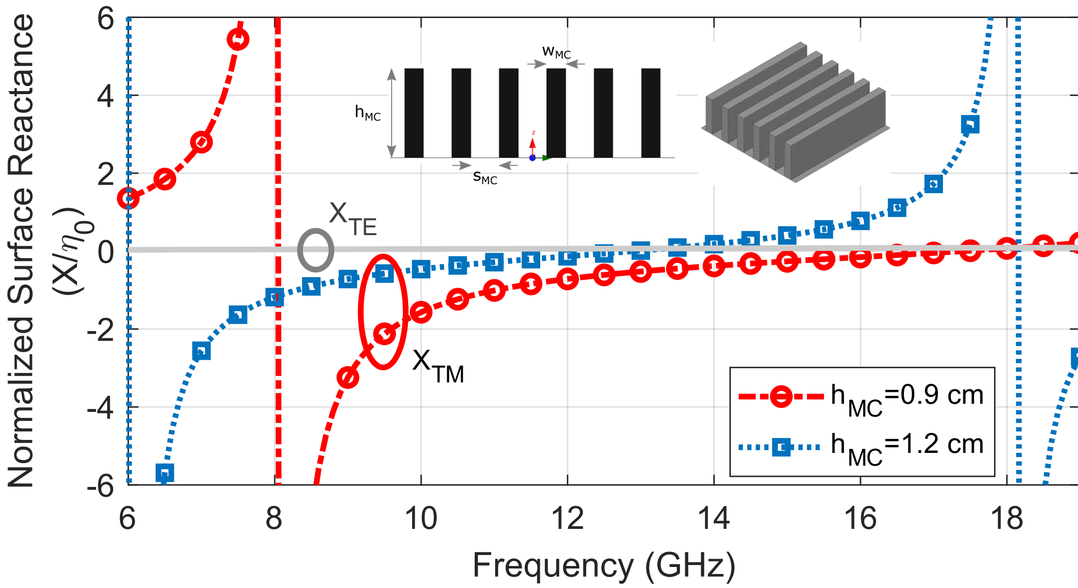

Figure 3.6: Normalized surface reactance of corrugations for TM and TE polarized waves, incident at near grazing angle ($\theta = 89°$).

-∞ and hence results in a highly capacitive surface, similarly, $h_{MC} = \lambda/2$ results in the surface with '0' surface reactance. Therefore, the surface is capacitive in the range 0.25$\lambda$to 0.5$\lambda$and is effective in inhibiting TM surface waves for a maximum of an octave of bandwidth. The surface impedance calculated using full wave simulation indicates similar behavior w.r.t to the depth of the corrugations, as shown in Fig. 3.6. The surface has '~0' reactance for the TE polarized wave since the E field will be tangential to the metal wall of corrugations. The multiplication factor in (3.3) controls the magnitude of the reactance, therefore the thinner the corrugations, the higher will be the surface reactance. However, the smallest achievable w_{MC} is limited by the fabrication. These surfaces can also be analyzed using a dispersion diagram (ω-β diagram), as outlined in [74]. The main disadvantages of metallic corrugations are limited bandwidth and increase in system weight and manufacturing cost.

3.4.2 Bed of Nails

Bed of nails (BON) are double periodic arrays of metallic pins (see inset of Fig. 3.7) that can be used to synthesize a desired surface reactance by suitably selecting the dimensions and periodicity of the

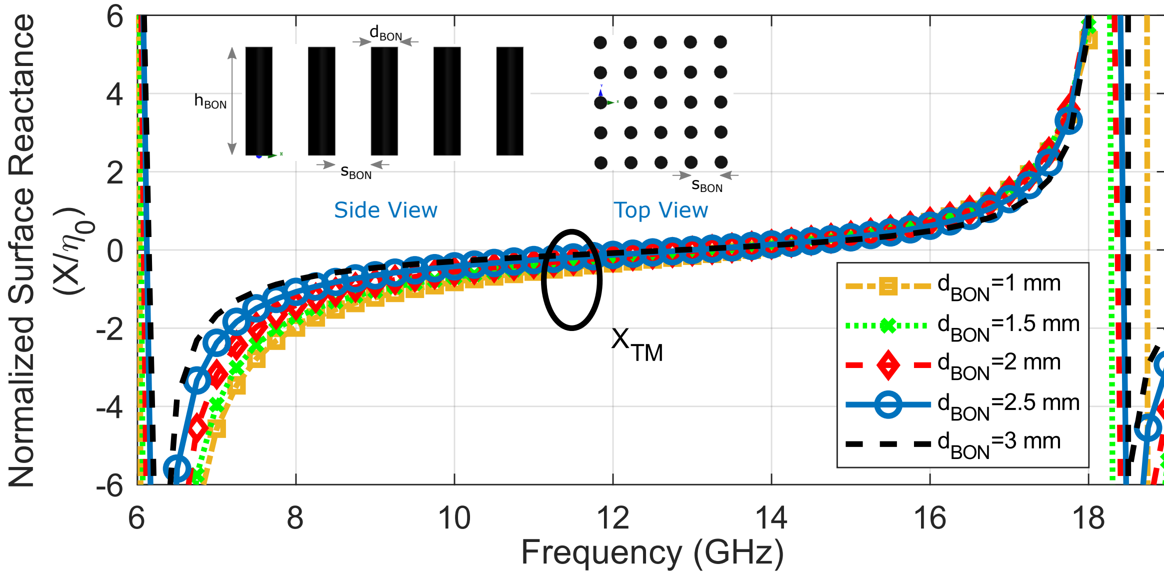

Figure 3.7: Normalized surface reactance of bed of nails for TM polarized wave, incident at near grazing angle ($\theta = 89°$) as a function of diameter of the pins (1 to 3 mm) for spacing, $h_{eff} = 7$ mm.

pins, as demonstrated in [43]. The structure can be analyzed by its surface reactance when the periodicity is smaller than the wavelength [43], analogous to the evaluation of metallic corrugations. Furthermore, this approximation of impedance is valid only when the diameter and spacing of the pins are selected such that there is no propagation in lateral directions X and Y for Z <0 over the frequency band of interest. Under these conditions, the surface reactance, X_{BON}, is only a function of the height of the pins and k_z (wave number along z direction), which can be approximately calculated using (3.4) [43]. Where h_{eff} is the effective height of the pin, (i.e. including the fringing field) and ϵ_x is the equivalent permittivity of the bed of nails in the direction of propagation.

$$X_{BON} = \frac{k_z h_{eff}}{\epsilon_x} tan(k_z h_{eff}) \tag{3.4}$$

The Z_s of the bed of nails as a function of pin diameter, d_{BON}, and height, h_{BON} is shown Fig. 3.7 and Fig. 3.8, respectively. The results indicate that the anti-resonance frequency is dependent on the pin height. Whereas the diameter and the spacing between pins have less influence on the parallel resonance. However, the maximum separation should be kept below $\lambda_g/2$ to prevent propagation in lateral directions [43], where

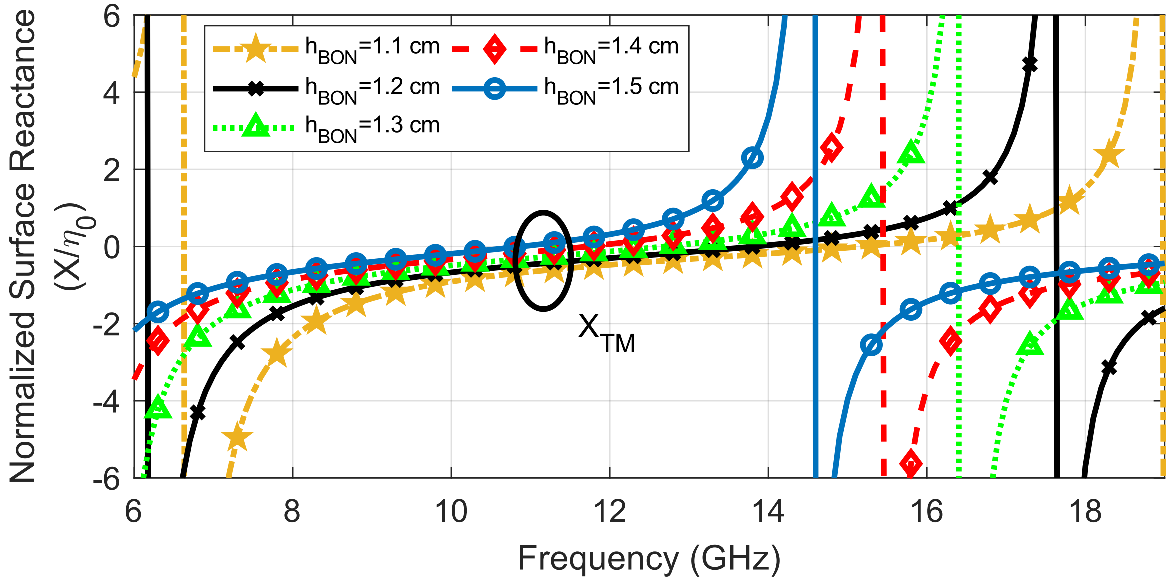

Figure 3.8: Normalized surface reactance of bed of nails for TM polarized wave, incident at near grazing angle ($\theta = 89°$) as a function of pins heights for spacing, $h_{eff} = 7$ mm.

λ_g is the guided wavelength for the effective permittivity of the bed of nails.

Furthermore, the surface impedance of the bed of nails as a function of θ and ϕ Fig. 3.9 indicates that the structure is isotropic. This behavior is mainly due to the geometrical symmetry of BON. Hence, the waves propagating in oblique directions after reflecting from the edges will also see the same Z_s, and therefore the structure can minimize coupling due to scattering from the finite ground plane edges. Note that the isotropic behavior is not supported in metallic corrugations. For the proposed design, the bed of nails with $d_{BON} = 3$ mm and $s_{BON} = 7$ mm is selected. Implementation of BON overcomes complexity and cost associated with metallic corrugations. However, the bandwidth is still limited to an octave and the surface is $\lambda/4$ thick.

3.4.3 Printed Reactive Surfaces

The bandwidth limitation of the bed of nails can be improved by top loading the pins with metallic patches, resulting in a structure known as metasurface [75, 76] or printed reactive surface (PRS). The improvement in bandwidth is mainly due to the additional resonant structure formed by the equivalent

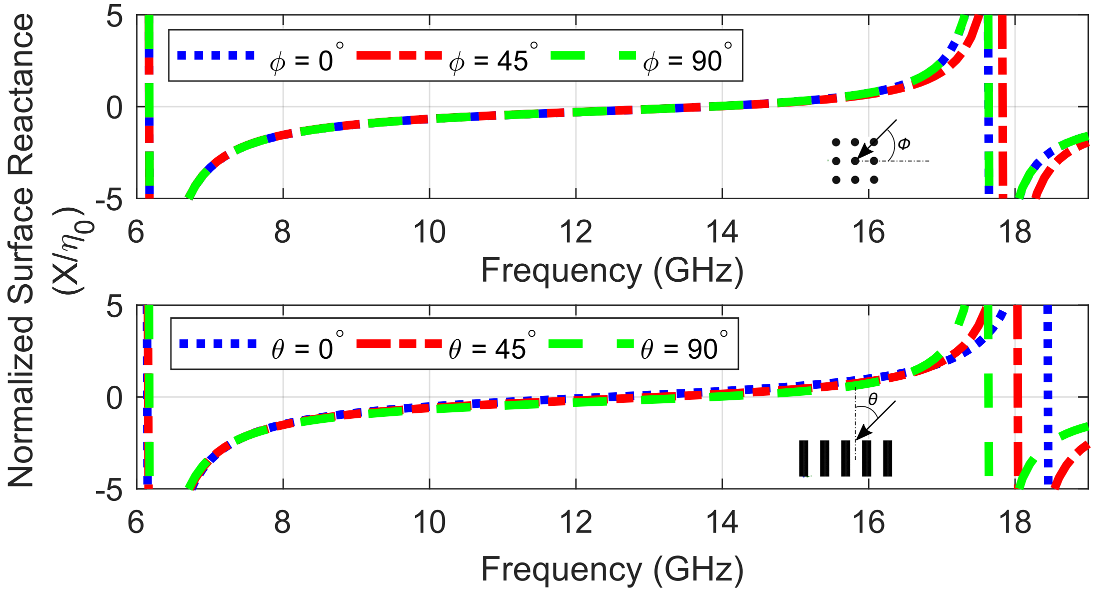

Figure 3.9: Normalized surface reactance of bed of nails for TM polarized wave for incident angle ($\theta = 0°$ to 89°) and ($\phi = 0°$ to 89°).

capacitance and inductance of the patches and pins [38]. Moreover, the height is significantly lesser than that of the metallic corrugations, and bed of nails. Specifically, it is 7 mm ($0.14\lambda_{6GHz}$) thick which is 56% thinner than the latter two. A PRS with $l_{PRS} = 6.5$ mm, $w_{PRS} = 6$ mm, and $\epsilon_r = 1$ is considered first. Importantly, the surface impedance of the PRS remains capacitive over more than a 3:1 bandwidth, unlike the octave bandwidth of metallic corrugations and bed of nails. The structure can also be evaluated as effective Z_s since the size of the unit cell is smaller than the wavelength [75]. Hence, the PRS is analyzed with a similar approach used for the other two HISs discussed before.

Studies highlight that the critical design parameters of PRS are pin height (h_{PRS}), patch length (l_{PRS}) and width w_{PRS}. The dependency of surface impedance on h_{PRS} and l_{PRS} is as shown in Fig. 3.10 and Fig. 3.11, respectively, where increasing the height lowers the anti-resonance frequency and vice versa.

An additional advantage of PRS is the feasibility to be fabricated on a dielectric substrate. The height of the surface is $\propto \frac{1}{\sqrt{\epsilon_r}}$, where ϵ_r is the permittivity of the substrate, and hence the surface thickness can be further reduced by choosing the dielectric with higher permittivity. However, increasing the ϵ_r raises the equivalent capacitance of the resulting unit cell, thereby, reducing the total capacitive reactance of the Z_s,

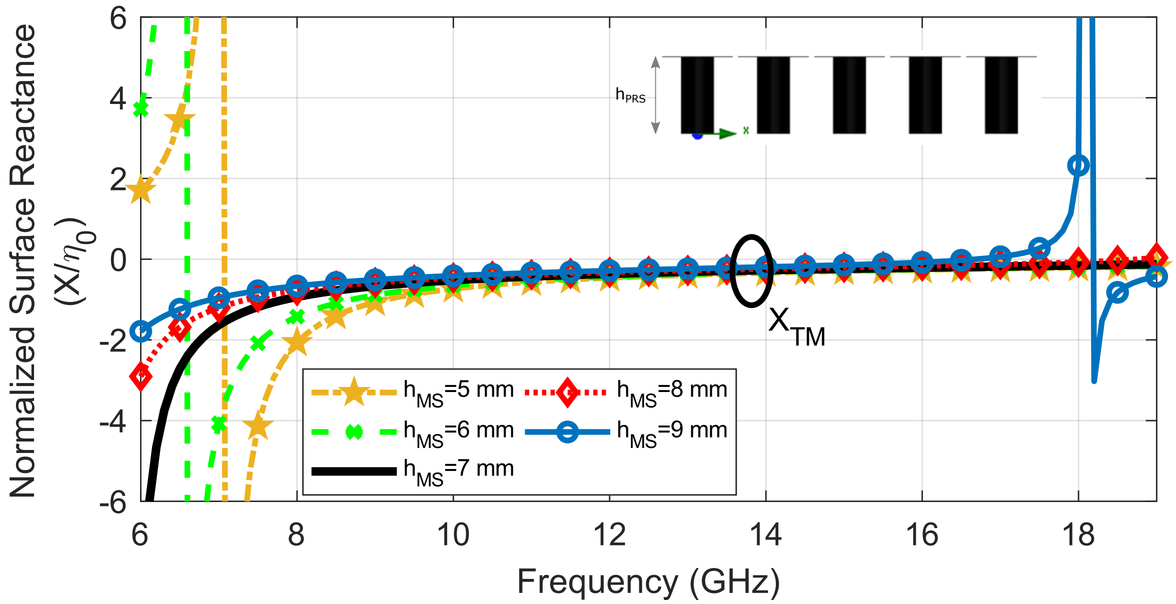

Figure 3.10: Normalized surface reactance of PRS for TM polarized wave, incident at near grazing angle ($\theta = 89°$), as a function of height of the PRS, where $w_{PRS} = 6$ mm, $d_{PRS} = 3$ mm and spacing, $s_{PRS} = 7$ mm.

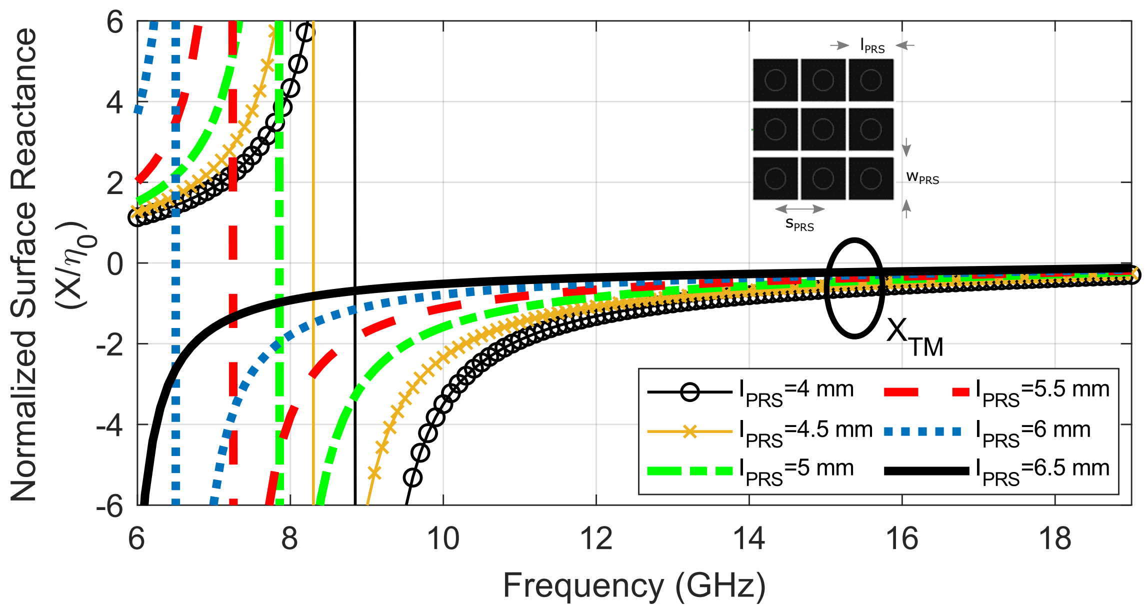

Figure 3.11: Normalized surface reactance of PRS for TM polarized wave, incident at near grazing angle ($\theta = 89°$), as a function of patch length, where $w_{PRS} = 6$ mm, $d_{PRS} = 3$ mm and spacing, $s_{PRS} = 7$ mm.

as evident from Fig. 3.12. This decrease in the surface reactance directly influences the relative reduction in coupling. Therefore, the permittivity of the substrate should be selected based on the required thickness and

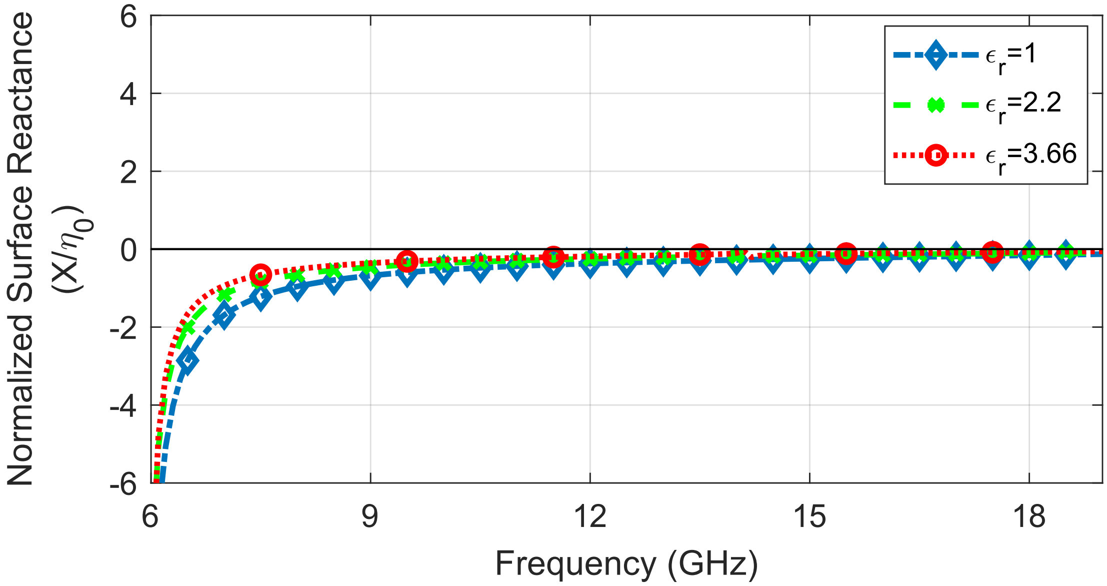

Figure 3.12: Normalized surface reactance of PRS for TM polarized wave as a function of permittivity of the substrate.

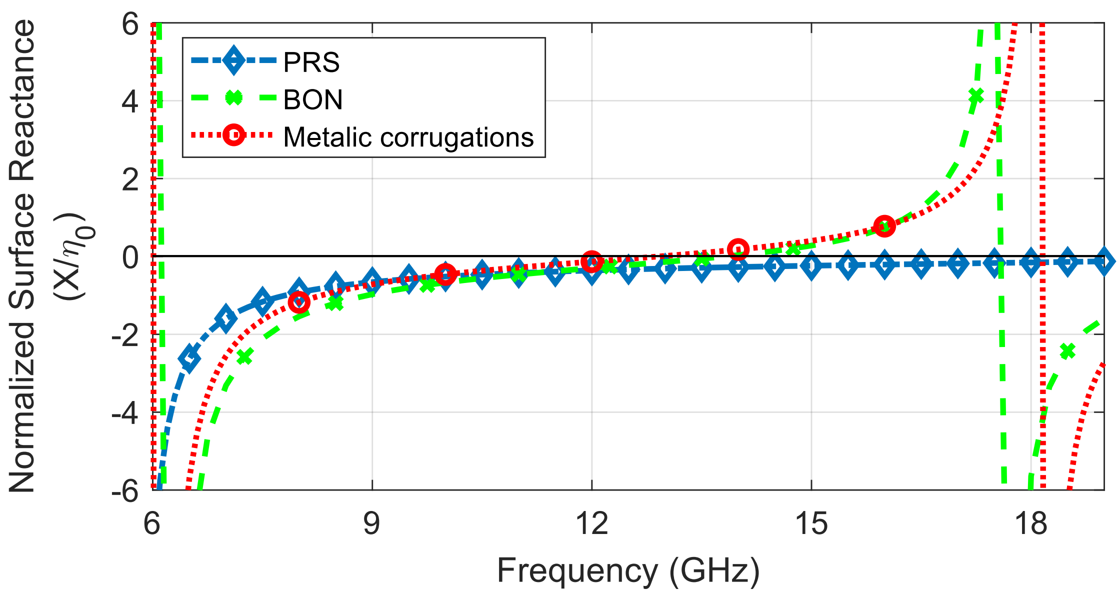

Figure 3.13: Comparison of normalized surface reactance of corrugations, bed of nails and PRS for TM polarized wave, incident at near grazing angle ($\theta = 89°$).

the desired improvement in isolation. Despite the reduction in reactance with higher permittivity, the surface will remain capacitive for >3:1 bandwidth. However, the structure is not isotropic with ϕ mainly because of the square geometry of the patches, in contrary to the bed of nails.

Table 3.1: Comparison between the considered HIS

Parameter	Metallic corrugations	Bed of Nails	PRS
Surface height	1.25 cm	1.25 cm	0.7 cm
Bandwidth	2:1	2:1	>3:1

The comparison of surface reactance of HISs for TM surface wave Fig. 3.13 indicates that the designed PRS is capacitive over 3:1 bandwidth, which is significantly higher than that achieved with metallic corrugations and bed of nails. Moreover, the former is thinner, lighter, and simple to fabricate, as summarized in Table 3.1.

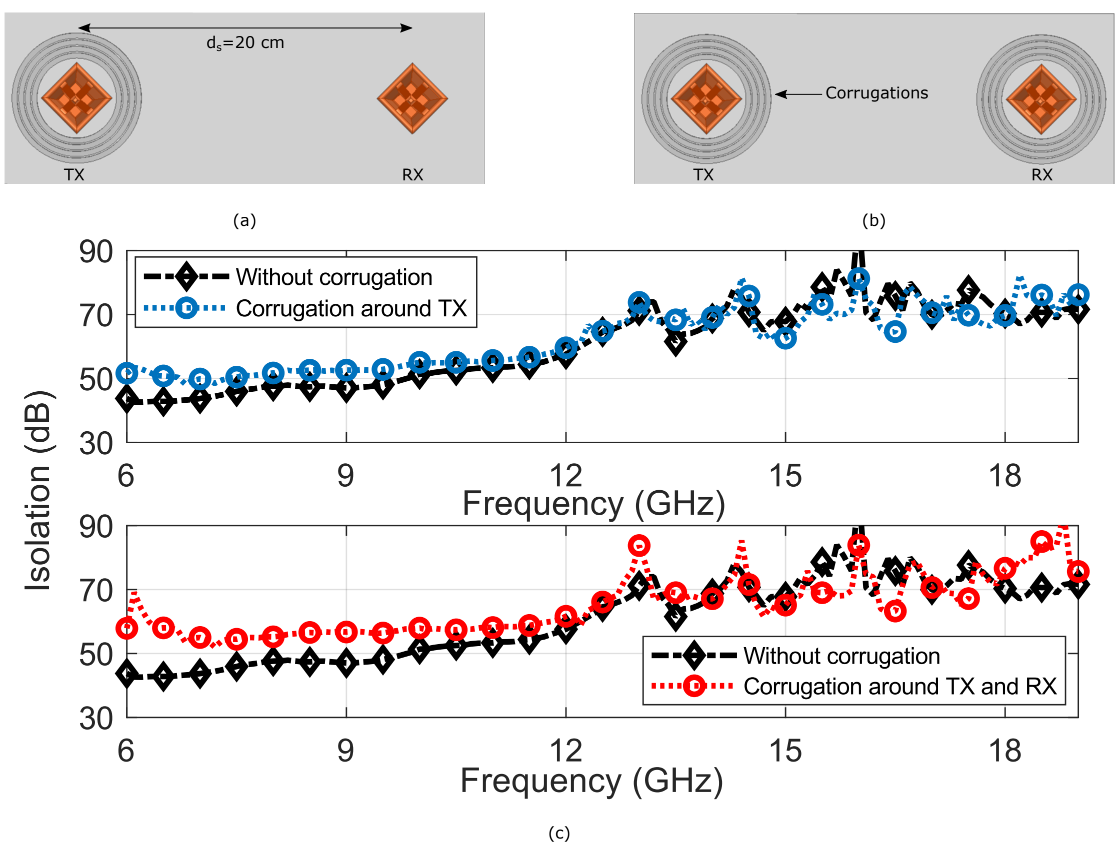

Figure 3.14: CAD models of corrugations around (a) TX only, (b) TX and RX, and (c) simulated TX and RX isolation on a finite ground plane.

3.4.4 Implementation

Theory, design steps, and the characteristics of HISs are explained in the preceding sub-sections. Following paragraphs discusses practical realizations and the effectiveness of those surfaces in reducing coupling. First, concentric corrugations are flush mounted with the TX and a maximum of 7 dB improvement in isolation is achieved. Up to 15 dB of reduction in coupling is obtained by embedding the corrugations around both of the antennas as shown in Fig. 3.14 [81]. The results indicate that the effectiveness of regular, and uniform corrugations in reducing the coupling is limited to an octave bandwidth, due to the variation of the surface reactance with frequency. Moreover, these structures increase the system weight and cost. Hence, other simple and relatively easy to realize variations of HISs are considered next.

When the designed bed of nails with 24 and 13 unit cells in the x-axis (i.e. towards the RX) and y-axis, respectively, is embedded between the TX and RX separated 20 cm edge-to-edge (see Fig. 3.15) the isolation increases from 42 dB to 59 dB, as described in Fig. 3.16. This 17 dB reduction in coupling is higher than that obtained in [44]. The comparison of isolation with the finite ground plane and bed of nails for two cases: h_{BON} = 1.5 cm and h_{BON} = 1.2 cm are shown in Fig. 3.16 and Fig. 3.17, respectively. The isolation > 60 dB is achieved over 95% of the operating bandwidth, with the bed of nails of h_{BON} = 1.2 cm. The impact of BON recedes around 10.2 GHz and coupling increases sharply about 12 GHz, for h_{BON} = 1.5 cm. Similarly, h_{BON} = 1.2 cm is effective until 13 GHz. This behavior is due to the dependency of Z_s as the function of

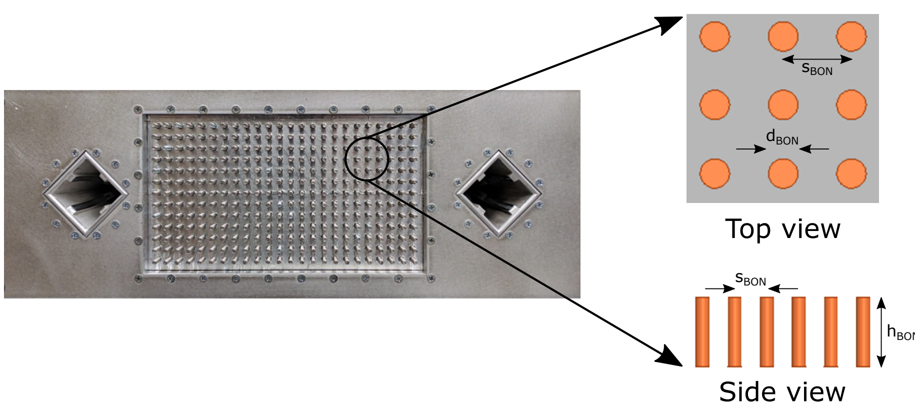

Figure 3.15: Bed of nails flush mounted between TX and RX. The TX and RX are separated edge-to-edge by 20 cm.

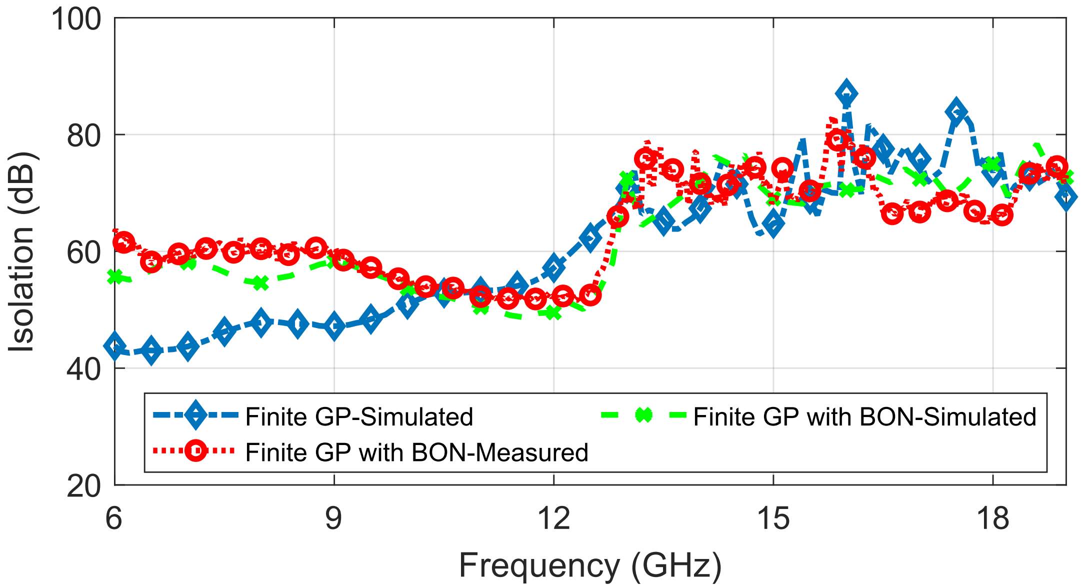

Figure 3.16: Isolation between TX and RX QRH in diagonal plane with the fabricated bed of nails between TX and RX when the height of bed of nails is 1.5 cm.

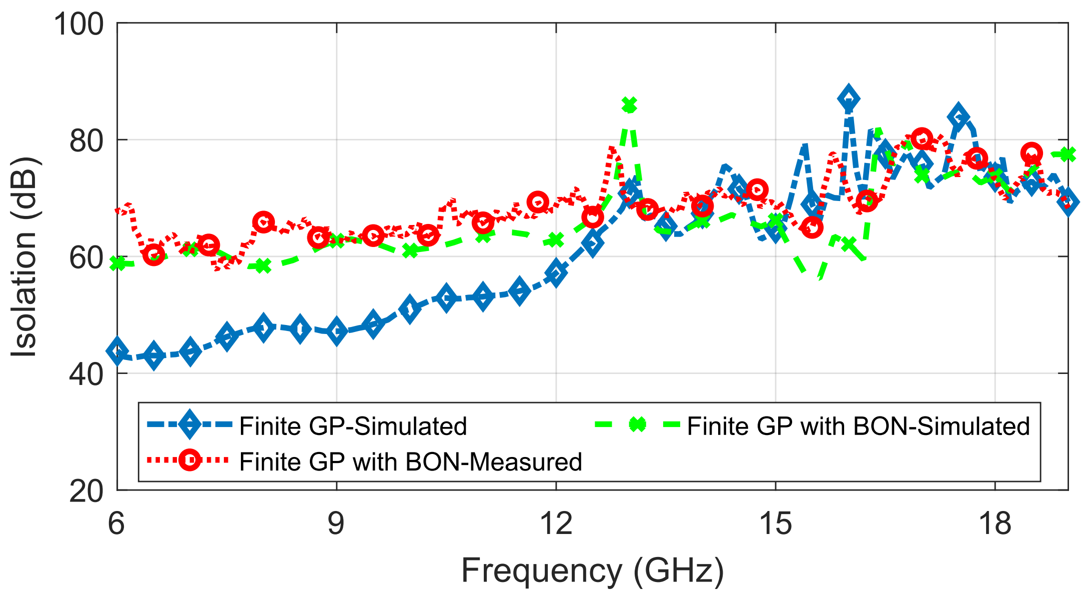

Figure 3.17: Isolation between TX and RX QRH in diagonal plane with the fabricated bed of nails between TX and RX when the height of bed of nails is 1.2 cm.

h_{BON} (see Fig. 3.8), which also proves the limited bandwidth of BON. The surface reactance of the bed of nails ($h_{BON} = 1.2$ cm) becomes inductive around 15 GHz which enhances the propagation of the TM_0 waves along the ground plane and thereby increases the coupling. The rise in the magnitude of the electric

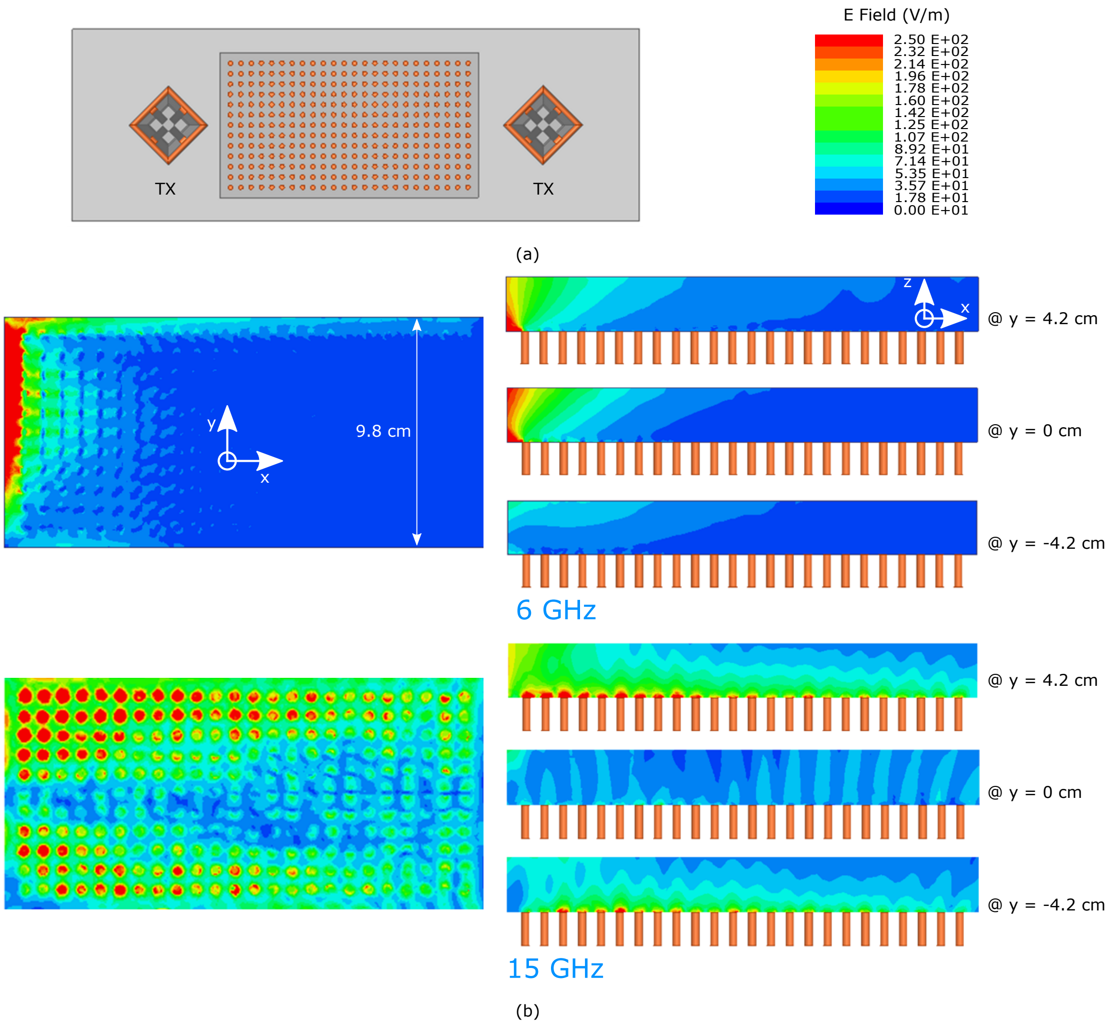

Figure 3.18: (a) CAD model of BON with TX and RX, (b) and (c) complex magnitude of E field along the surface and above the bed of nails when it is capacitive (@6 GHz) and inductive (@15 GHz), respectively.

field along the surface at 15 GHz, as depicted in Fig. 3.18 strengthens the above argument. Nonetheless, the measured coupling between TX and RX agrees well with the simulation results.

The bandwidth limitation of the BON is overcome by using the PRS as discussed in Section 3.4.3. The comparison of isolation, shown in Fig. 3.19, obtained with the bed of nails and PRS clearly highlights the bandwidth improvement of PRS, where the antennas are mounted in their E-plane over the finite ground plane. Moreover, isolation with and without PRS indicates that the capacitive reactance of the surface has significantly reduced the coupling at lower frequencies while maintaining the coupling equal to or less than

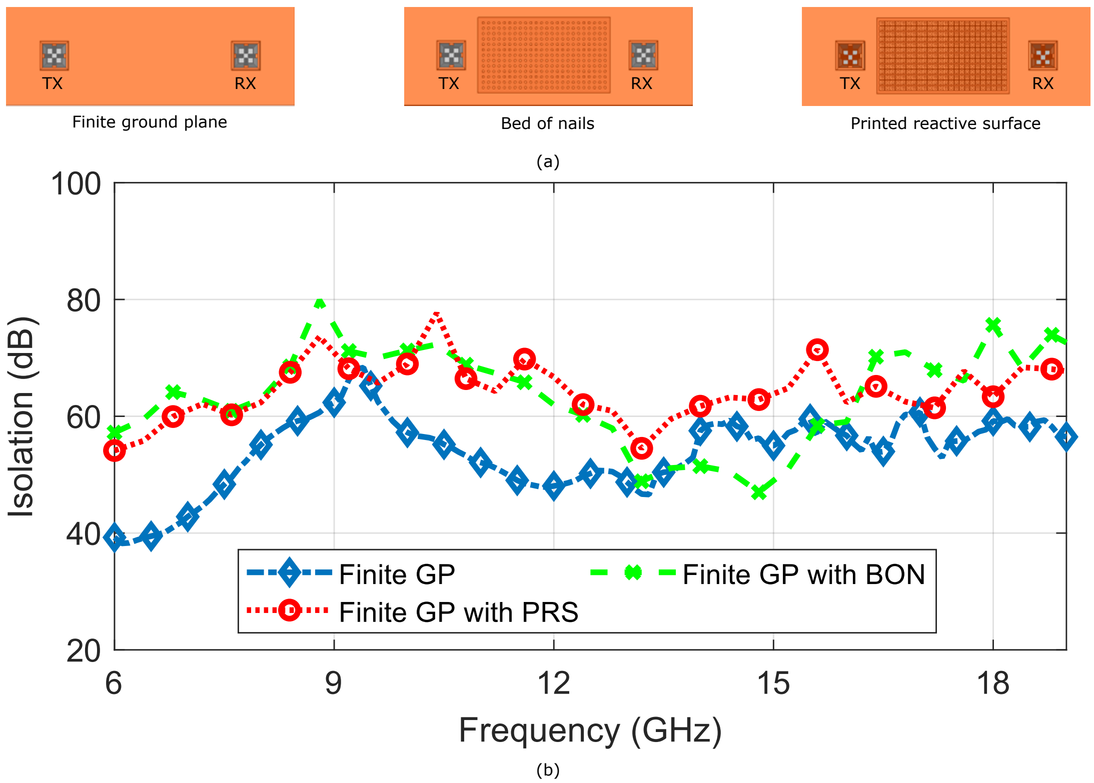

Figure 3.19: Simulated isolation between TX and RX in E-plane over finite ground plane, bed of nails, and PRS.

free space, for 3:1 bandwidth. The study of separation distance and number of unit cells between the TX and RX, shown in Fig. 3.20 and Fig. 3.21, indicates that the relative reduction in coupling and bandwidth is less sensitive to the number of unit cells. Specifically, at 7.2 GHz the increase in the isolation of 14 dB, and 15.7 dB are achieved with 11, and 24 unit cells, respectively. This study indicates that the bandwidth of the proposed PRS is not limited by the number of unit cells which is advantageous over the cascaded EBG in [44]. Hence, the considered approach with PRS is more suitable to reduce the coupling over a wide bandwidth when spacing between the TX and RX is limited. The fabricated surface consisting of 24, and 14 unit cells in the x-axis and y-axis, respectively, and flush mounted with QRH is shown in Fig. 3.22.

As discussed, the capacitive reactance of a PRS is a function of the permittivity of the substrate; the higher the permittivity, lower is the reactance offered by the surface (see Fig. 3.12). Therefore, the improvement in isolation obtained with a substrate of $\epsilon_r = 2.2$ is lesser than that of the air dielectric as

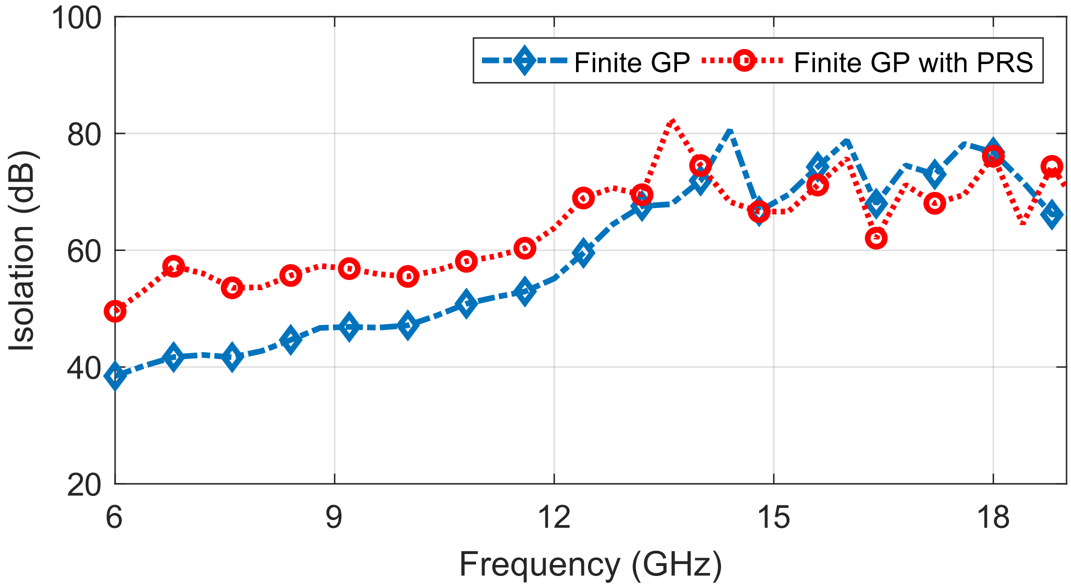

Figure 3.20: Isolation between the TX and RX for the separation 10 cm (11 unit cells), when the TX and RX are oriented in D-plane.

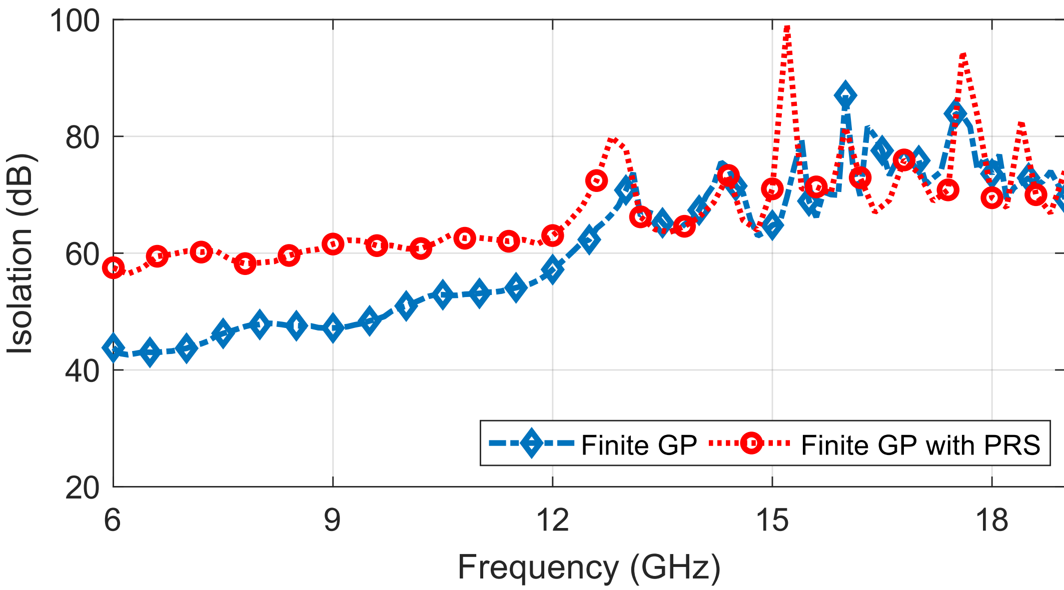

Figure 3.21: Isolation between the TX and RX for the separation 20 cm (24 unit cells), when the TX and RX are oriented in D-plane.

shown in Fig. 3.23. Nonetheless, the designed PRS on Taconic TLY 5 substrate remains capacitive for 3:1 bandwidth. The agreement between the measured and simulated coupling (see Fig. 3.24) between the antennas with PRS further strengthens all discussed arguments.

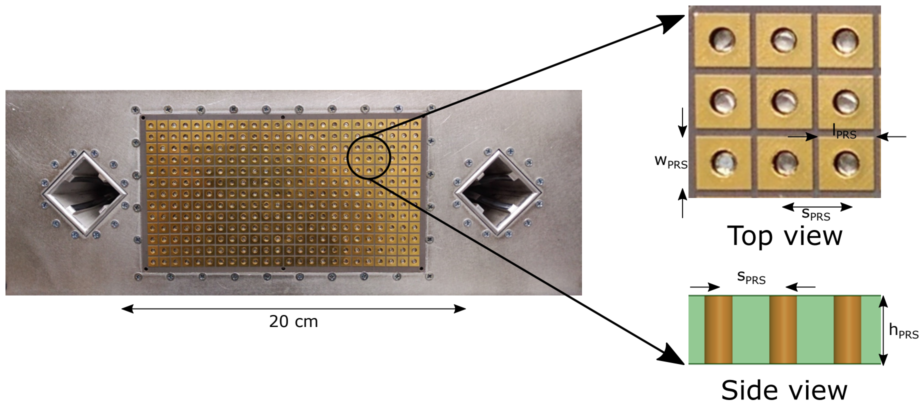

Figure 3.22: PRS flush mounted between TX and RX, which are separated edge-to-edge by 20 cm.

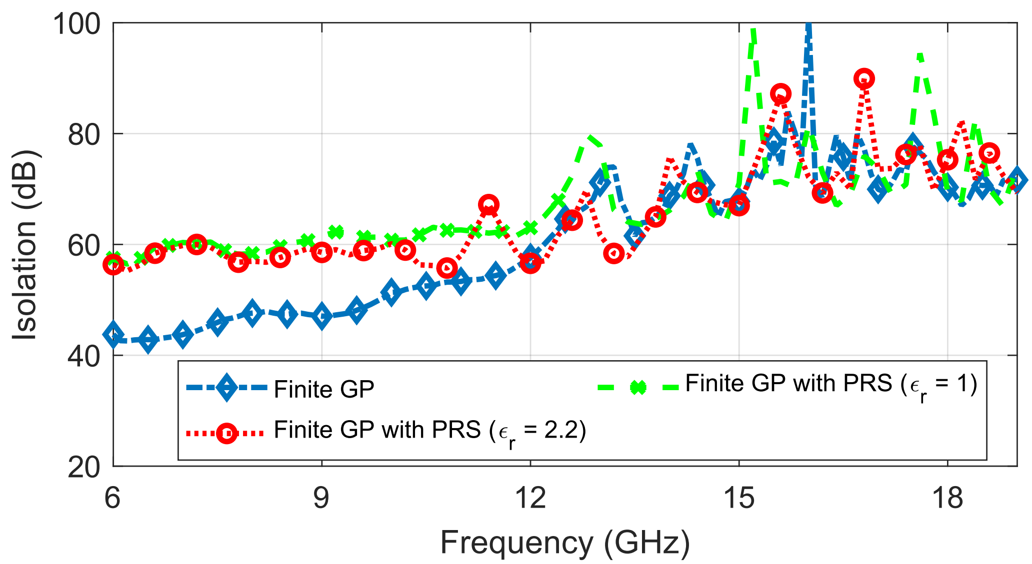

Figure 3.23: Simulated isolation between the TX and RX QRH with PRS between TX and RX with PRS in free space, and $\epsilon_r = 2.2$.

The HIS modifies the flow of currents on a ground plane and the proximity of these structures to the antenna will have an influence on its radiation patterns, which can be analyzed by comparing the radiation patterns with and without the surface. Radiation patterns in Fig. 3.25 indicate that the impact can be noticed only at higher elevation angles and is insignificant along boresight and over half-power beamwidth (HPBW). Also, it is important to note that the TX and RX antennas have similar radiation patterns. Further, envelope correlation coefficient (ECC) [17, 82] between the radiation patterns can be used to quantify the effect of HIS.

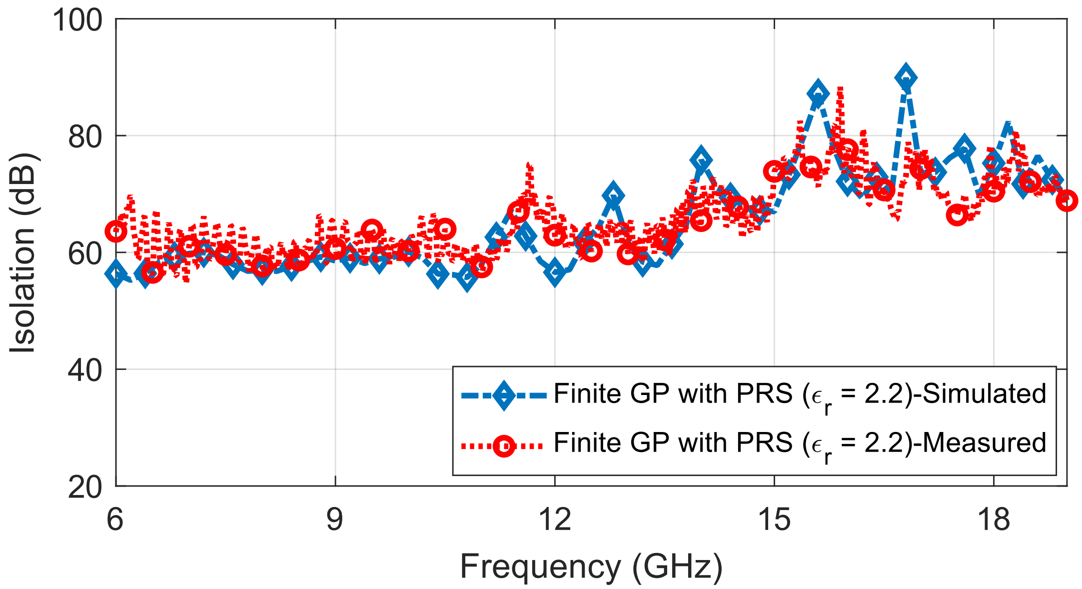

Figure 3.24: Simulated and measured isolation between the TX and RX QRH with PRS between TX and RX with PRS $\epsilon_r = 2.2$.

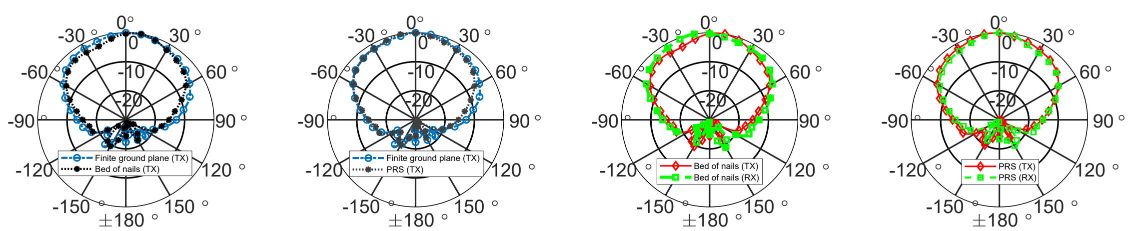

Figure 3.25: Simulated radiation patterns of TX, and RX when flush mounted in finite ground plane and embedded with HIS (bed of nails and PRS), at 6 GHz.

3.5 Absorber Loading

The other well-known technique to reduce the gain at the horizon and thus the coupling is to recess the antenna inside an absorber cavity [28]. To demonstrate that, an artificial absorber with ϵ_r = 1-j2.7 and μ_r = 1-j2.7 [83] is wrapped around the RX QRH, in the simulation. As shown in Fig. 3.26, up to 15 dB increase in isolation is achieved at the expense of the RX antenna efficiency, which drops to 15% at the lower frequency end. Note that a reduction in efficiency, such as one shown here, may be acceptable for some applications.

The coupling between TX and RX can be further reduced by combining the different techniques mentioned in the previous sections. For example, the HIS can be flushed mounted while the RX is recessed in an absorber cavity. In this approach, HIS reduces the coupling due to surface currents and recessing in the absorber lowers the gain of the RX antennas at horizon, thereby further increasing the isolation. The HFSS model of bed of nails and PRS with RX recessed in absorber cavity is shown in Fig. 3.27. The Fig. 3.28, and Fig. 3.29 indicate that 10 dB further improvement in isolation can be achieved with this technique, however, the efficiency of the RX antenna will drop by 15% (@6 GHz), as mentioned before. This efficiency can be

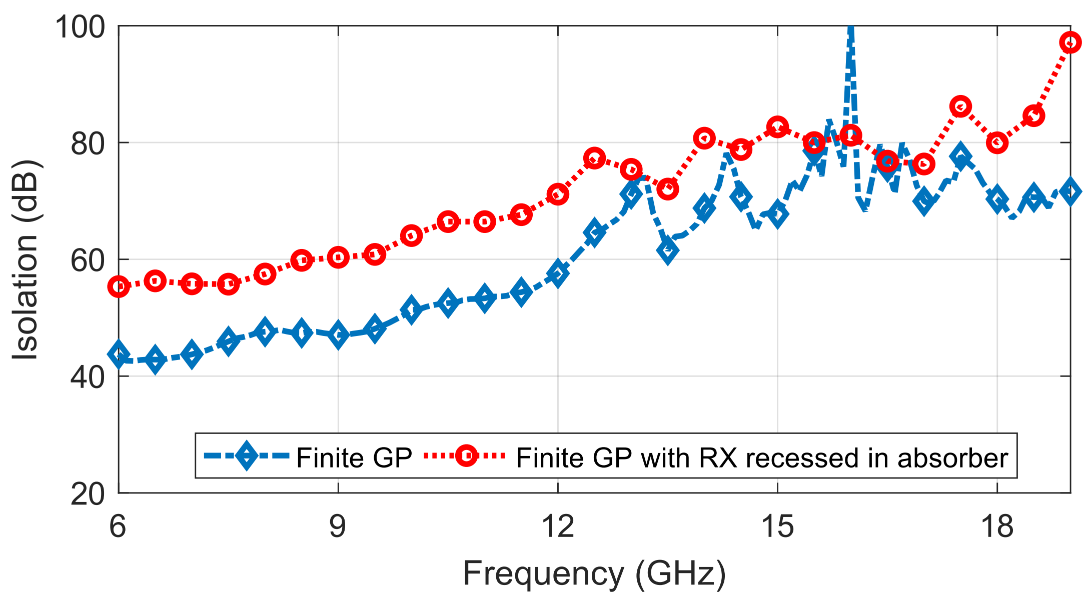

Figure 3.26: Simulated coupling between TX and RX for the antennas oriented in D-plane on finite ground plane when the receiver is recessed inside the absorber cavity. The TX and RX are separated edge-to-edge by 20 cm.

improved to 30% by using a step in the thickness of absorber cavity, that is by decreasing the thickness of the absorber with an increase in the height from the aperture to ground plane.

3.6 Influence of Scatterers

Often antennas from one band are placed next to radiators from other applications. Therefore, investigating the impact of neighboring scatterers and antennas on the system isolation is necessary. This influence is dominant at high and mm-wave frequencies. Specifically, the isolation dropped by 20 dB when the 18-45 GHz antennas are mounted on a 12” × 12” platform along with the spiral antenna, as shown in

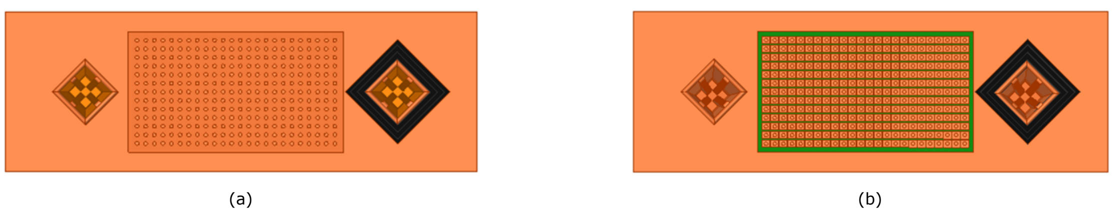

Figure 3.27: HFSS model of a (a) bed of nails in between TX and RX, combined with RX recessed in absorber, and (b) PRS in between TX and RX, combined with RX recessed in absorber.

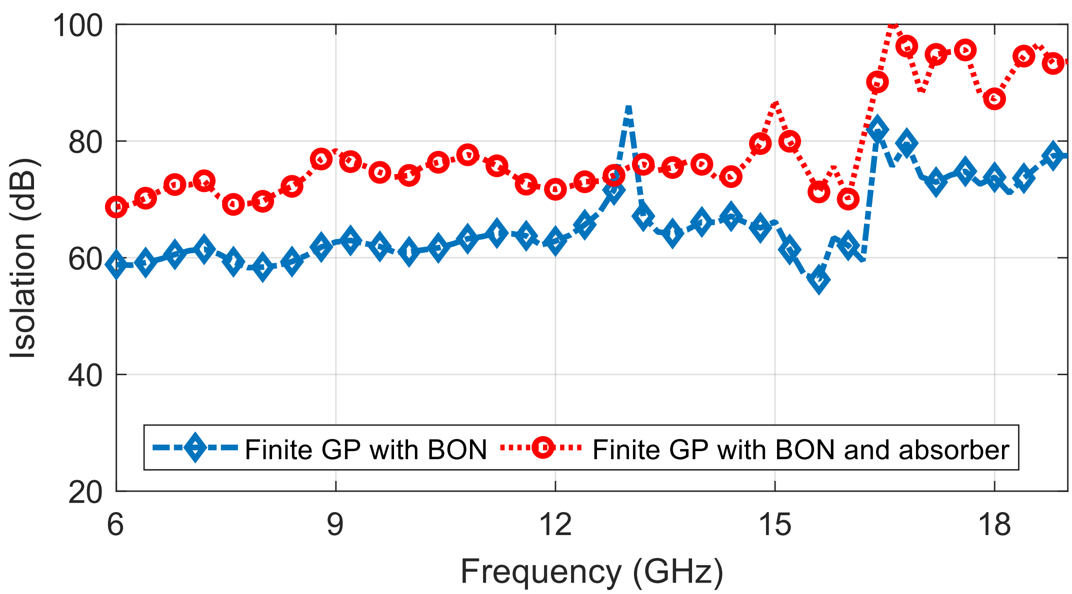

Figure 3.28: Simulated coupling between TX and RX QRH when the antennas are oriented in D-plane with bed of nails, where the RX is recessed in absorber.

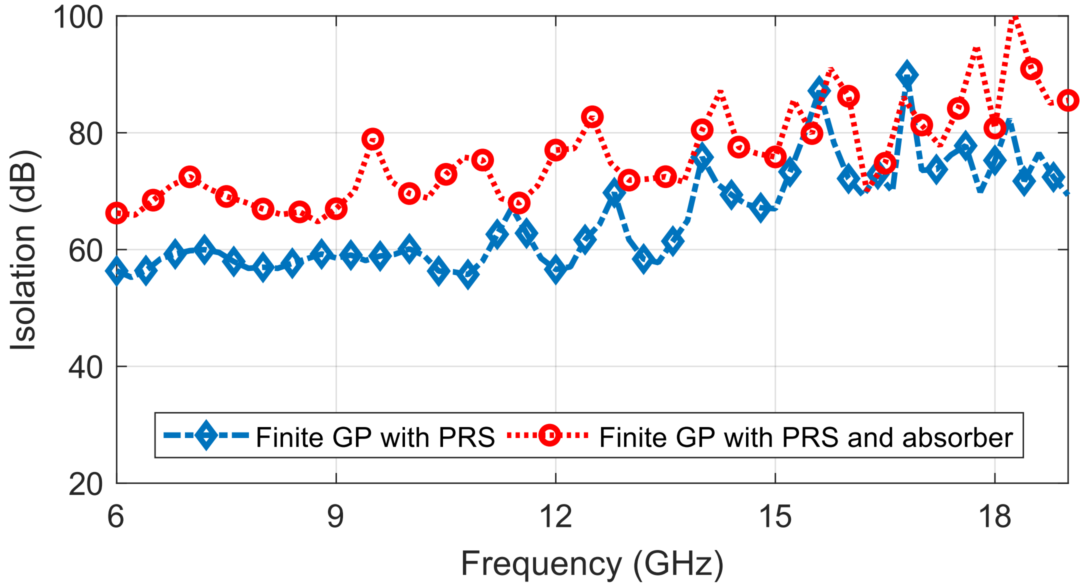

Figure 3.29: Simulated coupling between TX and RX QRH when the antennas are oriented in D-plane with PRS, where the RX is recessed in absorber.

Fig. 3.30 (a) and (d). The degradation is mainly due to the excitation of surface waves in the dielectric substrate. Comparison of the system isolation with only metal scatterers Fig. 3.30 (b) and (e) and with 60 mils substrate of $\epsilon_r = 3$ Fig. 3.30 (c) and (f), confirms the above statement. Nonetheless, isolation >60 dB is achieved by proper placement of the antenna in a platform operating from 0.5 to 110 GHz, as illustrated in Fig. 3.31.

3.7 Summary

The theory and design parameters of three types of HIS, namely, metallic corrugations, bed of nails and PRS are outlined. The surface impedance of these structures for the TM_0 plane wave incident at grazing angle is used as a design metric. Also, the chapter presents a comparison of operational bandwidth of HISs, where the bandwidth is defined as the frequency range for which the surface remains as capacitive for a TM_0 wave. Importantly, it is demonstrated that the PRS can achieve wider bandwidth, >3:1, than the rest of the HIS discussed herein. The realized bi-static STAR antenna subsystem with embedded PRS has measured isolation >60 dB over 6 - 19 GHz for antennas separated edge-to-edge by 20 cm ($4\lambda_{6GHz}$). Additionally, the

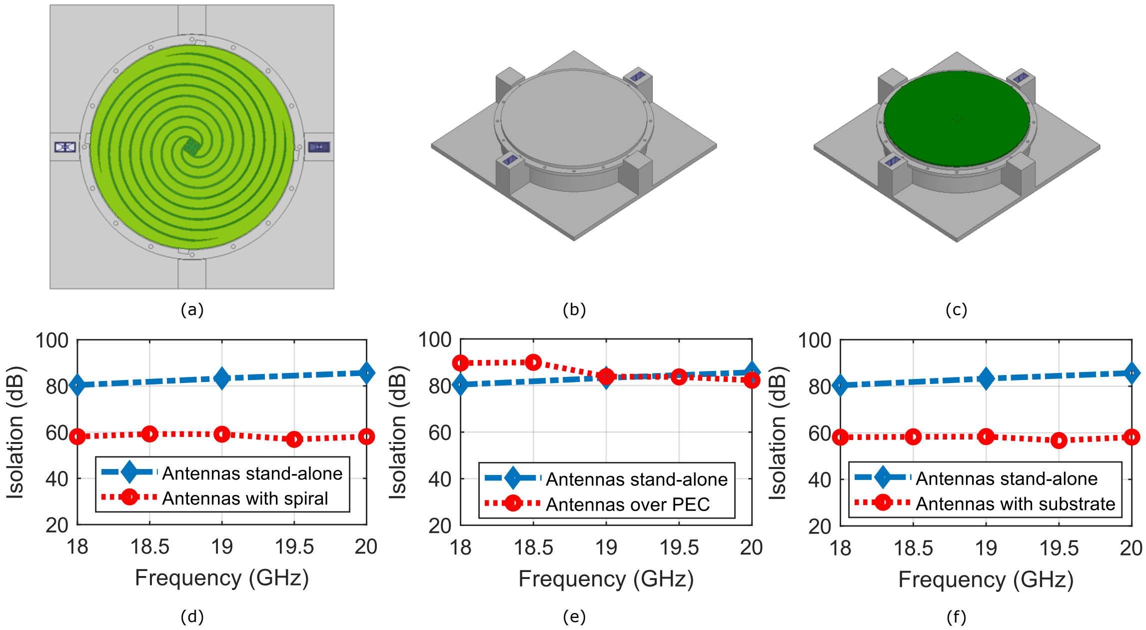

Figure 3.30: Simulated isolation between single polarized TX and RX mounted on SPEAR tray 12" × 12": (a) and (d) with spiral in between, (b) and (e) only PEC scatterers, and (c) and (f) with substrate.

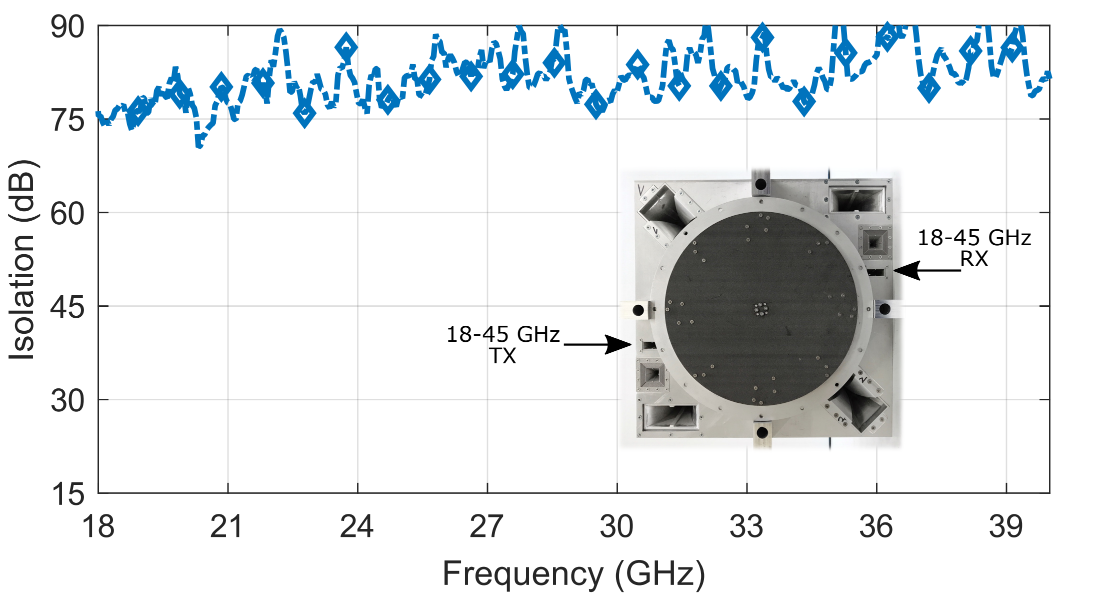

Figure 3.31: Measured isolation between single polarized TX and RX mounted on SPEAR tray 12" × 12" with antennas operating from 0.5-110 GHz.

influence of permittivity on the surface reactance and system isolation is discussed.

Chapter 4

Monostatic High Directivity STAR

4.1 Introduction

The sole focus of this chapter is to maximize the isolation from the antenna layer in a high directivity reflector-based STAR system, which could play a critical role in boosting the overall system performance given high isolation and good TX and RX radiation characteristics; particularly for a line-of-sight communication system. Implementing a long-range STAR system is more challenging due to the high TX power (i.e. higher self-interference) required to achieve the desired range. Alternatively, antennas with high gain can be employed to overcome the input power requirement of the long-haul microwave links. Various monostatic and bi-static full-duplex STAR antennas and antenna arrays with high isolation between TX and RX have already been proposed [22, 27, 30, 39, 68, 69, 81, 84, 84]. However, none of these systems have sufficiently high gain required for long-range communications, despite high isolation. The reflector-based antenna can be designed to overcome that, and if a feed with low SI between TX and RX is used, the desired features of STAR, greater EIRP, reasonable size, and low complexity can be achieved. Bi-static approaches [29, 84] are robust and less sensitive to the imbalances; however, they require significant spacing between TX and RX to achieve high isolation. When a bi-static approach is applied to reflector-based systems, as in [85], it further increases the overall size of the system. Specifically, in [85] the reflector separation is 57.2 cm, that is $19\lambda_{10GHz}$. When the same system is scaled to C-band (4 to 8 GHz) that corresponds to 143 cm, which is in addition to increase in the reflector dish size. Hence, the overall system dimensions can be on the order of 25λ, which may not be possible for many applications. Hence, a monostatic configuration is highly desired for a reflector-based system. In this research, it is achieved by feeding the circularly polarized (CP) coaxial cavity antenna with all-analog beamforming network (BFN) consisting of two 90° and 180° hybrids and two circulators. The BFN is arranged to cancel the coupled/leaked signal from the antenna and circulators, by creating 180° phase difference between the TX and RX reflected signals. The realized arrangement results in high isolation between the TX and RX [22–24, 86]; however, the practically achieved isolation is limited by the imbalances of the BFN and the asymmetry in the antenna geometry. The significance of these imbalances is also discussed later in the chapter.

Generally, directive antennas like pyramidal, conical, and corrugated horns are used as feed for reflector antennas [41, 45–47, 87–90], which can handle high power and have high radiation efficiency. However, these antennas have significant phase center variations [90], and asymmetric E and H plane patterns [91, 92]. Therefore, when they are used as feeds for reflectors, the variation in phase center can lead to reduced efficiency, axial defocusing, and increase in side lobe levels. Similarly, asymmetry in principal planes patterns result in higher cross-polarization [90]. Coaxial cavity antennas [93] can be designed with symmetric E and H plane patterns, constant phase center and low dispersion as mentioned in [94, 95]. Also, dual linear and circular polarization can be easily achieved by the coaxial cavity antenna. However, the coaxial cavity antennas discussed in the open literature are not well-matched over an octave bandwidth [93–95], something addressed in this research.

The reflector antenna is designed as axis-symmetric or prime fed reflector, which has symmetric radiation patterns, low SLL, and cross-polarization level. Apex matching technique [87, 90, 96] is used to reduce the impact of the reflector on the reflection coefficient of the feed. The prime fed configuration requires a support structure for the feed, which results in additional blockage and increase in SLL. This is overcome by extending the inner conductor of the coaxial cavity to the apex of the reflector, Fig. 4.1. The resulting self-supporting architecture resembles the ‘ring feed’ [87], and ‘hat feed’ antennas [89, 97, 98].

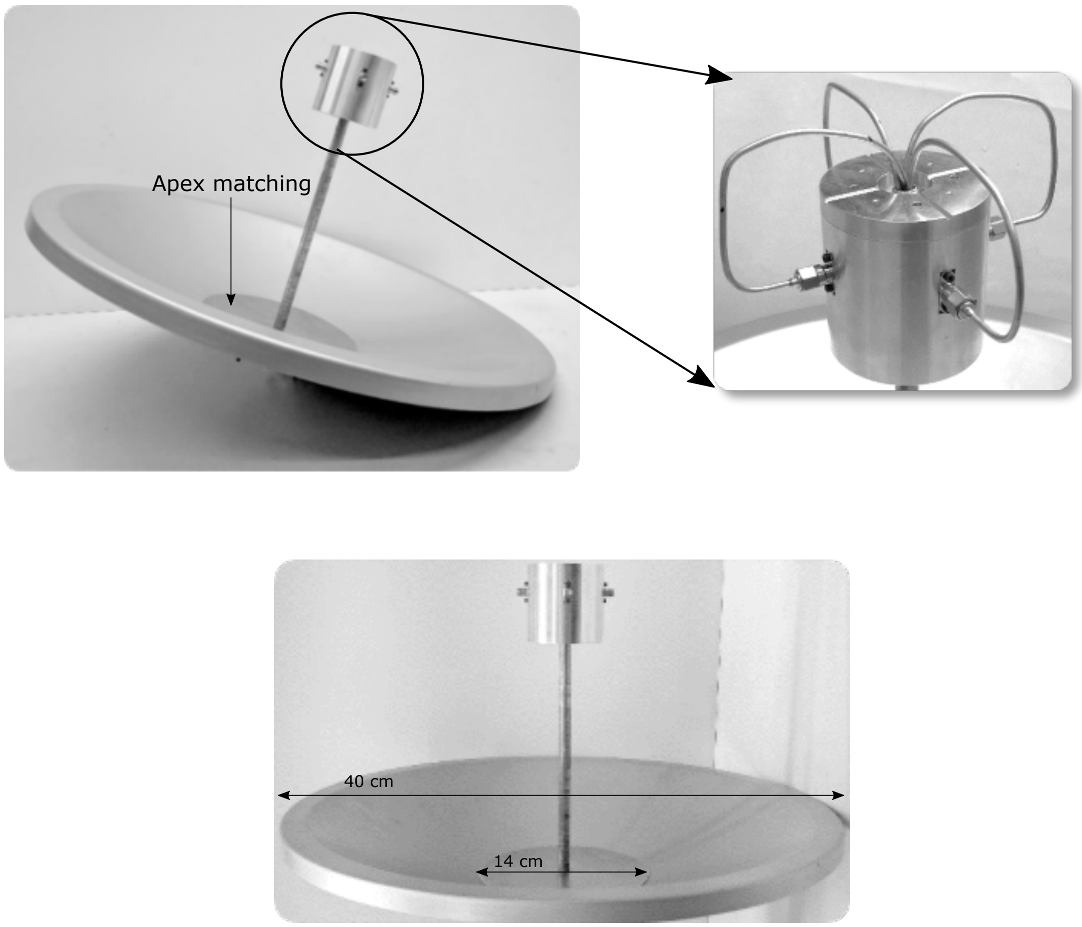

Figure 4.1: Fabricated self-supporting reflector antenna with coaxial cavity feed and apex matching.

However, the operation principle is different, and doesn't require a special paraboloid surface [99]. Also, the antenna has wider bandwidth than the single strut antennas in [87, 97, 98]

This chapter is organized into three sub-sections:

- Section 4.2 describes the design and performance of the coaxial cavity antenna stand-alone, and as a feed. Also, it outlines the implementation and far field results of a parabolic reflector antenna.

- Section 4.3 presents the architecture and signal cancellation approach of the monostatic high directivity STAR antenna. Further, the simulated and measured system isolation are discussed. In addition to the influence of electrical imbalances and geometrical asymmetries on the achievable isolation.

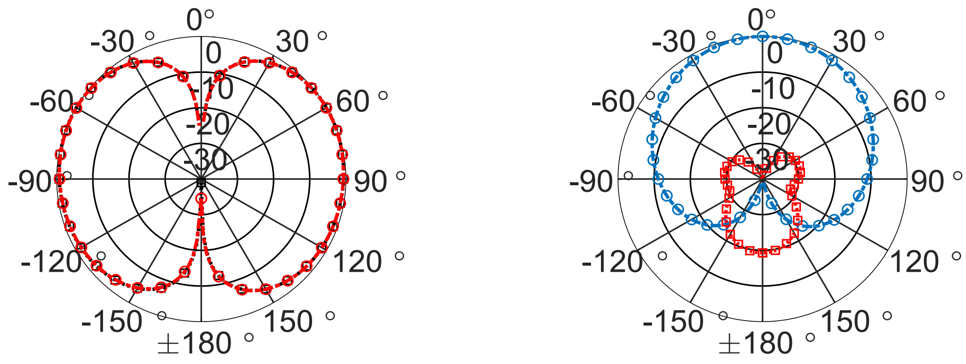

Figure 4.2: Far field patterns of (a) TEM and (b) TE_{11} mode of coaxial cavity antenna.

4.2 Reflector Antenna Design

4.2.1 Feed Design

The coaxial cavity antenna is an open-ended waveguide radiating into free space. Sometimes, this configuration is referred to as nested coaxial waveguide feed [91–95]. This antenna can be analyzed using the theory outlined in [37]. Fundamental mode of the waveguide is TEM with a null at boresight, Fig. 4.2. Hence, to achieve a directional beam, the waveguide is operated in its first higher order mode, i.e. TE_{11}. The cut-off frequencies of TE_{11} and TE_{21} (second higher order mode) are given by (4.1) and (4.2) [37, 100]. Thus, the inner (A_{id}) and outer (A_{od}) conductor radii are selected accordingly for single mode operation over an octave bandwidth (4 to 8 GHz). Linearly polarized TE_{11} mode can be excited by creating X or Y oriented current distribution, which is achieved by exciting opposite ports with 180° out of phase signals, as shown in Fig. 4.3. Exciting ports 1 and 3 generates horizontal polarization whereas exciting ports 2 and 4 generates vertical polarization. The orthogonality between the two excited TE_{11} modes ensures the dual polarized operation. Further, these ports can be excited with ±90° phase progressions to realize the desired CP operation (RHCP or LHCP), as illustrated in Fig. 4.3.

$$\lambda_{c11} = 1.873(\frac{\pi}{4})(A_{od} + A_{id}) \tag{4.1}$$

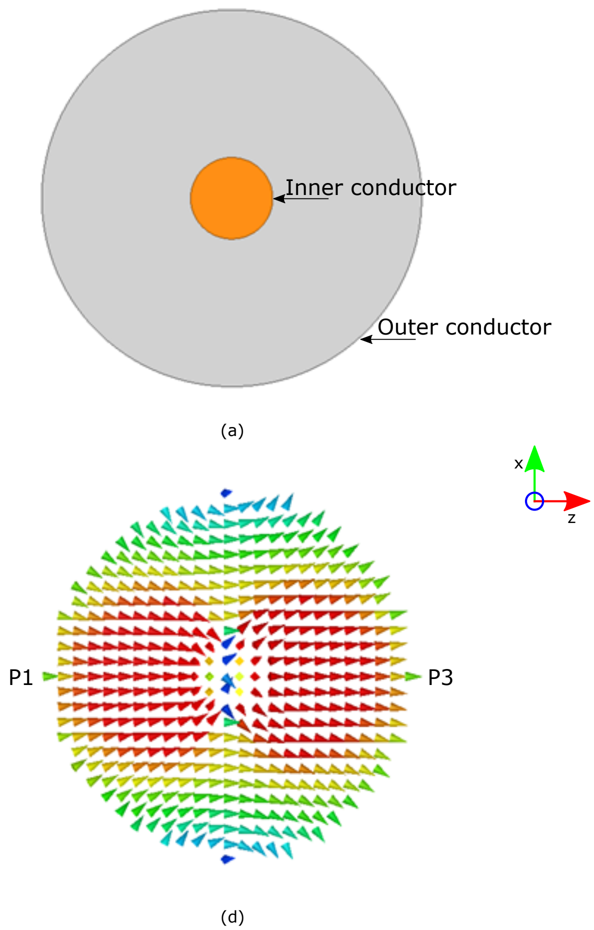

Figure 4.3: (a) Picture of coaxial waveguide, (b) fabricated antenna (top view) with excitation probes for TE11 mode, (c) and (d) E fields of TE_{11} mode in Y and X directed currents with corresponding ports.

$$\lambda_{c21} = 1.023(\frac{\pi}{4})(A_{od} + A_{id}) \tag{4.2}$$

Impedance match of the antenna is one of the crucial parameters for the system operation and it becomes critical when the antenna is intended for relatively high input power. In spite of its good far field performance, the broadband impedance match of the coaxial cavity antenna is not easy to achieve [93, 101]. This is addressed, herein. First, the ratio of inner to outer conductor diameter of an open-ended coaxial waveguide is varied to achieve reflection coefficient $|S_{11}|$ <-10 dB. In the simulation, this is conducted by exciting the waveguide with a wave port in TE_{11} mode. The reflection coefficient of the antenna, shown

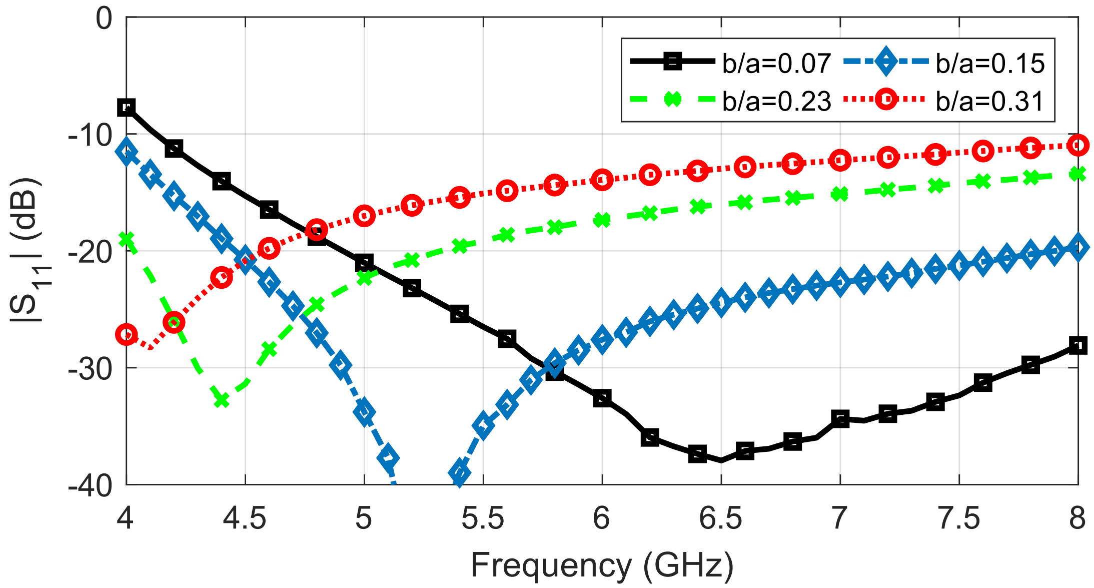

Figure 4.4: $|S_{11}|$ of the coaxial cavity antenna for different inner and outer conductor diameter ratios, A_{id}/A_{od}.

in Fig. 4.4, indicates that higher b/a ratio deteriorates the impedance match at higher frequencies. These results are in accordance with the similar study performed in [91, 101]. Moreover, the b/a ratio controls the E and H patterns' symmetry of the antenna, as mentioned in [101], which is essential for achieving uniform illumination of the reflector surface (in ϕ) and for symmetric radiation patterns. Hence, as a compromise between impedance match and pattern symmetry, $A_{id}/A_{od} = 0.23$ is selected for the designed antenna. Also, the asymmetry between E and H plane patterns negatively influences the cross-pol level and thus the axial ratio (AR) for the CP operation. Therefore, A_{id}/A_{od} is an important design parameter.

In addition to the cross section of the aperture/waveguide, the physical dimensions of the exciting probes are critical for achieving good impedance match of the antenna. Hence, in step two, the probes are shaped for $|S_{11}|$ <-10 dB over an octave bandwidth. The important parameters are length, P_{len}, shape, and height of the probes from bottom of the cavity, P_{ht}. Specifically, as shown in Fig. 4.5, a cylinder (probe II) with diameter of 0.127 cm and length of 1.64 cm has narrower bandwidth ($|S_{11}|$ <-10 dB) in comparison to the mono-cone shaped probe (probe I), which is due to the reduction in reactance of the input impedance seen at the port, Fig. 4.6, with frequency. Further, P_{ht} and P_{len} are determined to achieve $|S_{11}|$ <-10 dB over the band by performing the parametric study in HFSS. Thus, the studies conducted herein indicate

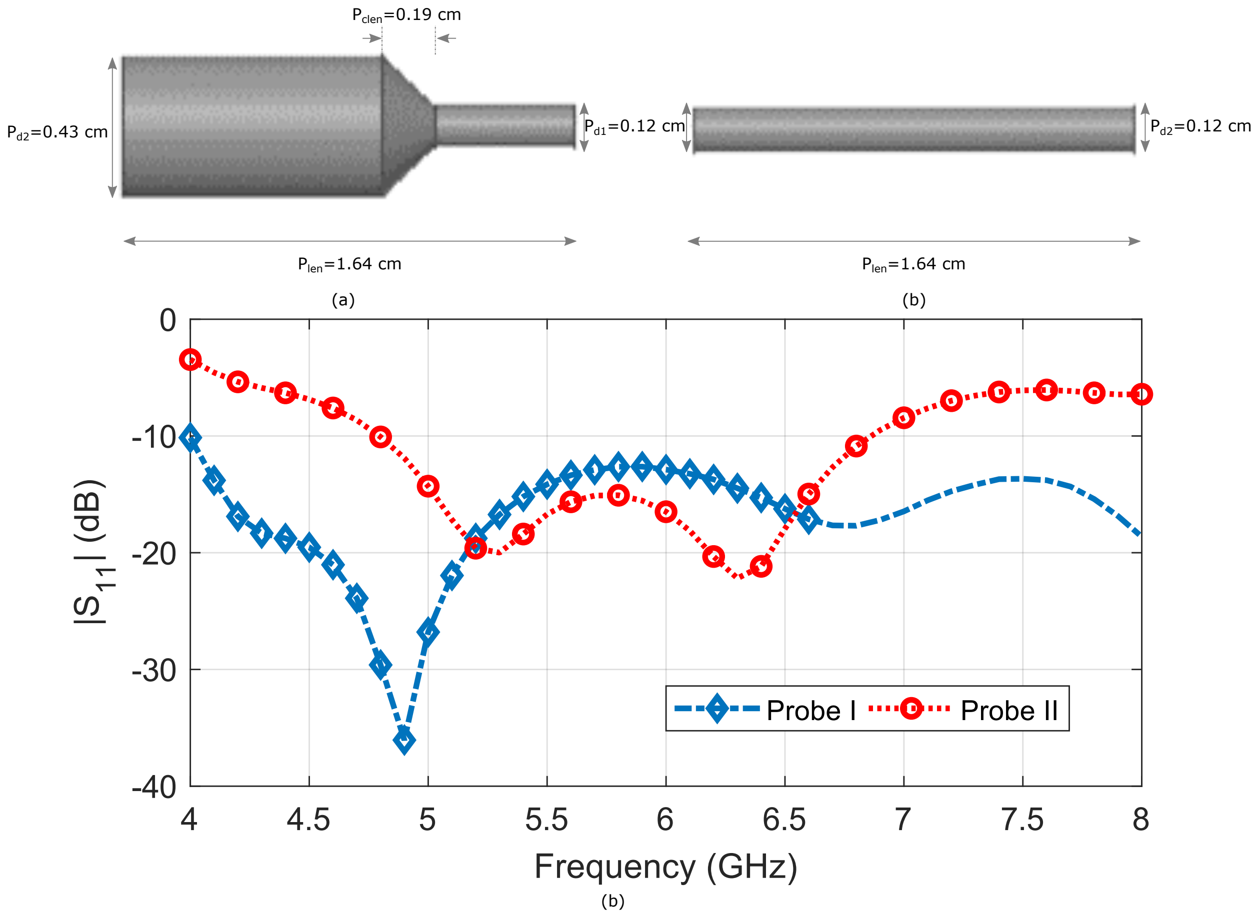

Figure 4.5: (a) and (b) Shape and dimensions of the modified and cylinder probe, respectively, and (c) active reflection coefficient of the coaxial cavity antenna for different probe shapes

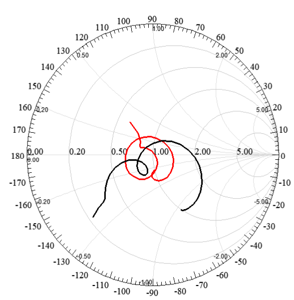

Figure 4.6: Smith chart showing the impedance of probes I (red) and II (black).

that with proper selection of A_{id}/A_{od} ratio and probes dimensions, an octave of bandwidth ($|S_{11}|$ <-10 dB) can be achieved for a coaxial cavity antenna. The antenna is fabricated with $A_{id} = 1$ cm, $A_{od} = 4.62$ cm and height, $A_{ht} = 5.06$ cm, which is same as the height of inner and outer conductors (see Fig. 4.7). The

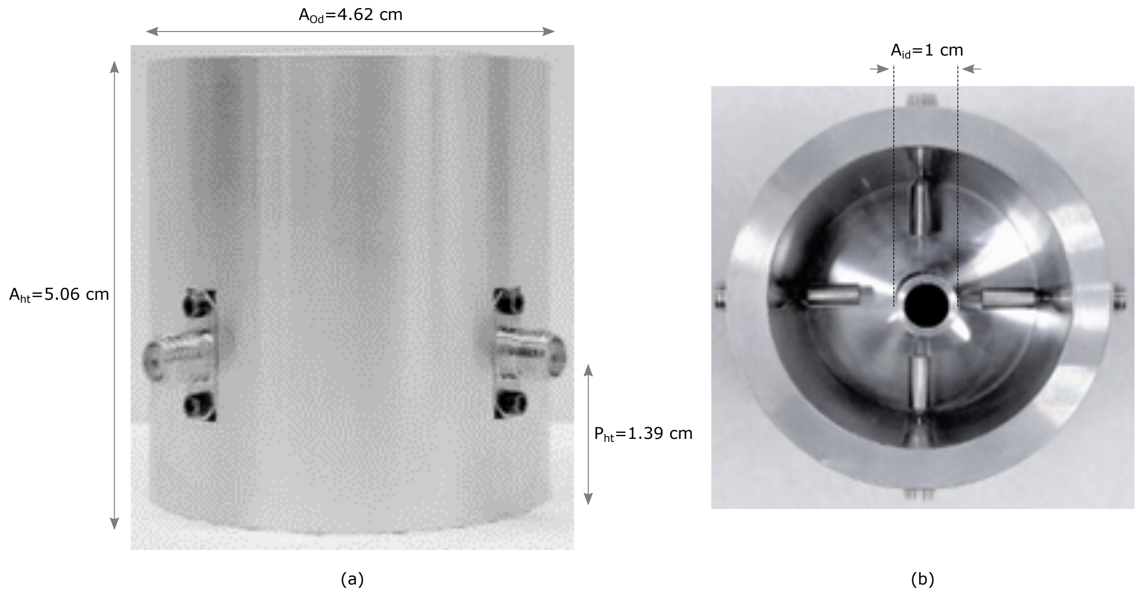

Figure 4.7: Fabricated coaxial cavity antenna and its dimensions.

fabricated antenna has measured $|S_{11}|$ <-10 dB over an octave bandwidth, and the impedance match with BFN measured at the input of 90° hybrids is depicted in Fig. 4.8. The 90° hybrids in conjunction with 180° hybrids are used to realize CP. The reflection coefficient at the input of 90° hybrids is low (<-20 dB) since all the reflected signals from the antenna and the 180° hybrids are routed to unused port, which are terminated with a matched load. It should be noted that all the terminated signals account for the system total loss and, hence, it is important to minimize their level.

The antenna has an excellent far field performance. Specifically, gain >6 dBic with aperture efficiency >87% (@8 GHz), AR <3 dB for $\theta = \pm 30°$, symmetric radiation patterns over ϕ (0° to 360°), are shown in Fig. 4.9, Fig. 4.10, Fig. 4.11, and Fig. 4.12 respectively. The results indicate good agreement between the measurement and simulation. The designed coaxial cavity antenna has phase center variation <5% and <15% for CP and linear polarization operations, respectively for the angular span of 106° in θ (the angle subtended by the designed reflector at the focus), as illustrated in Fig. 4.13. The phase center is calculated using the slope method [102], where the reference coordinate system is considered at the aperture of the antenna.

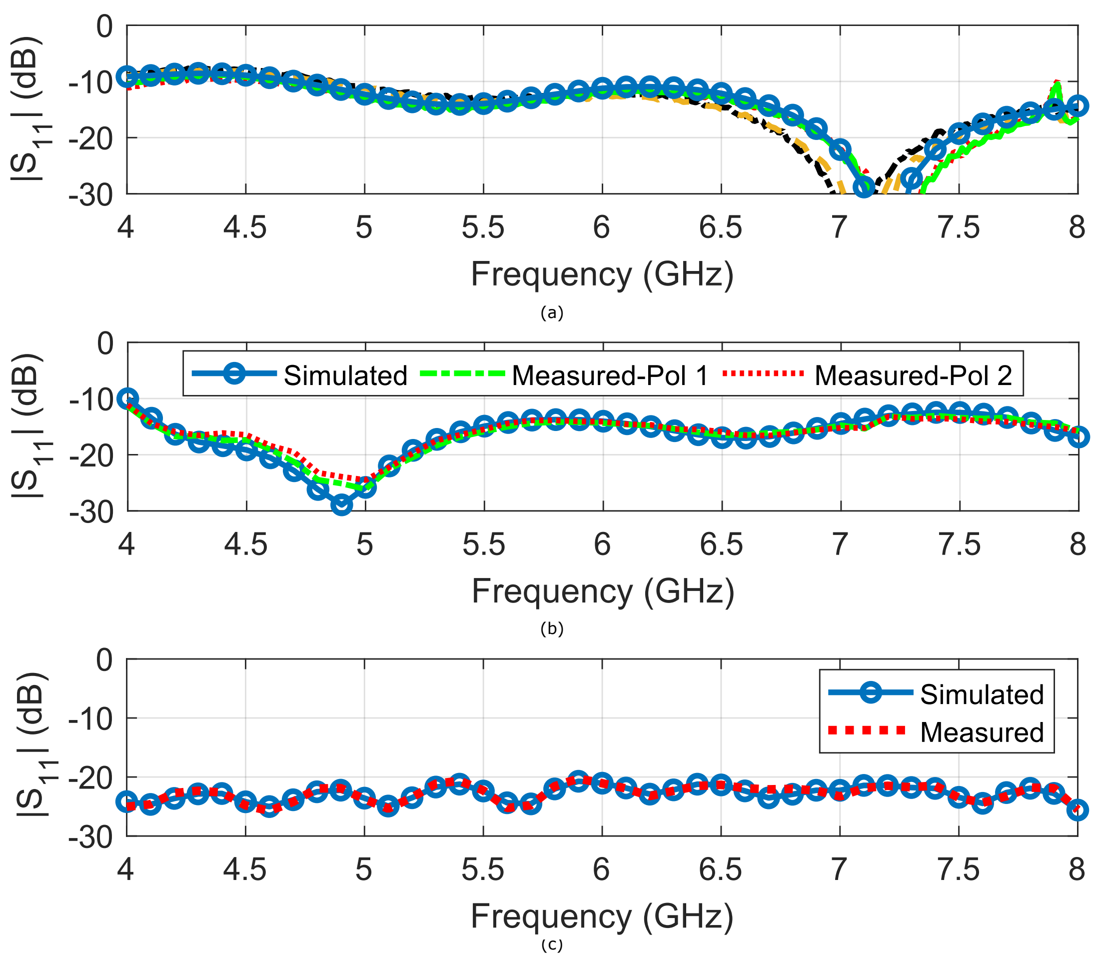

Figure 4.8: Simulated and measured active reflection coefficients of the coaxial cavity antenna at the input ports of the (a) antenna, (b) 180° hybrids, and (c) 90° hybrids.

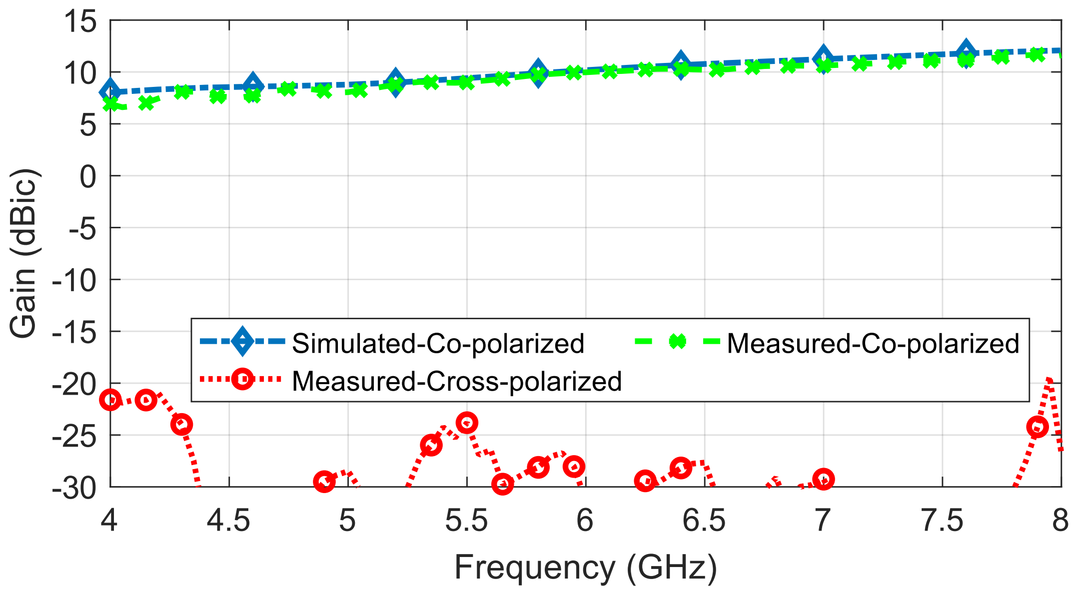

Figure 4.9: Measured and simulated broadside gain of the designed coaxial cavity antenna.

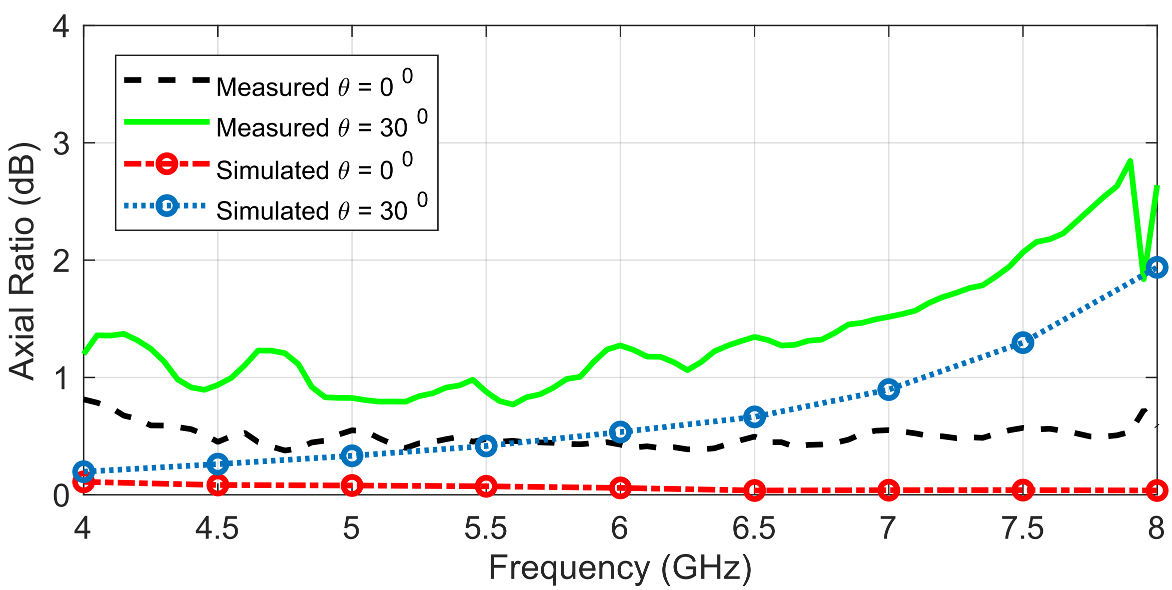

Figure 4.10: Measured and simulated axial ratio at $\theta = 0°$, and $30°$ of the designed antenna.

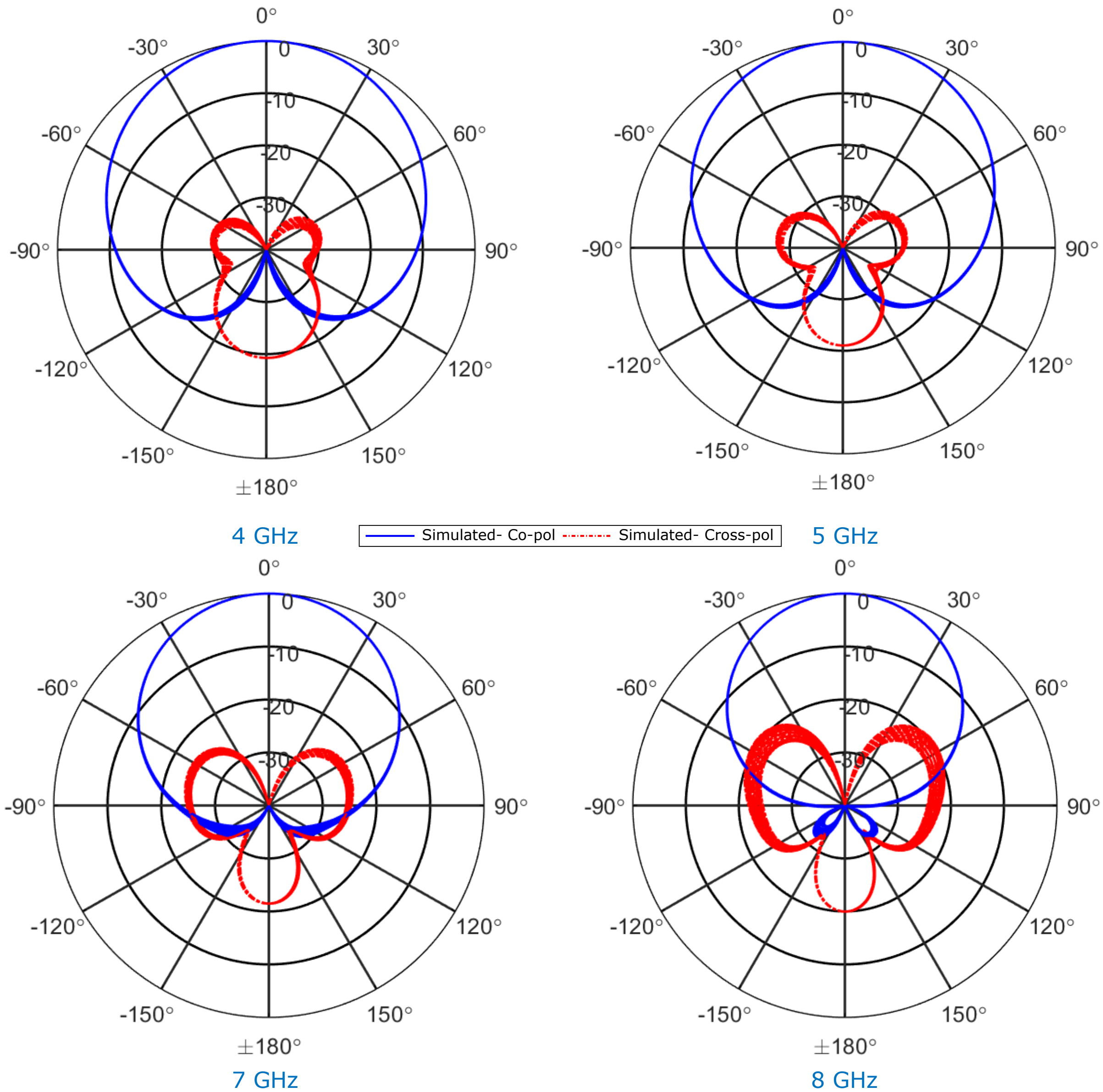

Figure 4.11: Simulated co-and cross-polarized radiation patterns of the coaxial cavity antenna over $\phi = 0°$ to 180°.

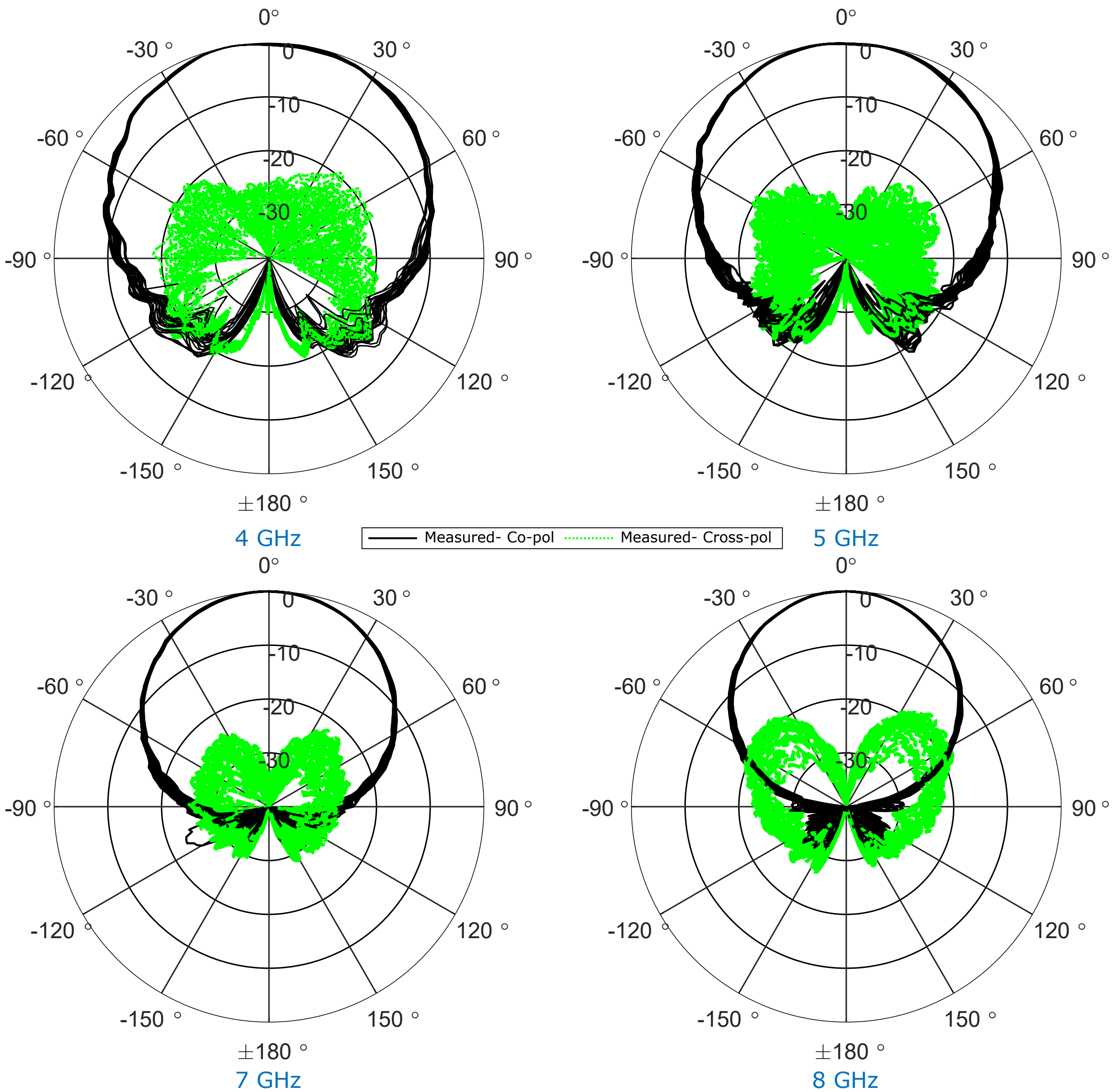

Figure 4.12: Measured co-and cross-polarized radiation patterns of the coaxial cavity antenna over $\phi = 0°$ to 180°.

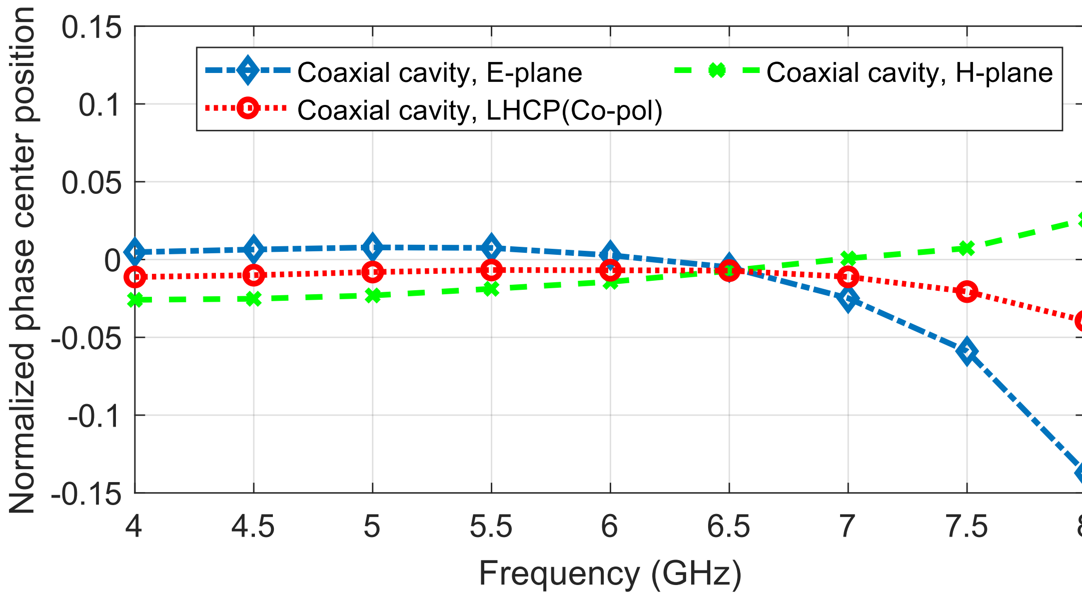

Figure 4.13: Normalized phase center (w.r.t. wavelength) of the designed coaxial cavity antenna for CP and linear polarization (in E and H planes). Phase center is calculated for the angular span $\theta = \pm 53°$.

4.2.2 Reflector Design

A prime-feed or axis-symmetric paraboloid reflector is designed to achieve high gain desired for long-range communication and EW applications. The diameter and the focal length of the reflector are computed through a parametric study conducted in HFSS, to achieve gain >20 dBi while maintaining low side lobe and cross-polarization level. The antenna has diameter, D = 40 cm and F/D of 0.495 and achieves aperture efficiency above 60% over 87.5% of the bandwidth with peak efficiency of 70%. Also, the antenna has gain >21 dBic over the band of operation with maximum of 28 dBic at 8 GHz, as shown in the Fig. 4.14. The radiation patterns are directive and symmetric around ϕ (0° to 360°) as shown in Fig. 4.15 (b), and HPBW of the antenna is 6° at 8 GHz. Well-known short comings of the prime feed reflectors are aperture blockage and deterioration in the impedance match of the feed due to the reflected fields from the reflector [90, 97]; the later can be observed from the reflection coefficient response in Fig. 4.16. An approach to minimize the impact on impedance match is to reduce F/D [46]. However, it is observed that the improvement in the impedance match is not significant at the expense of reduced gain and the aperture efficiency.

Contrarily, an offset-fed reflector can be designed to reduce the feed blockage and to improve the

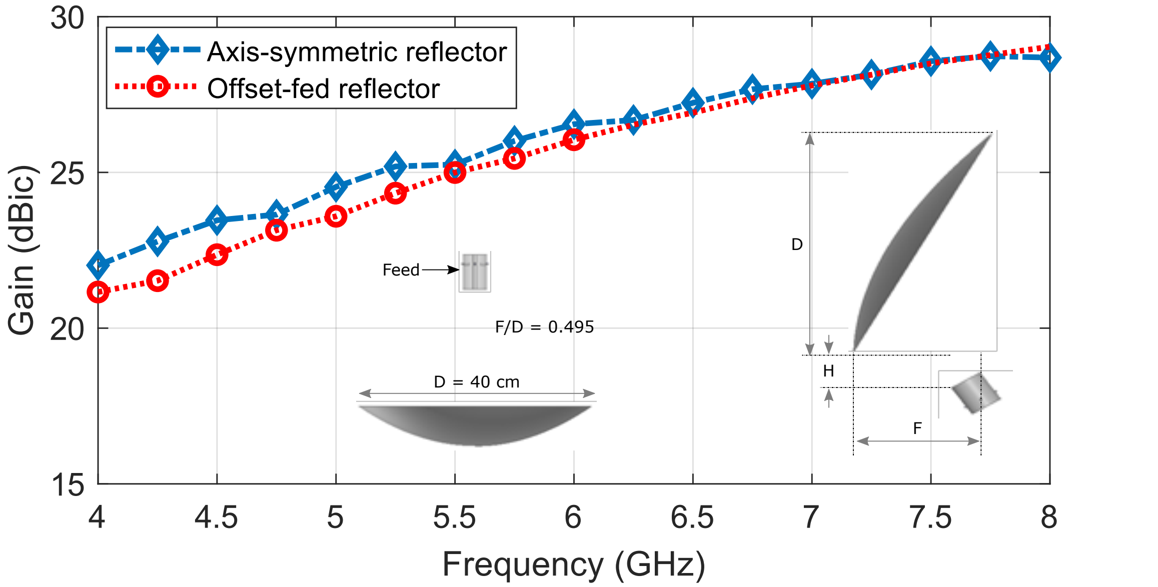

Figure 4.14: Comparison between the broadside gains of symmetric and offset-fed reflectors. The geometries of the symmetric and offset fed reflectors are shown in the inset.

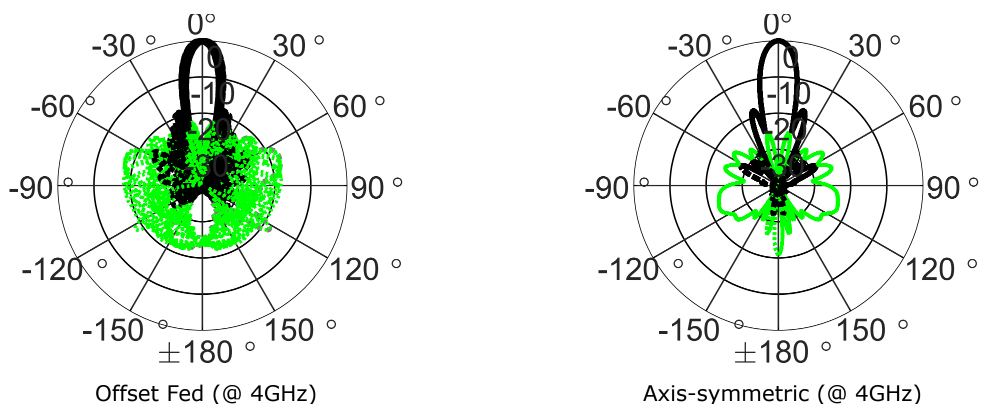

Figure 4.15: Co and cross-polarized radiation patterns of (a) offset-fed, and (b) symmetric reflectors @ 4 GHz over several azimuthal cuts from $\phi = 0°$ to 360°.

impedance match [45, 46]. Therefore, an offset reflector is designed with lower rim offset, H = 4.4 cm, which is selected such that the top most point of the feed clears the bottom most point of the reflector. The corresponding feed orientation angle is calculated using equations in [45, 46]. Also, the projected diameter is the same as that of the prime feed case. The comparison of reflection coefficient in Fig. 4.16, clearly indicates the improvement with the offset fed reflector. However, the radiation patterns are asymmetric, with the squint in the symmetric plane, and have higher cross-polarization (in the asymmetric plane) in

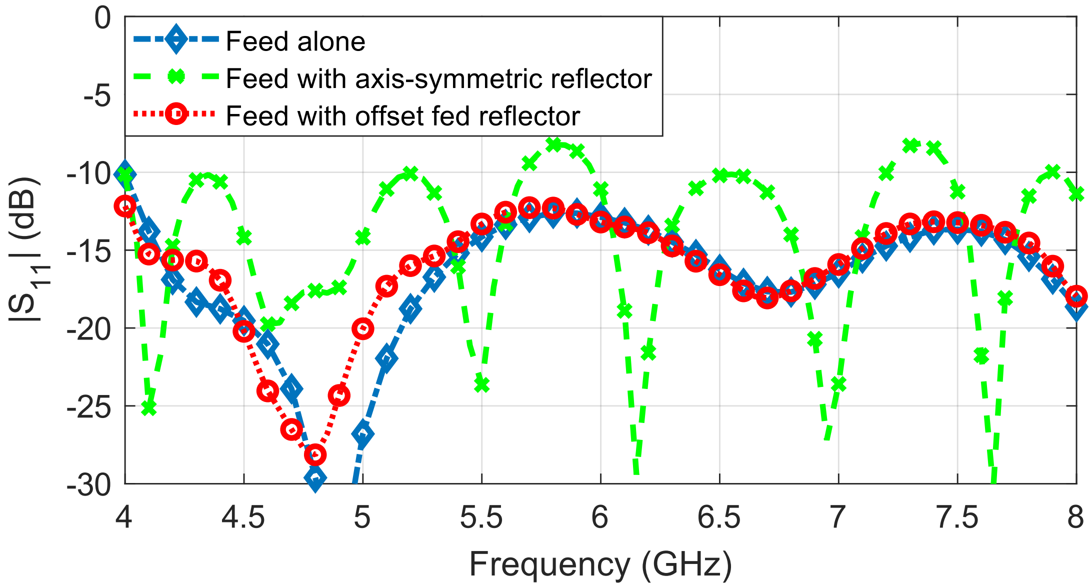

Figure 4.16: Simulated reflection coefficient of the coaxial cavity feed (standalone) compared to that of symmetric and offset-fed reflector antenna.

comparison to the prime feed reflector, as shown in Fig. 4.15. Also, the gain of the offset fed reflector is lower than the later, mainly at lower frequencies (see Fig. 4.14), due to the increased spill over losses. Additionally, the asymmetry in the antenna geometry and radiation patterns deteriorate the isolation of the proposed system, which will be discussed later in Section 4.3.

Hence, the axis-symmetry reflector configuration is selected for the design. To reduce the impact of reflector on impedance match, apex matching technique is applied [87, 96]. In this technique, a flat metallic disk is mounted at the origin of the parabola, as shown in the Fig. 4.17. Further, the diameter of the plate is selected to create 180° phase difference between the reflected signal from the apex matching and the rest of the reflector surface at the focal point (or feed). Hence, these signals cancel (see Fig. 4.18); thereby reducing the effect on the impedance match of the feed. The significance of apex matching can be clearly seen in Fig. 4.18. Gaussian or cone shaped structures can be used to increase the impact over wider bandwidth [103]; however, the flat disk is chosen to minimize the fabrication cost and complexity. Apex matching can have some effect on the far field of the antenna because of the modification in the parabolic surface [96]. In the proposed design, apex matching lowered the gain by 0.4 dB at 8 GHz. Nonetheless, the antenna has SLL

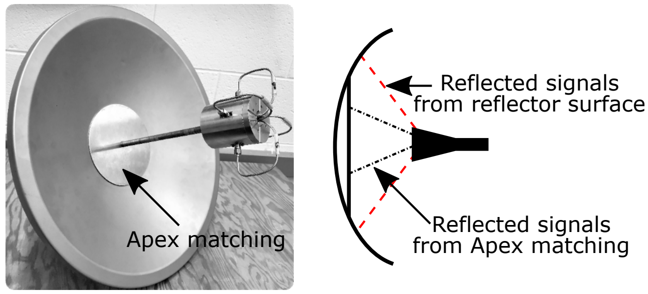

(a) (a)

Figure 4.17: Illustration of apex matching technique, showing the reflected signals from the flat disk and reflector surface at the feed point.

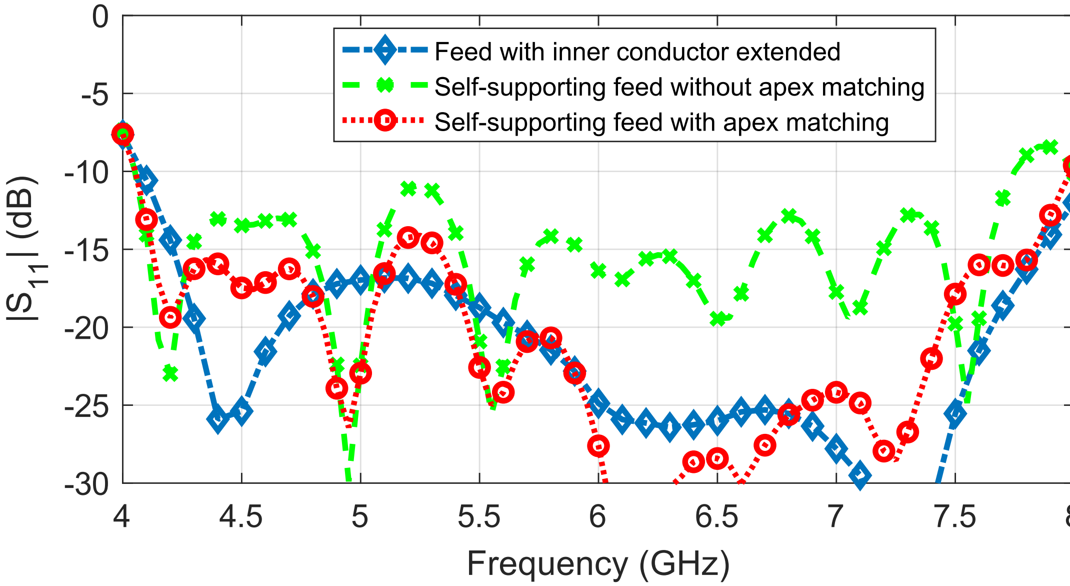

Figure 4.18: Simulated reflection coefficient of the coaxial cavity antenna with probe extended to support the feed, and reflection coefficient of the self-supporting reflector antenna with and without apex matching.

<-16 dB and cross-pol level <-20 dB over the operating frequencies. Moreover, the symmetry in antenna geometry and radiation patterns is retained.

The prime feed reflector requires supporting struts for the feed, which increase aperture blockage and side lobe levels [85]. Therefore, the inner conductor of the feed is extended to the apex of the reflector, improving the impedance match of the feed (standalone) at the mid-band, as shown in Fig. 4.18, in accordance with [101], without any noticeable deterioration in the far field performance. The self-supporting feed maintains the symmetry of the antenna structure while eliminating the need for complex struts. The fabricated antenna with its dimensions is shown in Fig. 4.1. The required BFN is housed below the reflector (not pictured)and the feeding cables are routed through the inner conductor, as illustrated in Fig. 4.1.

The radiation patterns of the self-supporting apex matched reflector are symmetric with cross-polarization level <-20 dB, SLL <-16 dB, and gain >21 dBic over the operating bandwidth (see Fig. 4.19 and Fig. 4.20). The deviation in measured to simulated directivity at higher frequencies, Fig. 4.19, is mainly due to the slight variation in the focal and feed point of the fabricated antenna, which has led to defocusing. The extended inner conductor is tilted by approximately 2.5°, approx., corresponding to a feed offset of 0.33 cm and 0.83 cm (X and Y axis, respectively). By incorporating these offsets in the simulation, the gain dropped by 1.79 dB and is in good agreement with measurement, as shown in Fig. 4.19. However, the design of reflector is not optimal, and hence the far field performance can be improved further. Also, the feed has -4 dB amplitude taper at $\theta = \pm 53°$ (@ 4 GHz).

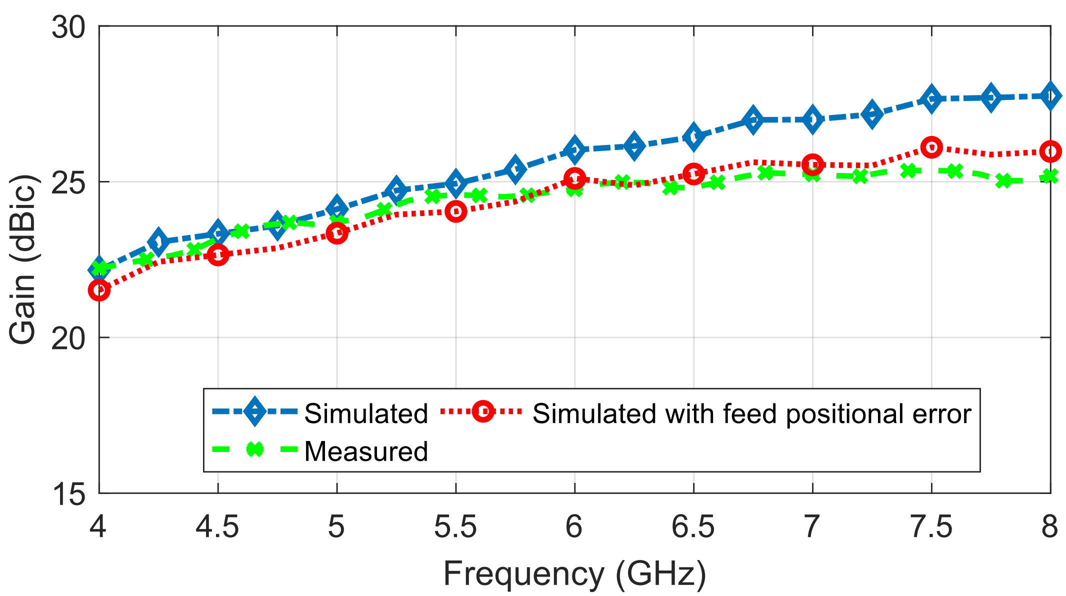

Figure 4.19: Measured and simulated broadside directivity of the proposed self-supporting reflector antenna. Also shown, the simulated directivity with error in feed position.

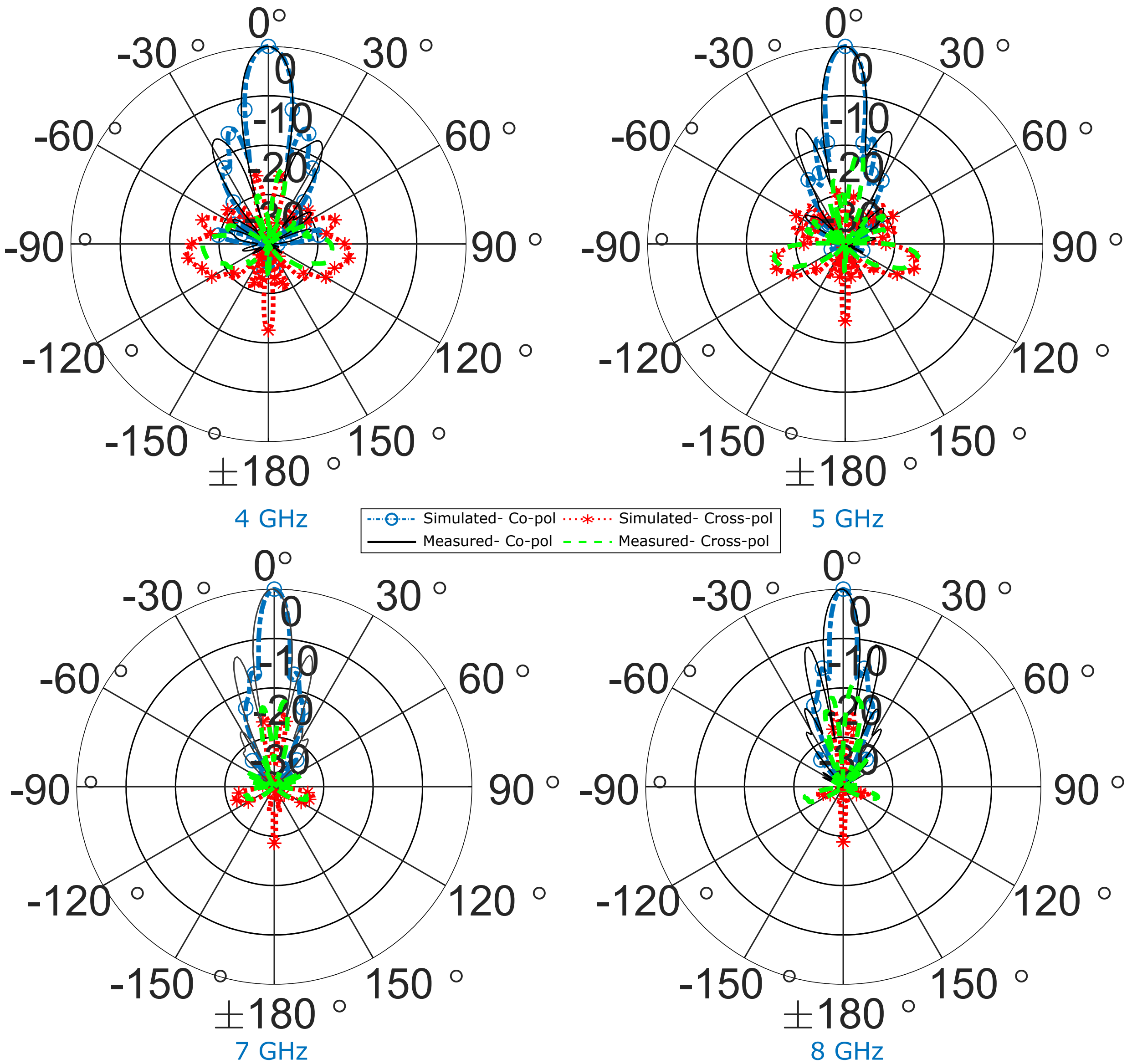

Figure 4.20: Measured and simulated co (LHCP) and cross-polarized (RHCP) radiation patterns of the self-supporting reflector antenna with apex matching, at $\phi = ,0°$.

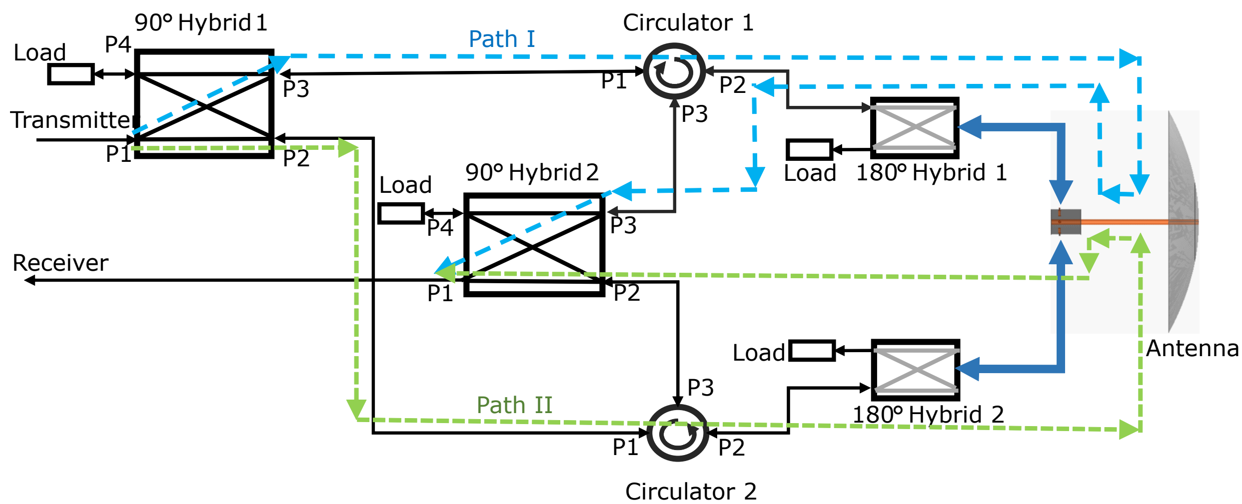

Figure 4.21: Signal flow diagram of the proposed monostatic STAR system, consisting of circularly polarized reflector antenna, 90° and 180° hybrids, and circulators.

4.3 Full Duplex Configuration

The monostatic STAR is realized by feeding the designed CP antenna through the BFN consisting of 90° and 180° hybrids as well as circulators. The schematic and the signal flow of the proposed architecture are shown in Fig. 4.21. The realized approach is similar to the full-duplex system outlined in [22].

First, the input signals (or the TX signals) are connected to the port 1 of the TX 90° hybrid 1. Then, the TX signals are split into two signals of equal magnitude and quadrature phase, $(j/\sqrt{2})e^{j\phi}$ and $(1/\sqrt{2})e^{j\phi}$. Further, these signals are routed through Paths I and II, as illustrated in Fig. 4.21. The signals fed to the input of circulators I and II undergo attenuation due to the finite insertion loss (IL) of the circulators. The outputs of circulators are connected to the inputs of 180° hybrids, which are used to generate two signals with equal magnitude and 180° phase difference. These signals are required to excite TE_{11} mode in the coaxial cavity antenna (feed of the reflector). The impedance mismatch of the feed results in reflected signals, Eq. (4.3) and Eq. (4.4), which travel back to the respective circulators through 180° hybrids, where S_{21}^{C1} and S_{21}^{C2} are the S_{21} of circulators 1 and 2, respectively.

$$|\Gamma_1|\frac{j}{\sqrt{2}}e^{j\phi}\cdot S_{21}^{C1} \tag{4.3}$$

$$|\Gamma_2|\frac{1}{\sqrt{2}}e^{j\phi} \cdot S_{21}^{C2} \tag{4.4}$$

These signals are further attenuated, due to IL from port 2 to port 3 of the circulators, before reaching RX 90° hybrid 2. At the hybrid 2, the signals from Path I undergo another 90° phase shift resulting in (4.5), whereas the signals from Path II go through the hybrid without any phase shift (4.6); similarly, for the signals from circulators leakage. Thereby, these two signals are combined 180° out of phase at the RX port, resulting in theoretically infinite isolation when $|\Gamma_1| = |\Gamma_2|$, $S_{21}^{C1} = S_{21}^{C2}$, $S_{32}^{C1} = S_{32}^{C2}$, and the leakage from circulators 1 and 2 are the same (4.7). However, any asymmetry in the BFN and the antenna geometry will create imbalances in amplitude and phase which results in finite isolation of the system. The signals combined in-phase at the port 4 of hybrid 2 are terminated in matched load.

$$|\Gamma_1|\frac{-1}{\sqrt{2}}e^{j\phi}S_{21}^{C1} \cdot S_{32}^{C1} \tag{4.5}$$

$$|\Gamma_2|\frac{1}{\sqrt{2}}e^{j\phi}S_{21}^{C2} \cdot S_{32}^{C2} \tag{4.6}$$

$$|\Gamma_1|\frac{-1}{\sqrt{2}}e^{j\phi}S_{21}^{C1} \cdot S_{32}^{C1} + |\Gamma_2|\frac{1}{\sqrt{2}}e^{j\phi}S_{21}^{C2} \cdot S_{32}^{C2} = 0 \tag{4.7}$$

The prototyped STAR system achieves isolation >30 dB with high amplitude and phase imbalances from the COTS hybrids used in the BFN, as illustrated in Fig. 4.22. Specifically, the used 180° hybrids have amplitude and phase imbalances of ±0.6 dB and ±10° [104], respectively. Similarly, 90° hybrids have ±0.5 dB and ±3° amplitude and phase imbalances, respectively [105]. Nevertheless, with the proposed approach, an average improvement of 15 dB in isolation is achieved in comparison to the conventional single circulator configuration (see Fig. 4.23), as demonstrated in Fig. 4.22. The similarity in the measured isolation of the standalone feed and the feed with the reflector is mainly due to the geometrical symmetry of the self-supporting reflector antenna. COTS circulators with 20 dB isolation, 0.35 dB IL and VSWR <1.25 are used [106].

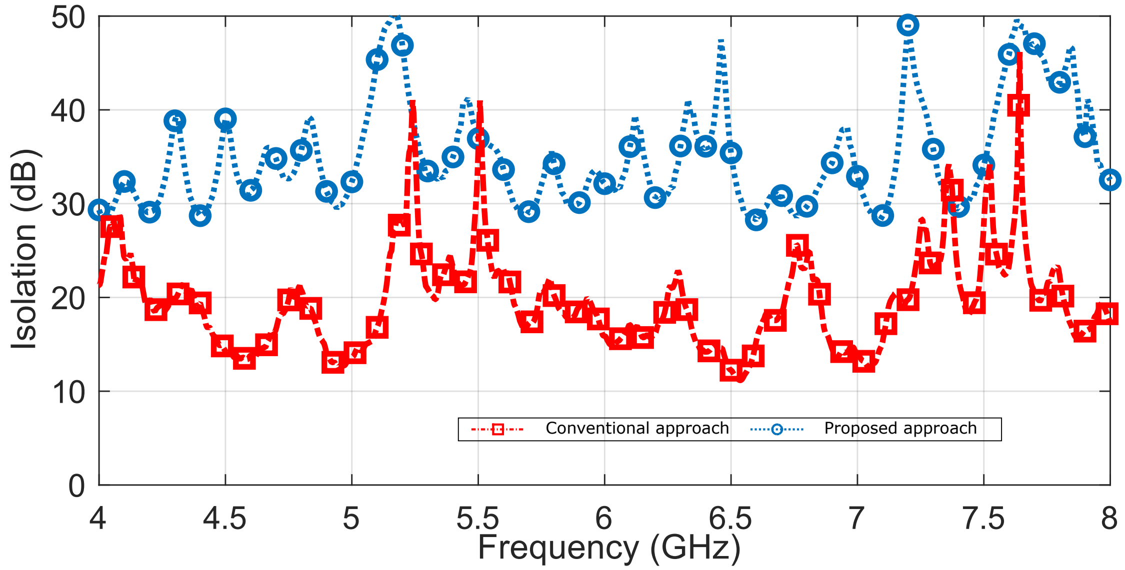

(a)

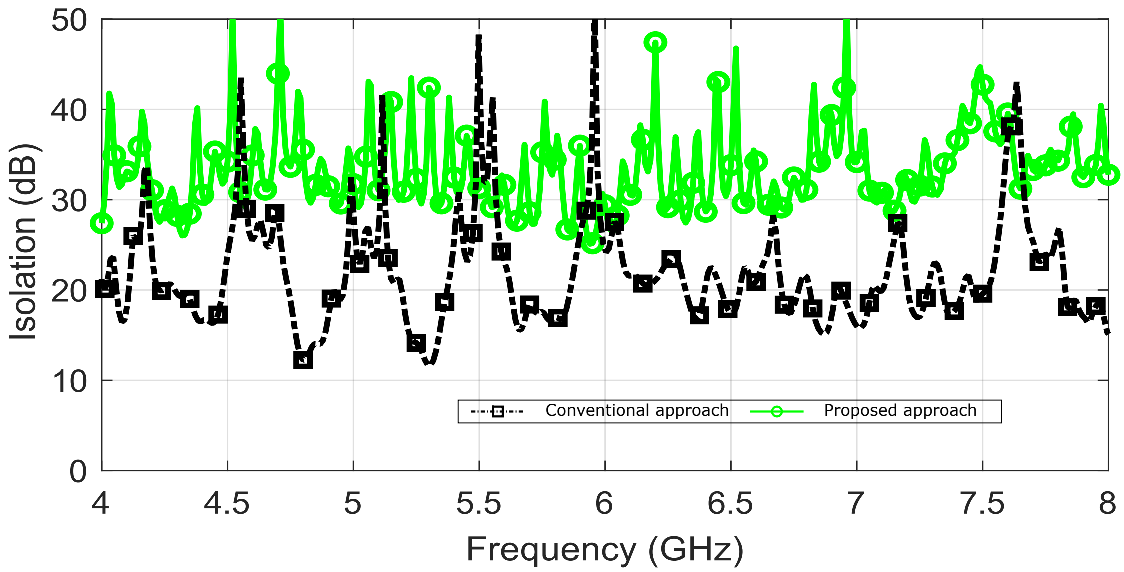

(b)

Figure 4.22: Measured isolation (a) without reflector, and (b) with reflector, using proposed monostatic approach and the isolation of the full-duplex system for the conventional approach.

4.3.1 Impact of asymmetry

The imperfections in the antenna geometry degrades the system isolation because of its impact on the cancellation process (4.7). For example, the asymmetry of the offset-fed reflector resulted in approximately 8 dB lower isolation in comparison to the prime feed reflector, as shown in Fig. 4.24. Also, the electrical

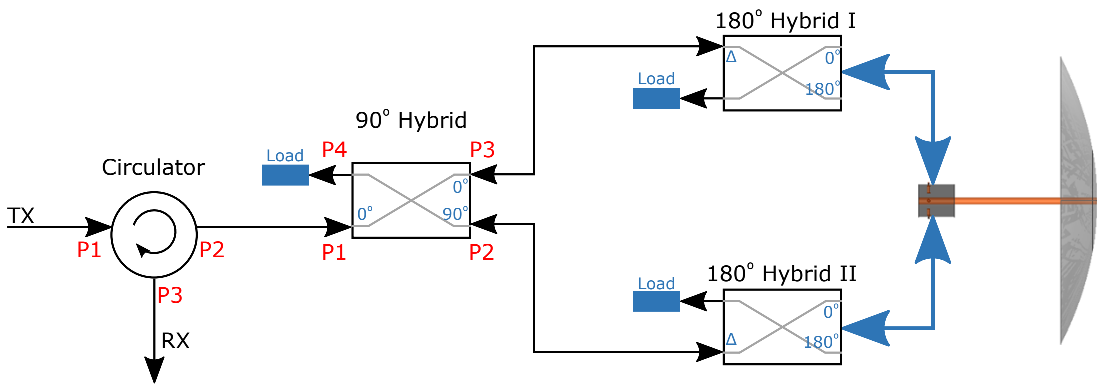

Figure 4.23: Schematic diagram of conventional approach

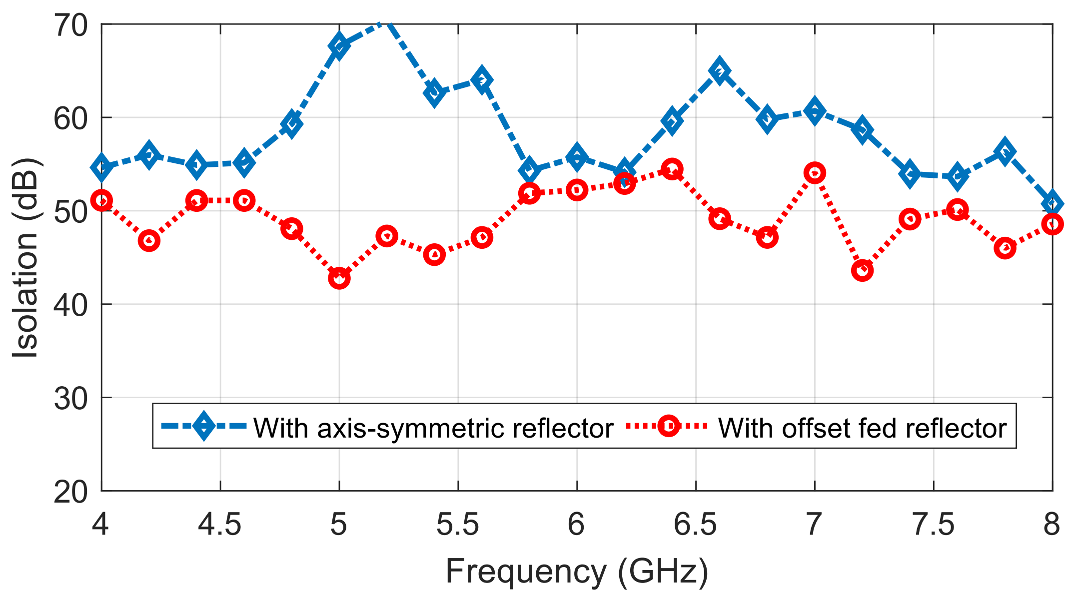

Figure 4.24: Simulated isolation of the proposed system symmetric self-supporting and offset-fed reflectors.

inequalities due to amplitude and phase imbalances of the BFN deteriorates the isolation of the system. As shown in Fig. 4.25, when frequency independent phase imbalance of ±6° and amplitude imbalance of ±0.4 dB are introduced into the system BFN using a circuit simulator (AWR Microwave Office), the achievable system isolation dropped to 30 dB. It should be noted that though the system isolation has seen the drop due to the imbalances, it is still higher than that provided by the circulators (ideal circulator with 15 dB isolation is used in this analysis).

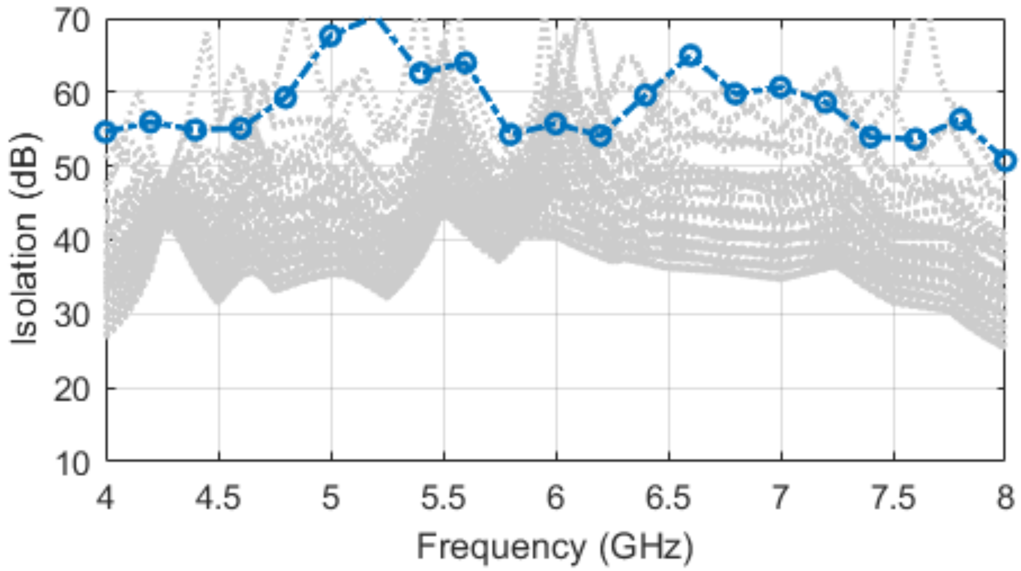

Figure 4.25: Simulated isolation of the proposed system self-supporting reflector antenna with imbalances in BFN.

4.3.2 Impact of roughness

Roughness or random deformations in the reflector surface create phase errors, of which the impact on directivity is well documented in [47, 107, 108]. In addition to decreasing directivity, these anomalies can deteriorate the isolation of the proposed STAR antenna system. Random roughness can be modeled using various statistical models or distributions [107]. Herein, we use a Gaussian distribution with correlation interval comparable to wavelength and root mean square (RMS) height much less than the wavelength [47]. Specifically, the surface roughness with correlation length 10 cm (1.33 λ_{4GHz}) and RMS height of 0.2 cm (0.026 λ_{4GHz}), when projected on XY plane, is considered. The resulting random rough surface (RRS) is shown in Fig. 4.26 and Fig. 4.27. The deterioration in isolation up to 14 dB is observed as illustrated in Fig. 4.28. Furthermore, the directivity of the antenna with roughness considered is reduced to 24.9 dB from 25.6 dB and 26.9 dB from 28.2 dB, at 6 GHz and 8 GHz, respectively. Also, deformations have increased the SLL of the antenna by 8 dB at 8 GHz.

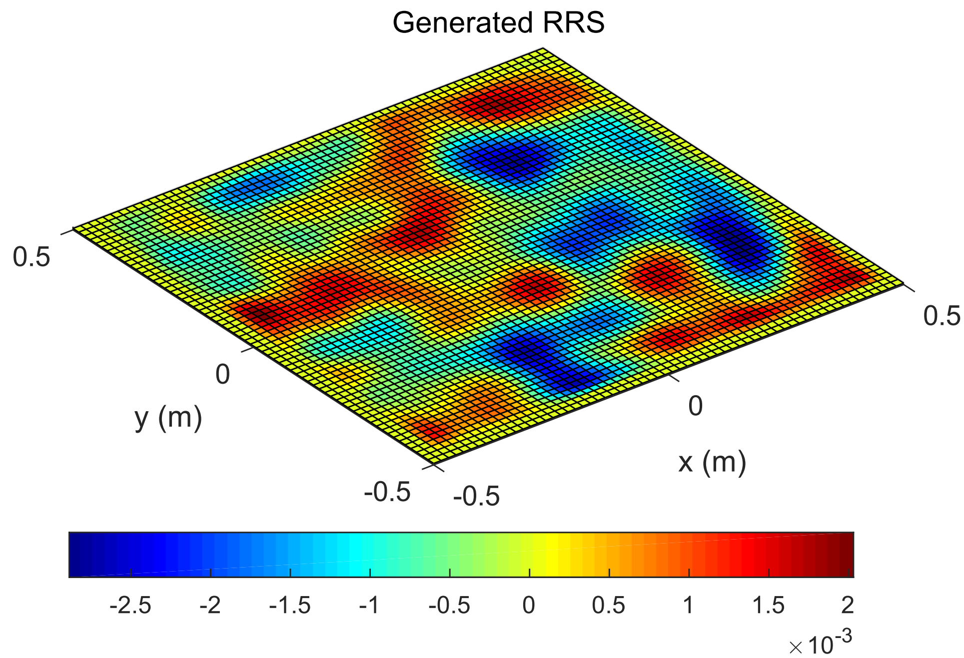

Figure 4.26: Generated Gaussian roughness with RMS height = 0.2 cm

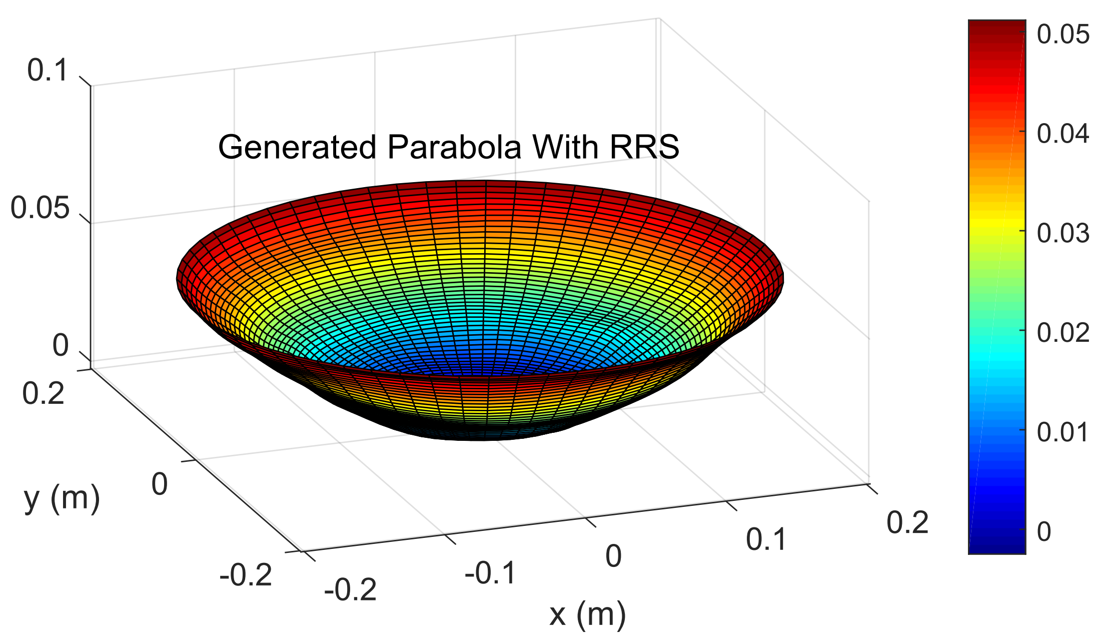

Figure 4.27: Parabolic surface with Gaussian roughness.

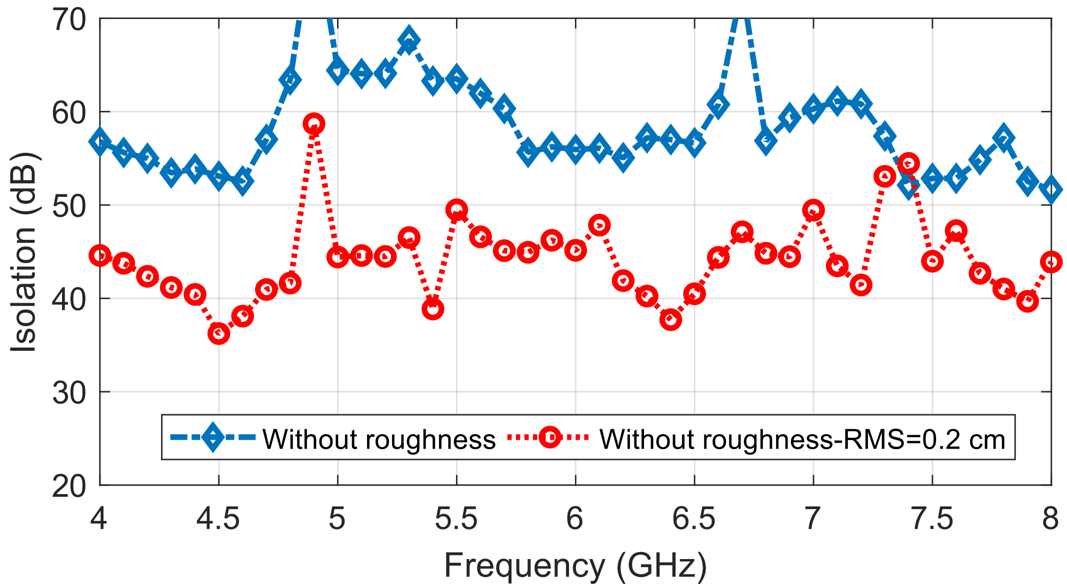

Figure 4.28: simulated systems isolation with and without roughness.

4.3.3 Isolation Improvement Techniques

The isolation of the system can be increased by using analog cancellation technique [18], where the signals from ports 4 and 1 of 90° Hybrid 2 are combined to compensate for the imbalances in the BFN components, as shown in Fig. 4.29. SI can be reduced up to 32 dB over a narrow bandwidth using this technique, as illustrated in Fig. 4.29 (b). In addition, the improvement in the isolation over a wider bandwidth can be achieved by employing a dynamic cancelation network, as demonstrated by the results in Fig. 4.29 (c). The measured S-parameters of the BFN components, and the simulated antenna are used in the circuit simulator [109] to realize the circuit and results in Fig. 4.29.

4.4 Summary

An approach to increase the isolation between the TX and RX channels of a high gain reflector antenna is proposed and practically demonstrated. The feed is the well-performing coaxial cavity antenna which bandwidth is extended through simple geometrical modifications. The high isolation in the introduced monostatic STAR approach is achieved by canceling the coupled/leaked signals using a BFN consisting

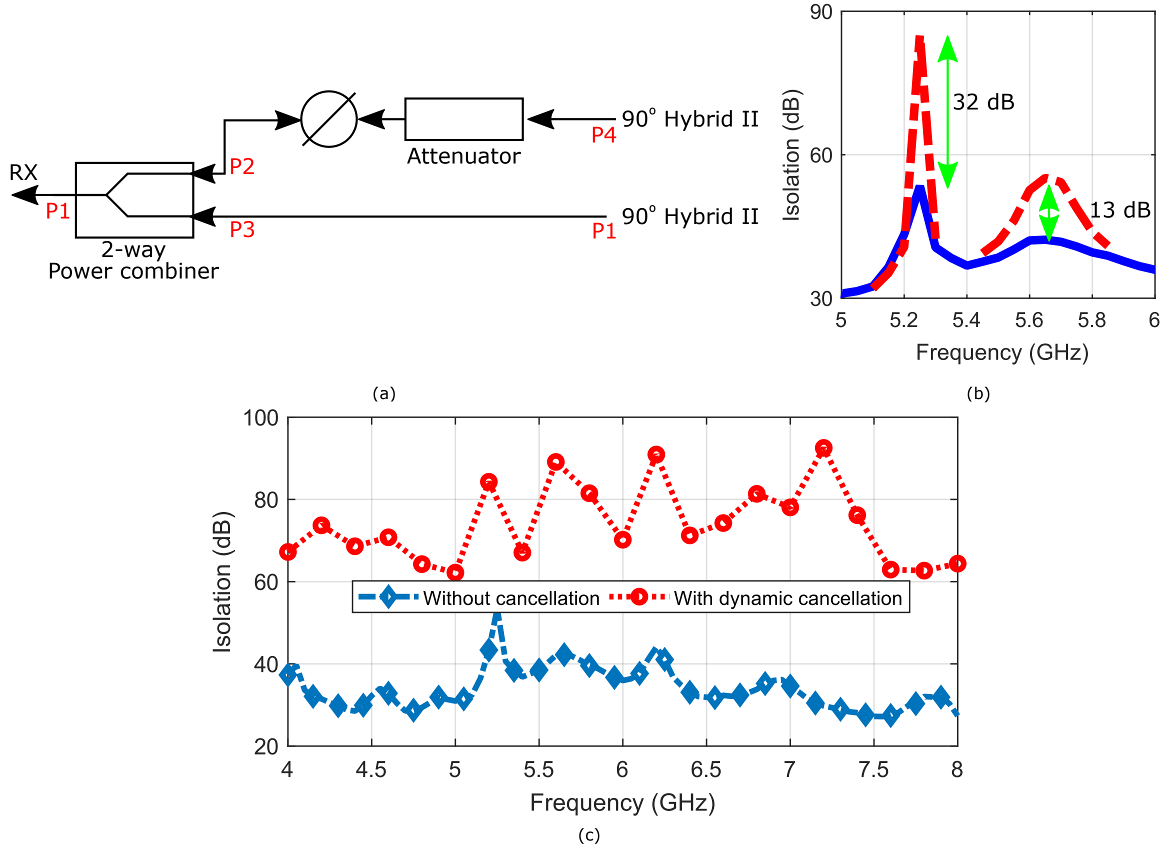

Figure 4.29: simulated systems isolation with and without roughness.

of 90° and 180° hybrids and circulators. It is explained that theoretically high isolation can be achieved between the TX and RX through the proposed method. However, it is shown that the asymmetry in the antenna geometry and the BFN can significantly deteriorate the achievable isolation, which is demonstrated by considering an offset-fed reflector, surface roughness of the reflector, and imbalances in BFN. Using COTS components with noticeable imbalances and, more importantly, variation between thereof, average isolation > 30 dB is achieved with the fabricated system; in average, 15 dB higher than the isolation achieved with the conventional circulator approach. The proposed antenna exhibits symmetric radiation patterns, with gain >20 dBic, axial ratio <1 dB, and $|S_{11}|$ <-10 dB over the operating bandwidth.

Chapter 5

Wideband Quasi-Monostatic STAR

5.1 Introduction

This chapter upholds the ongoing thesis argument that higher isolation from the antenna layer itself is critical. Hence, the robustness of the STAR performance to asymmetries and imbalances are necessary for practical implementation. In Chapter 4, it is demonstrated that a monostatic configuration [32] is a preferred approach for high gain, long-range, in-band full-duplex systems. The adopted method showed the potential to achieve theoretically infinite isolation. However, the practical realization is plagued by the amplitude and phase imbalances in the COTS hybrids and circulators. Nonetheless, isolation up to 30 dB is achieved. Therefore, to overcome these limitations, a new system architecture called quasi-monostatic STAR is devised in this chapter.

The proposed configuration can achieve 30 dB (on average) higher isolation than the approach in [32] with the same BFN components. It is demonstrated that quasi-monostatic STAR can facilitate, simultaneously, linearly co-polarized transmission and reception with isolation >40 dB, and gain >20 dBi (for TX antenna) while retaining the overall system's physical footprint (in xy-plane) of a transmitting antenna alone. The chapter also outlines the techniques to enhance the antennas F/B ratio and thereby, further improve the system isolation. Finally, to address bandwidth extension to more than an octave, wideband spiral antenna

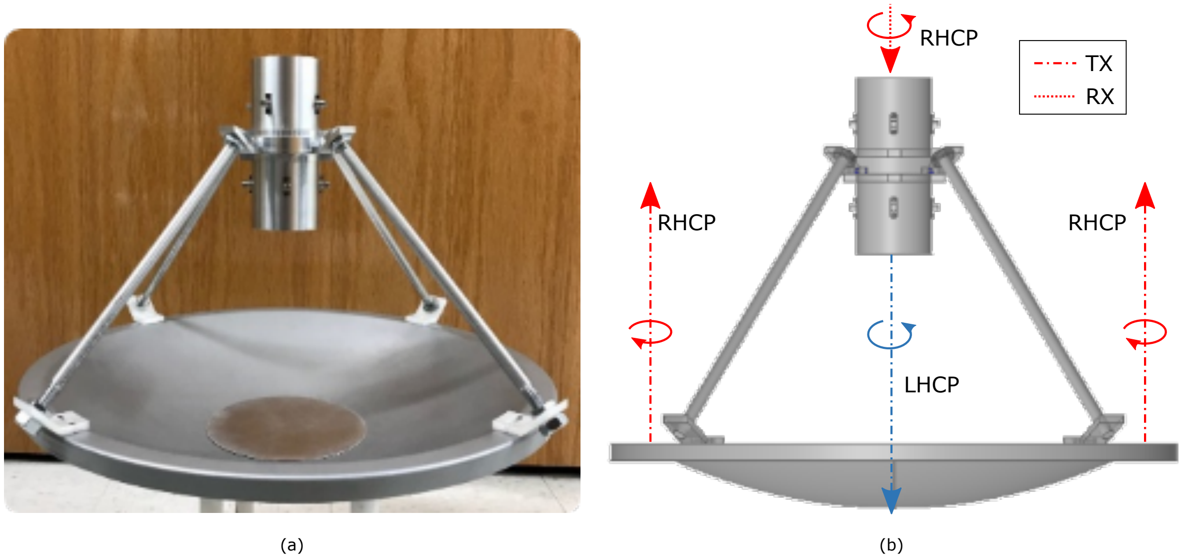

Figure 5.1: (a) Photograph of the fabricated antenna, and (b) sketch illustrating the system operation.

is employed for the feed and RX and high isolation is reported.

The system consists of a center fed axis symmetric parabolic reflector [110] for TX operation and a coaxial cavity antenna [93] mounted above the feed for RX. The resulting configuration is shown in Fig. 5.1. The presence of the RX within the volume occupied by the TX helps reduce the system's physical size, analogous to a monostatic case. Further, in a baseline operational concept both TX feed and the RX antenna are circularly polarized. That is, (to achieve true-co-pol STAR) the former is left-hand CP (LHCP) whereas the latter is RHCP. The physical orientation of the antennas and the presence of the metallic reflector leads to the same polarization operation for the TX and RX (see Fig. 5.1 (b)). It is seen that the system isolation is related to the front-to-back ratio (F/B), and the cross-polarization levels of the two back-to-back antennas. The polarization diversity between the two antennas provides an additional cancellation layer, resulting in high system isolation. Additionally, due to the inherent low mutual coupling between the TX and RX feeds, the proposed approach is less sensitive to the BFN imbalances and geometrical asymmetries. An average measured isolation of 61 dB is obtained using commercial off-the-self (COTS) components with relatively-high amplitude and phase imbalances.

This chapter is formulated in four sub-sections:

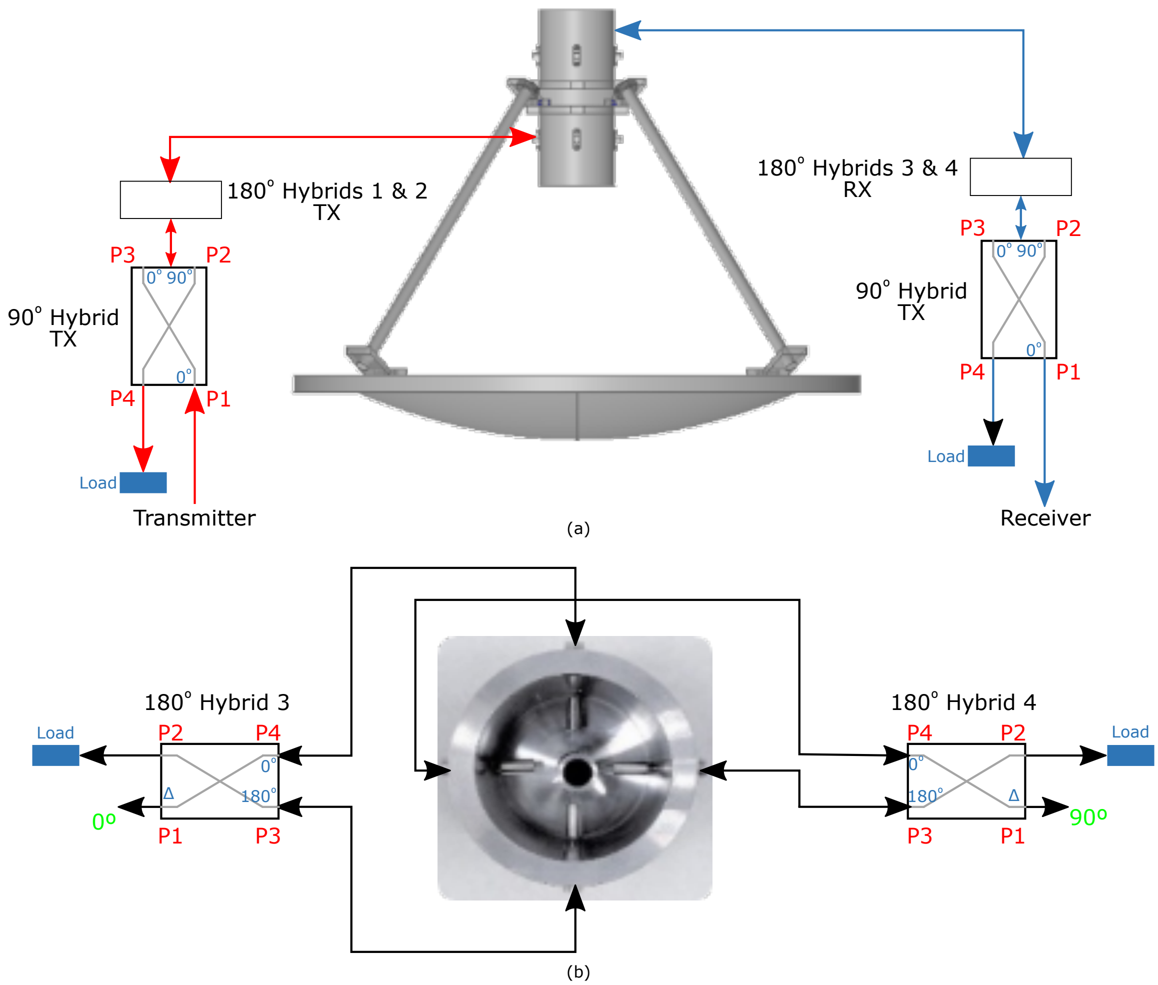

Figure 5.2: Schematic of the proposed system along with the BFN consisting of 90° and 180° hybrids.

- Section 5.2 explains the design and methodology of the quasi-monostatic STAR. Further, the underlying coupling channels of the architecture is analyzed with simulated and measured isolation results.
- Section 5.3 presents the far field and impedance performance of the feed and reflector.
- Section 5.4 outlines the techniques for improving operational bandwidth and system isolation.

5.2 System Description

5.2.1 System Architecture

The proposed quasi-monostatic STAR antenna system consists of a parabolic reflector antenna for transmission and a receiving antenna mounted back-to-back with the reflector feed, as shown in Fig. 5.1. The physical size of the RX antenna should be comparable to or smaller than that of the TX feed, in order to prevent additional reflector blockage. To increase the system isolation both the TX feed and the RX antenna are CP. To achieve same TX and RX polarization (i.e. no polarization multiplexing) the TX feed is LHCP and the RX antenna is RHCP. The LHCP fields from the TX feed undergo polarization reversal after bouncing back from the reflector. Thereby, the TX and RX operate in the same polarization, as illustrated in Fig. 5.1 (b). This approach can also support simultaneous dual polarized operation if appropriate feed and RX antenna are used.

In the proposed system, a dual-polarized coaxial cavity antenna is used as a reflector feed and RX antenna [32]. The antenna is selected because of its stable phase center, symmetric radiation patterns, and high radiation efficiency over the desired bandwidth of operation. The required CP is realized by existing the antenna using 2×4 Butler matrix BFN consisting of a 90° hybrid and two 180° hybrids (see Fig. 5.2).

5.2.2 Coupling Sources

When the back-to-back antennas are in the far-field of each other, the coupling is through the back lobes. To save the space and easy mechanical integration, the TX feed and RX antenna are arranged as in Fig. 5.3. Coupling mechanisms are now more complicated as they include currents on the sides of the antennas and antenna's near field. Instead of separating the individual contributions to the overall coupling, the aggregate effect can be readily simulated. The coupling between the individual exciting probes (ports) is in the order of -40 dB, as shown in the Fig. 5.4. Similarly, the isolation between the linearly polarized (LP) antennas is >40 dB (see Fig. 5.5). The increase in isolation with frequency is well correlated with the higher F/B, as shown in Fig. 5.6. Separating the antennas further away is one simple approach to enhance the isolation. For example, doubling the separation between antenna apertures enhances isolation by 6.36 dB (maximum), as shown in Fig. 5.7. However, this is not a preferred method, since it enlarges the overall system size. Placing the absorber between the two antennas can also improve isolation, at the expense of higher complexity.

Contrarily, the isolation of the system can be enhanced to >60 dB (see Fig. 5.8) by operating the designed antennas in CP. This increase in system isolation with the CP is due to the additional layer of signal cancellation from the polarization diversity, and due to the higher F/B of the antennas in comparison to the linear polarization, as shown in the Fig. 5.9. The S-parameters of the simulated antenna along with ideal BFN are used in the circuit simulator (AWR microwave office [109]) to obtain the results in Fig. 5.8. The isolation of the system is dependent on the imbalances and symmetry in the BFN and antenna geometry, respectively. Hence, imbalances in amplitude and phase of the COTS components can deteriorate the isolation of the system, which is clear from Fig. 5.8. The measured S-parameters of the COTS 90° hybrids [105], and 180° hybrids [104] with amplitude and phase imbalances ±0.5 dB and ±3°, ±0.6 dB and ±10°, respectively are used.

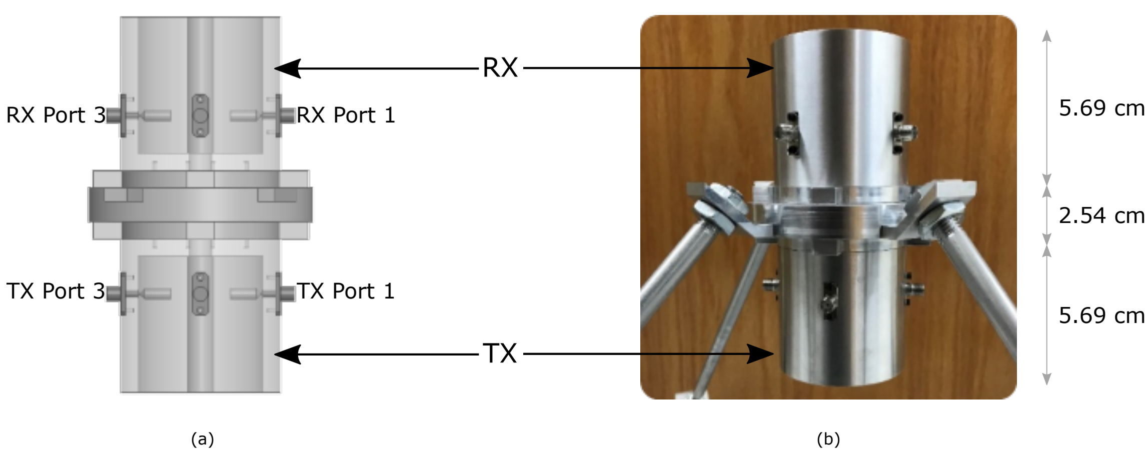

Figure 5.3: Coaxial cavity antennas (RX and TX feeds) mounted back-to-back, (a) CAD models, and (b) fabricated prototype.

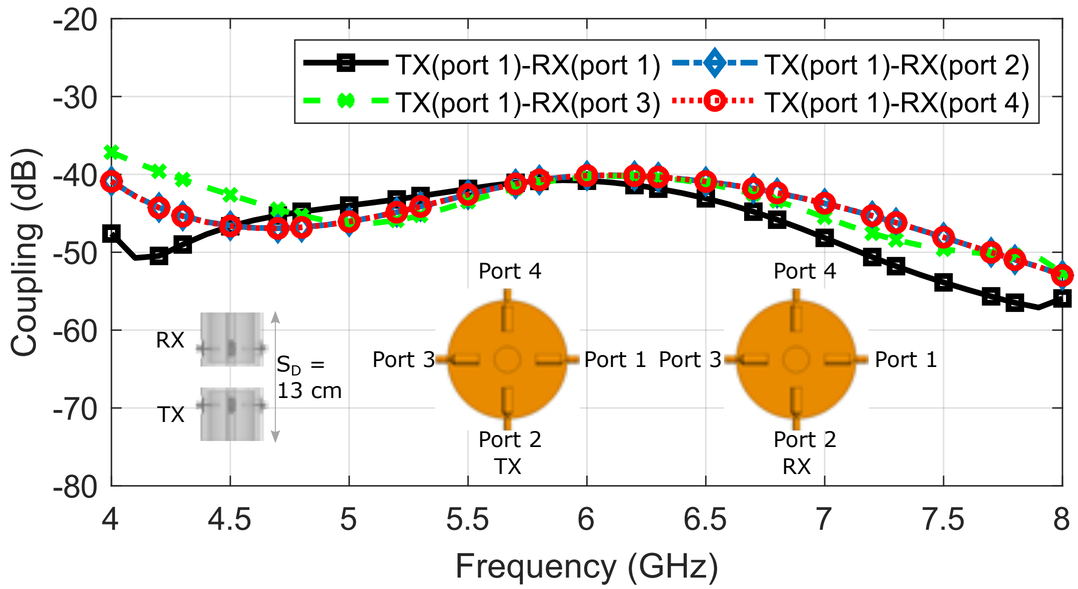

Figure 5.4: Simulated mutual coupling between the TX and RX ports of the coaxial cavity antennas.

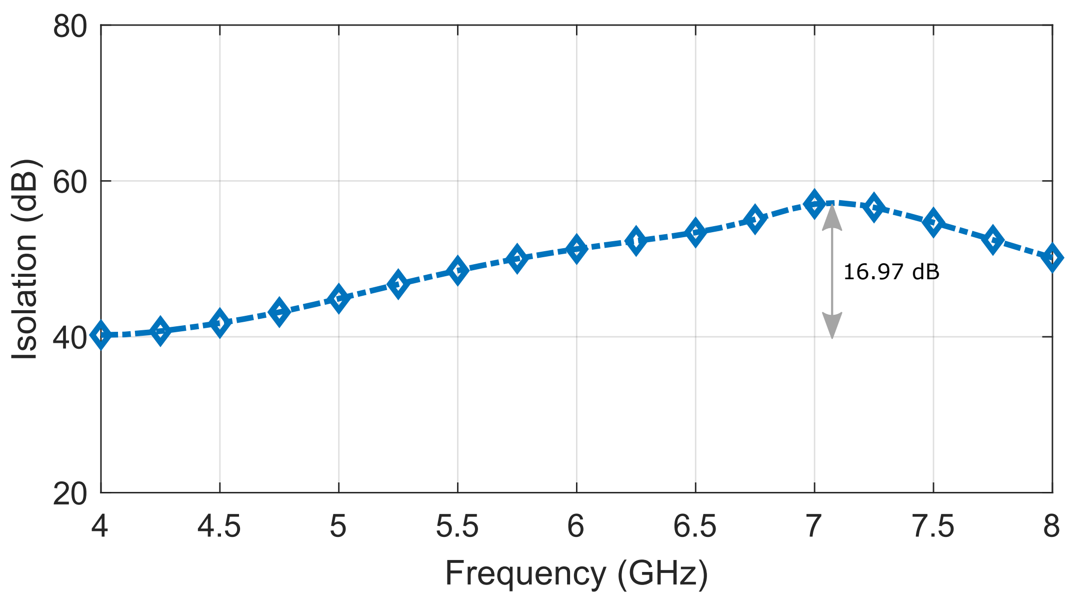

Figure 5.5: Simulated isolation between TX and RX for linear polarization and separation distance of 13 cm.

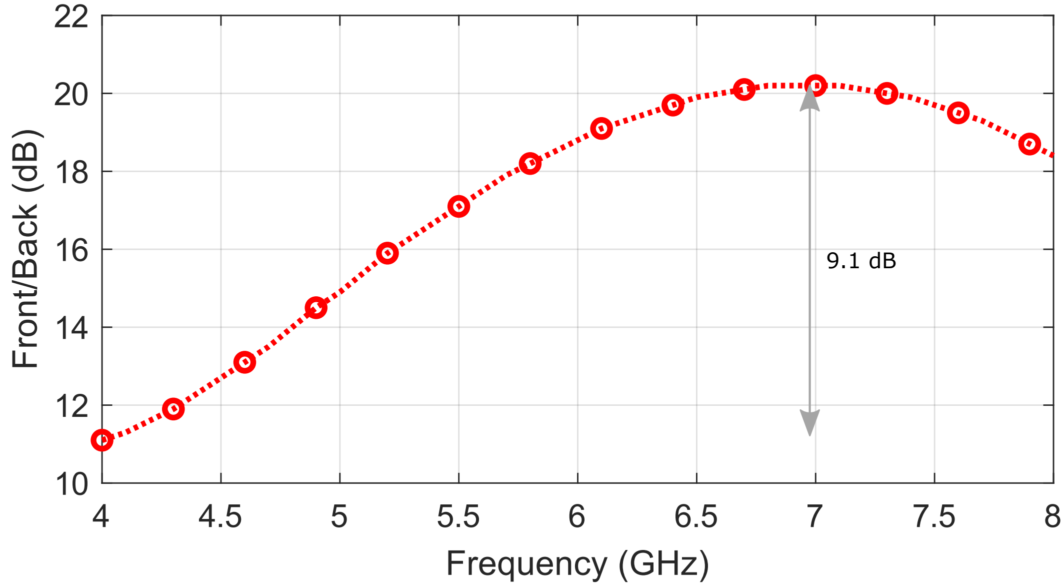

Figure 5.6: Simulated F/B of coaxial cavity antenna for linear polarization.

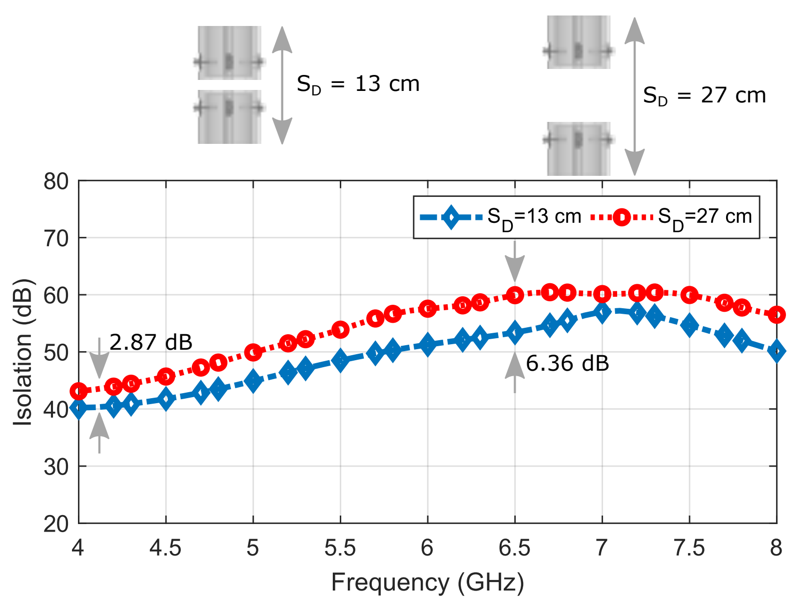

Figure 5.7: Simulated isolation between linearly polarized antennas mounted back-to-back at separation distances of 13 and 27 cm.

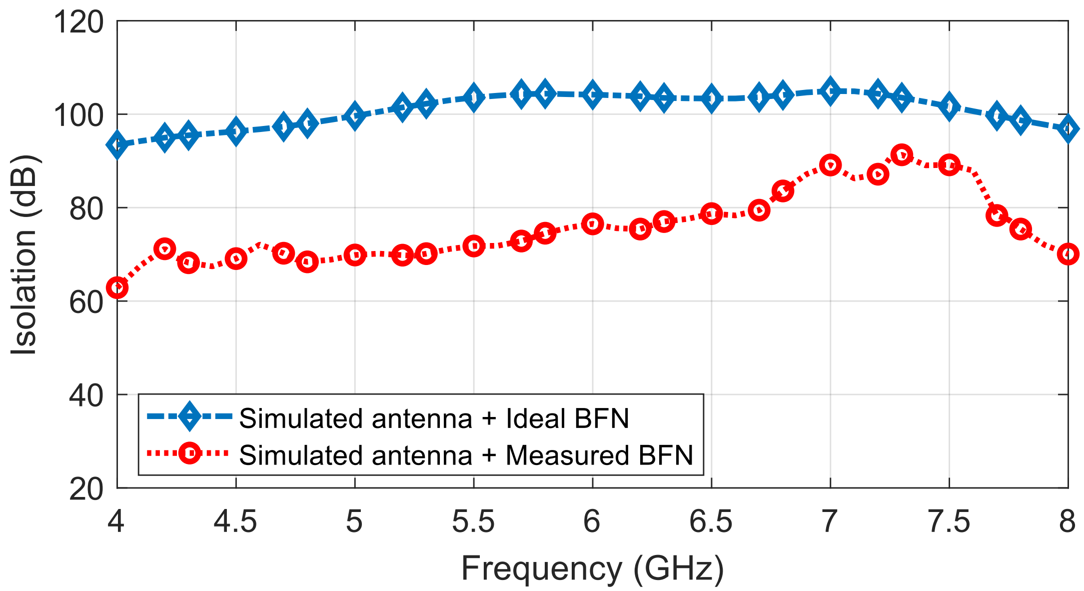

Figure 5.8: Isolation between coaxial cavity antennas (RX and TX feeds) connected back-to-back when operated in CP.

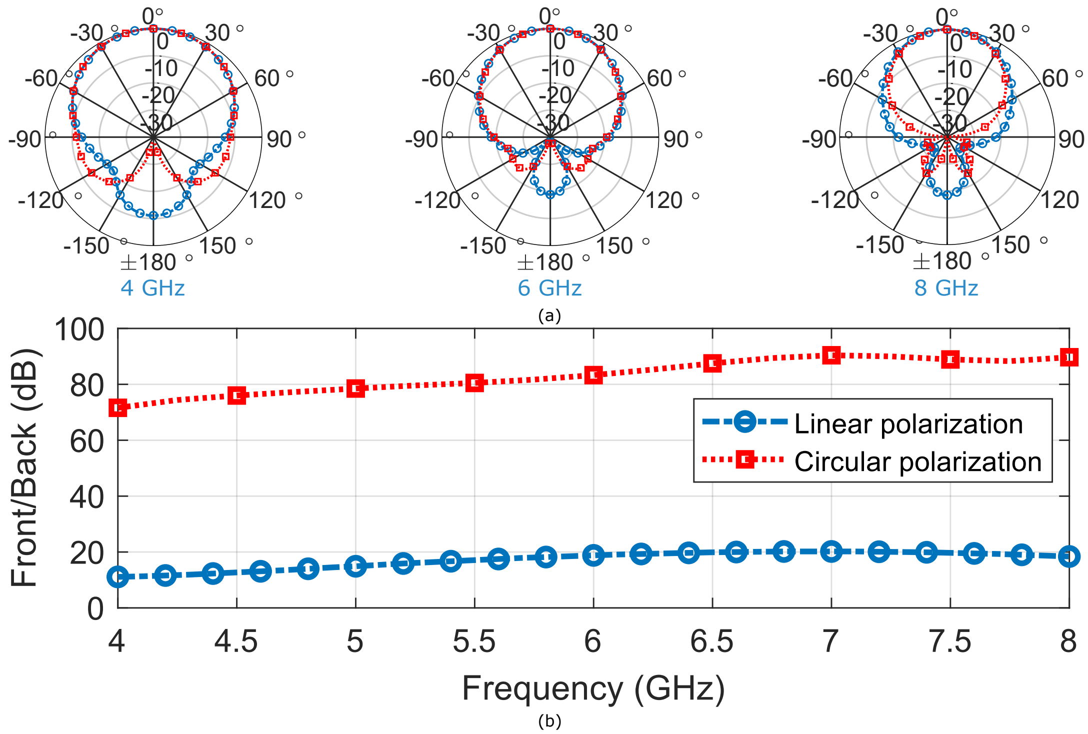

Figure 5.9: Simulated (a) the radiation patterns for linear and circular polarization at 4, 6, and 8 GHz, and (b) F/B of the coaxial cavity antenna.

When the antennas are integrated with the reflector, the reflected fields from the parabolic surface provide two additional coupling paths. Specifically, in the path I, the reflected LHCP fields from the reflector will couple to the LHCP fields (co-pol) of the RX. Similarly, in path II, the cross-pol of the feed (LHCP) is radiated as RHCP (cross-pol) from the reflector resulting in coupling to the RHCP fields (cross-pol) of the RX. The influence of the additional paths can be inferred from the ripples (or standing waves) in the mutual coupling between ports with reflector, as illustrated in Fig. 5.10. These additional paths will also deteriorate the system isolation as shown in Fig. 5.11. Nevertheless, the impact of asymmetries on system isolation is significantly reduced in comparison to that in [32], and >60 dB can be achieved. This makes the quasi-monostatic configuration more robust towards imbalances. Importantly, at higher frequencies, the system isolation is even less sensitive because of the higher F/B and lower mutual coupling, which is an added benefit of the system.

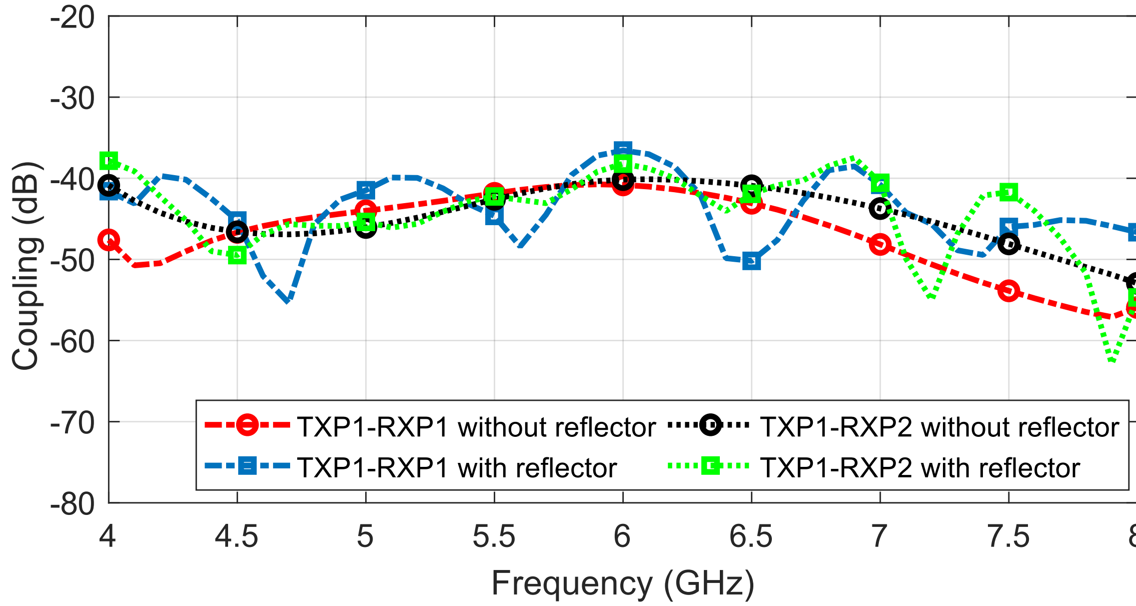

Figure 5.10: Simulated mutual coupling between the TX and RX ports of the antennas with and without reflector.

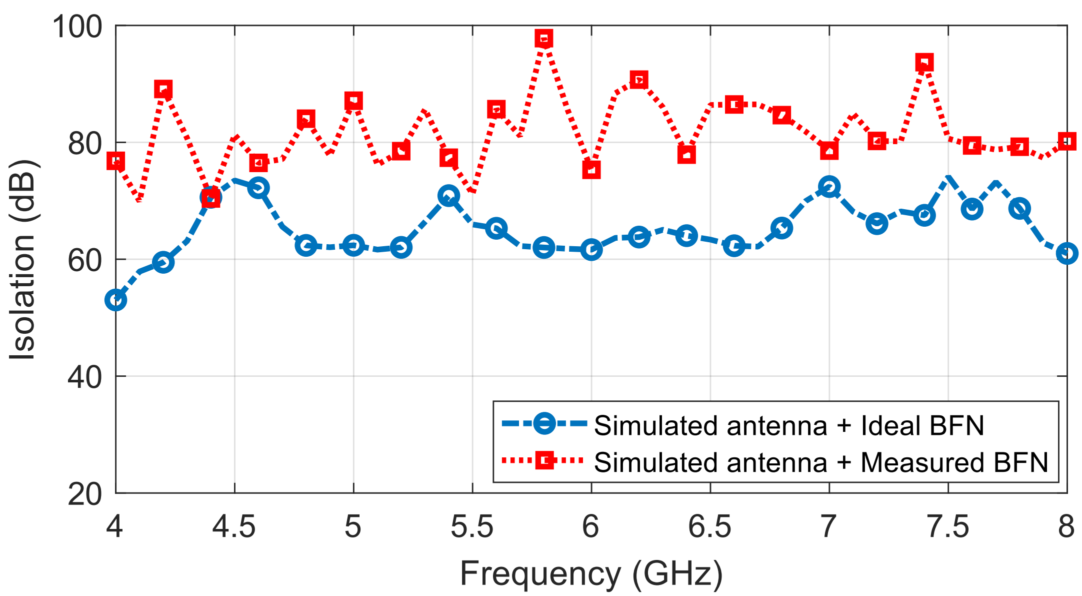

Figure 5.11: Simulated system isolation with reflector.

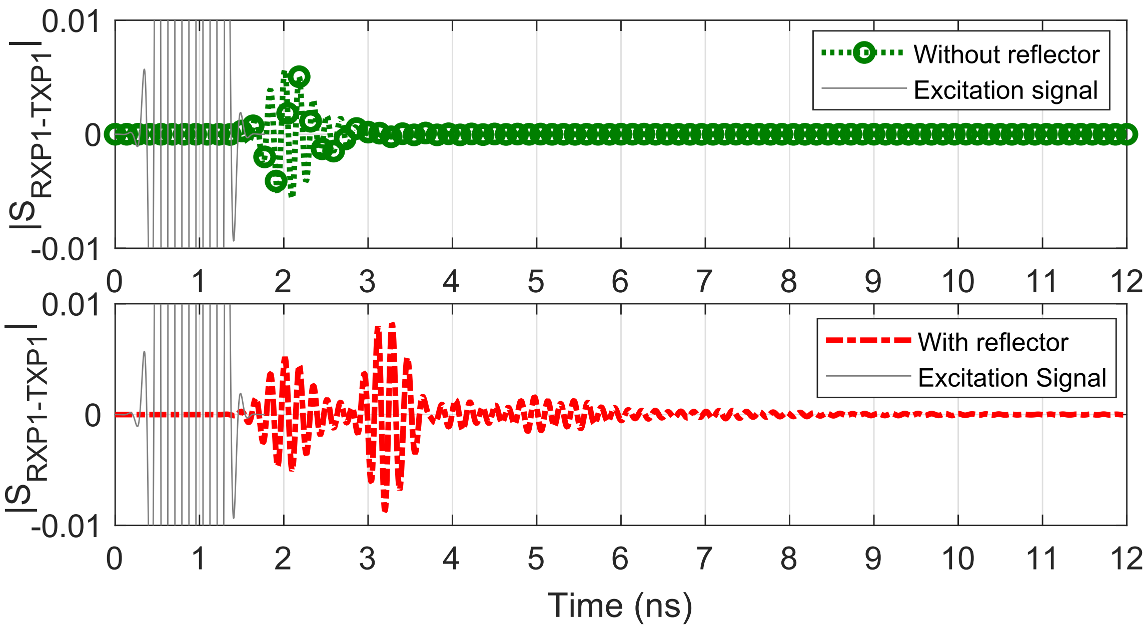

(a)

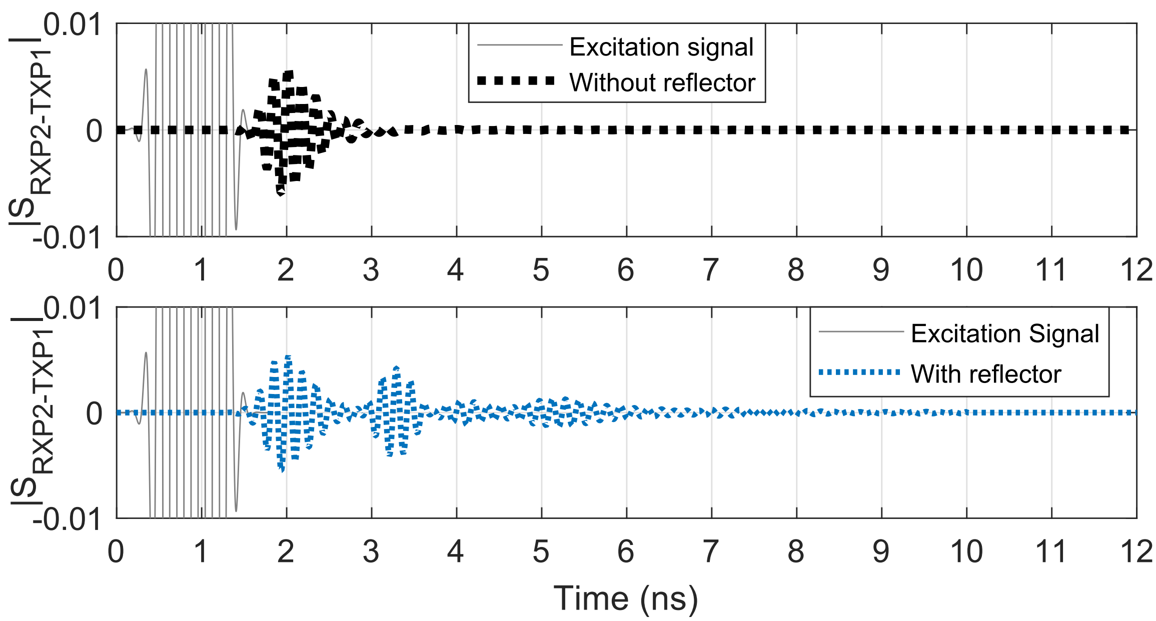

(b)

Figure 5.12: Transient analysis (in CST) of coaxial cavity antennas (RX and TX feed) mounted back-to-back with and wihtout reflector, (a) co-pol to co-pol, and (b) co-pol to cross-pol.

Further insight on the coupling mechanism of the proposed architecture can be obtained by analyzing the problem in the time domain. In this analysis, a transient pulse of 1 ns duration is transmitted from the feed (see Fig. 5.12). The signal coupled to the co-polarized port (RX-Port1) from the transmitting port (TX-Port 1) with and without reflector is shown in Fig. 5.12 (a), where the second signal pulse with higher amplitude highlights the importance of coupling through co-pol. Similarly, an additional signal pulse of lower magnitude in the signal coupled from TX-port 1 (co-pol) to RX-port 2 (cross-pol), in Fig. 5.12 (b), affirms the coupling through the cross-pol, in the presence of the reflector. The time domain analysis is carried out in CST transient solver [111].

The measured system isolation with and without reflector is shown in Fig. 5.13. Some degradation in the system isolation can be observed from the measured results in comparison to the simulation. This degradation is mainly due to the small asymmetries in the fabricated antenna geometry inclusive of mounting. Nonetheless, the system has average high isolation of 61 dB, which is 30 dB higher than the system isolation in [31]. Most importantly, the isolation is less sensitive to the imbalances.

The roughness and deformations in a reflector surface lead to asymmetries and may deteriorate system

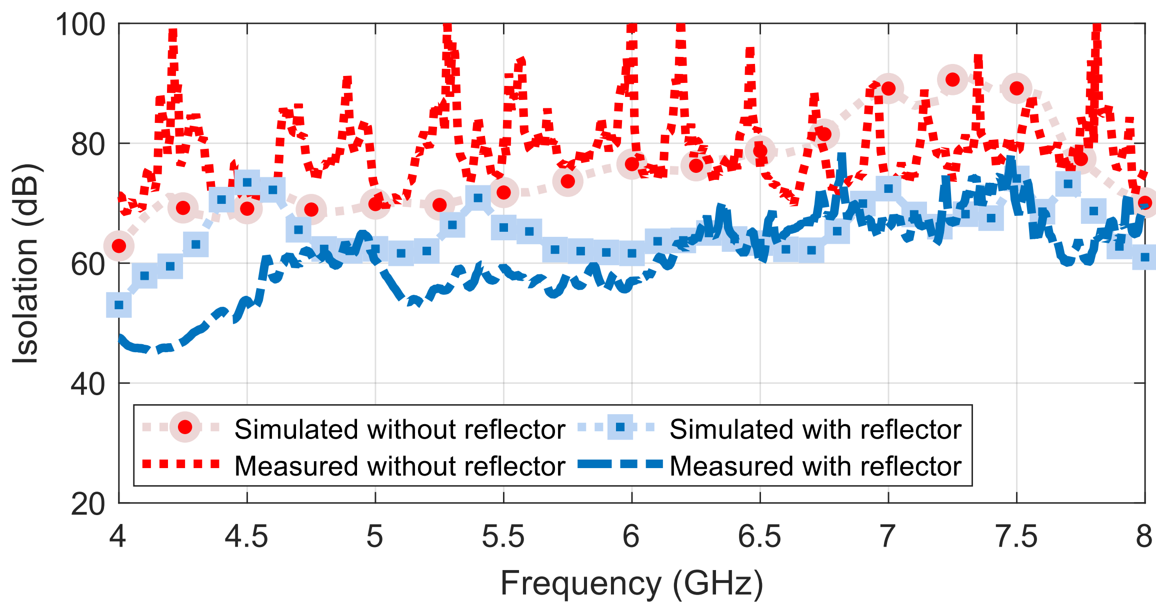

Figure 5.13: Measured and simulated system isolation of the proposed quasi-monostatic reflector STAR antenna.

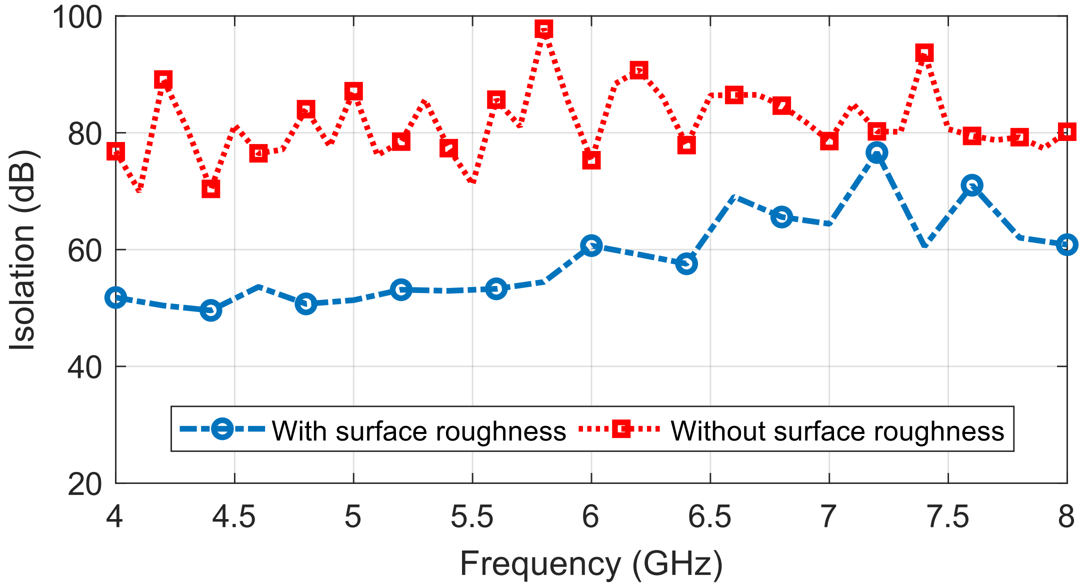

Figure 5.14: Comparison of simulated system isolation with and without reflector surface roughness.

isolation as discussed in Chapter 4. They can also negatively affect far-field performance [108]. Hence, random roughness is modeled as Gaussian distribution with correlation length 10 cm (1.33 λ_{4GHz}) and root mean square (RMS) height of 0.2 cm (0.026 λ_{4GHz}). The asymmetries due to surface roughness have tolerable impact on system isolation in the proposed quasi-monostatic system, as shown in Fig. 5.14, further highlighting the robustness towards asymmetries.

5.3 System Performance

5.3.1 Feed and RX Antenna

A coaxial cavity antenna operating in its first higher order mode, TE_{11}, is used as the feed for the reflector [93, 110]. The antenna is excited by four probes which are oriented and phased 90° to each other to achieve CP operation. The antenna has a height of 5.06 cm, and outer and inner conductor diameters 4.62 cm and 1 cm, respectively, as shown in Fig. 4.3. These physical parameters are selected as a compromise between impedance match and the far field performance over the bandwidth, as explained in detail in Chapter 4. The phase center of the antenna is stable with <5% variation for CP. Additionally, the antenna has symmetric

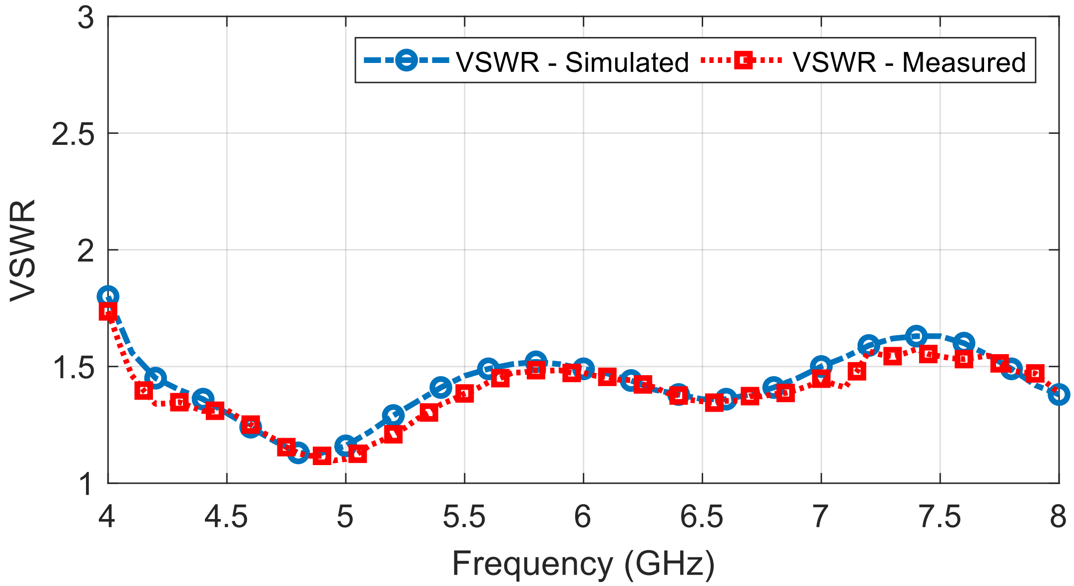

Figure 5.15: Measured and simulated VSWR of the RX antenna with and without reflector.

radiation patterns with axial ratio <3 dB for $\theta = \pm 30°$, VSWR <2, and gain >6 dBic over the 4 to 8 GHz operating frequency band. The impedance match of the antenna is less impacted by the presence of another antenna, and the reflector mounted behind it which are required for the proposed configuration (see Fig. 4.8 and Fig. 5.15). However, the reflector has increased the gain of the RX at frequencies where the reflected fields from the reflector add constructively in the far field. Similarly, an increase in the cross-pol level of the RX is noticed in the presence of the reflector behind the antenna. The gain, and radiation patterns of the antenna with and without reflector are shown in Fig. 5.16, Fig. 5.17, and Fig. 5.18, respectively. Nonetheless, these deteriorations in the far field are not significant for the intended application.

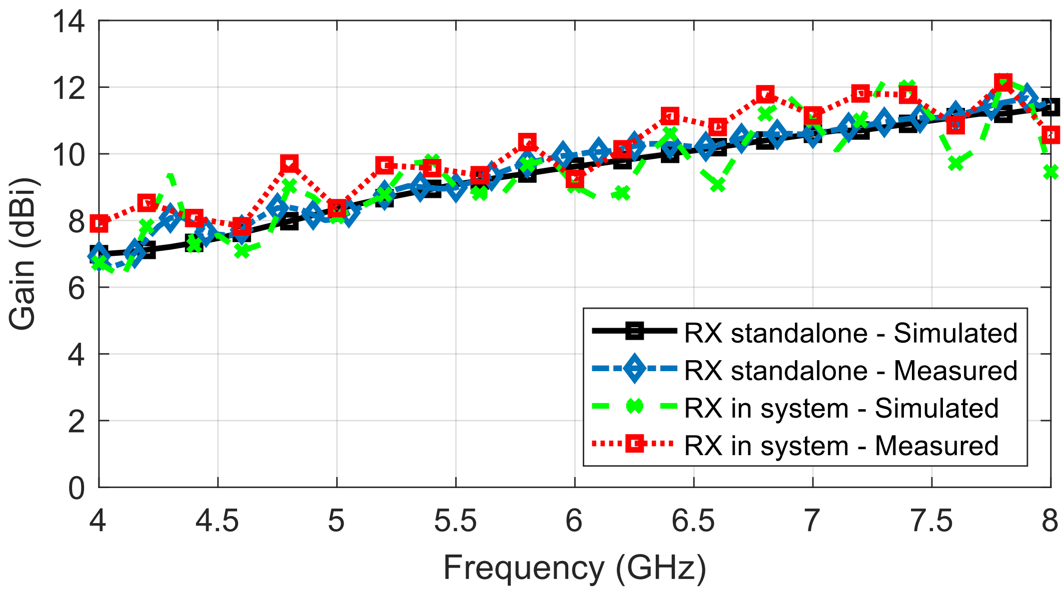

Figure 5.16: Measured and simulated gain of the RX antenna with and without reflector.

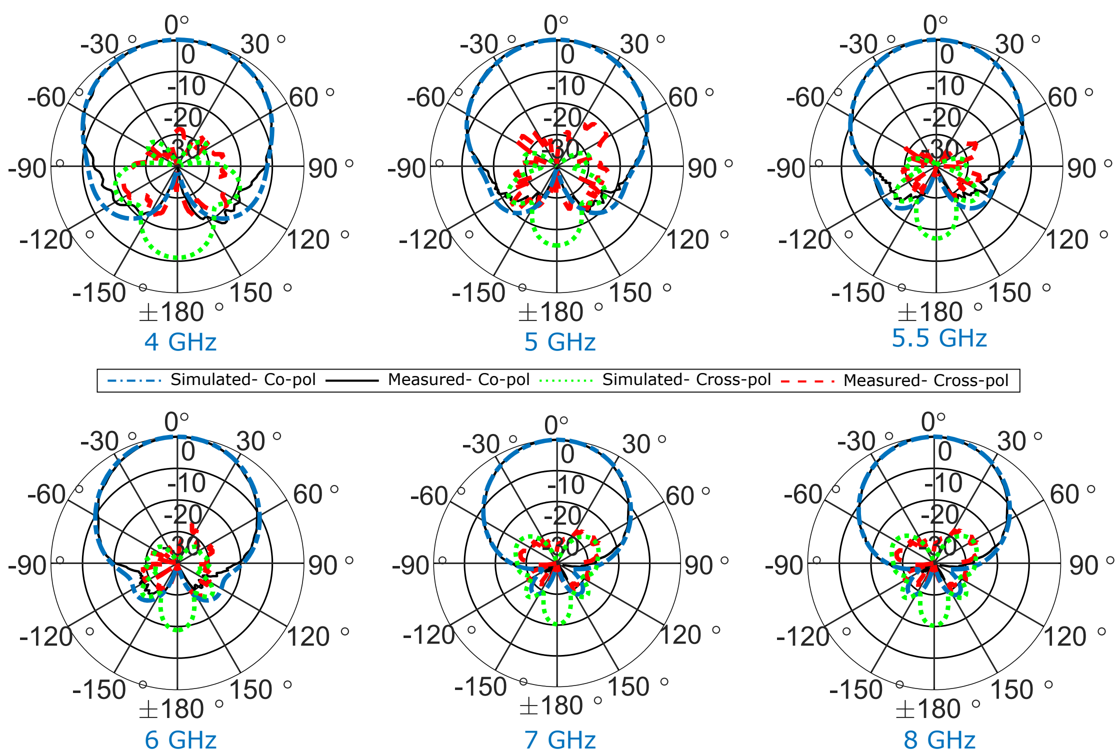

Figure 5.17: Measured and simulated radiation patterns of the RX antenna without reflector.

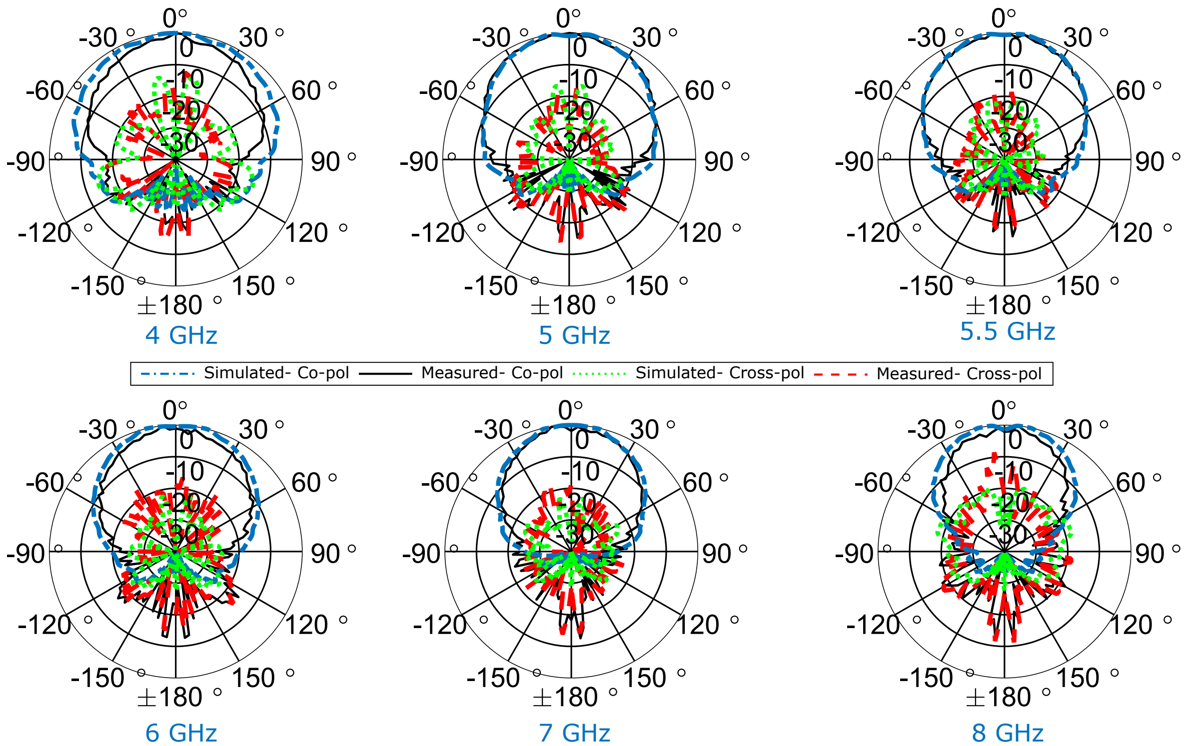

Figure 5.18: Measured and simulated radiation patterns of the RX antenna with reflector.

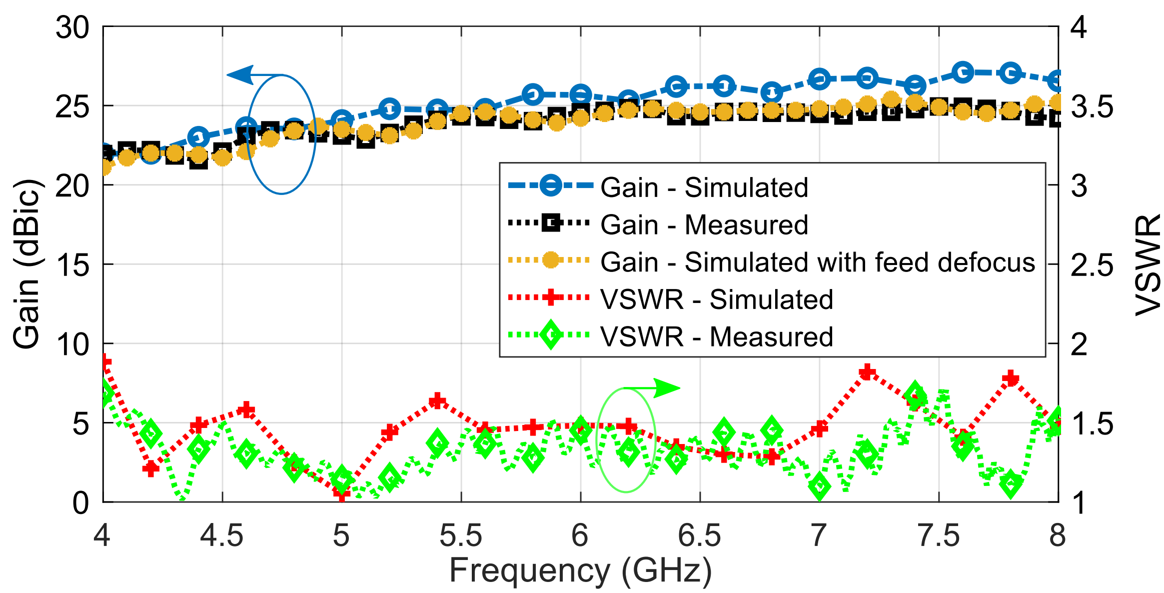

Figure 5.19: Simulated and measured gain, and VSWR of the TX antenna.

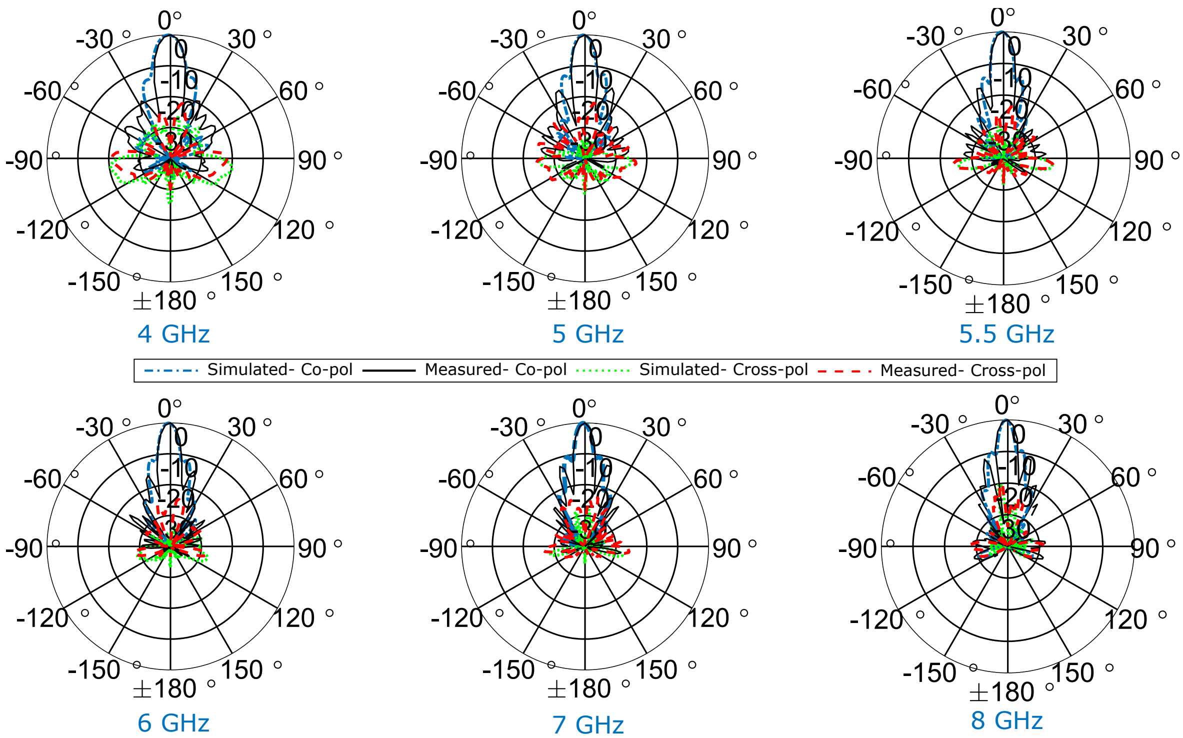

Figure 5.20: Measured and simulated radiation patterns of the TX.

5.3.2 Reflector Antenna

The existing axis-symmetric parabolic reflector with F/D = 0.49, and diameter = 40 cm is employed in the proposed system (see Fig. 5.1). The feed and the RX antennas are supported using a conventional four struts approach [45]. This mount provides extra sturdiness in comparison to a single- and three- struts approach and help maintain the symmetry, which is preferred for high isolation. The struts are constructed as 1 cm outer diameter hollow cylindrical tubes, therefore, aiding the routing of RF cables to the reflector backside through it. A maximum drop of 1.16 dB (@ 6.8 GHz) in gain is observed over the band with the struts and the RX antenna mounted behind the TX feed antenna, which indicates that its influence is minimal. The quasi-static reflector antenna has gain >20 dBic, VSWR <2, and maximum aperture efficiency of 70% over the operating frequencies, 4-8 GHz, as shown in Fig. 5.19. The drop in the measured gain is primarily due to the defocus and slight offset of the feed from the center of the parabola. Hence, good agreement between measurement and simulation is achieved by incorporating the focal point offset of 1.5 cm in z-axis,

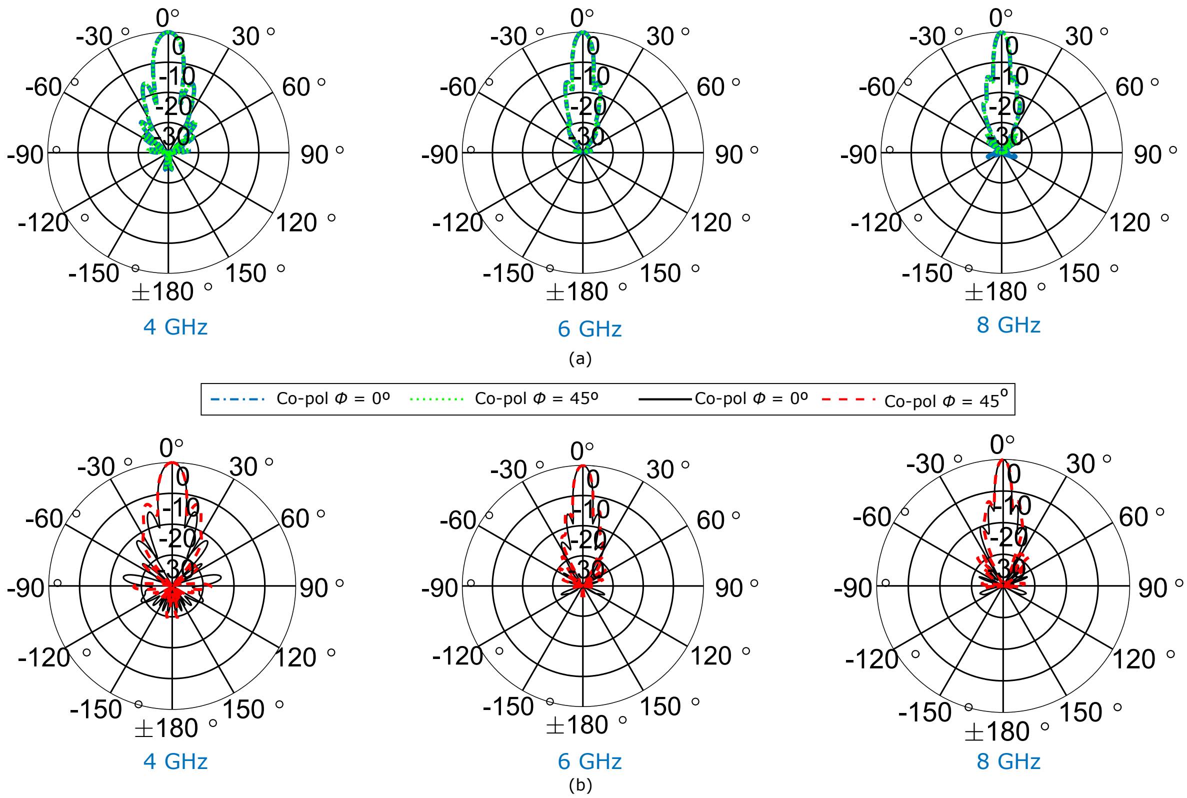

Figure 5.21: Simulated reflector co-polarized radiation patterns for $\phi = 0°$ and $45°$ (a) without, and (b) with struts.

0.3 cm and 0.8 cm in x-and y-axis, respectively, as illustrated in Fig. 5.19. The antenna has side lobe level (SLL) <-10 dB over the operating frequency band, as shown in Fig. 5.20. The influence of the struts (oriented at 45°) on SLL at $\phi = 45°$ is seen in Fig. 5.21. Note that this impact can be minimized by using polygonal, dielectric or corrugated struts, as explained in [112, 113].

5.4 Improving isolation and operational bandwidth

5.4.1 Improving Isolation

Radiation from the back lobe is the primary source of coupling in the proposed configuration, as mentioned in Section 5.2. Reducing the mutual coupling is important, since the lower the coupling, the greater will be the robustness of the system isolation to the asymmetries and imbalances. Therefore,

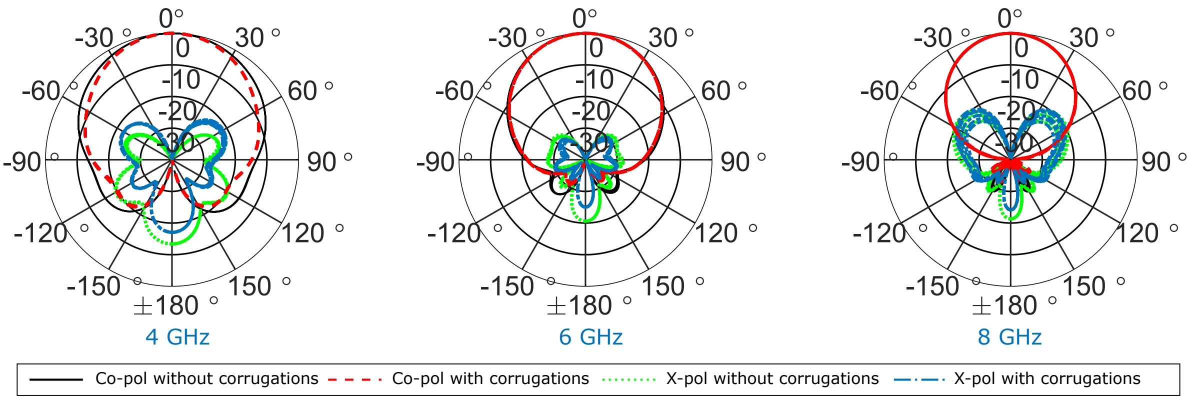

(a)

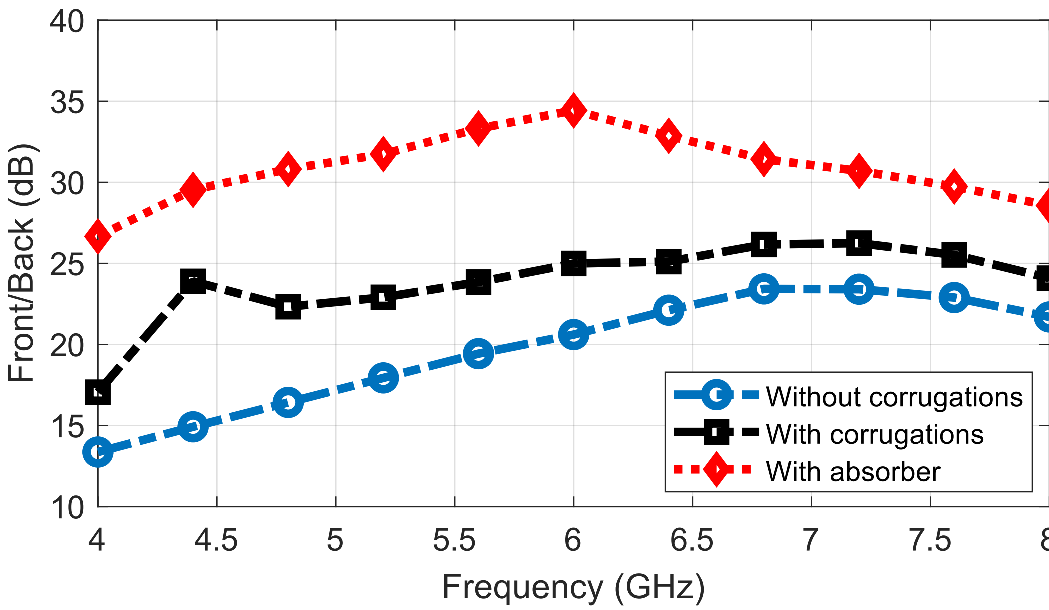

(b)

Figure 5.22: (a) Simulated radiation pattern, and (b) front/back ratio of the coaxial cavity antenna with and without corrugations, and when recessed in absorber.

improving the F/B of both antennas will reduce the coupling between the TX feed and RX, and thereby sensitivity of the system isolation to the BFN's imbalances. The F/B can be increased using various techniques, such as, corrugations at the aperture, aperture matching, and recessing the antenna inside the absorber cavity. The metallic corrugations are quarter wavelength (at resonant frequency) chokes (Section 3.4). High impedance offered by these surfaces reduces the diffracted fields from the aperture edges of the antenna, and thus, increases the F/B. Similarly, aperture matching minimizes diffracted fields radiated behind the antenna and improves F/B. When the antenna is recessed inside the absorber cavity, the losses in the

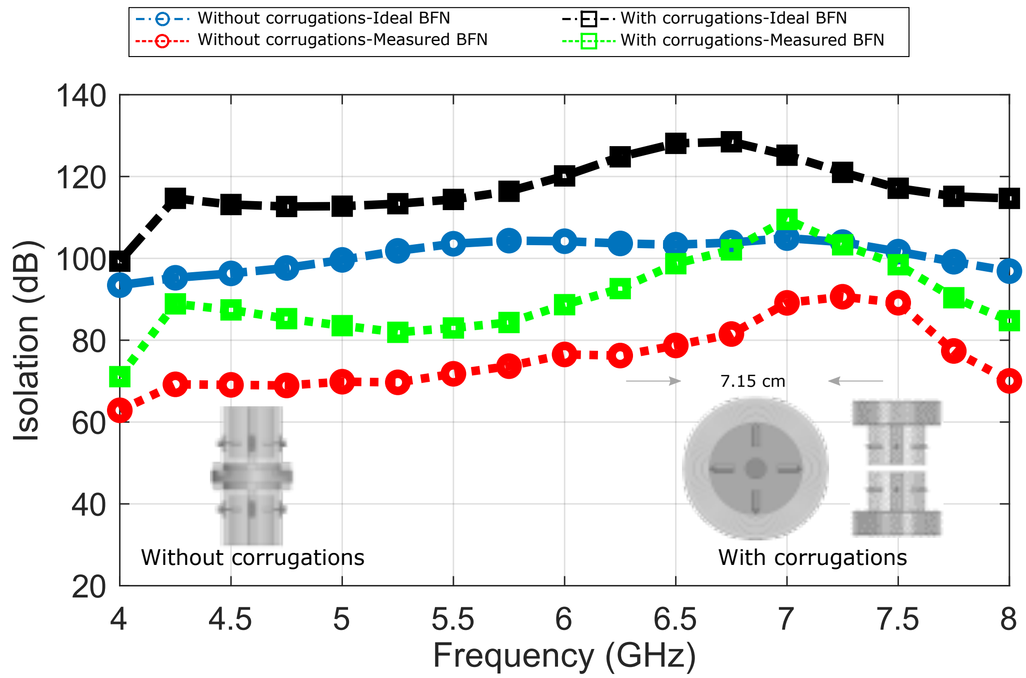

(a)

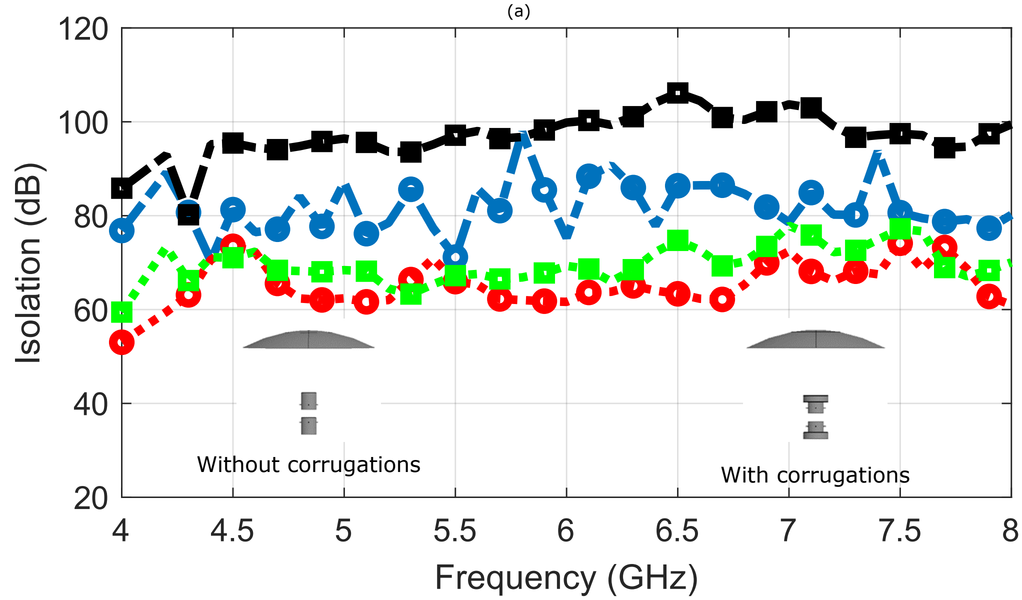

(b)

Figure 5.23: Simulated isolation between the antennas with and without corrugations for the ideal and measured BFN, (a) without reflector, and (b) with reflector.

absorber will help reduce the diffracted fields resulting higher F/B. However, the absorber may reduce the radiation efficiency of the antenna. The reduction in back lobe by 5-10 dB can be observed by comparing the radiation patterns of coaxial cavity antenna with and without corrugations, as shown in Fig. 5.22 (a) and (b). Metallic corrugations of depth 1.87 cm ($\lambda_{4GHz}/4$), with four slots, resulting in a total diameter of 7.15 cm are used. It should be noted that the resulting feed size with corrugations is smaller than the size of the supporting structure for the struts used (see Fig. 5.1). Similarly, improvement in F/B can be achieved by recessing the RX antenna inside the absorber as shown in Fig. 5.22 (b). A numerical absorber [83] with ϵ_r = 1-j2.7, and μ_r = 1-j2.7 is used for the study shown in Fig. 5.22 (b). Further, the reduction in the back lobe directly corresponds to the reduction in the mutual coupling, and hence, will result in increased system isolation. Importantly, the lower mutual coupling will improve the tolerance of the system isolation to the imbalances as illustrated in the Fig. 5.23 (a) and (b).

5.4.2 Extending Bandwidth

Isolation >60 dB over an octave bandwidth (4-8 GHz) is demonstrated in the proposed quasi-monostatic STAR using coaxial cavity antennas as the feed and RX. The operation bandwidth over which high isolation can be achieved is mainly limited by the impedance bandwidth and far-field performance of the antenna employed, and not by the approach. Hence, the bandwidth of the proposed approach can be extended by employing a wideband radiator such as dual polarized quad ridge horn [29] or cavity-backed spiral as reflector feed and RX antenna (see Fig. 5.24). The number of components (180° and 90° hybrids) required in the BFN can be reduced significantly by employing a CP antenna, such as, cavity backed two-arm spirals as the feed and RX. Therefore, to demonstrate wideband operation with high isolation, two, cavity backed, absorber loaded two-arm Archimedean spirals operating from 3-18 GHz are considered herein. The 4.3 cm spiral has 10 turns with equal metal to slot ratio and is fabricated on Taconic TLY 5 [114] substrate with $\epsilon_r = 2.2$, and $\tan\delta = 0.0009$. A 2.7 cm tall metallic cavity loaded with absorber backs the aperture. The antenna has VSWR <1.55, and AR <3 dB for $\theta = \pm 30°$, when fed by a microstrip balun.

The system isolation of 61 dB (average) can be achieved over 6:1 bandwidth when the spiral antenna is used in the proposed configuration, as shown in the Fig. 5.25. The high isolation achieved is mainly due to the low cross-pol and high F/B of the spiral antenna (see Fig. 5.26). Hence, any feed with good axial ratio and low back lobes can be employed in the proposed configuration to realize high isolation wideband

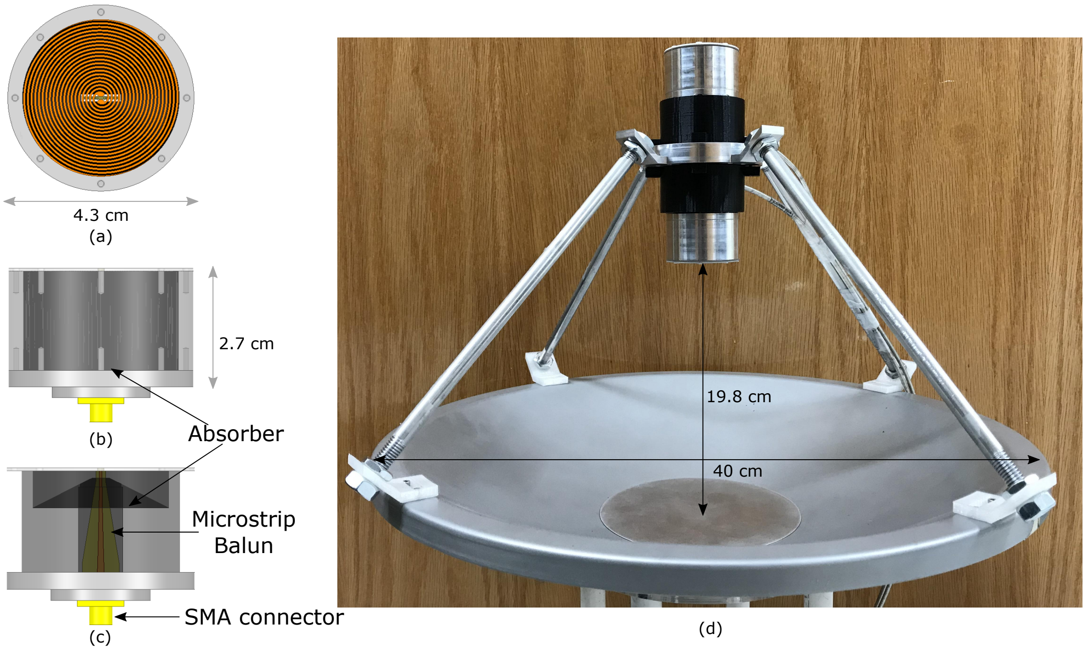

Figure 5.24: (a), (b), and (c) CAD model of cavity backed spiral, (d) picture of back-to-back spiral with reflector.

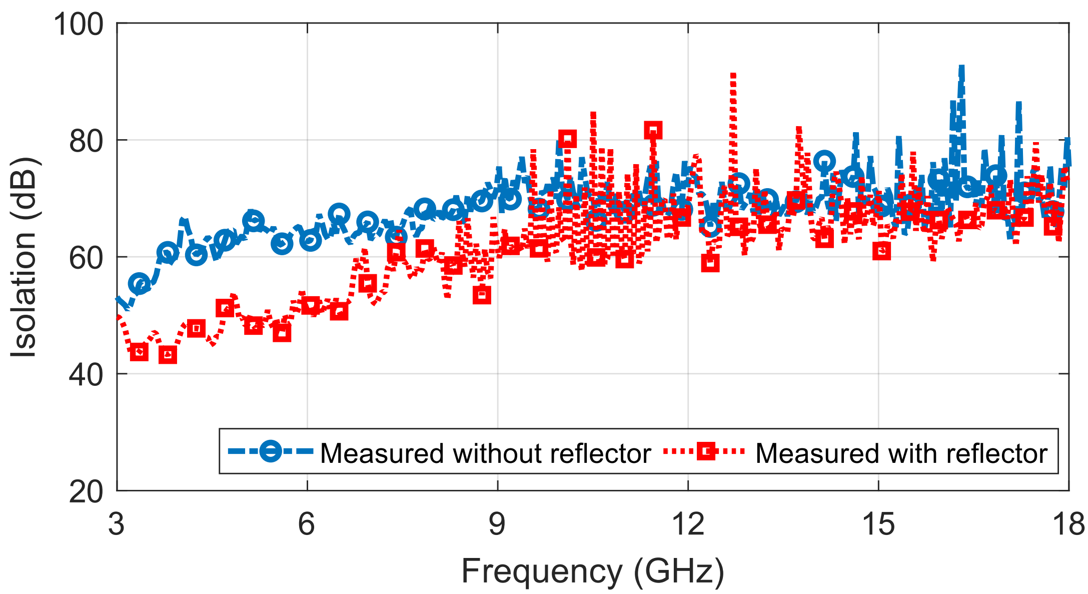

Figure 5.25: Measured system isolation of the quasi-monostatic STAR with cavity backed spiral.

quasi-monostatic STAR system. Note that the reflector antenna with the spiral feed supports only the single polarization operation, in contrast to the reflector fed by the coaxial cavity antenna, which facilitates simultaneous dual polarization.

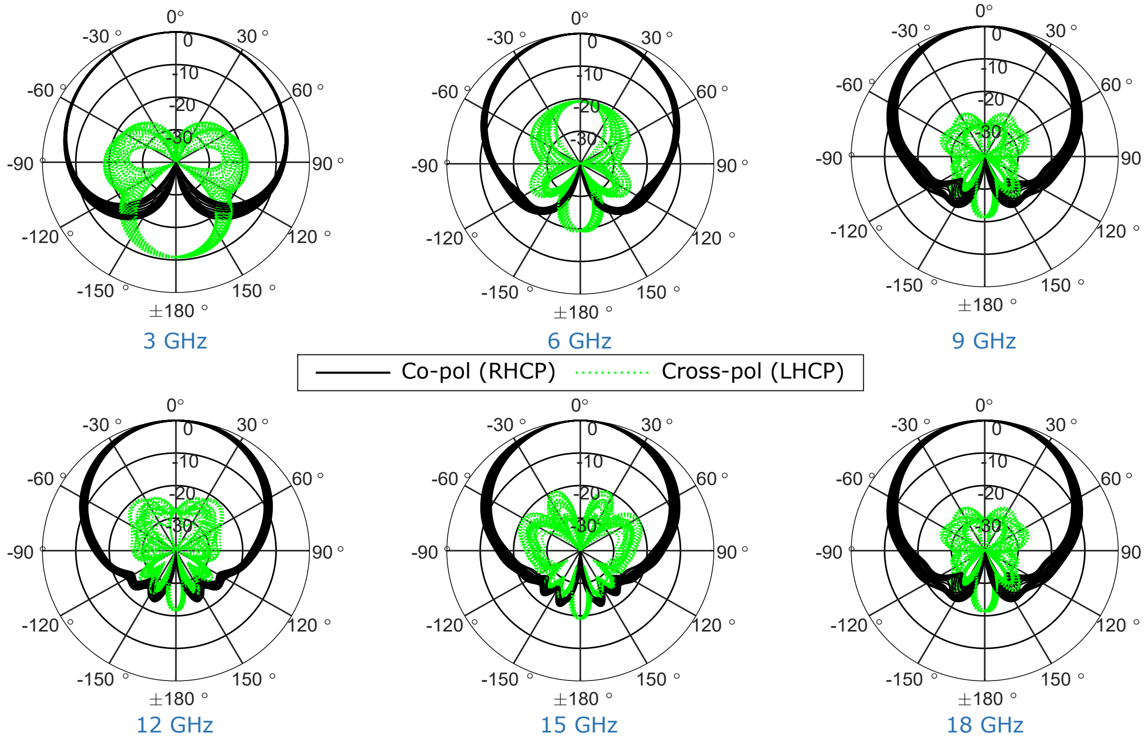

Figure 5.26: Simulated radiation pattern of the cavity backed spiral.

5.5 Summary

The design and implementation of a quasi-monostatic STAR antenna system is presented. It is shown that the radiation properties of the feed and RX antennas, specifically, F/B and cross-pol level are important to achieve high isolation. The antennas are operated in CP to achieve additional improvement in isolation. It is demonstrated that the approach is less sensitive to the asymmetries in the antenna geometry and the BFN. Average measured isolation of 61 dB using COTS components proves that the proposed STAR system can be practically realized with high system isolation. Further, it is shown that the system can maintain isolation >50 dB even in case of deformation to the reflector surface, which may happen over time. Known techniques to improve F/B of the feed and thereby system isolation are also discussed. Furthermore, it is shown that the operation bandwidth can be improved to more than one octave while maintaining high isolation, 61 dB (average), by using wideband cavity backed spiral antennas. The designed system with coaxial cavity antenna has gain >20 dBic and >7 dBic for the TX and RX, respectively, and VSWR <2 over an octave bandwidth

(4-8 GHz). The RX has a wider beam compared to the TX due to the difference in the effective aperture sizes. This difference in directivity and patterns can be used as advantage in certain applications where a wide field of view for a sensor is desired and high gain beam is preferred for the TX.

Chapter 6

Quasi-Monostatic STAR Dual Reflector

6.1 Introduction

Interest in frequencies, K-band and above is on the rise among both civilian applications, and in defense and aerospace areas [115, 116]. The former is driven by communication technologies such as proposed fifth generation wireless networks due to large available instantaneous bandwidth, and for automotive radars for better range resolution [117]. Similarly, mm-Wave has the unexplored potential for electronic warfare and support (EW and S), and signals intelligence (SIGINT) [118]. Additionally, antennas, feeding networks, and passive components are physically small [116, 117]. Hence, these could be efficiently housed inside cars and airborne vehicles like UAVs. Further, the current capabilities of additive manufacturing foster the design and fabrication of mm-Wave components.

$$Pathloss = 20\,log_{10}\frac{4\pi d}{\lambda} \tag{6.1}$$

Despite its benefits, implementing a STAR system in mm-Wave frequencies is even more challenging. First, the signals will undergo greater path loss as given by (6.1) [47]. Secondly, the atmospheric absorption of the waves is higher as depicted in Fig. 6.1 [119]. Hence, it is desired to have high gain antennas such

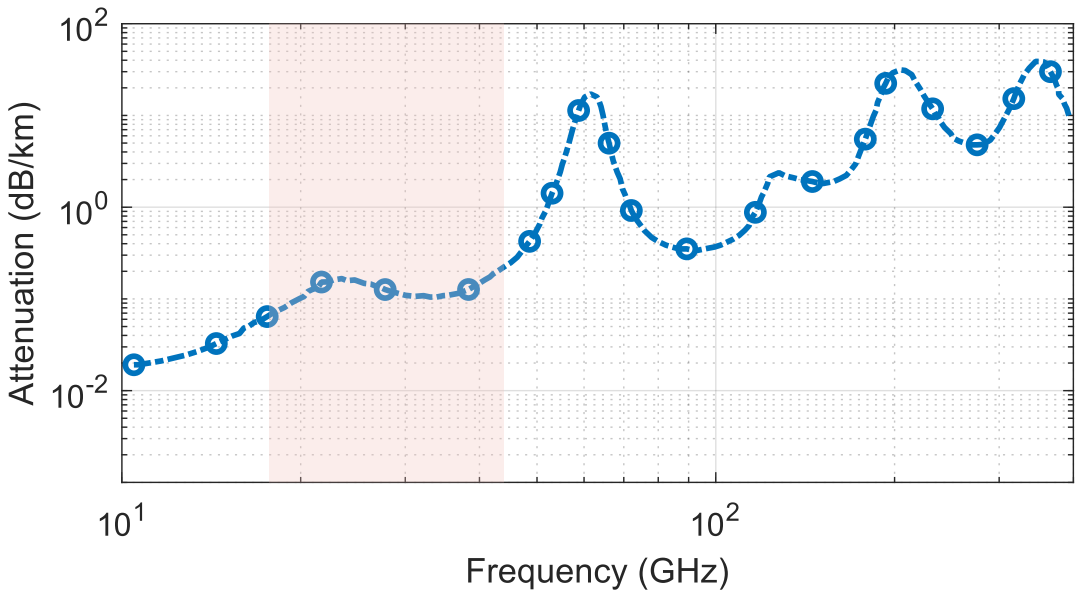

Figure 6.1: Atmospheric attenuation of microwave at sea level.

as reflectors. In-band full-duplex configuration explained in Chapter 4 is a lucrative choice. However, the inner conductor of the coaxial cavity Fig. 4.1 becomes small, that is, 2 mm which is mechanically feeble to self-support the feed. Importantly, the availability of the COTS circulators covering the full 18-45 GHz frequency band is meager [7, 8], and the system isolation will have increased sensitivity towards imbalances and asymmetries. Contrarily, the quasi-monostatic approach is the other favorable option. However, the reflector topology used for realizing STAR system in Chapter 5 requires the feed to be placed at the focus of the axis-symmetric reflector. Thus, the TX path will have greater attenuation and routing of waveguides, desired for high power, is cumbersome and could contribute to the reflector blockage. Therefore, a dual reflector based quasi-monostatic configuration is developed in this chapter, which addresses the challenges mentioned above.

Conventionally, Cassegrain and Gregorian reflectors have primary and secondary dishes in the order of 100λ and 10λ in diameter, respectively [45–47, 120]. Hence, they are preferred for ground station, on board satellites, and radars. However, reflectors in the order of 166 cm ($100\lambda_{18\,GHz}$) is not desired for small UAVs and decoys platforms. Therefore, the research focuses on designing small size dual-reflectors of diameter 30 cm (12”) and 15 cm (6”) for in-band full-duplex antenna systems.

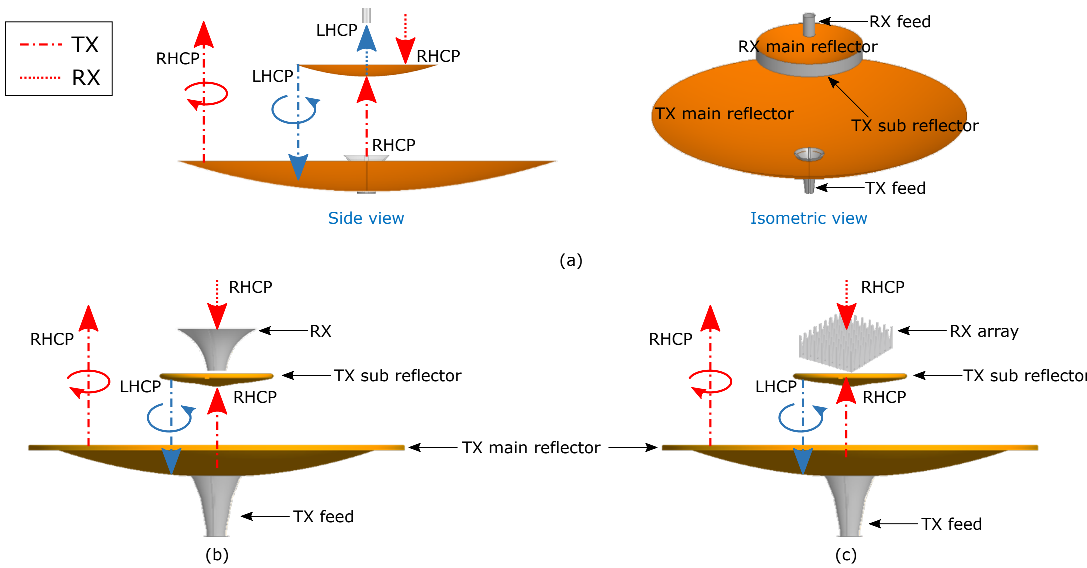

Figure 6.2: CAD models of proposed dual reflector STAR configurations (a) approach I, (b), and (c) approach II - QRH, and Vivaldi array as RX, respectively.

Two STAR topologies are outlined in this chapter. In the first approach, TX is a Cassegrain antenna, and the RX is a prime feed single reflector. Unlike, typical dual reflector, the unused backside of the secondary reflector is utilized as the main dish for the RX, as illustrated in Fig. 6.2 (a). Second configurations also employ dual reflector for TX, whereas, the RX can be a QRH or tightly coupled array, mounted on the secondary reflector, as shown in Fig. 6.2 (b) and (c), respectively. Relatively small main dish size deteriorates the far field performance due to the increased blockage, which is compounded by the difficulties in achieving required amplitude taper from the feed and the sub-reflector [120]. This influence on radiation patterns is minimized by modifying the profile of the QRH and shape of the secondary reflector while accounting for the feed's phase center variations as explained in the following sections. Furthermore, the trade-off between the primary and secondary reflector diameter ratio, and its impact on far-field is presented. Importantly, the chapter describes the STAR functionality with achievable system isolation >65 dB and far-field performance of the TX and RX antennas.

This chapter is organized into four sub-sections:

- Section 6.2 discusses the theory and construction of a standard Cassegrain reflector and highlight the challenges in the design of relatively small primary and secondary dishes. Specifically, influence on maximum aperture efficiency and far field patterns quality.

- Section 6.3 presents the two variants of dual reflector-based STAR configurations. Further, evaluates the benefits and limitations of each approach and its potential applications.
- Section 6.4 describes the design, fabrication, and performance of the approach II in detail. Explicitly, the TX feed, lens loaded RX antenna, and the 6” STAR Cassegrain reflector system.
- Section 6.5 outlines the system isolation and techniques to minimize the coupling.

6.2 Dual Reflector Design

6.2.1 Conventional

Dual reflectors are one of the extensively researched and deployed antenna systems for high gain applications, because of its benefits over front-fed or prime feed reflectors. Specifically, the location of the feed close to the source and the receiver, reduced spillover which minimizes the noise temperature, and its ability to provide equivalent focal length shorter than the physical/actual focal length leading to compact systems. Cassegrain and Gregorian are the two commonly used configurations [45,46]. However, the former is preferred due to the proximity of the sub-reflector and the feed to the main dish, which results in smaller overall system volume. Fig. 6.3 depicts the arrangement of a Cassegrain reflector antenna with critical design parameters. These parameters are broadly classified as independent and dependent variables and are mainly decided by the far field requirements and the mechanical feasibility of the system. Therefore, a dual reflector antenna can be designed employing two principal approaches to result in the maximum aperture efficiency or gain, while minimizing the spillover and blockage loss [46, 120].

In the first procedure, diameter of the main reflector, D_M, is decided, independently, according to the desired antenna gain. Next, the size of the secondary dish, D_S, is computed for the least blockage using (6.2) [46, 120]. Consequently, the feed is designed to provide the 10 dB taper at the edges of the

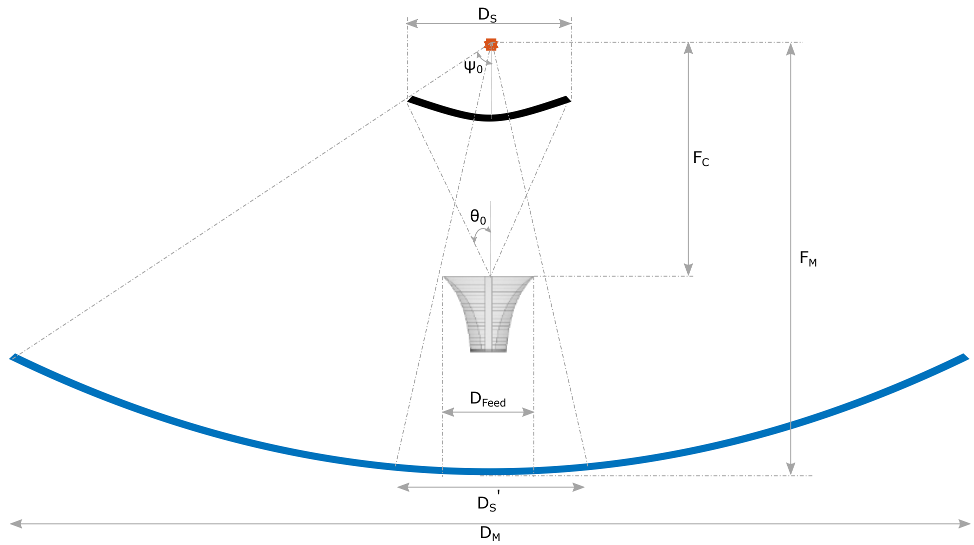

Figure 6.3: Cassegrain reflector with design variables.

sub-reflector, while satisfying the minimum blockage condition. This condition is achieved by maintaining the feed diameter D_{Feed} and its shadow smaller than that of the secondary reflector, as illustrated in Fig. 6.3 and given by (6.3).

$$\frac{D_S}{D_M} = \left[\frac{cos^4(\theta_0/2)}{(4\pi)^2(sin\psi_0)} E \frac{\lambda}{D_M} \right]^{1/5} \tag{6.2}$$

$$\frac{F_C}{F_M} \approx \frac{1}{2} \frac{kD^2_{Feed}}{F_c\lambda} \approx \frac{D_{Feed}}{D'_S} \tag{6.3}$$

In the second approach, primary reflector and the feed are designed first according to the requirements, followed by the secondary dish for minimum blockage condition using (6.4), where P is given by (6.5) and C is distance between sub-reflector foci. Furthermore, a balance between blockage and diffraction loss is achieved by modifying the sub-reflector diameter for highest gain [46].

$$\left[\frac{2F_m sin(tan^{-1}(D_{Feed}/2C))}{1 + cos(tan^{-1}(D_{Feed}/2C))} \right] = \frac{2(F_{Eff}/D_M)P sin\psi_0}{1 + (F_{Eff}/D_M)cos\psi_0} \tag{6.4}$$

$$P = \frac{2C(e^2 - 1)}{2e^2} \tag{6.5}$$

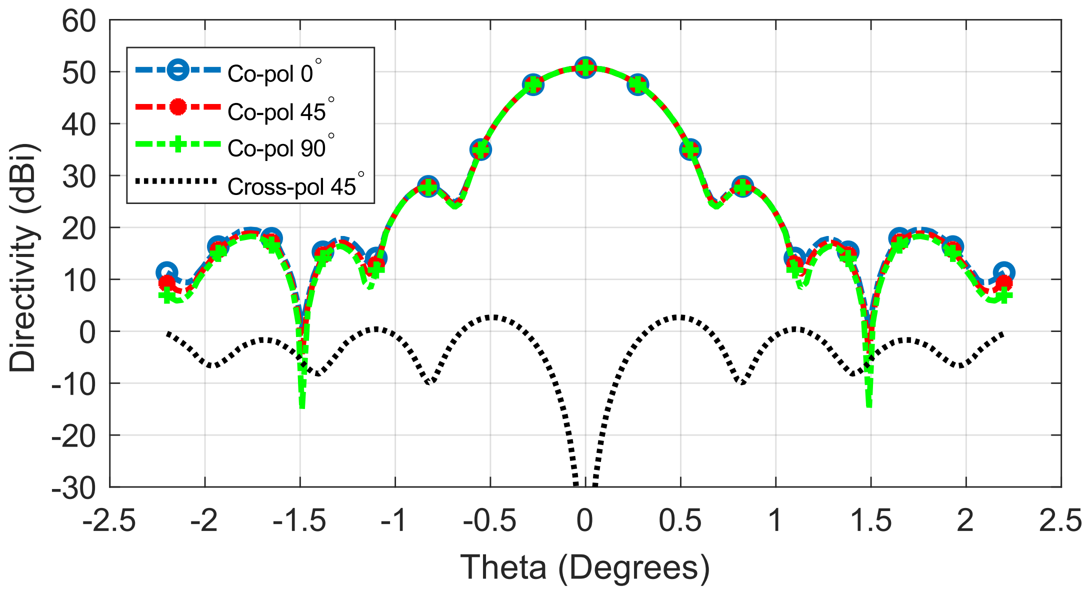

Figure 6.4: Simulated directivity of Cassegrain reflector @ 3.9 GHz.

For example, a 10 m (130λ) diameter primary reflector of a Cassegrain antenna with F/D_M = 0.3 and F_{Eff}/ D_M = 1.5 operating at 3.9 GHz is designed in [46]. Secondary dish of diameter, D_S = 0.894 m (11.62λ), eccentricity, e, of hyperbola = 1.5, is obtained for corrugated horn feed, D_{Feed} = 0.415 m by using (6.2) and (6.3). The feed has 10 dB taper illumination at the subtended angle, $\theta = 18.9°$. The resulting dual reflector antenna has directivity, 50.77 dBi, at 3.9 GHz, resulting in 71% aperture efficiency (AE), as shown in Fig. 6.4. The simulations are carried out in GRASP using geometrical optics (GO) and physical optics (PO) and accounting for the sub-reflector and feed blockage [121]. These results indicate that greater AE, and high gain can be attained from a well designed Cassegrain reflector antenna.

6.2.2 Small Reflectors

This research is focused on dual reflector antennas for compact airborne systems as discussed in Section 6.1. These platforms demand the overall system size to be in the order 12" to 6", which becomes limitation to achieve maximum AE. That is, for the 12" ($18.2\lambda_{18GHz}$) diameter main reflector, operating over 18-45 GHz, variation of F/D_M and F_{Eff}/D_M from 0.3 to 0.5, and from 0.75 to 0.25, respectively will result in sub-reflector diameter 1.47" to 1.6", which is obtained using (6.4), (6.5), and minimum blockage

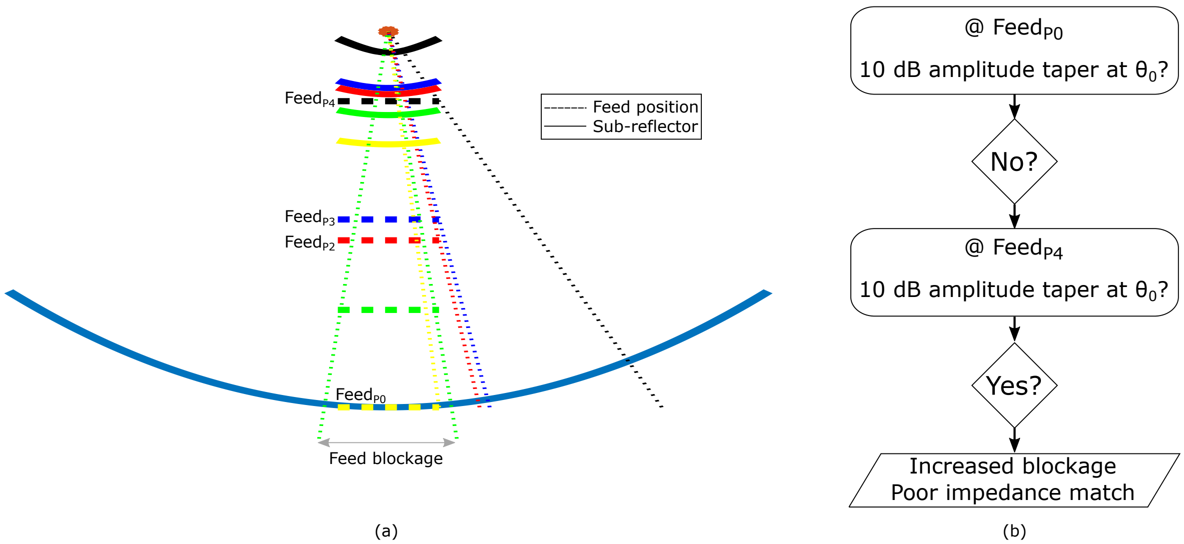

Figure 6.5: (a) Diagram of dual reflector with feed locations and corresponding sub-reflector position, and (b) flow chart explaining design steps.

condition. However, the size of the secondary dish, subtended angle, and the required 10 dB amplitude taper illumination makes the design of feed nearly unrealistic for maximum AE and gain, as illustrated in Fig. 6.5. Contrarily, if approach II is followed, for 12" main reflector and 1.7" feed diameter, the secondary dish should be of 7.9" diameter (6.2), which is impractical and results in high blockage loss. Therefore, achieving optimum AE and gain from a small dual reflector system, 9.1-18.2λ, is nearly impossible. Hence, this research focuses on the design of Cassegrain antenna with acceptable radiation pattern quality and AE in the order of 40%, importantly, STAR functionality with high isolation and minimum difference between the TX and RX gains, as explained in the following sections.

6.3 STAR Topologies

6.3.1 Approach I

The configuration consists of Cassegrain and prime feed reflector antennas for the TX and RX, as illustrated in Fig. 6.2 (a). The RHCP fields from the TX feed are reflected from the secondary reflector as LHCP, which illuminates the primary dish. These incident waves will undergo polarization reversal due

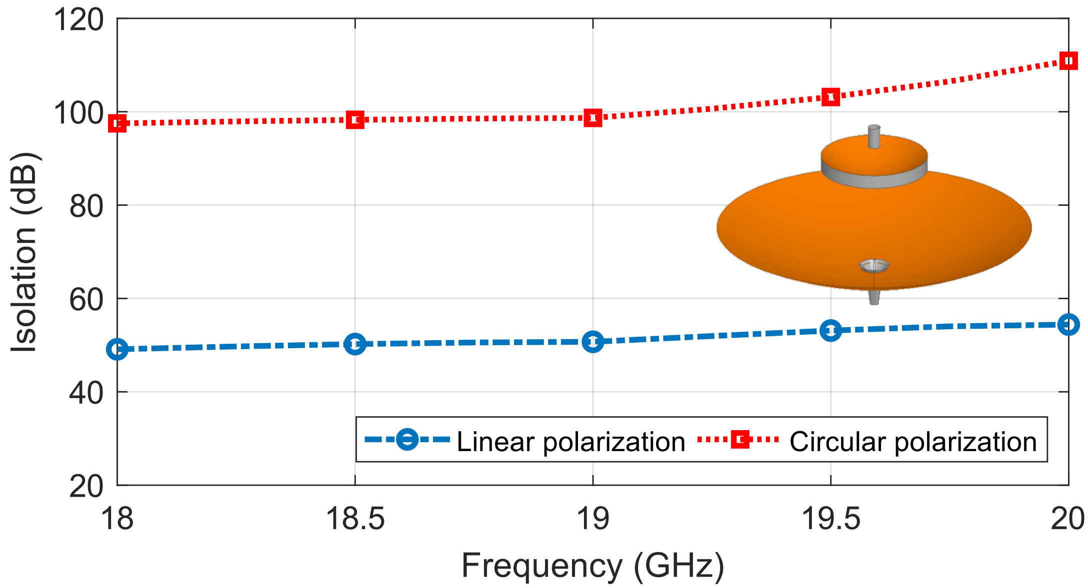

Figure 6.6: Simulated isolation of 12” dual reflector for linear and circular polarizations.

to the boundary condition and are re-radiated as RHCP. Analogously, the RHCP fields impinging on the receiving main reflector will flip the polarization such that all the power is transferred to the LHCP RX feed. Thereby, the STAR configuration operates in same sense of CP, without using any polarization diversity. The presence of RX within the space occupied by TX (in the xy plane) makes the architecture quasi-monostatic.

The power from the TX feed couples to RX feed through two paths. First, via cross-pol fields of both the antennas, as demonstrated in Fig. 6.2 (a). Hence, CP antennas with a low axial ratio (AR) will provide high isolation. Further, the presence of sub and main reflector of TX and RX, respectively, provides additional shielding. Contrarily, the spillover from these dishes will account for the second path of coupling. Therefore, minimizing the diffracted fields or increasing amplitude taper of the feeds is beneficial for obtaining high isolation. Nonetheless, high isolation >45 dB and >90 dB is achieved for LP and CP, in simulation with ideal BFN components as shown in Fig. 6.6. The radiation patterns and gain of both the TX and RX are shown in Fig. 6.7.

Notice that the TX and RX have dissimilarity in their gain, which is due to the difference in their radiating aperture areas. Therefore, increasing the sub-reflector diameter will minimize the inequality in the gains, however, at the expense of TX's AE as shown in the Fig. 6.8 and Table 6.1. Hence, the primary and

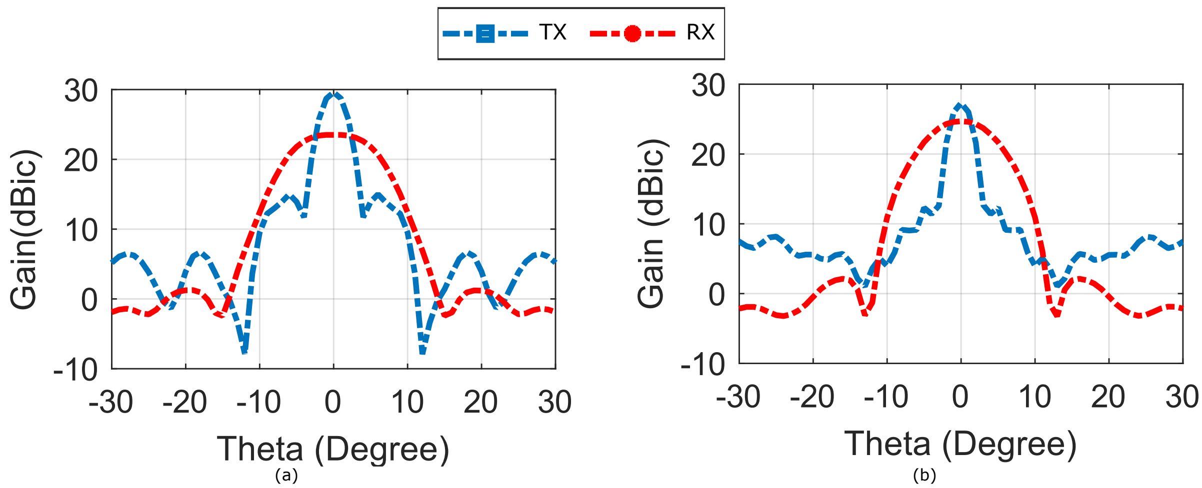

Figure 6.7: Simulated TX and RX radiation patterns at $\phi = 0°$ (a) 18 GHz, and (b) 20 GHz.

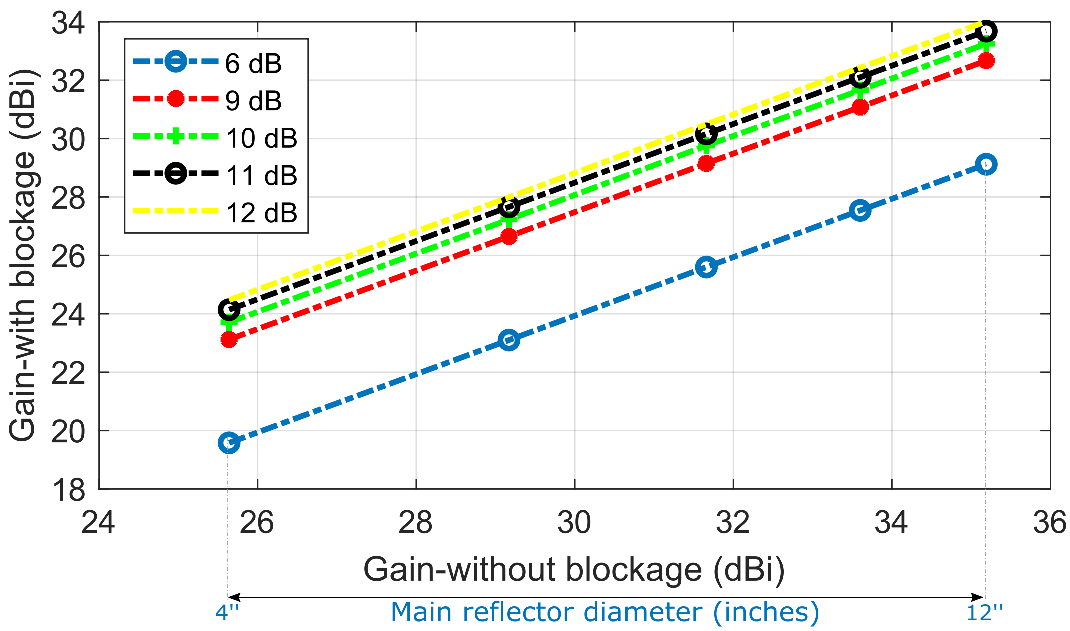

Figure 6.8: Gain (IEEE) of the dual reflector with (x-axis) and without (y-axis) sub-reflector blockage. For TX and RX gain differences 6 dB, 9 dB, 10 dB, 11 dB, and 12 dB. Note that 100% AE, and no-loss are assumed in calculating the gain at 18 GHz.

secondary diameter ratio, 0.35, is selected in the studies presented, which lead to the 9 dB gain difference compared to >16 dB of the configuration in Chapter 5.

Further, reducing the main reflector diameter from 12" to 6" will deteriorate the far field and impedance performance of both the TX and RX. This degradation is due to the increased proximity and the interaction

Table 6.1: Sub-and main reflector diameter ratio trade-off

Gain Difference (dB) @ 18 GHz	Diameter Ratio	Blockage Loss (dB)	Aperture Efficiency
6	0.5	6.06	24.76%
9	0.35	2.51	55.98%
10	0.32	1.93	64%
11	0.28	1.50	70.75%
12	0.25	1.17	76.35%

between the reflectors and feeds, and higher spillover. Hence, the approach is not suitable for the system size <12".

6.3.2 Approach II

The configuration depicted in Fig. 6.2 (b) and (c) are more appealing than the approach I, when a high gain STAR antenna system needs to be accommodated inside small payloads, which are in the order of 6" diameter, and it is necessary to minimize the difference in the TX and RX gain. In this architecture

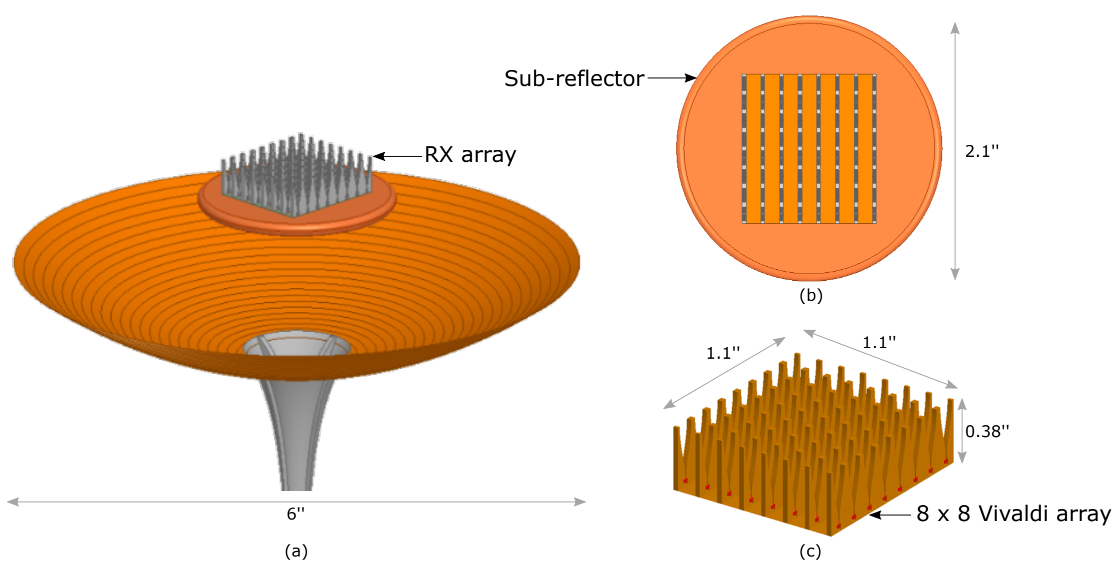

Figure 6.9: (a) CAD model of dual reflector with array, (b) sub-reflector top view, and (c) 8 x 8 Vivaldi array.

(see Fig. 6.2 (b) and (c)) the unused area behind the sub-reflector is utilized for mounting a single aperture antenna or a tightly coupled array. Thus, the configuration provides two benefits. One, the available area can be effectively utilized to achieve 100% AE, and thereby, maximize RX gain. Secondly, the construction of the antenna is simple, robust, and enables easy integration of a radome.

The coupling phenomenon is similar to that in a quasi-monostatic STAR of Chapter 5, where the significant part of the SI comes from the back lobe of the RX and the cross-pol of the TX feed. However, the presence of metallic sub-reflector provides additional isolation. Additionally, part of the power couples through the side lobes of the receiving antenna, hence the array should be designed for low SLL.

A 6” Cassegrain reflector TX antenna and a tightly coupled Vivaldi RX array are designed as shown in the Fig. 6.9. The secondary dish is 2.1” and can accommodate a maximum of 12 x 12 dual polarized Vivaldi elements, which can theoretically achieve 19.6 dBi gain at 18 GHz, thereby, reducing the TX and RX gain difference to 4.85 dB. A comparison of the number of elements, array size, and gain is summarized in Table 6.2. A single polarized 8 x 8 tightly coupled Vivaldi array with a dual reflector in proposed STAR configuration is simulated in FEKO, for the proof of concept. Picture of the CAD models is shown in Fig. 6.9. System isolation >40 dB is achieved for LP, which could result in >60 dB for CP. Importantly, >10 dB improvement in isolation is achieved by exciting the elements with Tschebysheff distribution, which is primarily due to the reduction in the SLL, as depicted in Fig. 6.10. Note that 8 x 8 elements and single LP are selected due to the limitation of computational resources. Nonetheless, the studies presented herein indicates that the configuration has the potential to provide high system isolation, minimize TX and RX gain differences, and facilitate multiple beams (simultaneously) for the receiving/sensing applications.

The similar operation can also be achieved from a wideband QRH with ~100% AE as an RX antenna. Specifically, a 2” diameter aperture antenna can provide ~19 dBi, which reduces the TX and RX gain difference to 6 dB. Additionally, the system is simple for practical implementation. Hence, the design, fabrication and performance of the dual reflector STAR antenna system are explained in the following sections.

Table 6.2: Number of array elements vs directivity difference - Approach II

Number of Elements	Array Size (cm $\times$ cm)	Array Directivity (dB)	TX and RX Directivity Difference
8	3×3	16.1	8.37 dB
10	3.75×3.75	18.03	6.44 dB
12	4.5×4.5	19.61	4.85 dB
14	5.25×5.25	20.93	3.48 dB

6.4 System Design-Approach II

6.4.1 Feed Design

Dual polarized conical QRH with single mode operation from 18-45 GHz is used as the feed for the reflector. This antenna is selected because of its bandwidth, high power handling, no loss, and ability to attain symmetric E-and H-plane patterns [122] and greater AE [81]. The symmetry in radiation patterns is beneficial for achieving uniform illumination of sub-reflector and low cross-pol level in CP operation. First, the cross-section of the circular quad-ridge waveguide and the horn aperture are designed. The former is designed to provide modal purity over the frequency of interest, and the latter for required amplitude taper while maintaining the blockage smaller than that of the sub-reflector. The dimensions of the resulting geometries are shown in Fig. 6.11 (a) and (b). Furthermore, the taper of the ridges and the flare profile are chosen based on the parametric study, in HFSS, to achieve RL $\geq$10 dB, and patterns without the ripple and low SLL. The designed QRH has exponential tapered aperture and spline profile ridges (see Fig. 6.11 (c)). The antenna has gain >11 dB, $|S_{11}|$ <-10 dB, as shown in Fig. 6.12 and Fig. 6.13, respectively. Also, amplitude taper >10 dB for $\theta = \pm 32.8°$ and $\theta = \pm 28.8°$ from 24 and 28 GHz, respectively, as illustrated in Fig. 6.14. The QRH is fed using the turnstile junctions discussed in Chapter 2.

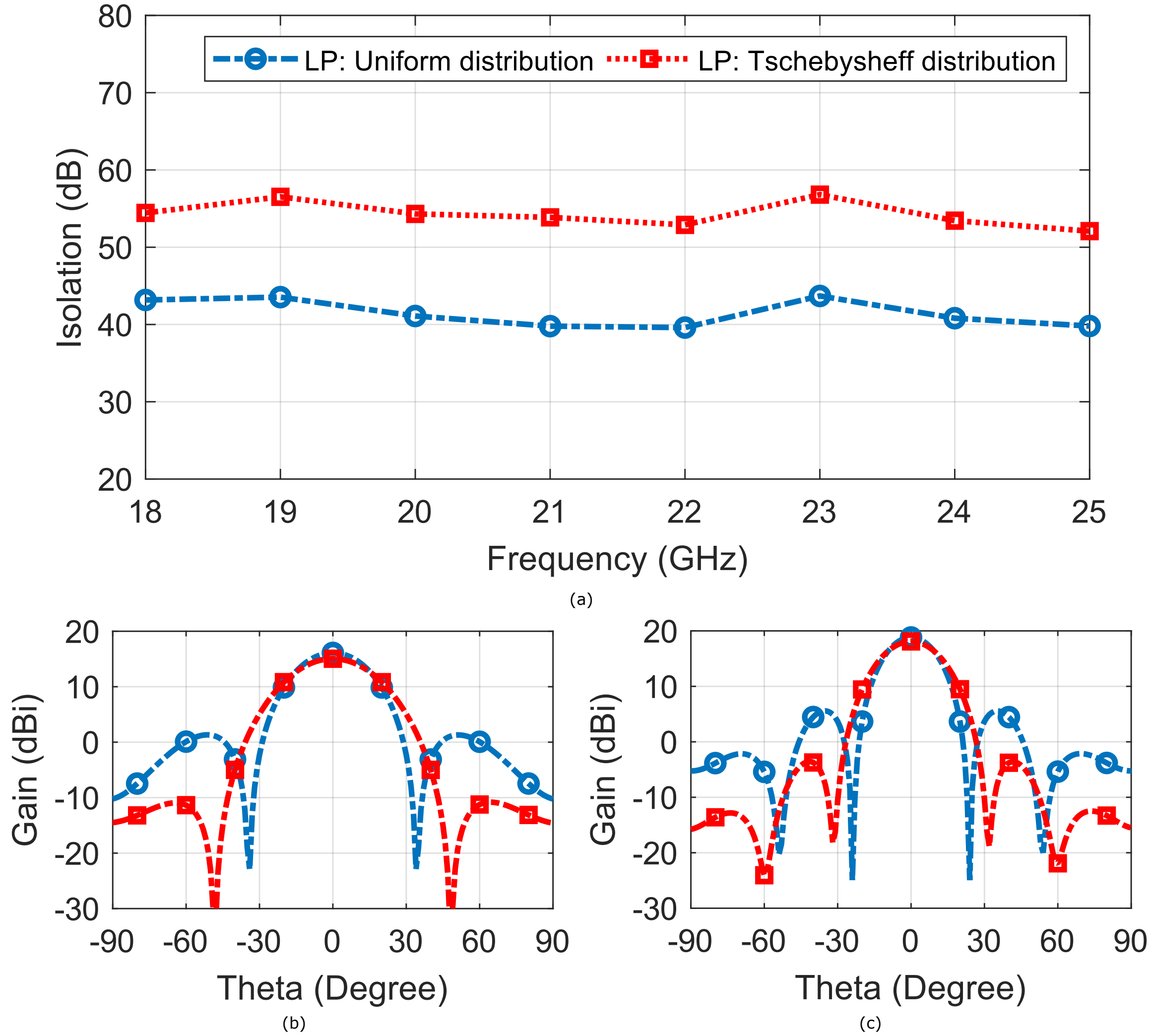

Figure 6.10: (a) Simulated isolation of dual reflector STAR with array, (b), and (c) radiation patterns of 8 x 8 Vivaldi array for uniform and Tschebysheff distribution at 18 GHz, and 25 GHz, respectively.

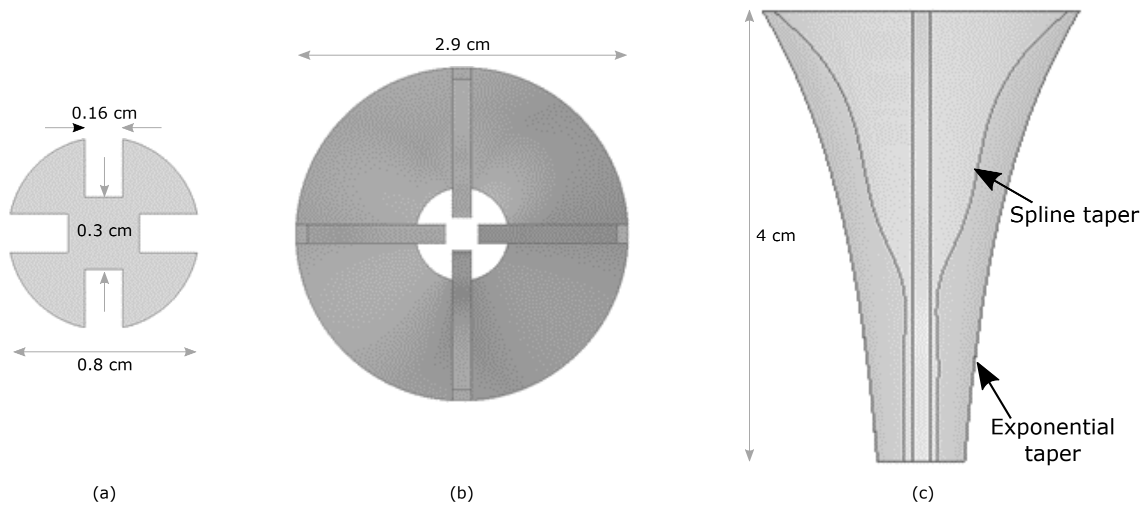

Figure 6.11: CAD model with dimensions of (a) quad ridge waveguide, (b) QRH aperture, and (c) QRH.

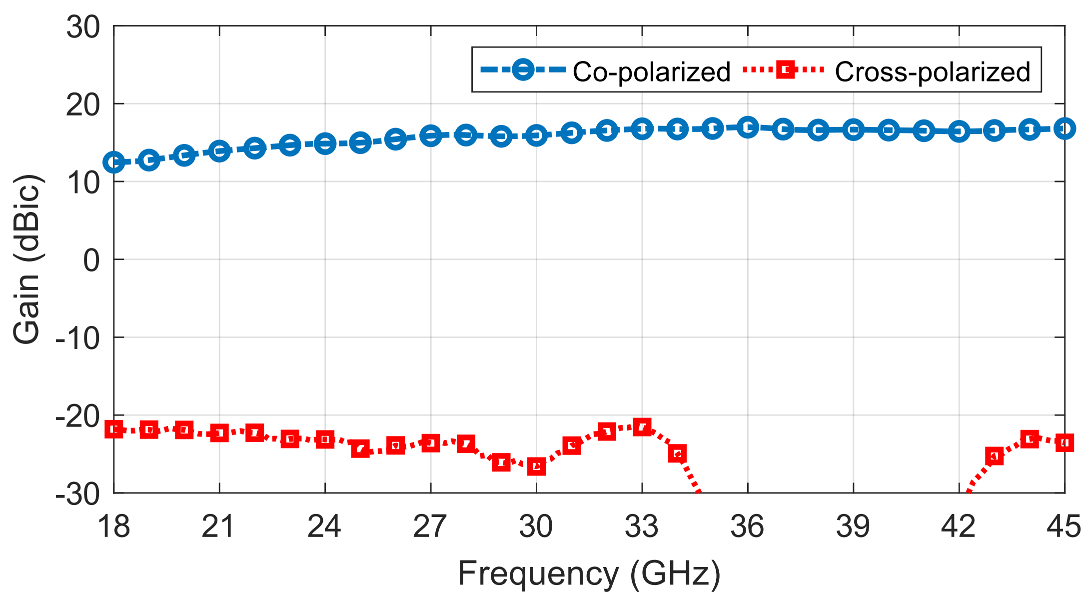

Figure 6.12: Simulated co-and cross-polarized gain of the TX feed.

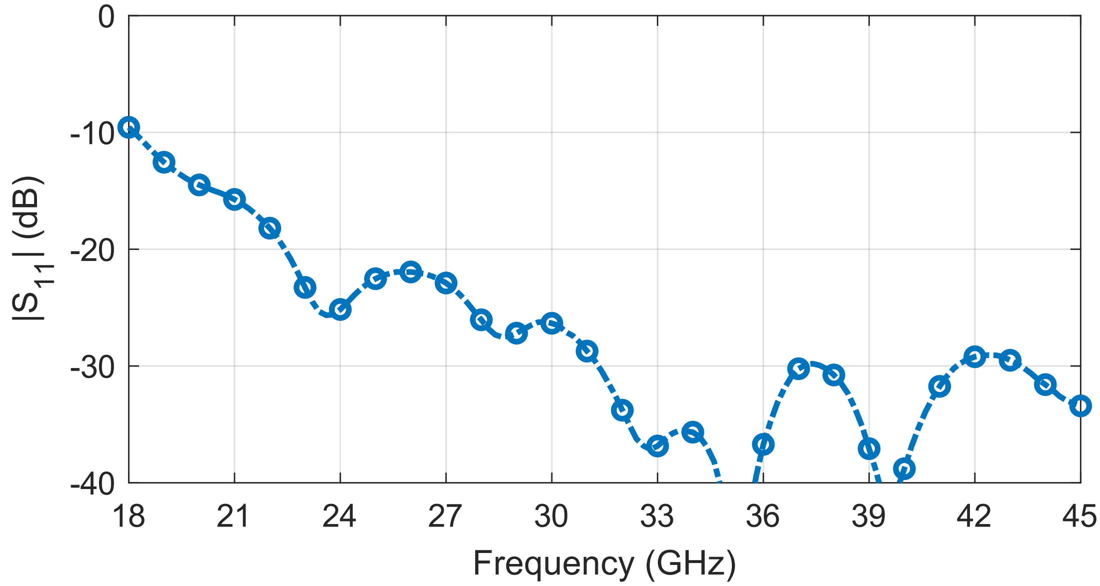

Figure 6.13: Simulated $|S_{11}|$ dB of the TX feed.

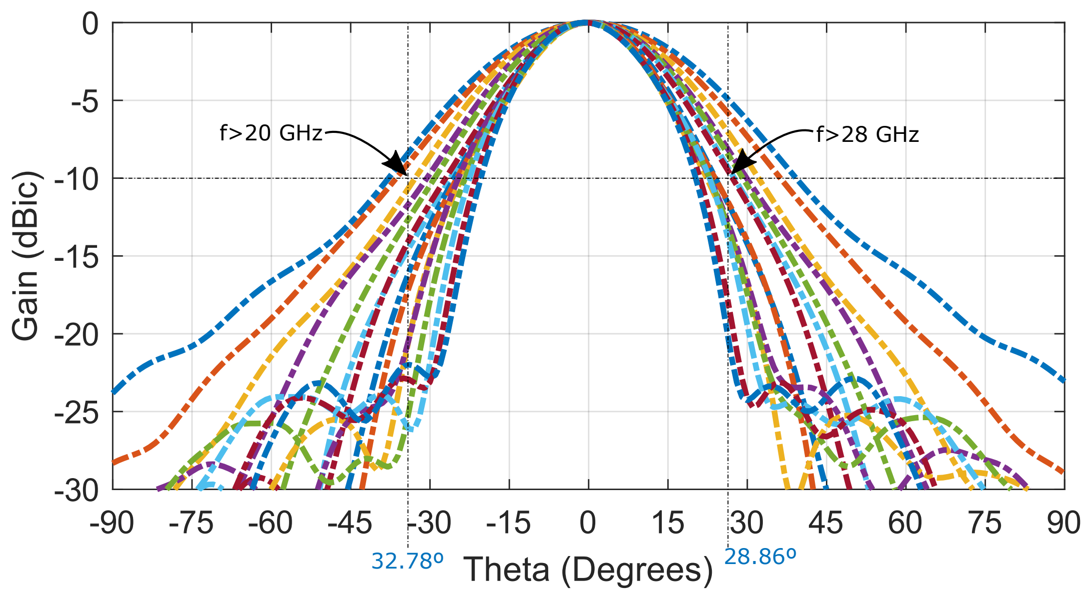

Figure 6.14: Normalized radiation patterns of the TX feed at $\phi = 0°$.

Table 6.3: Design parameters of dual reflector - Iteration I

Parameter	Value
D_M	6”
F/D_M	0.35
Focal Distance	2”
D_S	2.1”

6.4.2 TX Design

A 6” Cassegrain reflector operates as the TX of the proposed STAR system. The parameters of the antenna are given in Table 6.3. In this design, the ratio, D_M/D_S is 0.31 which results in blockage loss 2.45 dB, computed using (6.6) [120]. Therefore, the maximum attainable AE drops to 47.9%. Nonetheless, directivity >25 dBi, and SLL <12 dB is achieved when symmetric Gaussian beam is employed as the source, as shown in Fig. 6.15. These simulations are carried out in GRASP using GO and PO.

$$Blockage\ Loss = 20\,log\left(1 - \left[\frac{D_S}{D_M}\right]^2\right)(dB) \tag{6.6}$$

However, the realized gain deteriorates in comparison to the ideal case, when the designed QRH is employed as the feed, as demonstrated in Fig. 6.16. Importantly, large drops are observed at frequencies 23, 27, and 31 GHz (see Fig. 6.16). Similar behavior is noticed in the $|S_{11}|$ response of the feed, as highlighted in Fig. 6.17, which indicates the presence of standing waves. Through full-wave analysis, it is found that the primary reasons for this trend are the interaction between the main, sub-reflector and feed, and offset in the phase center (PC) of the QRH from the focus. This interaction creates multiple bounces of the radiated fields, which results in under illumination of the main reflector, as illustrated in the Fig. 6.18 currents plots. Also, the distance between the apex of the sub-reflector and the feed aperture, 3.6 cm, corresponds to the frequency of the standing wave.

These problems are minimized by accommodating three changes. First is aimed to minimize the

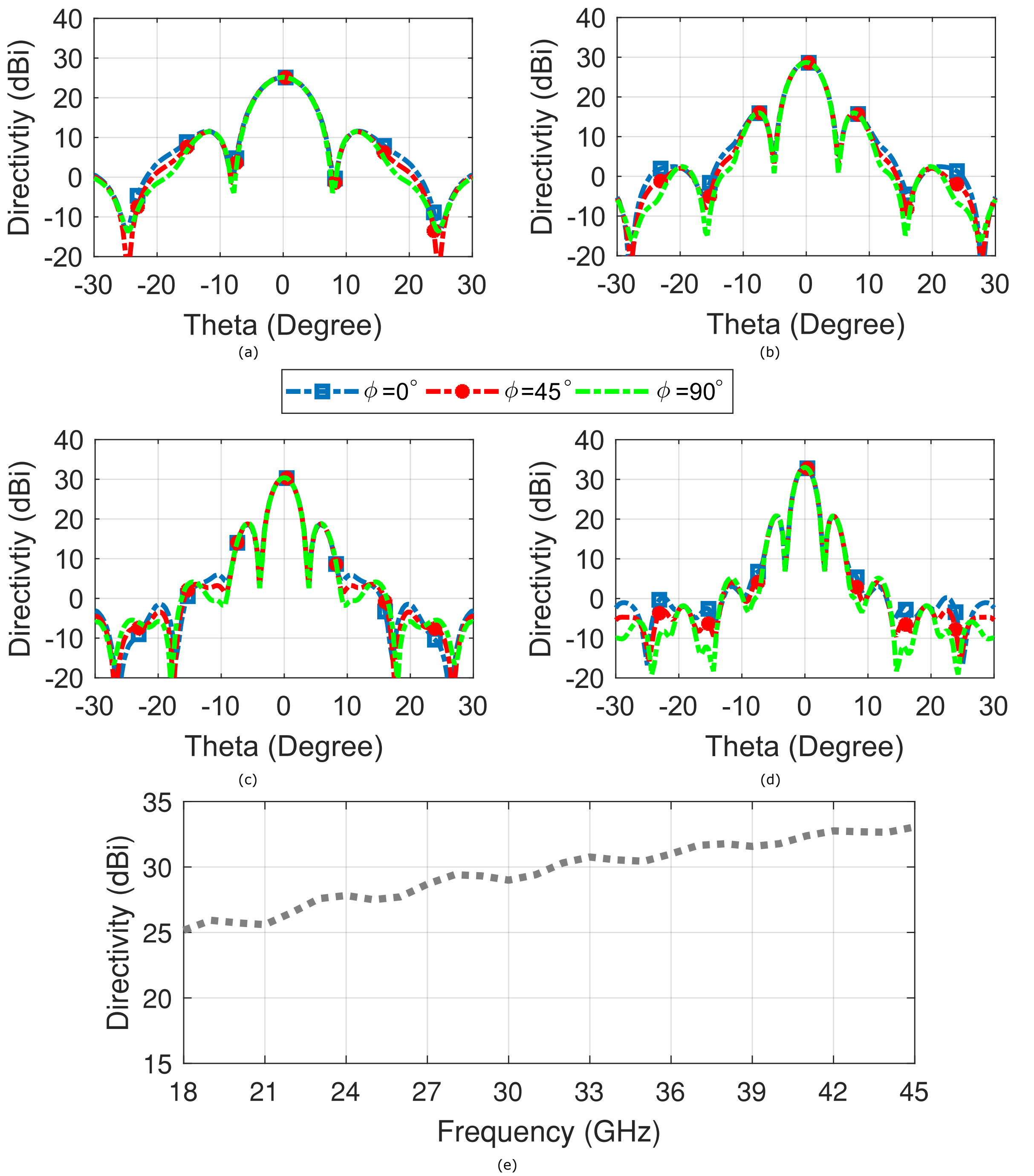

Figure 6.15: (a)-(d) Simulated radiation patterns of dual reflectors at 18, 27, 35, and 45 GHz, respectively, and (d) directivity

interaction. Increasing the F/D$_M$ of the reflector will lead to higher focal length (Table 6.4), which translates to the larger space between the secondary dish and the feed. Hence, the new F/D$_M$ is set to 0.5 corresponding

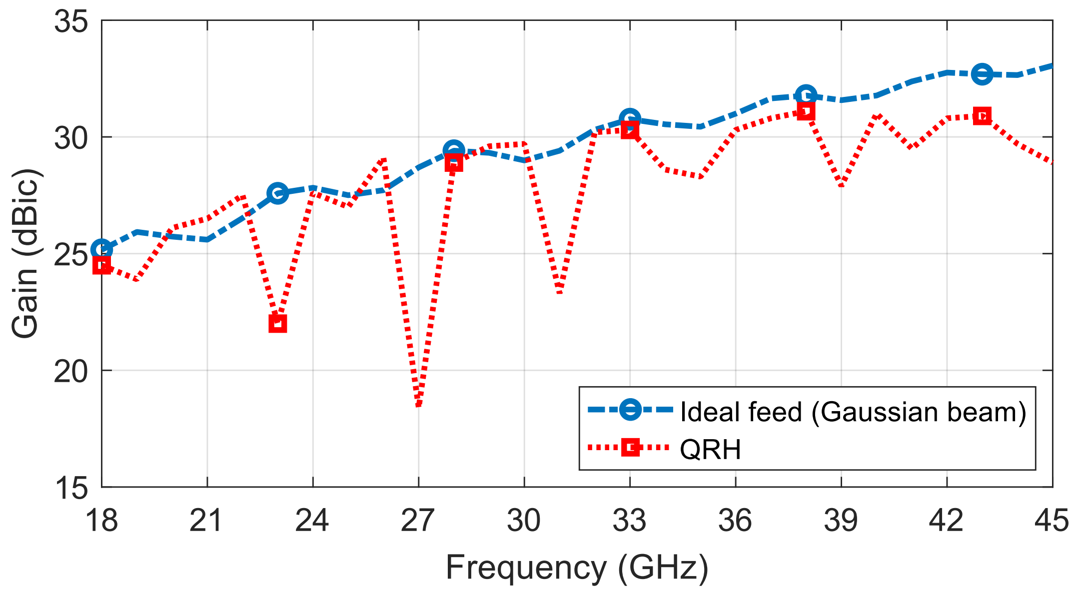

Figure 6.16: Simulated gain of the dual reflector symmetric with Gaussian beam and QRH.

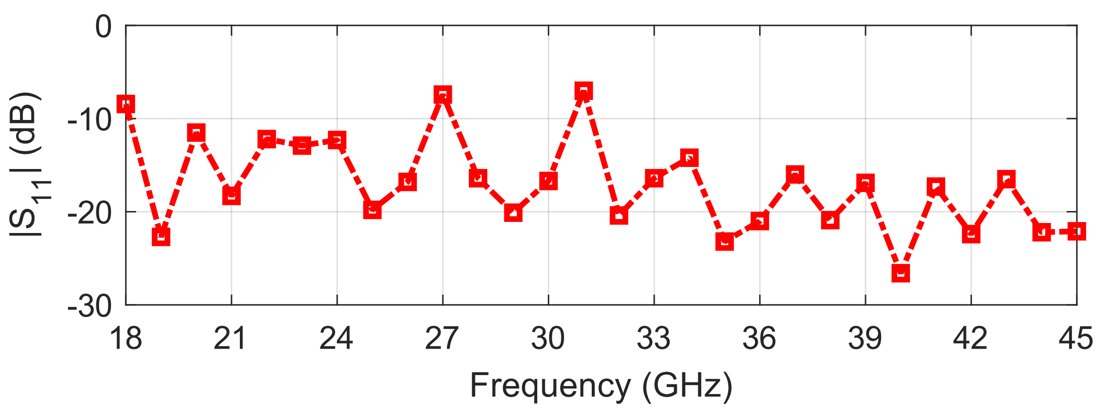

Figure 6.17: Simulated $|S_{11}|$ of QRH with dual reflector.

to 5.6 cm between the apex of primary and sub-reflector (see Fig. 6.19). Note that F/D$_M$ is limited to 0.5 to maintain the subtended angle relatively high such that the feed can satisfy 10 dB amplitude taper over a significant portion of operating frequencies.

Second, the shape of the sub-reflector is modified from its regular hyperbola to vary the phase of the reflected fields [123, 124], thus, improving main dish illumination, as demonstrated in Fig. 6.20. These simulations are performed in FEKO. Finally, the feed position is altered to compensate for the change in PC. The PC variation is higher due to the flaring and the aperture size of the horn. Hence, it is cumbersome to

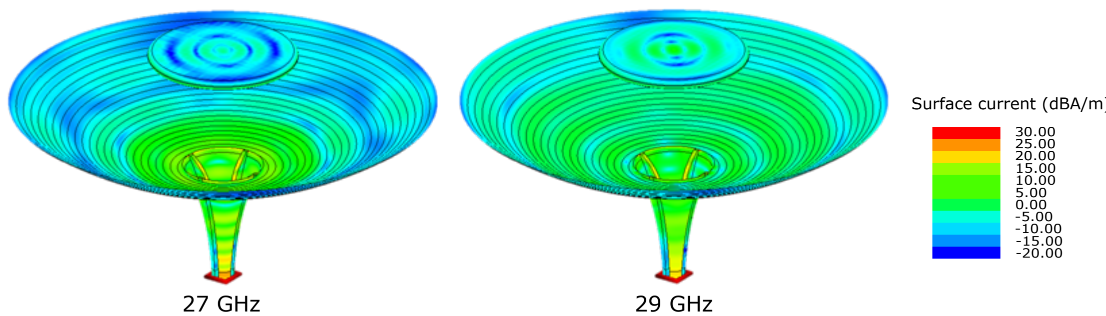

Figure 6.18: Simulated surface current distribution of the dual reflector at 27 GHz, and 29 GHz.

Table 6.4: Design parameters of dual reflector - Iteration II

Parameter	Value
D_M	6"
F/D_M	0.5
Focal Distance	2.9"
D_S	1.89"

compensate over 2.5:1 frequency bandwidth by adjusting the antenna position. Nonetheless, a significant reduction in the ripples has been observed post modifications, as shown in Fig. 6.21. Further, the impedance match of the feed also reciprocates the similar trend (see Fig. 6.22). The radiation patterns of the TX are shown in Fig. 6.23 where the antenna has SLL less than 10 dB, cross-pol level <-30 dB. The dimensions of the final design are listed in Table 6.4.

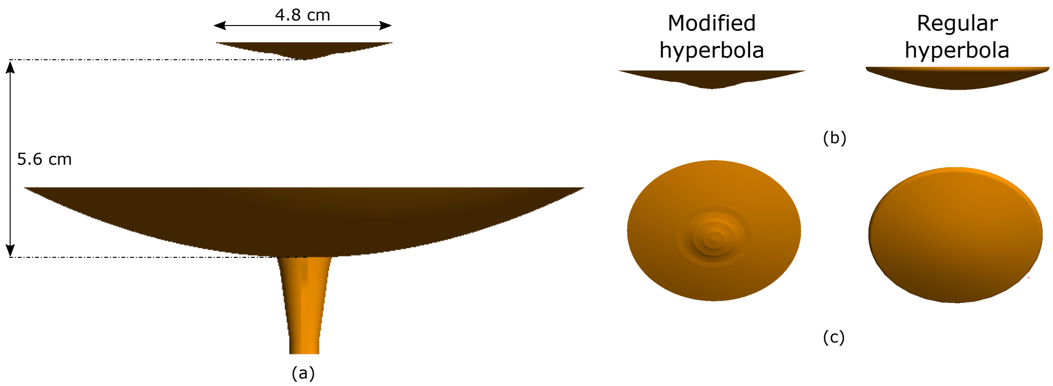

Figure 6.19: CAD models of (a) dual reflector, (b) and (c) side view bottom view of modified and regular sub-reflector, respectively.

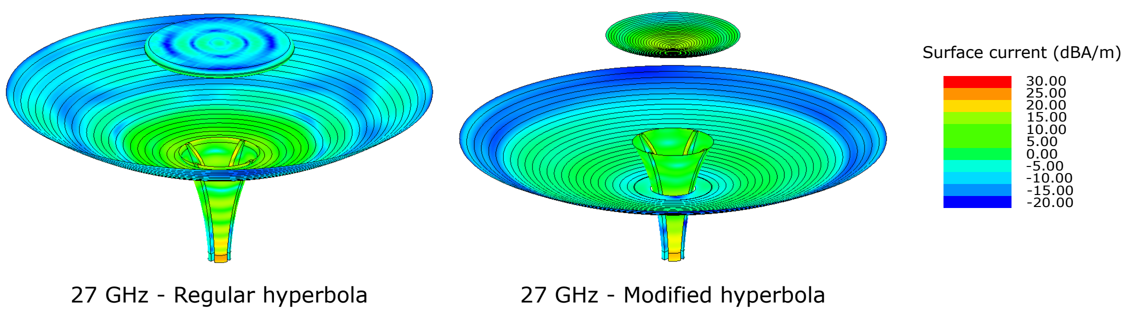

Figure 6.20: Simulated surface current distribution of the dual reflector with modified and regular hyperbola at 27 GHz.

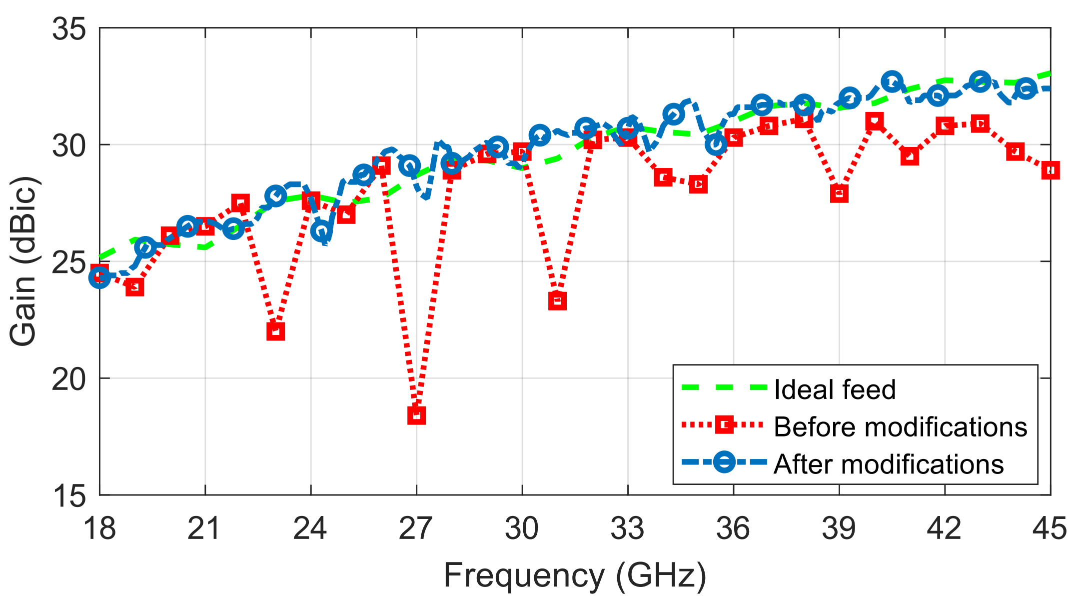

Figure 6.21: Simulated gain of the dual reflector with ideal feed, modified and regular hyperbola fed by QRH.

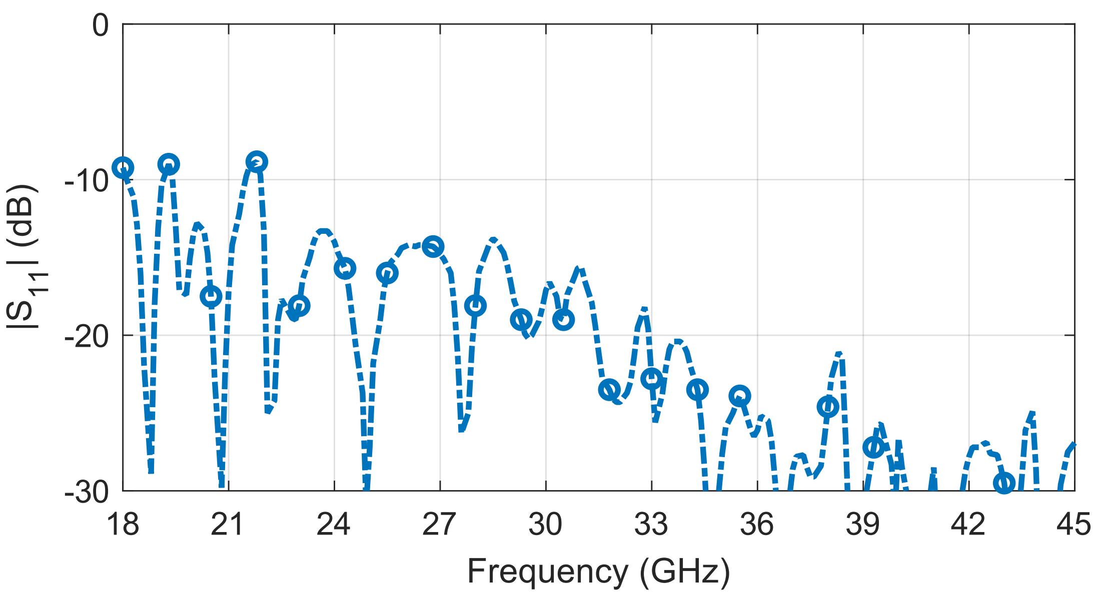

Figure 6.22: Simulated $|S_{11}|$ of QRH with modified dual reflector.

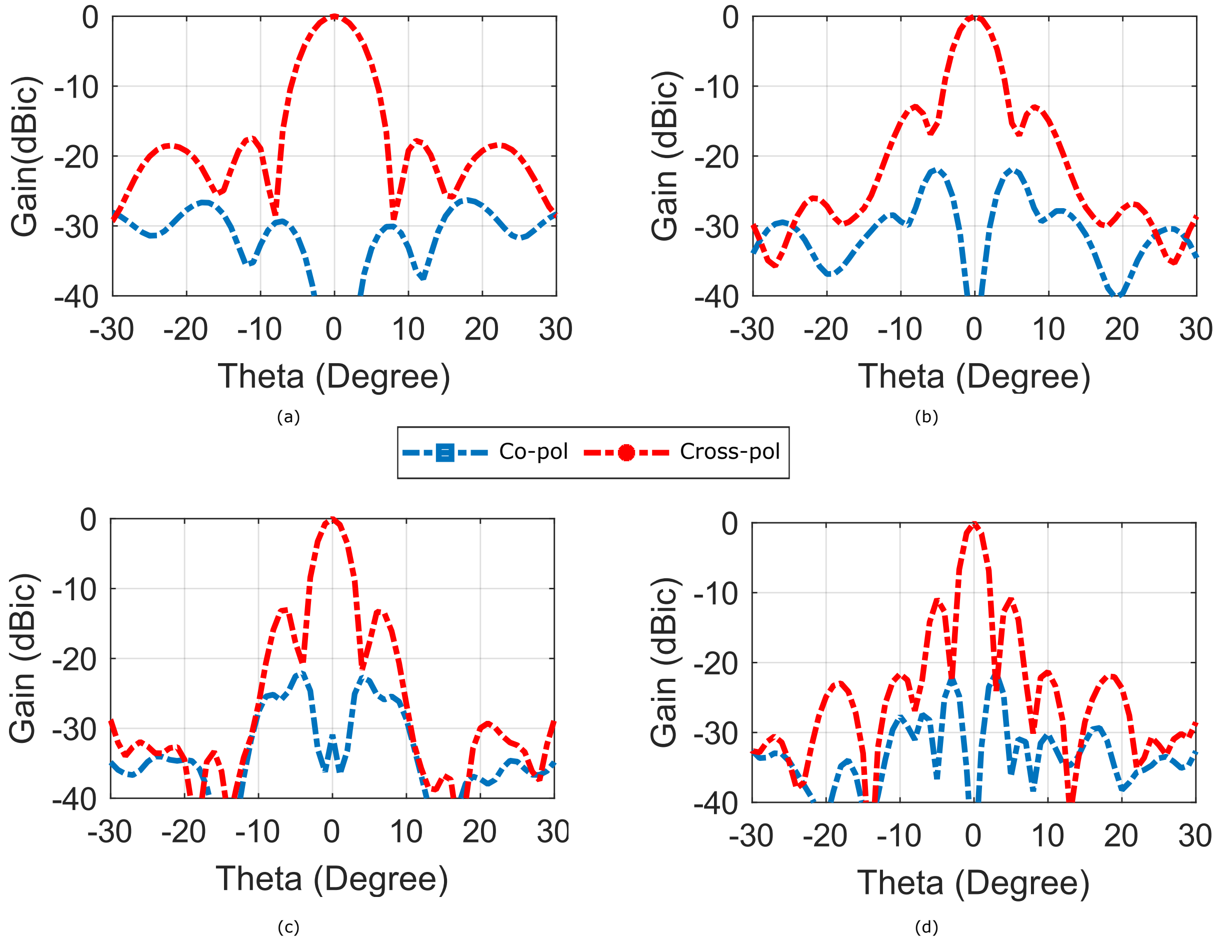

Figure 6.23: Simulated co- and cross-pol of the dual reflector with modified hyperbola fed by QRH at $\phi = 0°$ (a) 18 GHz, (b) 27 GHz, (c) 35 GHz, and (d) 45 GHz.

6.4.3 RX Design

The receiving QRH is designed to meet two goals. First, to minimize the TX and RX gain difference. Second, to contain the profile of the RX antenna within the sub-reflector size while keeping low height. The circular quad ridge waveguide designed in previous section is employed to excite the RX. Further, the aperture diameter is selected as 3.5 cm to cover the maximum available area behind the sub-reflector. The profile of the fare and ridges are modified to low $|S_{11}|$and SLL. The resulting antenna has an exponential taper for aperture and asymmetric sine taper for the rides, as shown in the Fig. 6.24. The QRH has $|S_{11}|$ <-20 dB, gain 15±1.2 dB over the operational band shown in the Fig. 6.25, and Fig. 6.26, respectively. Thus, the difference in TX and RX gain is 10 dB, at 18 GHz, which is satisfactory. However, the margin increases to 18 dB at 45 GHz (see Fig. 6.26), mainly due to the reduction in AE of the horn. Hence, the antenna gain needs to be improved.

The wide aperture ($5.25\lambda_{45\,GHz}$) and the flare angle are the causes for deterioration in the AE. Loading the horn aperture with a dielectric (ϵ >1) will cause the incident fields to refract and in collimating the beam, thereby, increase the directivity [90]. These antennas are referred to as lens corrected horns [90], which are implemented using various ways. Specifically, four types are mentioned in [90], where shape and permittivity

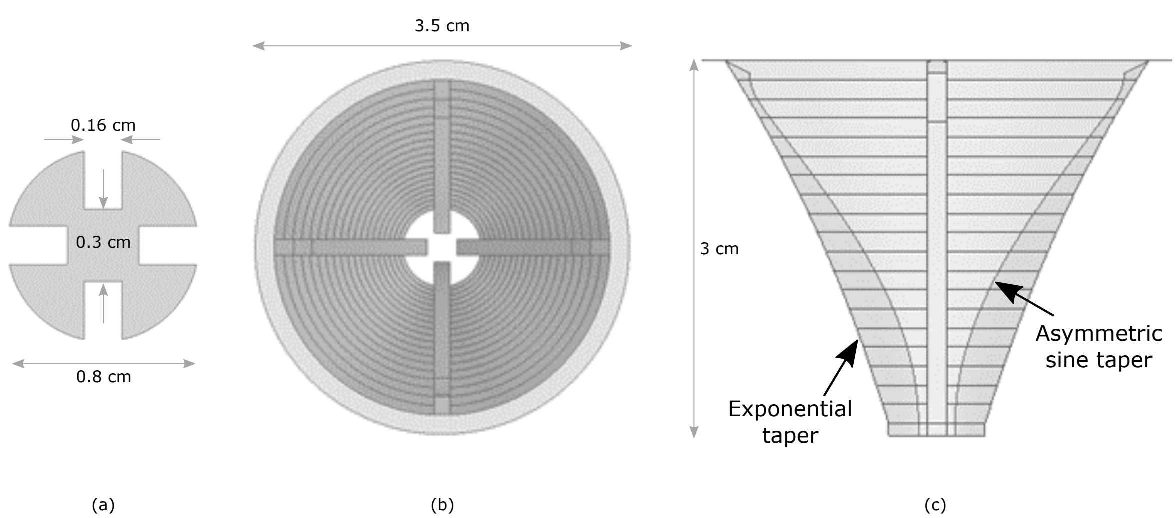

Figure 6.24: CAD model with dimensions of (a) quad ridge waveguide, (b) RX QRH aperture, and (c) RX QRH.

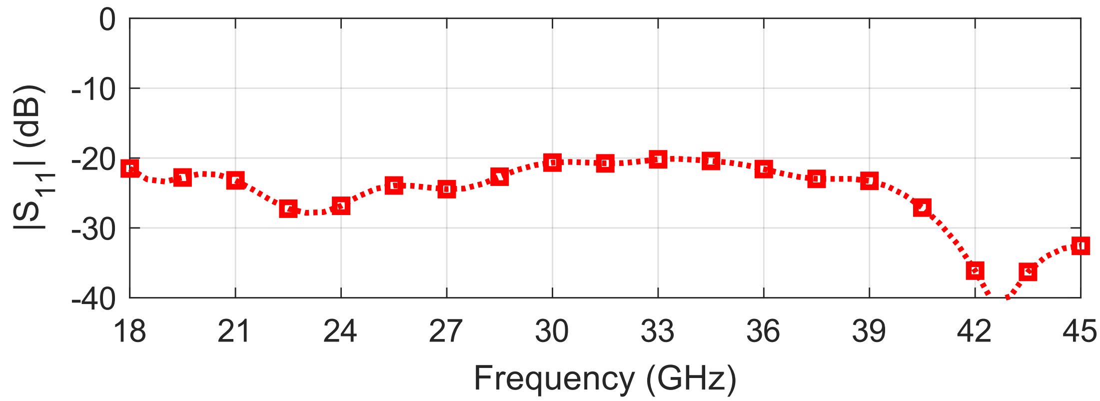

Figure 6.25: Simulated $|S_{11}|$ of the RX QRH without lens.

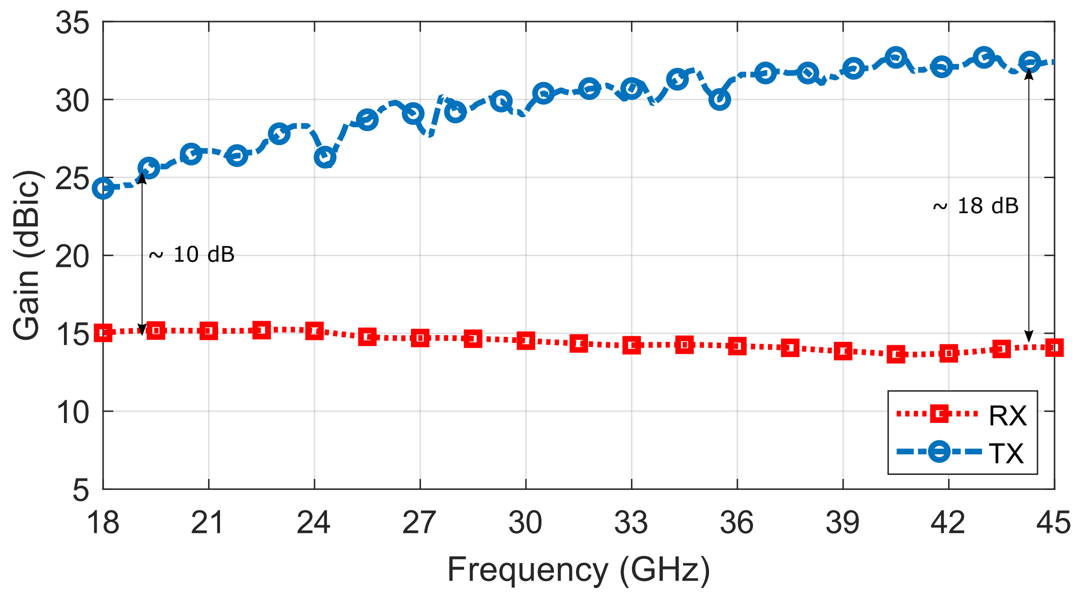

Figure 6.26: Simulated gain of the RX without lens and TX (dual reflector).

of the dielectric play the critical role.

Type 3 lens or dual surface lens is one of the commonly used approaches, because of the easy integration with a horn. In these lens types, the fields undergo refraction at two faces as shown in Fig. 6.27. The design equations are given by (6.7)-(6.10) [90]. Hence, the permittivity of the lens is a design trade-off, that is, higher the permittivity greater will be the mismatch between the waves inside the horn and the free space. Therefore, a lens of diameter 3.5 cm (same as the aperture) and height 1.14 cm, made of Teflon with $\epsilon_r = 2.1$ is designed in this research. Importantly, the gain of the resulting lens corrected horn has an increase

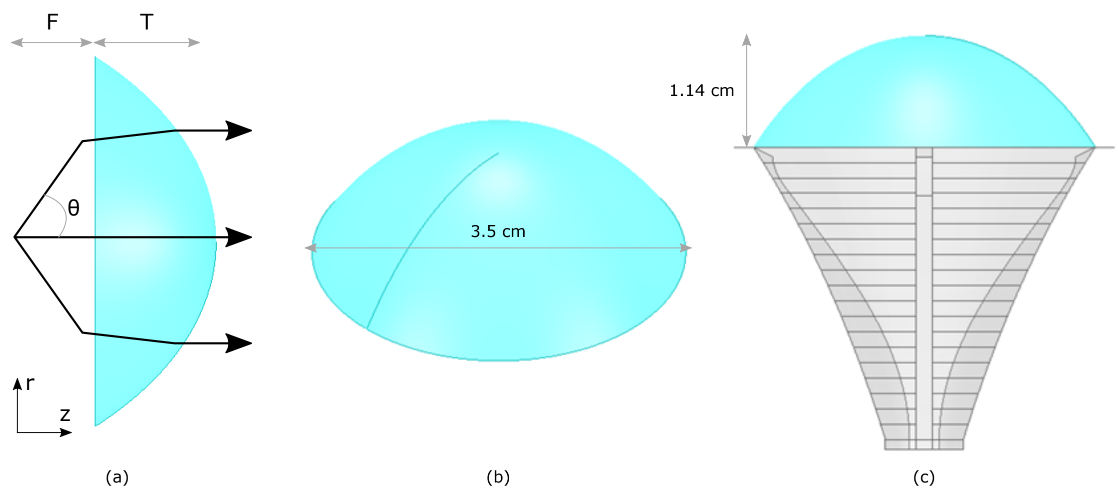

Figure 6.27: CAD models of (a) and (b) dual surface lens with dimensions, and (c) RX QRH with lens.

from 15 dB to 24 dB, at 45 GHz, which reduces the maximum difference between the TX and RX gain to 9.69 dB as shown in Fig. 6.28. Further, the horn is excited using turnstile junction fed by coaxial probes (shown in inset of Fig. 6.29) and the antenna has $|S_{11}| < 10$ dB over the operational band (see Fig. 6.29). Also, the radiation patterns of the RX are shown in Fig. 6.30.

$$r = \frac{F + (n-1)T + (n^2-1)Fsec\theta - FStan\theta}{\left(\dfrac{n^2}{sin\theta} - S\right)} \tag{6.7}$$

$$z = (r - Ftan\theta)S \tag{6.8}$$

$$S = \left[\left(\frac{n}{sin\theta}\right)^2 - 1\right]^{1/2} \tag{6.9}$$

$$\frac{T}{D} = \left[\left\{1 + \frac{1}{(2F/D)^2}\right\}^{1/2} - 1\right]\frac{F/D}{n-1} \tag{6.10}$$

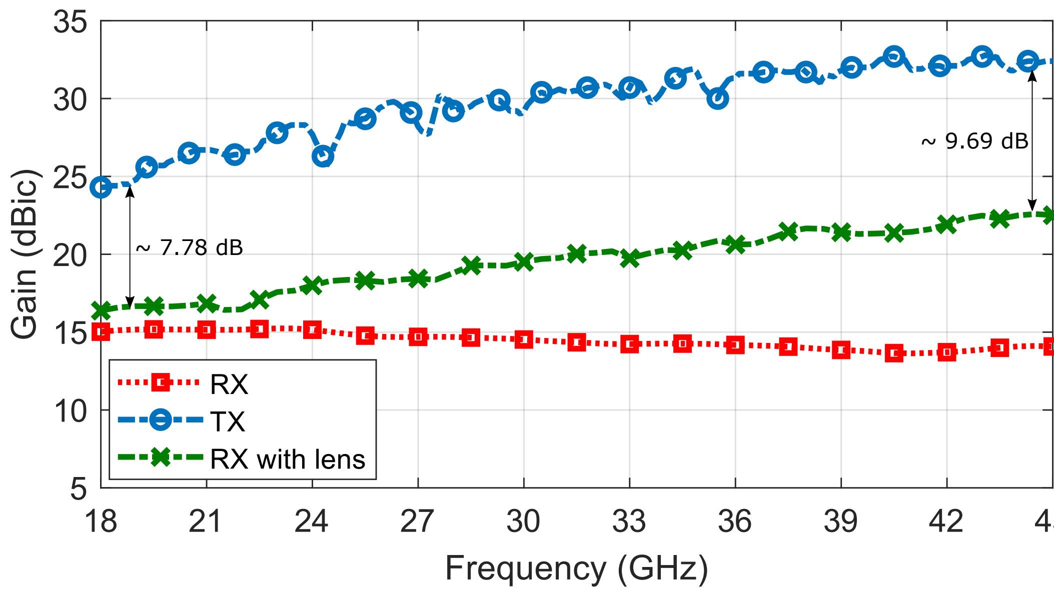

Figure 6.28: Simulated gain of the TX, RX with and without lens.

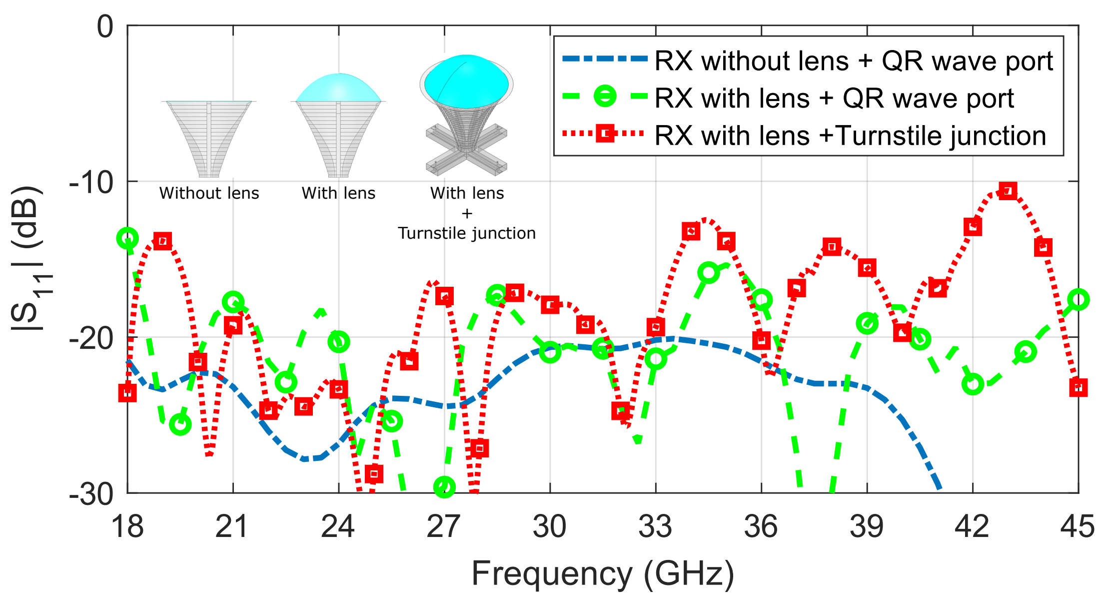

Figure 6.29: Simulated $|S_{11}|$ of the RX QRH without and with lens, and fed turnstile junction. CAD models are shown in the inset.

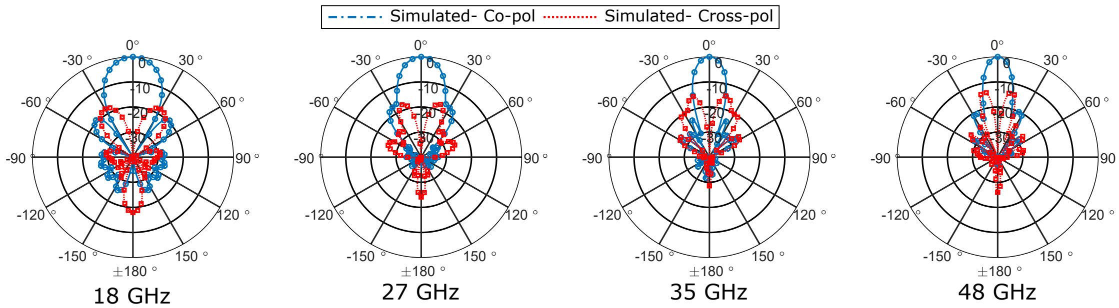

Figure 6.30: Simulated Co-and cross-pol radiation patterns of RX with lens.

6.5 System Isolation

The coupling between the TX and RX is mainly through the back-lobe of the receiving antenna and the cross-pol of the TX feed, also, due to the scattering and spillover from the sub-reflector, as discussed in Section 6.3.2. The system isolation is >40 dB for LP which is governed by the inherent power coupling between the antennas. Furthermore, the isolation >80 dB is achieved when the TX and RX are CP, as illustrated in Fig. 6.31. This increase in isolation is due to the additional cancellation provided by the BFN, and the higher F/B of the antennas. Also, the presence of struts has negligible influence on the system isolation because of the geometrical symmetry in the structure (see Fig. 6.31).

The configuration employs COTS 90° hybrids for realizing CP, and these components will have imbalances in amplitude and phase [104, 105], which can influence system isolation as demonstrated previously in Chapter 4 and 5. Hence, frequency independent asymmetry of ±6° in phase and ±0.5 dB in amplitude is introduced in circuit simulator (AWR Microwave office [109]) to analyze the impact on isolation. This imbalance deteriorates the attainable signal cancellation by 40 dB as illustrated in Fig. 6.32. However, the isolation is 30 dB higher than that obtained in Chapter 4, which brings out the robustness of the configuration towards electrical asymmetries. Similarly, the isolation remains >60 dB when mechanical offset is incorporated into the structure, as shown in Fig. 6.33. The picture of the prototype antenna and the measured isolation is illustrated in Fig. 6.34. The reflector and the QRHs are fabricated using CNC machining. The system has 63 dB (average) measured isolation with COTs 90° hybrids and 0.086” coaxial cables. Note that

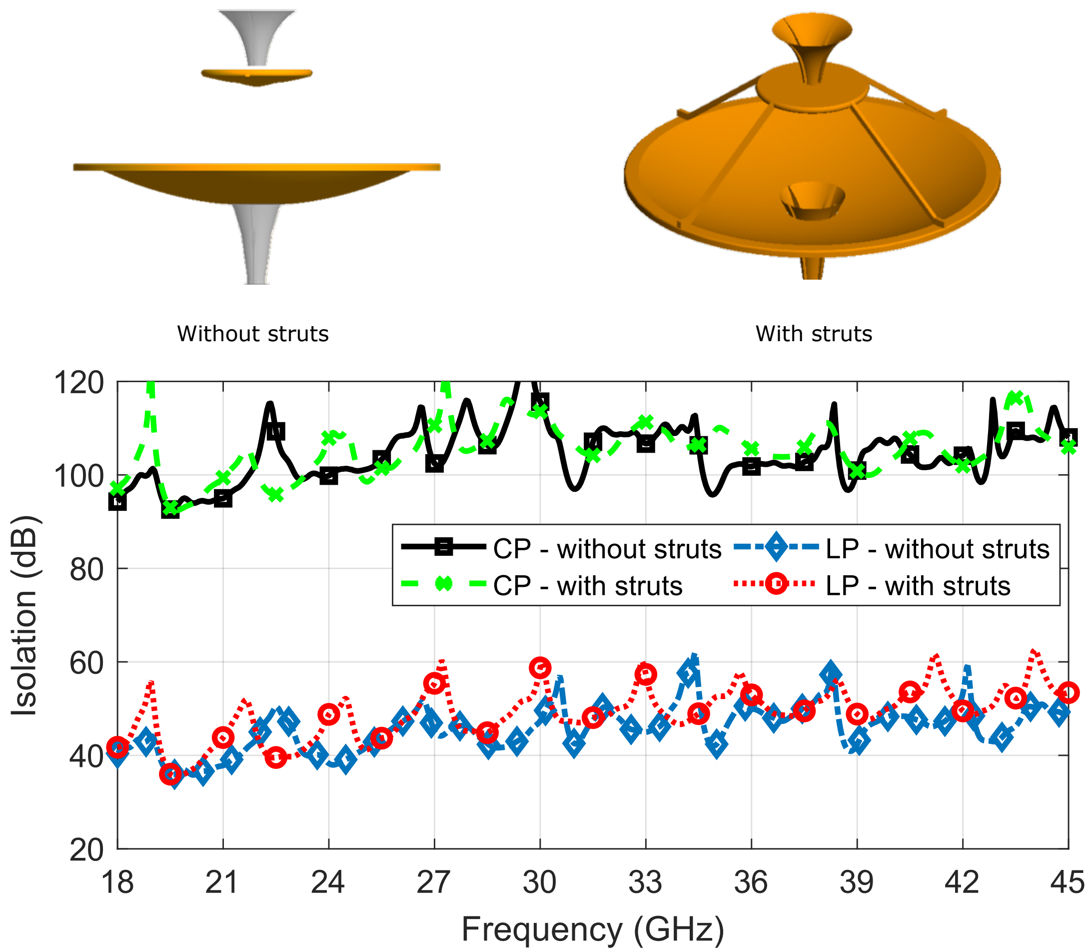

Figure 6.31: Simulated (in CST) isolation of the system without and with the metallic struts.

rectangular double ridge (WRD1845) to circular quad ridge transitions are used to feed the antennas, and the measured S-parameters of the QRHs with cables and hybrids are combined in a circuit simulator to obtain CP isolation.

Furthermore, recessing the RX antenna inside the absorber cavity will result in lower SLL, as well as reduce the back-lobe level. Thereby, reducing the mutual coupling between the TX feed and the RX. Hence, the system will have higher tolerances towards the imbalances, that is, 10 dB higher isolation than the base case, as illustrated in Fig. 6.35.

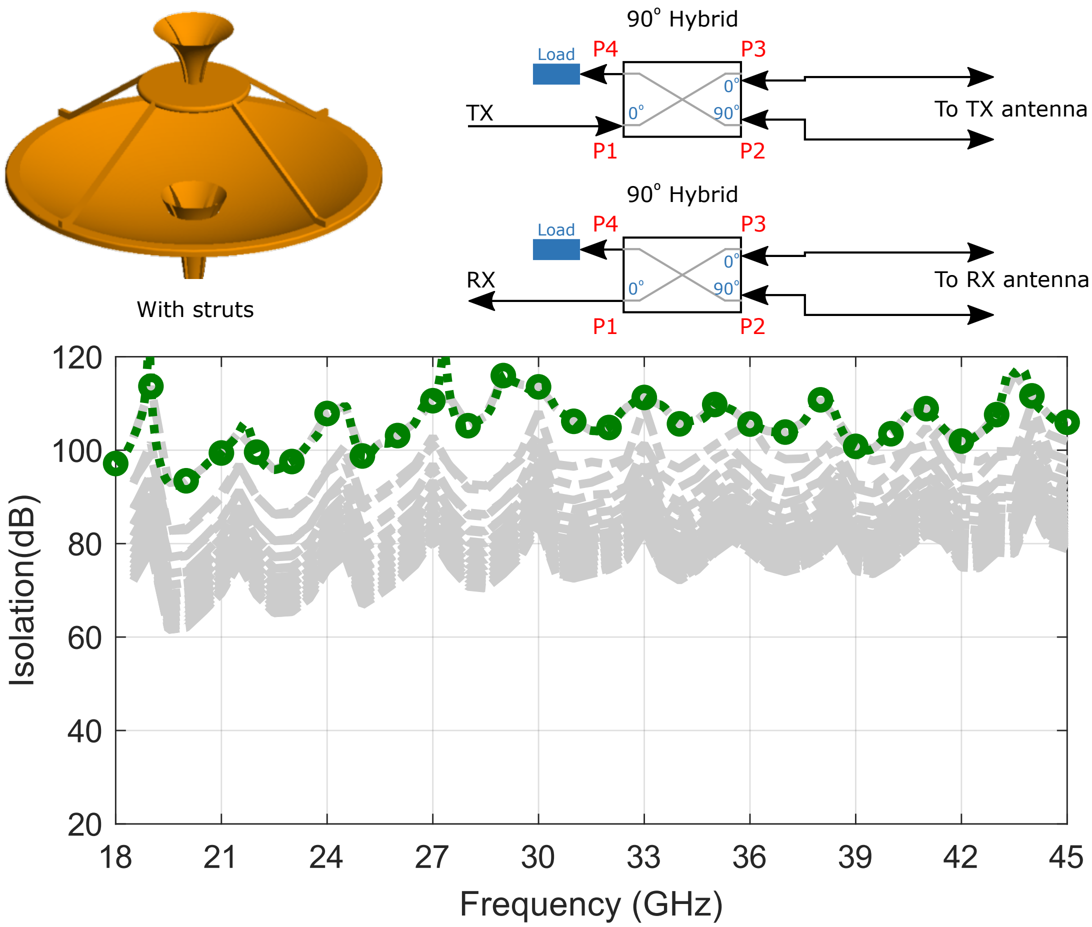

Figure 6.32: Simulated (in CST) isolation of the system with frequency independent electrical imbalances ±6° in phase, and ±0.5 dB in amplitude.

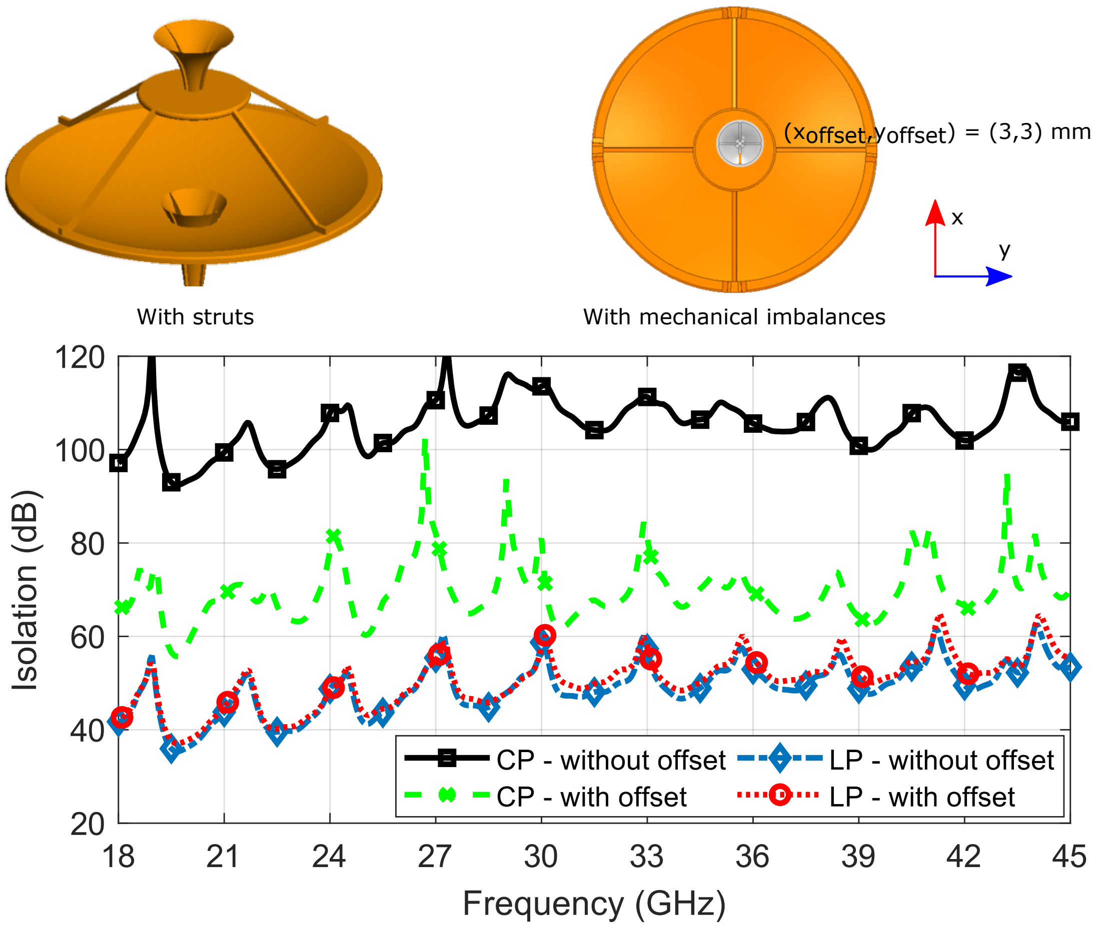

Figure 6.33: Simulated (in CST) isolation of the system with mechanical asymmetries.

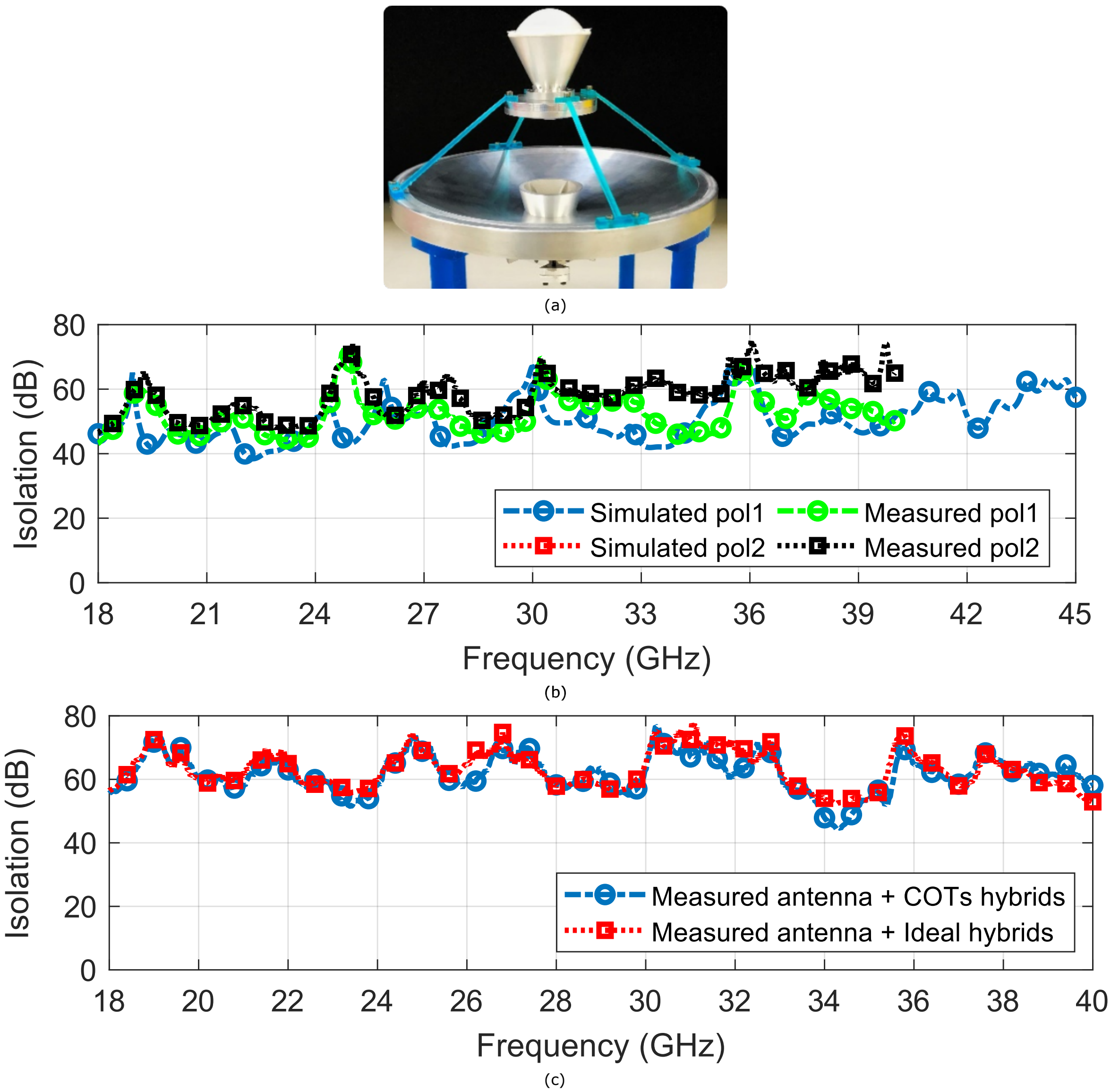

Figure 6.34: (a) Picture of dual reflector prototype, (b) simulated and measured isolation for LP, and (c) measured system isolation with ideal and COTs hybrids.

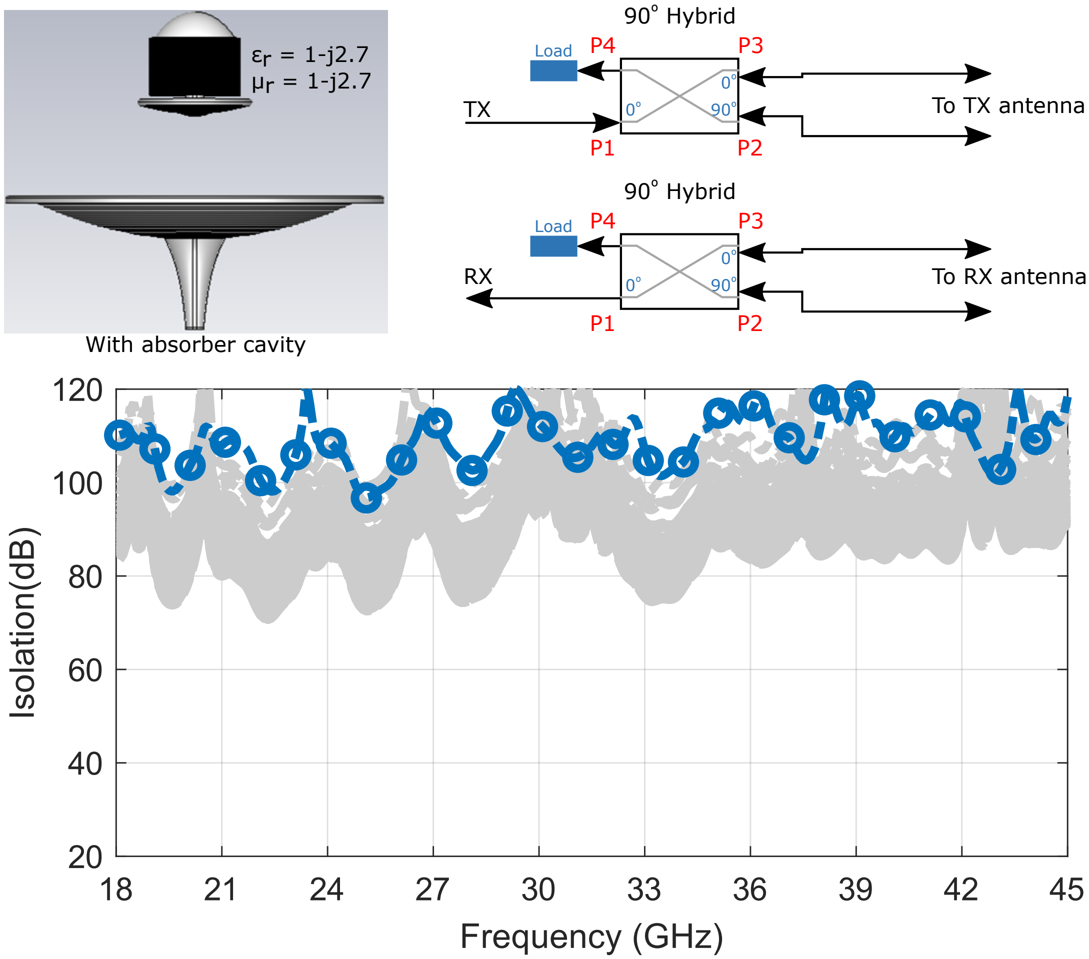

Figure 6.35: Simulated (in CST) isolation of the system with frequency independent electrical imbalances ±6° in phase, and ±0.5 dB in amplitude, when the RX is recessed inside the absorber cavity.

6.6 Summary

The chapter outlines the importance and advantageous of implementing a STAR system in mm-Wave, and the associated challenges from the isolation and fabrication perspective. Importantly, a new dual reflector antenna based in-band full-duplex configuration is proposed. The approach relies on inherent low coupling between the TX feed and the RX to achieve high isolation. Moreover, the antennas are operated in CP to reduce the SI. Also, the steps of designing a conventional Cassegrain reflector are summarized. Specifically, the impact of reducing the main dish diameter and D_M/D_S ratio on the far field are discussed in detail. Further, three ways of realizing a STAR system consisting of 12” and 6” dual reflector in conjunction with prime feed reflector, tightly coupled array and high gain QRH are outlined, along with the pros and cons of each approach. An in-band full-duplex 6” Cassegrain reflector system is implemented which has a gain >24 dB and >16 dB for the TX, and the RX, respectively. The chapter discusses the effect of interaction between the sub-reflector and the TX feed on the far field and the measures to minimize this influence. Additionally, a lens corrected QRH in designed to improve the AE of RX, thus, reducing the difference in TX and RX gains. The system has isolation >60 dB for CP and >40 dB for LP, which can be potentially improved by 10 dB as demonstrated.

Chapter 7

Conclusion and Future Work

7.1 Conclusion

Theory, design and practical realization of wideband STAR antenna systems are researched in this thesis The wideband dual polarized antenna is first developed and described in Chapter 2. Chapters 3 and 4 describe two in-band full-duplex configurations and the techniques to improve their performance. Chapters 5 and 6 propose a new approach, called quasi-monostatic STAR, which addresses some of the limitations of bi-static and monostatic architectures. The antenna systems operating over frequencies from 4 GHz to 45 GHz are developed in this research, which includes small apertures to the multiple wavelength wide reflectors. Hence, this thesis explores the challenges, advantages, and solutions to various STAR antenna configurations.

The design of wideband quad ridge horn (QRH) antenna, which can handle high power and can be flush mounted with the platform is described first. Despite extensive research on QRHs, the existing feeding techniques, in open literature, are either limited in power handling or relative operational bandwidth, as discussed. To address this, the focus is on the design of 3:1 impedance bandwidth (VSWR <2) antenna fed by double ridge waveguide based OMT. This task is accomplished in two steps. First, the aperture is designed to achieve $|S_{11}|$ <-20 dB over the operational frequencies, by modifying the ridge profile and using aperture matching technique. Further, the OMT consisting of turnstile junction and waveguide bends are developed to support the desired impedance match requirement. The fabricated antenna has VSWR <2, and gain >7 dBi with worst SLL of -15 dB over 6-19 GHz, as demonstrated. In doing so, the antenna retains a small footprint, that is, the aperture size of $3.3 \times 3.3\,\text{cm}^2$ corresponding into ($0.66\lambda \times 0.66\lambda$). Additionally, a QRH operating over 18-45 GHz is developed using a similar design analogy, while accounting for the small dimensions and the fabrication tolerances. The antenna is fed through a turnstile junction based OMT, and it is compatible with the modified WRD1845 double ridge waveguide.

The QRHs designed in Chapter 2 are used to implement a bi-static STAR antenna system. These are also employed to cover two sub-bands of in-band full-duplex systems operating from 0.5-45 GHz and 0.5-110 GHz. Understanding the underlying physics of power coupling between the co-located TX and RX is one of the primary goals of the thesis. Hence, in Chapter 3 this is carried out methodologically by first examining a single and dual polarized system mounted on a ground plane. Further, the area between the antennas is treated with HISs to minimize the coupling due to the surface currents/waves. Specifically, three types of reactive surfaces are analyzed, namely, metallic corrugations, bed of nails, and PRS. These HISs are compared against each other in terms of bandwidth, ease of fabrication, cost, size, and weight. Importantly, it is demonstrated that a PRS can reduce the TM0 surface waves propagation over 3:1 bandwidth by providing capacitive reactance. The realized bi-static STAR antenna subsystem with embedded PRS has measured isolation >60 dB over 6-19 GHz for antennas separated edge-to-edge by 20 cm ($4\lambda_{6GHz}$). Additionally, the influence of scatterers and the neighboring antennas on system isolation is discussed.

A bi-static configuration involves two independent antennas placed wavelengths apart to achieve STAR functionality. Hence, it occupies a significant area of the host platform where high gain and isolation is desired, especially at low frequencies. Contrarily, a monostatic approach supports STAR features from a single aperture. Therefore, this approach is preferred for a high gain reflector based in-band full-duplex antenna system, as discussed. A BFN consisting circulators, 90°, and 180° hybrids and a CP antenna are employed to realize a monostatic configuration. High isolation between the TX and RX is achieved by careful rerouting of the coupled/leaked signals through the BFN. A coaxial cavity antenna operating from 4-8 GHz with symmetric radiation patterns, AR <3 dB for $\theta = \pm 30°$, and phase center variation <5% and <15% for CP and LP, respectively is designed as the feed for the axis-symmetric parabolic reflector. Despite the excellent far field performance, the coaxial cavity antennas discussed in the literature have a poor impedance match, which is a limiting factor for high power applications. Hence, this is improved by modifying the shape of exciting probes as discussed. Thus, the antenna has VSWR <2 over an octave of bandwidth. Further, the inner conductor of the feed is used as the support, thereby, eliminating complex struts and minimizing the resulting reflector blockage. It is demonstrated that theoretically high isolation can be achieved with ideal BFN. However, the achievable isolation drops due to the amplitude and phase imbalances in COTS components. Nonetheless, it is demonstrated that SI <30 dB can be obtained between the TX and RX. Also, it is shown that the presence of reflector has a negligible influence on the system isolation. Additionally, the influence of the dish's surface roughness on SI cancellation is studied. The designed reflector antenna has symmetric radiation patterns, with gain >20 dBic, axial ratio <1 dB, and $|S_{11}|$ <-10 dB over the operating bandwidth.

After the analysis of bi-static and monostatic STAR, a new approach called quasi-monostatic is proposed, which minimizes certain limitation of both configurations. The system consists of a center fed axis symmetric parabolic reflector for TX operation and a coaxial cavity antenna mounted above the feed for RX. The presence of the RX within the volume occupied by the TX helps reduce the system's physical size, analogous to a monostatic case. Further, in a baseline operational concept, both TX feed and the RX antenna are circularly polarized. That is, (to achieve true-co-pol STAR) the former is left-hand CP (LHCP) whereas the latter is RHCP. The physical orientation of the antennas and the presence of the metallic reflector leads to the same polarization operation for the TX and RX. It is demonstrated that the isolation is primarily influenced by the F/B and the cross-polarization level of the two back-to-back antennas. High isolation is achieved by combining the polarization diversity between the TX feed and the RX antenna with the inherent low mutual coupling. Importantly, this combination provides the robustness to the system isolation towards electrical and geometrical asymmetries. That is, 61 dB average isolation is achieved by employing the COTS hybrids with high amplitude and phase imbalances as demonstrated. Further, the bandwidth of operation is dependent on the feed and the RX. Hence, an absorber loaded cavity-backed spiral is employed to extend the operational frequencies over nearly 3 octaves (3-18 GHz). The designed system with coaxial cavity antenna has a gain >20 dBic and >7 dBic for the TX and RX, respectively, and VSWR <2 over an octave bandwidth.

Finally, a high gain, dual reflector based quasi-monostatic STAR configuration is introduced for mm-Wave frequencies. Three different approaches are researched all aimed at minimizing the difference between TX and RX gains while achieving high isolation. The Cassegrain reflector is employed due to the proximity of the feed antenna to the source, which reduces the loss in the TX chain. Importantly, the unused area behind the secondary dish is utilized to house the RX antenna. Further, the size of the main dish is reduced to $\sim 10\lambda$, unlike the conventional dual reflectors where prime reflector size is at least $100\lambda$to reduce blockage. Hence, the far field performance deteriorates as explained in Chapter 7. Therefore, techniques to minimize these influences are demonstrated using full-wave simulations. A balance between the difference in TX and RX gain, high isolation, and far-field quality is achieved by using design trade-offs. Additionally, three variants of antennas are proposed for the RX. Specifically, a prime feed single reflector, a tightly coupled Vivaldi array, and a lens corrected high gain QRH. Note, that all these approaches provide isolation >60 dB as illustrated through full-wave simulations and measurements. A 15.24 cm (6") Cassegrain reflector antenna as TX and the RX implemented from QRH is fabricated and characterized. The former has the gain >24 dBi and the latter >16 dBi, with VSWR <2 over the operational bandwidth. By adding the absorber around RX antenna the isolation can be further improved by at least 10 dB.

7.2 Original Contributions

The original contributions of this thesis are:

- Demonstration of novel flush-mountable QRH with turnstile junction based OMT,with 118% bandwidth (VSWR <2.1), and high power handling capability [29].
- A theoretical analysis approach for design of HISs to improve SI cancellation in bi-static STAR antenna systems is developed [29].

- Demonstration of PRS design to provide capacitive reactance over >3:1 frequency bandwidth for TM_0 surface wave [29].

- Implementation of a bi-static STAR system with isolation >60 dB over 3.16:1 bandwidth for the antennas separated by a $4_{\lambda GHz}$ spacing is discussed. This high isolation is achieved by integrating the developed HISs with the TX and RX [29].

- Analysis of impact of scatterers and neighboring antennas on STAR performance through the design and fabrication of multi-band platforms operating from 0.5-45 GHz and 0.5-110 GHz [84].

- Demonstration of first reflector based monostatic in-band full-duplex antenna system with measured isolation > 30 dB [99].

- Improving the impedance bandwidth of a coaxial cavity antenna to an octave bandwidth while maintaining excellent far field performance [99].

- Demonstrates that the conventional struts of an axis-symmetric reflector can be eliminated by employing the inner conductor of the coaxial cavity antenna (feed) as a support therefore reducing the blockage [99].

- A new STAR antenna configuration termed quasi-monostatic is proposed [31, 32]. Demonstrated robustness of quasi-monostatic STAR aperture to electrical and geometrical asymmetries [31, 32].

- Development of three novel dual reflector, quasi-monostatic in-band full-duplex antenna systems. The approaches utilize of the unused space behind the sub-reflector for the RX [125].

7.3 Future Work

In section 6.3.1 it is demonstrated that STAR functionality with high gain and isolation can be attained from a topology, where, the TX is realized from Cassegrain and the RX from the single reflector. This approach results in poor far field performance and deterioration in the impedance match when the size of the main dish is reduced to 9λ (or 6" at 18 GHz). Hence, it is not fully explored in this thesis and further improvement can be made in the future.

However, the configuration is advantageous for the applications/platforms which can support antenna size >12" (or 20λ). The approach will provide high gain >20 dBi for the RX. This increase in gain is beneficial, especially, at mm-Wave frequencies. The increase in size will also increase the separation between the sub-reflector and the TX feed, thereby, minimizing the interaction between them. A low permittivity dielectric support can be employed to provide additional support for sub-reflector. The effect of dielectric, struts, and the radome on far field and STAR performance is an interesting research topic and has not been explored in the existing literature.

A STAR system demonstrated in section 6.4 employs a lens loaded QRH for the RX and Cassegrain reflector for the TX. Therefore, the antennas have a 9.7 dB maximum gain difference, as explained in the section. A feasibility study of integrating an additional lens, either flat or variations of conic sections, can be performed. This modification could minimize the gain difference without significantly deteriorating the TX and STAR performance.

A technique of using a tightly coupled array as the RX instead of an aperture antenna is briefly discussed in section 6.3.2. It is shown that the approach facilitates STAR performance with high isolation, and can be further improved by modifying the amplitude distribution of the array elements. Also, it is demonstrated that 12×12 planar array will reduce the gain difference between the TX and RX to 5 dB. In addition to that, a digital beam forming network can be used to feed the array, which will provide additional functionalities, such as multiple beams, shaped beams, and so forth. Importantly, direction finding (DF) capability can be added along with STAR. Thus, further improving the effectiveness of EW and S operations. Moreover, some components of the RX block such as LNA and frequency down converter can be mounted behind the sub-reflector, thereby, further increasing the received signal strength. A feasibility study of housing entire receiver components under the RX can be carried out. Mounting the receiver would allow the data to be sent digitally, thereby, reducing the number of cables through the struts and in turn the losses. However, an estimation of noise figure (NF) and the solutions to improve should be performed before the practical implementation.

Impact of radome on performance of quasi-monostatic STAR antenna systems can be further researched. Effect of high power on electro-mechanical stress and impact thereof on SI cancellation is of future interest.

Bibliography

[1] Fast track teaching. (2019) Alexander graham bell. [Online]. Available: https:http://www.fasttrackteaching.com/ffap/Unit_3_Industry/U3_Inventions_Telephone.html 1

[2] The Telegraph Office. (2019) Telegraph key. [Online]. Available: http://www.telegraph-office.com/pages/photo_gallery.html 1

[3] T. S. Rappaport, *Wireless Communications: Principles and Practice*, 2nd ed. NJ: Prentice Hall, 2002. 1

[4] The FCC. (2019) Electromagnetic spectrum auctions. [Online]. Available: https://www.fcc.gov/auctions 1

[5] A. Graham, *Communications, Radar and Electronic Warfare*, 1st ed. West Sussex, UK: John Wiley & Sons, 2011, ch. 17. 2, 4

[6] Radar Tutorial. (2019) Radar basics. [Online]. Available: http://www.radartutorial.eu/06.antennas/Duplexer.en.html 3

[7] Ditoml. (2019) Circulators. [Online]. Available: https://www.ditom.com 3, 108

[8] RF Lambda. (2019) Circulators. [Online]. Available: https://www.rflambda.com/search_circulator.jsp 3, 108

[9] M. Duarte and A. Sabharwal, "Full-duplex wireless communications using off-the-shelf radios: Feasibility and first results," in *2010 Conference Record of the Forty Fourth Asilomar Conference on Signals, Systems and Computers*. IEEE, 2010, pp. 1558–1562. 4, 5, 6, 7

[10] D. Bharadia, E. McMilin, and S. Katti, "Full duplex radios," in *ACM SIGCOMM Computer Communication Review*, vol. 43, no. 4. ACM, 2013, pp. 375–386. 4, 7, 8

[11] A. Sabharwal, P. Schniter, D. Guo, D. W. Bliss, S. Rangarajan, and R. Wichman, "In-band full-duplex wireless: Challenges and opportunities," *IEEE Journal on selected areas in communications*, vol. 32, no. 9, pp. 1637–1652, 2014. 4

[12] M. Katanbaf, K.-D. Chu, T. Zhang, C. Su, and J. C. Rudell, "Two-way traffic ahead: Rf\/analog self-interference cancellation techniques and the challenges for future integrated full-duplex transceivers," *IEEE Microwave Magazine*, vol. 20, no. 2, pp. 22–35, 2019. 4, 6

[13] B. Luciano, D. Clayton, G. Joel, M. Matthew, P. David, S. Sanghoon, and W. Naomi, "Star performance with spear (signal processing electronic attack rfic)," *Naval Research Laboratory*, 2014. 4, 14, 37

[14] National Telecommunications & Information Administation. (2019) Usdc. [Online]. Available: https://www.ntia.doc.gov/category/aws3transitionl 4

[15] R. Cacciola, E. Holzman, L. Carpenter, and S. Gagnon, "Impact of transmit interference on receive sensitivity in a bi-static active array system," in *2016 IEEE International Symposium on Phased Array Systems and Technology (PAST)*. IEEE, 2016, pp. 1–5. 4, 9

[16] X. Liu and A. Goldsmith, "Wireless communication tradeoffs in distributed control," in *42nd IEEE International Conference on Decision and Control (IEEE Cat. No. 03CH37475)*, vol. 1. IEEE, 2003, pp. 688–694. 5

[17] E. A. Etellisi, M. A. Elmansouri, and D. S. Filipovic, "Wideband monostatic simultaneous transmit and receive (star) antenna," *IEEE Transactions on Antennas and Propagation*, vol. 64, no. 1, pp. 6–15, 2016. 8, 11, 51

[18] J. Ha, M. A. Elmansouri, P. V. Prasannakumar, and D. S. Filipovic, "Monostatic co-polarized full-duplex antenna with left-or right-hand circular polarization," *IEEE Transactions on Antennas and Propagation*, vol. 65, no. 10, pp. 5103–5111, 2017. 8, 81

[19] H.-S. Jang, W.-G. Lim, W.-I. Son, S.-Y. Cha, and J.-W. Yu, "Microstrip patch array antenna with high isolation characteristic," *Microwave and Optical Technology Letters*, vol. 54, no. 4, pp. 973–976, 2012. 8

[20] A. Kee, M. Elmansouri, and D. S. Filipovic, "Circularly polarized pifa array for simultaneous transmit and receive applications," in *2017 IEEE International Symposium on Antennas and Propagation & USNC/URSI National Radio Science Meeting*. IEEE, 2017, pp. 2303–2304. 8

[21] M. A. Elmansouri, A. J. Kee, and D. S. Filipovic, "Wideband antenna array for simultaneous transmit and receive (star) applications," *IEEE Antennas and Wireless Propagation Letters*, vol. 16, pp. 1277–1280, 2017. 8

[22] M. E. Knox, "Single antenna full duplex communications using a common carrier," in *WAMICON 2012 IEEE Wireless & Microwave Technology Conference*. IEEE, 2012, pp. 1–6. 9, 11, 57, 58, 75

[23] W.-G. Lim, W.-I. Son, K. S. Oh, W.-K. Kim, and J.-W. Yu, "Compact integrated antenna with circulator for uhf rfid system," *IEEE Antennas and Wireless Propagation Letters*, vol. 7, pp. 673–675, 2008. 9, 58

[24] W.-G. Lim and J.-W. Yu, "Balanced circulator structure with enhanced isolation characteristics," *Microwave and Optical Technology Letters*, vol. 50, no. 9, pp. 2389–2391, 2008. 9, 58

[25] P. V. Prasannakumar, M. A. Elmansouri, and D. S. Filipovic, "Broadband reflector antenna with high isolation feed for full-duplex applications," *IEEE Transactions on Antennas and Propagation*, vol. 66, no. 5, pp. 2281–2290, 2018. 9

[26] E. A. Etellisi, M. A. Elmansouri, and D. Filipovic, "Broadband full-duplex monostatic circular-antenna arrays: Circular arrays circular arrays reaching simultaneous transmit and receive operation," *IEEE Antennas and Propagation Magazine*, no. 99, pp. 1–1, 2018. 9

[27] E. A. Etellisi, M. A. Elmansouri, and D. S. Filipović, "Wideband multimode monostatic spiral antenna star subsystem," *IEEE Transactions on Antennas and Propagation*, vol. 65, no. 4, pp. 1845–1854, 2017. 9, 57

[28] J. A. Lyon, M. Ibrahim, C. J. Digenis, A. G. Cha, N. G. Alexopoulos, D. Brundage, and W. W. Parker, "Electromagnetic coupling reduction techniques," 1968. 9, 53

[29] P. V. Prasannakumar, M. A. Elmansouri, and D. S. Filipovic, "Wideband decoupling techniques for dual-polarized bi-static simultaneous transmit and receive antenna subsystem," *IEEE Transactions on Antennas and Propagation*, vol. 65, no. 10, pp. 4991–5001, 2017. 9, 57, 103, 143, 144

[30] K. Kolodziej, P. Hurst, A. Fenn, and L. Parad, "Ring array antenna with optimized beamformer for simultaneous transmit and receive," in *Proceedings of the 2012 IEEE International Symposium on Antennas and Propagation*. IEEE, 2012, pp. 1–2. 10, 33, 57

[31] P. V. Prasannakumar, M. A. Elmansouri, and D. S. Filipovic, "High-directivty broadband simultaneous transmit and receive (star) antenna system," in *2018 IEEE International Symposium on Antennas and Propagation & USNC/URSI National Radio Science Meeting*. IEEE, 2018, pp. 387–388. 10, 94, 144

[32] P. V. Prasannakumar, M. A. Elmansouri, B. Ljubodrag, I. Maxim, and D. S. Filipovic, "High-directivty broadband simultaneous transmit and receive (star) antenna system," *IEEE Transactions on Antennas and Propagation,(under review)*, 2017. 10, 83, 86, 91, 144

[33] M. A. Elmansouri and D. S. Filipovic, "Low-dispersion spiral antennas," *IEEE Transactions on Antennas and Propagation*, vol. 60, no. 12, pp. 5522–5530, 2012. 11

[34] J. Ha and D. S. Filipovic, "Numerical and experimental electro-thermal characterization of log-periodic antennas," in *2016 IEEE International Symposium on Antennas and Propagation (APSURSI)*. IEEE, 2016, pp. 621–622. 11

[35] N. Jastram, M. Radway, and D. S. Filipovic, "Integrated passive front-ends for towed decoys," in *2014 USNC-URSI Radio Science Meeting (Joint with AP-S Symposium)*. IEEE, 2014, pp. 300–300. 11

[36] M. J. Radway, "Mode theory of multi-armed spiral antennas and its application to electronic warfare antennas," Ph.D. dissertation, The University of Colorado, Boulder, 7 2011. 11, 14, 15, 28

[37] N. Marcuvitz, *Waveguide handbook*, 1st ed. NY,USA: McGrawHill, 1951. 11, 16, 23, 60

[38] D. Sievenpiper, L. Zhang, R. F. Broas, N. G. Alexopolous, E. Yablonovitch *et al.*, "High-impedance electromagnetic surfaces with a forbidden frequency band," *IEEE Transactions on Microwave Theory and techniques*, vol. 47, no. 11, pp. 2059–2074, 1999. 11, 33, 42

[39] A. T. Wegener and W. J. Chappell, "Simultaneous transmit and receive with a small planar array," in *2012 IEEE/MTT-S International Microwave Symposium Digest*. IEEE, 2012, pp. 1–3. 11, 33, 57

[40] G. Breed, "An introduction to defected ground structures in microstrip circuits," *High Frequency Electronics*, vol. 7, pp. 50–54, 2008. 11

[41] C. C.C, "Electromagnetic eaves guided by corrugated surfaces," *Bell Telephone Lab., Unpublished Mem.*, 1944. 11, 33, 38, 58

[42] Z. Ying, P.-S. Kildal, and A. Kishk, "Bandwidth of some artificially soft surfaces," in *IEEE Antennas and Propagation Society International Symposium. 1995 Digest*, vol. 1. IEEE, 1995, pp. 390–393. 11

[43] R. King and K. Park, "Synthesis of surface reactances using grounded pin bed structure," *Electronics Letters*, vol. 17, no. 1, pp. 52–53, 1981. 11, 33, 40

[44] D. Shrekenhamer, J. A. Miragliotta, R. Scott, A. Jablon, J. Friedman, D. Harshbarger, and D. F. Sievenpiper, "Cascaded metasurfaces for broadband antenna isolation," in *Metamaterials, Metadevices, and Metasystems 2015*, vol. 9544. International Society for Optics and Photonics, 2015, p. 954424. 11, 46, 49

[45] S. K. Sharma, S. Rao, and L. Shafai, *Handbook of reflector antennas and feed systems volume I: theory and design of reflectors*. Artech House, 2013. 12, 58, 70, 99, 108, 110

[46] T. A. Milligan, *Modern antenna design*. John Wiley & Sons, 2005. 12, 14, 38, 58, 69, 70, 108, 110, 111, 112

[47] C. A. Balanis, *Antenna theory: analysis and design*. John wiley & sons, 2016. 14, 38, 58, 79, 107, 108

[48] N. J. Jastram, "Passive front-ends for wideband millimeter wave electronic warfare," Ph.D. dissertation, University of Colorado at Boulder, 2014. 14, 15, 21, 23, 28

[49] A. Akgiray, S. Weinreb, W. A. Imbriale, and C. Beaudoin, "Circular quadruple-ridged flared horn achieving near-constant beamwidth over multioctave bandwidth: Design and measurements," *IEEE Transactions on antennas and propagation*, vol. 61, no. 3, pp. 1099–1108, 2013. 14, 15, 17, 28

[50] T. S. Beukman, P. Meyer, M. V. Ivashina, and R. Maaskant, "Modal-based design of a wideband quadruple-ridged flared horn antenna," *IEEE Transactions on Antennas and Propagation*, vol. 64, no. 5, pp. 1615–1626, 2016. 14, 15, 19

[51] R. J. Bauerle, R. Schrimpf, E. Gyorko, and J. Henderson, "The use of a dielectric lens to improve the efficiency of a dual-polarized quad-ridge horn from 5 to 15 ghz," *IEEE Transactions on Antennas and Propagation*, vol. 57, no. 6, pp. 1822–1825, 2009. 14

[52] F. F. Dubrovka and S. Piltyay, "A high performance ultrawideband orthomode transducer and a dual-polarized quad-ridged horn antenna based on it," in *2011 VIII International Conference on Antenna Theory and Techniques*. IEEE, 2011, pp. 176–178. 14, 15

[53] A. Giacomini, A. Potenza, R. Morbidini, and L. Foged, "Quad-ridge dual polarized antenna for use in the 2–32ghz band," in *2012 6th European Conference on Antennas and Propagation (EUCAP)*. IEEE, 2012, pp. 769–772. 14

[54] K. V. Hoel, T. Hellum, and S. Kristoffersen, "High power properties of 3d printed antennas," in *2016 IEEE International Symposium on Antennas and Propagation (APSURSI)*. IEEE, 2016, pp. 823–824. 15

[55] E. F. Kuester, *Theory of waveguides and transmission lines*. Crc Press, 2016. 16

[56] K. Walton and V. Sundberg, "Broadband ridged horn design," *Microwave J*, vol. 4, no. 2, pp. 96–101, 1964. 17

[57] P. U. Ansys, Canonsburg. (2019) Electronics desktop-hfss. [Online]. Available: https://www.ansys.com/products/electronics/ansys-hfss 17, 21

[58] W. Burnside and C. Chuang, "An aperture-matched horn design," *IEEE Transactions on Antennas and Propagation*, vol. 30, no. 4, pp. 790–796, 1982. 18

[59] A. Bøifot, E. Lier, and T. Schaug-Pettersen, "Simple and broadband orthomode transducer," in *IEE Proceedings H (Microwaves, Antennas and Propagation)*, vol. 137, no. 6. IET, 1990, pp. 396–400. 20

[60] A. Navarrini and R. L. Plambeck, "A turnstile junction waveguide orthomode transducer," *IEEE Transactions on Microwave Theory and Techniques*, vol. 54, no. 1, pp. 272–277, 2006. 20, 21

[61] G. Engargiola and A. Navarrini, "K-band orthomode transducer with waveguide ports and balanced coaxial probes," *IEEE transactions on microwave theory and techniques*, vol. 53, no. 5, pp. 1792–1801, 2005. 20

[62] G. Pisano, L. Pietranera, K. Isaak, L. Piccirillo, B. Johnson, B. Maffei, and S. Melhuish, “A broadband wr10 turnstile junction orthomode transducer,” *Ieee microwave and wireless components letters*, vol. 17, no. 4, pp. 286–288, 2007. 20

[63] A. Tribak, J. L. Cano, A. Mediavilla, and M. Boussouis, “Octave bandwidth compact turnstile-based orthomode transducer,” *IEEE Microwave and Wireless Components Letters*, vol. 20, no. 10, pp. 539–541, 2010. 20

[64] C. G. Montgomery, R. H. Dicke, and E. M. Purcell, *Principles of microwave circuits*. Iet, 1987, no. 25. 20

[65] N. U. [23] L3 Narda-ATM, Patchogue. (2019) Waveguide to coaxial adapters. [Online]. Available: http://www.atmmicrowave.com/waveguide/adapter/waveguide-to-coaxial-right-angle 21, 24

[66] A. Kerr, “Elements for e-plane split-block waveguide circuits,” *National Radio Astronomy Observatory, ALMA Memo*, vol. 381, p. 5, 2001. 21

[67] J. A. Lyon, R. M. Kalafus, Y. Kwon, C. J. Digenis, M. A. H. Ibrahim, and C.-C. Chen, “Derivation of aerospace antenna coupling-factor interference prediction techniques,” 1966. 32

[68] T. Dinc and H. Krishnaswamy, “At/r antenna pair with polarization-based reconfigurable wideband self-interference cancellation for simultaneous transmit and receive,” in *2015 IEEE MTT-S International Microwave Symposium*. IEEE, 2015, pp. 1–4. 33, 57

[69] W. F. Moulder, B. T. Perry, and J. S. Herd, “Wideband antenna array for simultaneous transmit and receive (star) applications,” in *2014 IEEE Antennas and Propagation Society International Symposium (APSURSI)*. IEEE, 2014, pp. 243–244. 33, 57

[70] P. Hannan and S. Litt, “Capacitive ground plane for a phased array antenna,” in *1968 Antennas and Propagation Society International Symposium*, vol. 6. IEEE, 1968, pp. 115–123. 33

[71] D. Sievenpiper, “High-impedance electromagnetic surfaces [ph. d. dissertation],” *Electrical Engineering Department University of California, Los Angeles, Los Angeles, Calif, USA*, 1999. 33

[72] J. L. Volakis, R. C. Johnson, and H. Jasik, *Antenna engineering handbook*. McGraw-Hill New York, 2007, vol. 1755. 33

[73] S. Tretyakov, *Analytical modeling in applied electromagnetics*. Artech House, 2003. 33

[74] D. A. Watkins, *Topics in electromagnetic theory*. Wiley, 1958. 33, 38, 39

[75] C. P. Scarborough, Q. Wu, D. H. Werner, E. Lier, R. K. Shaw, and B. G. Martin, “Demonstration of an octave-bandwidth negligible-loss metamaterial horn antenna for satellite applications,” *IEEE Transactions on Antennas and Propagation*, vol. 61, no. 3, pp. 1081–1088, 2013. 33, 38, 41, 42

[76] Q. Wu, C. P. Scarborough, D. H. Werner, E. Lier, and R. K. Shaw, “Inhomogeneous metasurfaces with engineered dispersion for broadband hybrid-mode horn antennas,” *IEEE Transactions on Antennas and Propagation*, vol. 61, no. 10, pp. 4947–4956, 2013. 33, 41

[77] C. H. Walter, *Traveling wave antennas*. Dover Publications,[1970, 1970. 38

[78] P.-S. Kildal, “Artificially soft and hard surfaces in electromagnetics,” *IEEE Transactions on Antennas and Propagation*, vol. 38, no. 10, pp. 1537–1544, 1990. 38

[79] R. Lawrie and L. Peters, “Modifications of horn antennas for low sidelobe levels,” *IEEE Transactions on Antennas and propagation*, vol. 14, no. 5, pp. 605–610, 1966. 38

[80] C. Mentzer and L. Peters, “Properties of cutoff corrugated surfaces for corrugated horn design,” *IEEE Transactions on Antennas and Propagation*, vol. 22, no. 2, pp. 191–196, 1974. 38

[81] P. V. Prasannakumar, M. A. Elmansouri, and D. S. Filipovic, “Wideband dual-polarized bi-static simultaneous transmit and receive antenna system,” in *2016 IEEE International Symposium on Antennas and Propagation (APSURSI)*. IEEE, 2016, pp. 1855–1856. 46, 57, 118

[82] M. P. Karaboikis, V. C. Papamichael, G. F. Tsachtsiris, C. F. Soras, and V. T. Makios, "Integrating compact printed antennas onto small diversity/mimo terminals," *IEEE Transactions on Antennas and Propagation*, vol. 56, no. 7, pp. 2067–2078, 2008. 51

[83] J. L. Volakis, A. Chatterjee, and J. Gong, "A class of hybrid finite element methods for electromagnetics: A review," *Journal of electromagnetic waves and applications*, vol. 8, no. 9-10, pp. 1095–1124, 1994. 53, 103

[84] M. Elmansouri, P. Valaleprasannakumar, E. Tianang, E. Etellisi, and D. Filipovic, "Single and dual-polarized wideband simultaneous transmit and receive antenna system," in *2017 IEEE International Symposium on Antennas and Propagation & USNC/URSI National Radio Science Meeting*. IEEE, 2017, pp. 1105–1106. 57, 144

[85] G. Wainwright and C.-C. Chen, "Low-profile broadband reflector antenna designed for low mutual coupling," in *2016 10th European Conference on Antennas and Propagation (EuCAP)*. IEEE, 2016, pp. 1–5. 57, 72

[86] J. Guy and D. Davies, "Novel method of multiplexing radiocommunication antennas using circular-array configuration," in *IEE Proceedings H (Microwaves, Optics and Antennas)*, vol. 130, no. 6. IET, 1983, pp. 410–414. 58

[87] C. Cutler, "Parabolic-antenna design for microwaves," *Proceedings of the IRE*, vol. 35, no. 11, pp. 1284–1294, 1947. 58, 59, 71

[88] Z. Ying, A. Kishk, and P.-S. Kildal, "Broadband compact horn feed for prime-focus reflectors," *Electronics letters*, vol. 31, no. 14, pp. 1114–1115, 1995. 58

[89] P.-S. Kildal, "Some reflector and feed antenna inventions that made a difference: Fundamentals and examples from radio telescopes, satellite communications and radio links," in *2013 Africon*. IEEE, 2013, pp. 1–3. 58

[90] A. D. Olver and P. J. Clarricoats, *Microwave horns and feeds*. IET, 1994, vol. 39. 58, 69, 129, 130

[91] S. L. Johns and A. Prata, "An ultra-wideband nested coaxial waveguide feed for reflector antenna applications," in *IEEE Antennas and Propagation Society International Symposium. 1999 Digest. Held in conjunction with: USNC/URSI National Radio Science Meeting (Cat. No. 99CH37010)*, vol. 1. IEEE, 1999, pp. 704–707. 58, 60, 62

[92] C. Profera, "Improvement of te 11 mode coaxial waveguide and horn radiation patterns by incorporation of a radial aperture reactance," *IEEE Transactions on Antennas and Propagation*, vol. 24, no. 2, pp. 203–206, 1976. 58, 60

[93] T. Holzheimer, "Applications of the coaxial cavity antenna in time and frequency," in *2004 Antenna Applications Symposium*, 2004, pp. 1–19. 58, 60, 61, 84, 95

[94] ——, "The low dispersion coaxial cavity as an ultra wideband antenna," in *2002 IEEE Conference on Ultra Wideband Systems and Technologies (IEEE Cat. No. 02EX580)*. IEEE, 2002, pp. 333–336. 58, 60

[95] T. Holzheimer and P. Raytheon, "Coaxial cavity antenna exhibiting low dispersion over a wide field of view," *2000 Antenna Appl. Symp*, p. 281, 2000. 58, 60

[96] A. Pippard and N. Elson, "The elimination of standing waves in aerials employing paraboloidal reflectors," *Journal of the Institution of Electrical Engineers-Part IIIA: Radiolocation*, vol. 93, no. 10, pp. 1531–1535, 1946. 58, 71

[97] P.-S. Kildal, "The hat feed: A dual-mode rear-radiating waveguide antenna having low cross polarization," *IEEE transactions on antennas and propagation*, vol. 35, no. 9, pp. 1010–1016, 1987. 58, 59, 69

[98] M. Denstedt, T. Ostling, J. Yang, and P.-S. Kildal, "Tripling bandwidth of hat feed by genetic algorithm optimization," in *2007 IEEE Antennas and Propagation Society International Symposium*. IEEE, 2007, pp. 2197–2200. 58, 59

[99] P. V. Prasannakumar, M. A. Elmansouri, and D. S. Filipovic, "Broadband monostatic simultaneous transmit and receive reflector antenna system," in *2017 IEEE International Symposium on Antennas and Propagation & USNC/URSI National Radio Science Meeting*. IEEE, 2017, pp. 553–554. 59, 144

[100] H. J. Gould, "Dual waveguide probes extending through back wall," Sep. 14 1993, uS Patent 5,245,353. 60

[101] L. Shafai, A. Ittipiboon, E. Bridges, and F. Hyjazie, "Dualband horn with inherent isolation between its transmit and receive ports," in *IEE Proceedings H (Microwaves, Optics and Antennas)*, vol. 131, no. 3. IET, 1984, pp. 143–146. 61, 62, 72

[102] B. H. Simakauskas, "Phase center stabilization of a horn antenna and its application in a luneburg lens feed array," 2015. 64

[103] E. G. Geterud, J. Yang, T. Ostling, and P. Bergmark, "Design and optimization of a compact wideband hat-fed reflector antenna for satellite communications," *IEEE Transactions on Antennas and Propagation*, vol. 61, no. 1, pp. 125–133, 2013. 71

[104] Pulsar microwave corporation, Clifton, NJ. (2019) Jso-04-471/1s. [Online]. Available: https://www.pulsarmicrowave.com/product/hybrid/JSO-04-471-1S 76, 87, 133

[105] RF-Lambda, Plano, TX. (2019) Rfhb04g08gvt. [Online]. Available: http://www.rflambda.com/pdf/hybrid/RFHB04G08GVT.pdf 76, 87, 133

[106] Ditom, Fresno, CA. (2019) D3c4080. [Online]. Available: https://www.ditom.com/cart/product/d3c4080 76

[107] A. Love, "Some highlights in reflector antenna development," *Radio Science*, vol. 11, no. 8-9, pp. 671–684, 1976. 79

[108] J. Ruze, “The effect of aperture errors on the antenna radiation pattern,” *Il Nuovo Cimento (1943-1954)*, vol. 9, pp. 364–380, 1952. 79, 95

[109] National Instruments, CA. (2019) Awr microwave office. [Online]. Available: https://www.awrcorp.com/products/ni-awr-design-environment/microwave-office-software 81, 87, 133

[110] G. Poulton and T. Bird, “Improved rear-radiating waveguide cup feeds,” in *1986 Antennas and Propagation Society International Symposium*, vol. 24. IEEE, 1986, pp. 79–82. 84, 95

[111] Dassault Systemes, Waltham, MA, USA. (2019) Cst microwave studio. [Online]. Available: https://www.cst.com/products/cstmws 94

[112] M. Riel, Y. Brand, Y. Demers, and P. De Maagt, “Performance improvements of center-fed reflector antennas using low scattering struts,” *IEEE Transactions on Antennas and Propagation*, vol. 60, no. 3, pp. 1269–1280, 2012. 100

[113] T. Satoh, S. Endo, N. Matsunaka, S. Betsudan, T. Katagi, and T. Ebisui, “Sidelobe level reduction by improvement of strut shape,” *IEEE transactions on antennas and propagation*, vol. 32, no. 7, pp. 698–705, 1984. 100

[114] Taconic Advanced Dielectric Division. (2019) Tly 5. [Online]. Available: http://www.4taconic.com/page/tly-87.html 103

[115] Microwaves and RF. (2018) What role will millimeter waves play in 5g wireless systems? [Online]. Available: https://www.mwrf.com/systems/what-role-will-millimeter-waves-play-5g-wireless-systems 107

[116] ——. (2014) Millimeter waves enhance military projects. [Online]. Available: https://www.mwrf.com/active-components/millimeter-waves-enhance-military-projects 107

[117] J. Hasch, E. Topak, R. Schnabel, T. Zwick, R. Weigel, and C. Waldschmidt, "Millimeter-wave technology for automotive radar sensors in the 77 ghz frequency band," *IEEE Transactions on Microwave Theory and Techniques*, vol. 60, no. 3, pp. 845–860, 2012. 107

[118] Strategy Analytics. (2016) Electronic warfare and military communications riding the millimeter-wave. [Online]. Available: https://www.strategyanalytics.com/strategy-analytics/blogs/components/defense/defense/2016/04/22/electronic-warfare-and-military-communications-riding-the-millimeter-wave 107

[119] RF Cafe. (2019) Rf atmospheric absorption / ducting. [Online]. Available: http://www.rfcafe.com/references/electrical/ew-radar-handbook/rf-atmospheric-absorption-ducting.htm 107

[120] P. Hannan, "Microwave antennas derived from the cassegrain telescope," *IRE Transactions on Antennas and Propagation*, vol. 9, no. 2, pp. 140–153, 1961. 108, 109, 110, 122

[121] TICRA. (2019) Grasp. [Online]. Available: https://www.ticra.com/software/grasp/ 112

[122] N. Jastram, C. Andrews, and D. S. Filipovic, "Design of circular dual and quad ridge horn antennas for millimeter wave applications," in *2017 11th European Conference on Antennas and Propagation (EUCAP)*. IEEE, 2017, pp. 764–767. 118

[123] W. Williams *et al.*, "High efficiency antenna reflector," *Microwave Journal*, vol. 8, pp. 79–82, 1965. 124

[124] G. Collins, "Shaping of subreflectors in cassegrainian antennas for maximum aperture efficiency," *IEEE Transactions on Antennas and Propagation*, vol. 21, no. 3, pp. 309–313, 1973. 124

[125] P. Valale Prasannakumar, M. Elmansouri, and D. S. Filipovic, "Wideband in-band full-duplex dual reflector antenna," in *2019 United States National Committee of URSI National Radio Science Meeting (USNC-URSI NRSM), Boulder, CO*. IEEE, 2019. 144

Appendix A

Single polarized horn antennas

A.1 Introduction

This chapter presents the simulated and measured impedance and far field performance of the single polarized dual ridge horns operating in 6-19 GHz and 18-45 GHz. These antennas are part of the multi-antenna, monostatic and bi-static STAR platform working from 0.5 to 110 GHz.

A.2 6-19 GHz

In Chapter 3, a single polarized bi-static in-band full-duplex system is presented. High isolation > 60 dB is achieved by the orienting the antennas in its H-plane and modifying the profile and the aperture size of the horns. Klopfenstein and exponential tapers are used for the ridges (in E-plane) and flare, respectively (in H-plane). The rate of exponential taper is selected from the parametric study to achieve side lobe level (SLL) less than 15 dB over the band while maintaining high isolation. The CAD model and the picture of the fabricated antenna is shown in Fig. A.1. The simulated and measured $|S_{11}|$, and gain, radiation patterns of the antennas are shown in Fig. A.2, Fig. A.3, and Fig. A.4, respectively.

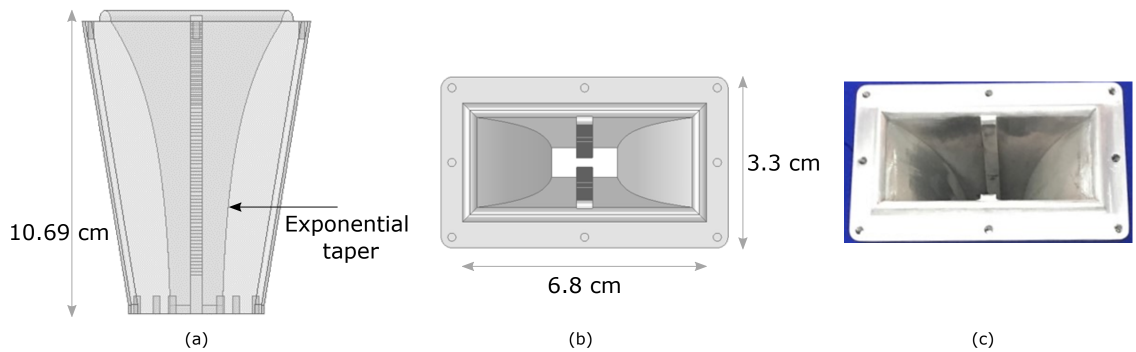

Figure A.1: (a) and (b) Pictures of CAD models and (c) photo of fabricated single polarized double ridge horn antenna.

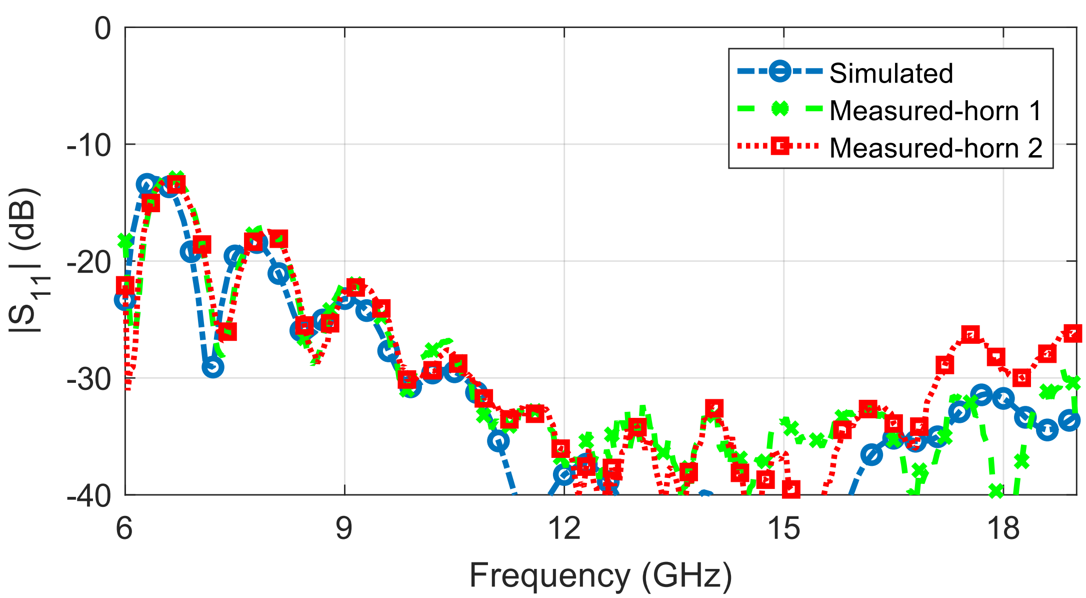

Figure A.2: Simulated and measured $|S_{11}|$ of the designed double ridge horn antenna.

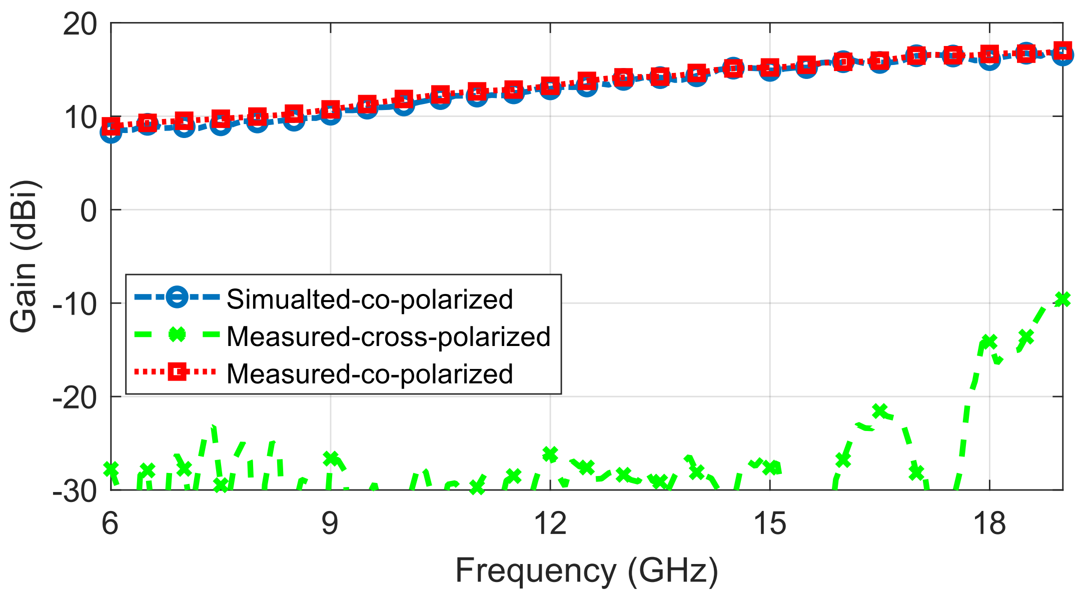

Figure A.3: Simulated and measured gain of the designed double ridge horn antenna.

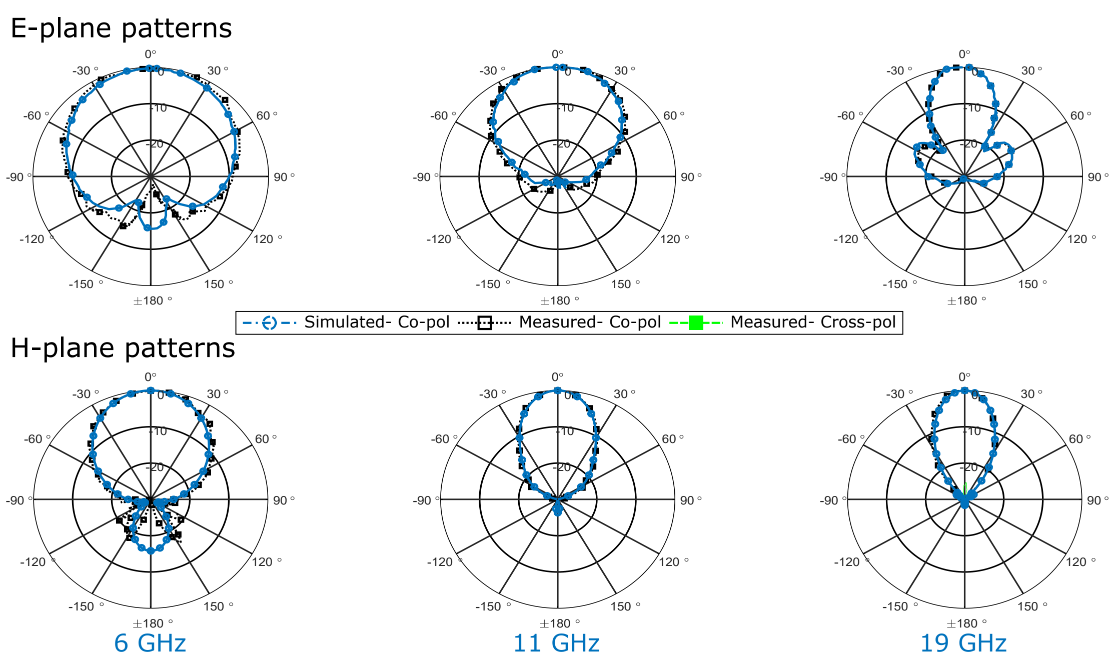

Figure A.4: Simulated and measured far field of the designed double ridge horn antenna at 6, 11 and 19 GHz.

A.3 18-45 GHz

Analogous to 6-19 GHz antenna, a double ridge, a single polarized horn antenna is designed and fabricated to implement a bi-static STAR antenna system, as described in Chapter 3. E-plane ridges of the horn are shaped as Klopfenstein taper, and the flare has the exponential profile. The fabricated antenna has an aperture size $2.26{\times}1.09\,cm^2$, and height 3.8 cm as depicted in Fig. A.5. The antenna has |S11| <-10 dB, and gain >7 dBi over the bandwidth as shown in the Fig. A.6 and A.7, respectively. Also, symmetric radiation patterns with low side lobes as illustrated in Fig. A.8.

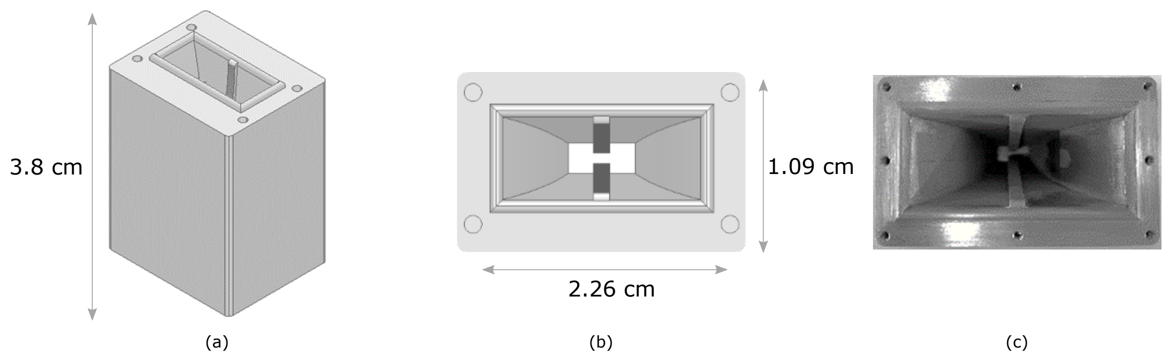

Figure A.5: Simulated and measured $|S_{11}|$ of the designed double ridge horn antenna.

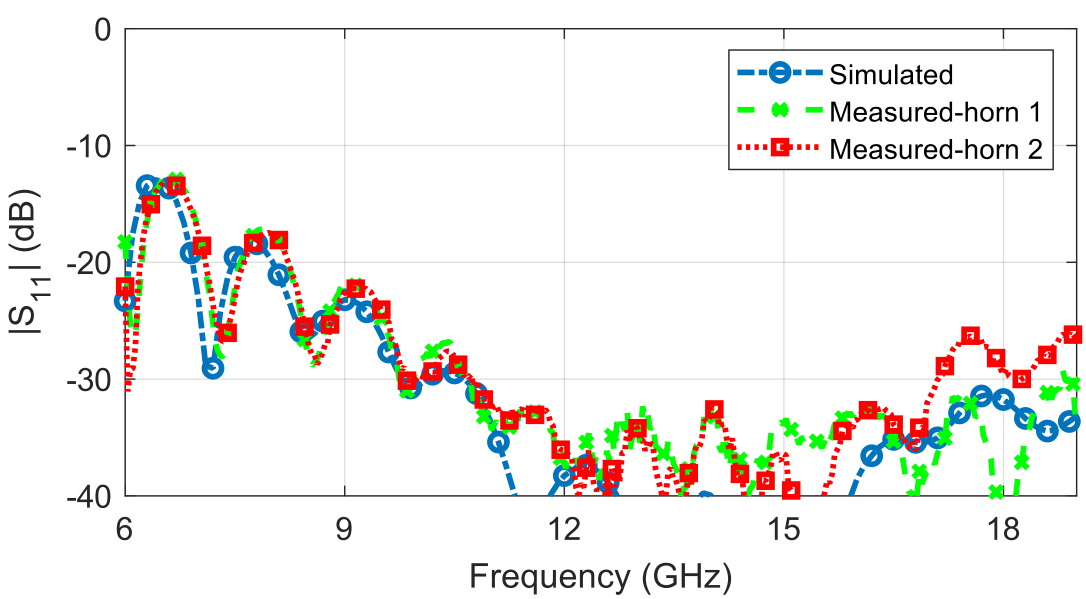

Figure A.6: Simulated and measured $|S_{11}|$ of the designed double ridge horn antenna.

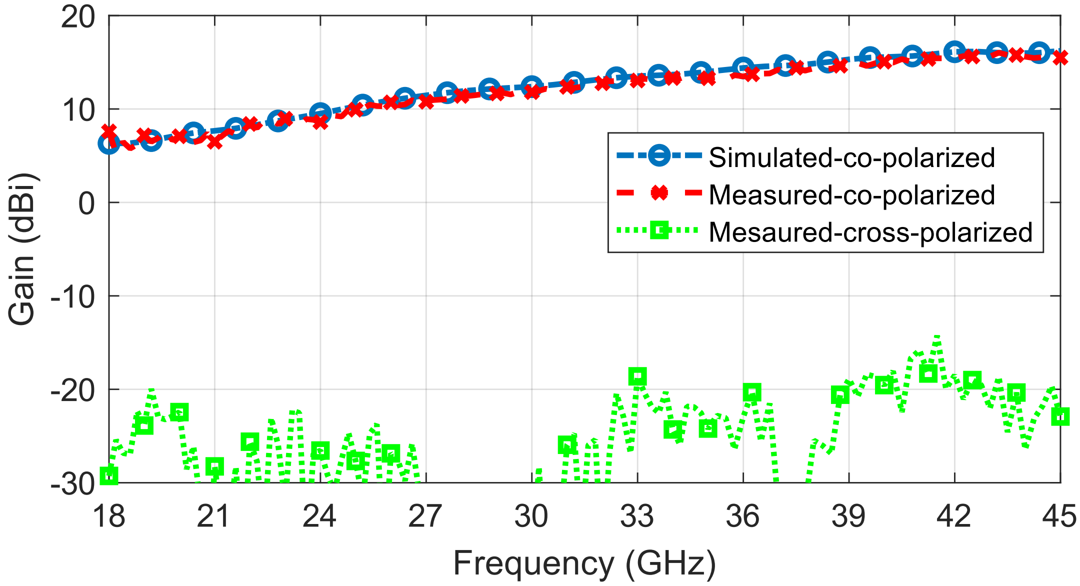

Figure A.7: Simulated and measured gain of the designed double ridge horn antenna.

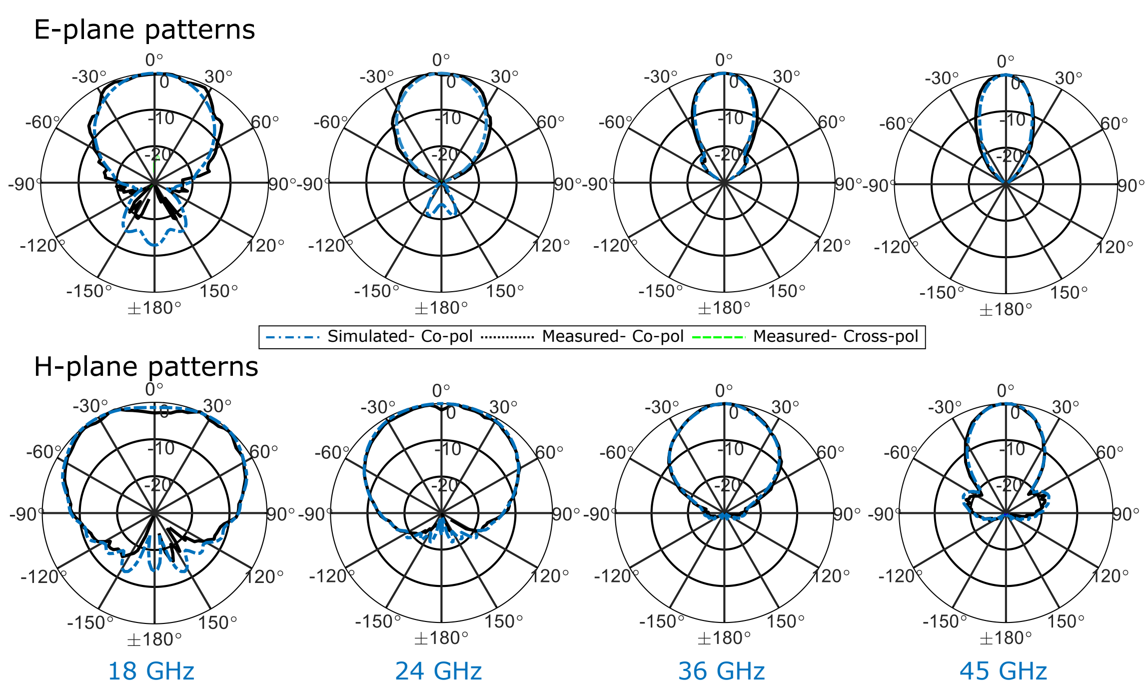

Figure A.8: Simulated and measured far field of the designed double ridge horn antenna at 18, 24, 36 and 45 GHz.